Thermo-Dynamical Measurements For Atlas Inner Detector

(Evaporative Cooling System)

Alexander Bitadze

University of Glasgow

Department of Physics and Astronomy

Submitted in fulfilment of the requirements

for the degree of Doctor of Philosophy

February 2013

Abstract

During the construction, installation and initial operation of the Evaporative Cooling System for the ATLAS Inner Detector SCT Barrel Sub-detector, some performance characteristics were observed to be inconsistent with the original design specifications, therefore the assumptions made in the ATLAS Inner Detector TDR were revisited. The main concern arose because of unexpected pressure drops in the piping system from the end of the detector structure to the distribution racks. The author of this theses made a series of measurements of these pressure drops and the thermal behavior of SCT-Barrel cooling Stave. Tests were performed on the installed detector in the pit, and using a specially assembled full scale replica in the SR1 laboratory at CERN. This test setup has been used to perform extensive tests of the cooling performance of the system including measurements of pressure drops in different parts of system, studies of the thermal profile along the stave pipe for different running conditions / parameters and coolant flow measurements in the system. The pressure drops in the system and the associated temperatures in the barrel cooling loops have been studied as a function of the system variables, for example; input liquid pressure, vapour back pressure, module power load and input liquid temperature. Measurements were performed with 10, 11, 12, 13 bar_{abs} inlet liquid pressure in system, 1.2, 1.6, 2.0, 2.5, 3.0, 4.0, 5.0, 6.0 bar_{abs} vapour back pressure in system, and 0 W, 3 W, 6 W, 9 W, 10.5 W power applied per silicon module. The measurements clearly show that the cooling system can not achieve the design evaporation temperature of

-25°C in every part of the detector (SCT Barrel loops) in case of 13 bar_{abs} nominal inlet liquid pressure, 1.2 bar_{abs} minimum possible back pressure and 6 W nominal power per SCT Barrel silicon module and especially at the end of the ATLAS ID operation period when modules will work on full power of 10.5 W. This will lead to the problem of thermal run-away of the ATLAS SCT, especially near the end of the operational period after significant radiation exposure has occurred. The LHC luminosity profile, depletion voltage and leakage current values and the total power dissipated from the modules were revised. Thermal runaway limits for the ATLAS SCT sub-detector were also revised. Results show that coolants evaporation temperature necessary for the sub-detector's safe operation over the full lifetime (10 years) is -15°C with a safety factor of 2. Laboratory measurements clearly show that the cooling system can not achieve even this necessary evaporation temperature of -15°C. It is now impossible to make mechanical modifications to the cooling system, for example; changing the diameter of the cooling pipes, or the thermal performance of the in-system heat exchanger or reducing the vapour back pressure. It was therefore decided to investigate changes to the cooling fluid and to test mixtures of Hexafluoroethane (R116) C_2F_6 and Octafluoropropane (R218) C_3F_8 at differing ratios instead of just pure C_3F_8 coolant presently used. For this purpose, a new "blending" machine was assembled in the SR1 laboratory, with a new device an "on-line acoustic flow meter and fluorocarbon coolant mixture analyzer" (Sonar Analyzer) attached to it. The Machines were connected to the already existing laboratory test station and new extensive tests were performed to investigate different proportion of C_3F_8/C_2F_6 blends to find the mixture ratio which resulted in the best operational performance as measured by: the temperature distribution, pressure drops and flow parameters over the system, to ensure best cooling performance of SCT Barrel cooling loops for long term ATLAS SCT operation. Measurements were performed with different percentage of C_2F_6 (1%, 2%, 3%, 5%, 10%, 20%, 25%) coolant in the C_3F_8/C_2F_6 mixture, for different power (0 W, 3 W, 6 W, 9 W, 10.5 W) applied to dummy modules on

the SCT cooling stave, with 13 bar_{abs} inlet liquid pressure and for different vapour back pressures (1.2, 1.6, 2.0, 2.5, 3.0 bar_{abs}) in the system.

Results prove that with 25% of C_2F_6 in the blend mixture, it is possible to lower the evaporation temperature by ≈10°C in the case of nominal operation parameters of the system. The ATLAS Inner Detector Evaporative Cooling System can therefore reach the necessary evaporation temperature and therefore can guarantee thermal stability of the SCT, even at the end of the operation period.

Acknowledgements

I would like to thank Scottish Funding Council and SUPA - Scottish Graduate School in Physics for funding me over the duration of my graduate studies. I would like to thank University of Glasgow, School of Physics and Astronomy and the experimental particle physics group and especially thank the experimental particle physics ATLAS group leader Dr.Craig Buttar

I want to express my gratitude to my supervisor Dr.Richard Bates who offered invaluable assistance, support and guidance.

I would like to thank ATLAS experiment for giving me the possibility to perform my work and I would like to thank the team that I am part of. This thesis would not have been possible without the support of my colleagues. It is an honour to work with them. I want to express special gratitude to Steve McMahon, the ATLAS SCT Project Leader, for financial and personal support, very useful advices and his aid in my work. Special thanks to Pippa Wells, the ATLAS SCT Project Leader, for her support. I want to thank all my colleagues and especially Michele Battistin head of the EN/CV group, Gregory Hallewell from Centre de Physique des Particules de Marseille, Cyril Degeorge from Indiana University, Georg Viehhauser from Oxford University, Vic Vacek and his students Michal Vitek and Martin Doubek from Czech Technical University in Prague, Koichi Nagai from Graduate School of Pure and Applied Sciences, University of Tsukuba, Sergei Katunin from B.P. Konstantinov Petersburg Nuclear Physics Institute (PNPI), Jan Godlewski and Lukasz Zwalinski from CERN,

Stephane Berry and Pierre Bonneau form CERN EN/CV group and Cecilia Rossi from University of Genoa.

I want to express my love and gratitude to my wife Dali Milorava and to my parents Inga Kintsurashvili and Nugzar Bitadze.

Declaration

I declare that except where explicit reference is made to the work of others, this dissertation is the result of my own work. This work has not been submitted for any other degree at the University of Glasgow or any other institution.

Contents

List of figures

List of tables

Chapter 1

Introduction

I have no special talents. I am only passionately curious.

Albert Einstein

From ancient times humans were curious to know what the world surrounding us is made of. This question remains a principal subject of interest for the many scientific studies over the centuries and with technological progress we have the possibility to learn more about the smallest building blocks of the world around us and find an answer to this question.

Particle physics studies the evolution of the Universe in terms of the smallest and fundamental particles and forces created after the Big Bang; the process resulting in the creation of atoms - the smallest elements as it was considered till the 19^{th} century. However, from the beginning of the 19^{th} century, physicists made several discoveries showing that the atom was divisible. It was found that the atom consists of the various subatomic particles: electrons, protons and neutrons. Later experiments proved that constituent of the atom could be broken down even to the smaller elements called quarks.

The nature and the behavior of these smallest particles can only be studied by using large accelerator machines; accelerating particles to the velocity close to the velocity of light and concentrating this energy in the smallest possible space for the collisions.

1.1 LHC Accelerator

The **L**arge **H**adron **C**ollider (The **LHC**) [2] is the largest particle accelerator - collider in the world. It is located at **CERN** near Geneva and extends under the Swiss-French borders having the circumference of 26.7 km. CERN is an international particle physics laboratory where over 6500 researchers from 85 different countries are working in close collaboration. Such huge international collaboration gives the possibility to have immense amount of knowledge, manpower and finances concentrated on the realization of a huge scientific projects like the LHC.

The circular proton-proton collider LHC is placed under the ground at a depth of from 50 m to 170 m. It contains two counter-rotating beams, each with a bunch frequency of 40 MHz, accelerated in this machine up to an energy of 7 TeV. The 3D representation of the LHC accelerator is presented in Figure 1.1 [3] and the design parameters of the LHC are summarised in Table 1.1 [2].

Parameter	**Value**
LHC circumference [km]	26.66
Beam energy [TeV]	7.0
Dipole field at 7 TeV [T]	8.33
Dipole magnet temperature [K]	1.9
Number of particles per bunch	1.15×10^{11}
Number of bunches per beam	2808
Bunch crossing frequency [MHz]	40.08
Time between bunches [ns]	25
Expected instantaneous luminosity [$cm^{-2}s^{-1}$]	10^{34}
Expected total integrated luminosity [fb^{-1}]	730

Table 1.1: Design parameters of the LHC.

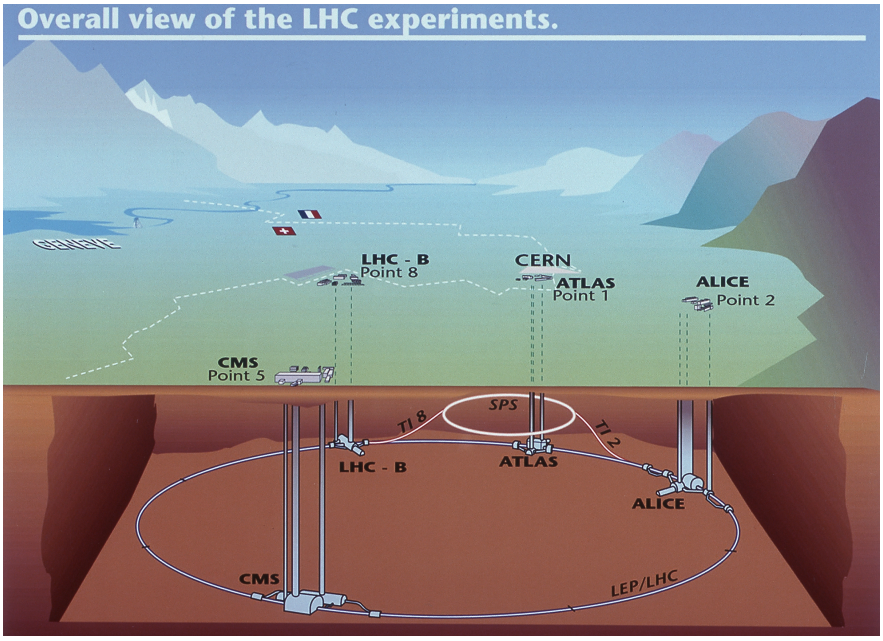

Figure 1.1: Large Hadron Collider, 3D Representation.

The LHC accelerator ring consists of eight straight sections and each of them are followed by the section which bends the particles. One of these straight sections contains the RF cavities [4] used to accelerate the particles and another one contains the beam dump. Two straight sections are used to clean the beam halo and in the remaining four straight sections there are beam interaction points around which detectors are installed. To bend the two counter - circulating beams 1232 superconducting dipole magnets are installed in the LHC ring. Magnets are cooled by Helium (He) to 1.9 K and provide a magnetic field of 8.3 T in the full operation mode. At the beginning of the acceleration process protons are injected from the small linear accelerator and following it boosted into the PS (Proton Synchrotron) and are accelerated to 26 GeV. From the PS accelerated protons are injected into the SPS (Super Proton Synchrotron) [5] which accelerates them at 450 GeV and injects into LHC. In the fully operational mode particles in the LHC are accelerated to 7 TeV (per counter - circulating beam).

In the LHC at the beam interaction points there are four experiments (particle detectors) installed: **ATLAS** (A Toroidal LHC ApparatuS) [6], **CMS** (Compact

Muon Solenoid) [7], **LHCb** (LHC beauty experiment) [8] and **ALICE** (A Large Ion Collider Experiment) [9].

1.2 ATLAS

Several thousand physicists, engineers and technicians from 172 institutes in 37 countries are involved in the large international collaboration working on the design, development, installation, commissioning and operation of the ATLAS detector. Physics goals of the ATLAS experiment, as one of the general purpose detectors at LHC collider, is the search for the Higgs boson, investigation of the extra dimensions, and search for the particles that could form dark matter. In the ATLAS experiment extensive measurements are performed to detect, analyse and identify the behavior of the particles created after the collisions by reconstructing and recording particles paths, their energies and properties. General requirements and design criteria of the ATLAS experiment based on the physics goals can be summarised as following [6]:

- Very good electromagnetic calorimetry with radiation-hard electronics and sensor elements for electron and photon identification and measurement and for accurate jet and missing transverse energy measurements;
- High-precision muon momentum measurements for the precise bunch crossing identification, ability to determine unambiguously the charge of high p_T muons and the accurate momentum measurements at the highest luminosity in the case of using the external muon spectrometer alone;
- Efficient tracking at high-luminosity for the high transverse lepton momentum measurement and at lower luminosity for the electron, photon, τ-lepton and heavy flavor identification and for the full event reconstruction.
- Large acceptance in pseudorapidity (η) with the almost full azimuthal angle coverage;

- Good resolution for charged-particle momentum identification and good reconstruction efficiency in the inner tracker;
- High efficiency of triggering and measurements of particles at low transverse momentum thresholds, providing high efficiencies for most physics processes at LHC.

The overall ATLAS detector layout is presented in Figure 1.2 [3] and the main performance goals are listed in Table 1.2 [6].

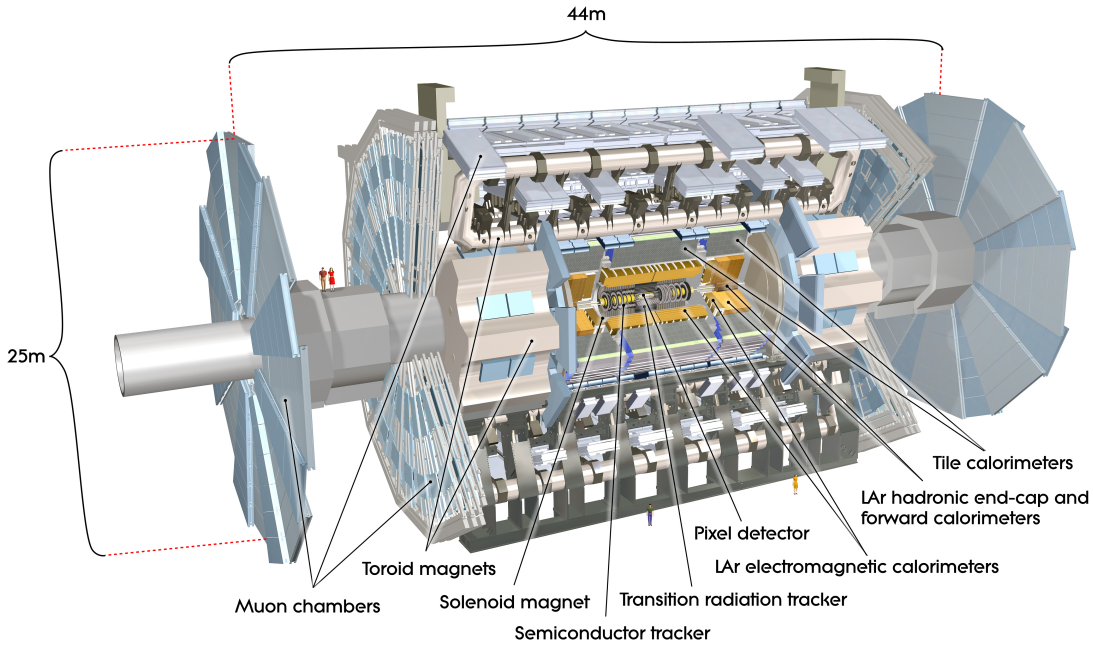

Figure 1.2: ATLAS detector, 3D Representation.

The ATLAS detector is assembled in Point 1 under the ground in the UX15 cavern. The total height of the detector equals to 25 m and the total length equals to 44 m. The overall weight of the detector is approximately 7000 tonnes. There are HS [10] and HO [11] service platforms assembled around the ATLAS detector and these are used to provide access of the personnel to the detector and to support the service equipment that should be located close to the ATLAS detector. There are two service caverns called US15 and USA15 connected by linking

galleries to the UX15 cavern, one on each side [6]. In these two caverns service racks, electrical control cabinets, cooling station and other service machinery are located.

Detector Component	**Required Resolution**	η **Coverage**	
		Measurement	Trigger
Tracking	$\sigma_{p_T}/p_T = 0.05\% p_T \oplus 1\%$	± 2.5	
EM calorimetry	$\sigma_E/E = 10\%/\sqrt{E} \oplus 0.7\%$	± 3.2	± 2.5
Hadronic calorimetry (jets)			
barrel and end-cap	$\sigma_E/E = 50\%/\sqrt{E} \oplus 3\%$	± 3.2	± 3.2
forward	$\sigma_E/E = 100\%/\sqrt{E} \oplus 10\%$	$3.1 < \lvert\eta\rvert < 4.9$	$3.1 < \lvert\eta\rvert < 4.9$
Muon spectrometer	$\sigma_{p_T}/p_T = 10\%$ at $p_T = 1\,TeV$	± 2.7	± 2.4

Table 1.2: General performance goals of the ATLAS detector.

note: for high p_T muons, the muon-spectrometer performance is independent of the inner-detector system. The units for E are in GeV and for p_T in GeV/c.

The proton-proton interaction point in the center of the ATLAS detector is defined as the origin of the ATLAS coordinate system. The z-axis is oriented parallel to the beam line positive to the anti-clockwise beam direction, the position of the positive x-axis is defined in direction from the interaction point to the center of the LHC ring and the position of the positive y-axis is defined as perpendicular to the x-axis and z-axis pointing upwards. The sides of the ATLAS detector are defined as side A - the side from the interaction point in the positive z direction and side C - the side at negative z. Since the detector is symmetrical use of cylindrical coordinates is very useful. The azimuthal angle ϕ is defined as angle in the XY-plane increasing clockwise from the x-axis and the polar angle θ is defined as an angle in the ZY-plane increasing clockwise from the z-axis. In the physics terminology pseudorapidity, $\eta = -\ln\tan(\theta/2)$ is often used instead of the angle θ since the particle multiplicity is approximately constant as function of η. The transverse momentum p_T, the transverse energy E_T and the missing transverse energy E_T^{miss} are defined in the x-y plane and the distance in the pseudorapidity - azimuthal angle space is defined as $\Delta R = \sqrt{\Delta\eta^2 + \Delta\phi^2}$.

The layout of the ATLAS detector consists of the three major components: Inner detector (Section 1.3), Calorimeter (Subsection 1.2.1), Muon Spectrome-

ter (Subsection 1.2.2), and the magnet system configuration consists of a thin superconducting solenoid assembled around the inner detector and large superconducting toroids: barrel and two end-caps surrounding the calorimeters. The inner detector is embedded in a 2 Tesla magnetic field generated by the solenoid magnet and this field deflects particles so the momentum and electrical charge of these particles can be measured based on their track trajectory. The momentum and vertex measurements are provided by the inner detector Pixel and SCT sub-detectors (high resolution silicon and strip detectors, subsection 1.3.1) and the electron identification by the transition radiation and the momentum measurements are provided by the TRT sub-detector (straw tube based tracking detector, subsection 1.3.2). The inner detector is surrounded by the high granularity liquid-argon (LAr) sampling calorimeters covering the pseudorapidity range of $|\eta|<4.9$. The hadronic calorimetry is provided by the LAr electromagnetic calorimeter, LAr hadronic end-cap and forward calorimeters and by the Tile calorimeters (Subsection 1.2.1). The only charged particles passing through the calorimeters are the muons and they are detected by the muon spectrometer (Subsection 1.2.2) surrounding the calorimeter system. The eight long coil barrel and two end-cap magnets (assembly of the eight flat, square coil units with keystone wedges) create the magnetic field of 0.5 T and 1 T respectively in the central and end-cap regions of the detector. Therefore bending the particle traveling trajectories, minimizing multiple-scattering effects and allowing the particle momenta and electric charge measurements by using the three layers of the high precision muon chambers.

The detail description of the inner detector and it's sub-detector system is presented in Section 1.3. The layout of the inner detector is presented in Figures 1.8 and 1.9 [3] [6] and the main parameters of the sub-detectors are listed in Tables 1.6 and 1.7 [6] [12].

1.2.1 Calorimetry

The ATLAS calorimeter system surrounding the inner detector and the solenoid magnet consists of the electromagnetic calorimeter used to identify photons and electrons and precisely measure their energy; the hadronic calorimeter used to measure the energy of the charged and neutral hadrons; and the radiation hard forward calorimeter providing both electromagnetic and hadronic calorimetry functions in the highest radiation region. The calorimeter system also prevents electromagnetic and hadronic showers from entering the muon system. The large $|\eta| < 4.9$ coverage of the the calorimeter system and the fine granularity gives the possibility to precisely measure particle energy and improves the detection of the missing transverse energy E_T^{miss}(important part for the jet reconstruction).

The layout of the ATLAS calorimeter system is presented in Figure 1.3 [6] and the main parameters are summarised in Table 1.3 [6]

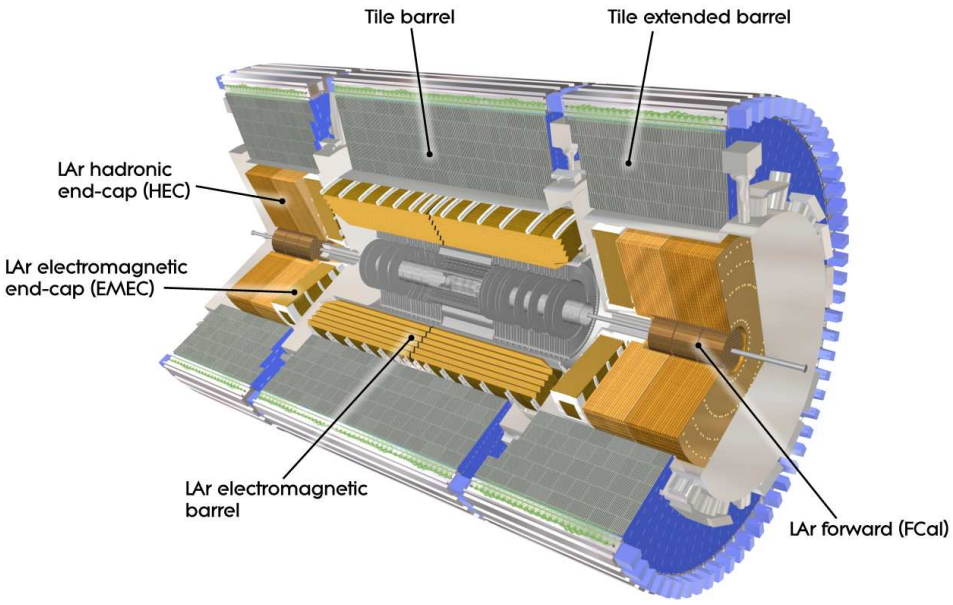

Figure 1.3: Cut-away view of the ATLAS calorimeter system.

	Barrel		End-cap	
EM calorimeter				
Number of layers and $\|\eta\|$ coverage				
Presampler	1	$\|\eta\| < 1.52$	1	$1.5 < \|\eta\| < 1.8$
Calorimeter	3	$\|\eta\| < 1.35$	2	$1.375 < \|\eta\| < 1.5$
	2	$1.35 < \|\eta\| < 1.475$	3	$1.5 < \|\eta\| < 2.5$
			2	$2.5 < \|\eta\| < 3.2$
Granularity $\Delta\eta \times \Delta\varphi$ versus $\|\eta\|$				
Presampler	0.025×0.1	$\|\eta\| < 1.52$	0.025×0.1	$1.5 < \|\eta\| < 1.8$
Calorimeter 1st layer	$0.025/8 \times 0.1$	$\|\eta\| < 1.40$	0.050×0.1	$1.375 < \|\eta\| < 1.425$
	0.025×0.025	$1.40 < \|\eta\| < 1.475$	0.025×0.1	$1.425 < \|\eta\| < 1.5$
			$0.025/8 \times 0.1$	$1.5 < \|\eta\| < 1.8$
			$0.025/6 \times 0.1$	$1.8 < \|\eta\| < 2.0$
			$0.025/4 \times 0.1$	$2.0 < \|\eta\| < 2.4$
			0.025×0.1	$2.4 < \|\eta\| < 2.5$
			0.1×0.1	$2.5 < \|\eta\| < 3.2$
Calorimeter 2nd layer	0.025×0.025	$\|\eta\| < 1.40$	0.050×0.025	$1.375 < \|\eta\| < 1.425$
	0.075×0.025	$1.40 < \|\eta\| < 1.475$	0.025×0.025	$1.425 < \|\eta\| < 2.5$
			0.1×0.1	$2.5 < \|\eta\| < 3.2$
Calorimeter 3rd layer	0.050×0.025	$\|\eta\| < 1.35$	0.050×0.025	$1.5 < \|\eta\| < 2.5$
Number of readout channels				
Presampler	7808		1536 (both sides)	
Calorimeter	101760		62208 (both sides)	
LAr hadronic end-cap				
$\|\eta\|$ coverage			$1.5 < \|\eta\| < 3.2$	
Number of layers			4	
Granularity $\Delta\eta \times \Delta\varphi$			0.1×0.1	$1.5 < \|\eta\| < 2.5$
			0.2×0.2	$2.5 < \|\eta\| < 3.2$
Readout channels			5632 (both sides)	
LAr forward calorimeter				
$\|\eta\|$ coverage			$3.1 < \|\eta\| < 4.9$	
Number of layers			3	
Granularity $\Delta x \times \Delta y$ (cm)			FCal1: 3.0×2.6	$3.15 < \|\eta\| < 4.30$
			FCal1: $\sim$ four times finer	$3.10 < \|\eta\| < 3.15$, $4.30 < \|\eta\| < 4.83$
			FCal2: 3.3×4.2	$3.24 < \|\eta\| < 4.50$
			FCal2: $\sim$ four times finer	$3.20 < \|\eta\| < 3.24$, $4.50 < \|\eta\| < 4.81$
			FCal3: 5.4×4.7	$3.32 < \|\eta\| < 4.60$
			FCal3: $\sim$ four times finer	$3.29 < \|\eta\| < 3.32$, $4.60 < \|\eta\| < 4.75$
Readout channels			3524 (both sides)	
Scintillator tile calorimeter				
	Barrel		Extended barrel	
$\|\eta\|$ coverage	$\|\eta\| < 1.0$		$0.8 < \|\eta\| < 1.7$	
Number of layers	3		3	
Granularity $\Delta\eta \times \Delta\varphi$	0.1×0.1		0.1×0.1	
Last layer	0.2×0.1		0.2×0.1	
Readout channels	5760		4092 (both sides)	

Table 1.3: Main parameters of the calorimeter system.

The electromagnetic calorimeter represents a sampling calorimeter with the working principle based on the use of lead as the absorber material and liquid argon (LAr) as the sampling material. The absorber plates have accordion style geometry ensuring the hermetic and complete coverage in ϕ [6]. The high granularity in the η-direction of the elements, especially in the inner section of the calorimeter, allows precise position measurements and gives the precise information about the energy deposition and shower development in this part of the ATLAS detector. The liquid-argon electromagnetic calorimeter consists of the barrel and two end-cap parts and in total covers the pseudorapidity range of $|\eta| < 3.2$ [6]. The total thickness of the barrel part of the electromagnetic calorimeter is more than 22 radiation lengths and the thickness of the end-cap parts is more than 24 radiation lengths. The energy resolution of the LAr EM calorimeter equals to $\Delta E/E = 11.5\%/\sqrt{E} \oplus 0.5\%$ and the resolution of the polar direction of the particle shower equals to $\Delta\theta = 50\,mrad/\sqrt{E}$ (E in GeV) [6].

The hadronic calorimeter surrounds the electromagnetic calorimeter and in total covers $|\eta|$ <1.7 region [6]. The barrel part of the HC consist of the tile barrel assembled around the barrel part of the EM calorimeter and two extended tile barrel parts assembled around the end-cap wheels of the EM calorimeter and end-cap wheels of the hadron calorimeter (see Figure 1.3). The tile barrel calorimeter employs the charged particle detection method based on use of the iron absorber tiles interleaved with scintillators as the detection material. These tiles are placed perpendicular to the beam axes and are radially staggered in depth. The end-cap hadronic calorimeter consists of two (one per side) wheels located behind the electromagnetic calorimeter end-cap wheels. Since the end-cap hadronic calorimeter receives higher radiation dose it employs different method based on use of radiation-hard liquid argon and copper absorbers positioned in a parallel plate geometry. The total thickness of the hadronic calorimeter is $9.7\,\lambda$ (λ - hadron interaction length) and in total the average jet energy resolution for the HC equals to $\Delta E/E = 50\%/\sqrt{E} \oplus 3\%$ (E in GeV), with a segmentation of

$\Delta\eta \times \Delta\phi = 0.1 \times 0.1$. [6].

The forward calorimeter wheels are integrated into the end-cap cryostat (placed at each end per side) and each of them consist of one electromagnetic compartment using the liquid argon technology with copper as the absorber material and two hadronic compartments using the tungsten as the absorber material. To minimize the amount of the backscattered neutrons into the inner detector volume the forward calorimeter is positioned 1.2 m further away from the interaction point (compared to the electromagnetic calorimeter end-cap). The thickness of the forward calorimeter is approximately 10 interaction lengths and it covers the region of $3.1 < |\eta| < 4.9$.

1.2.2 Muon System

The muon spectrometer illustrated in Figure 1.4 [6] covers the outer most layers of the ATLAS detector and determines its overall geometrical size.

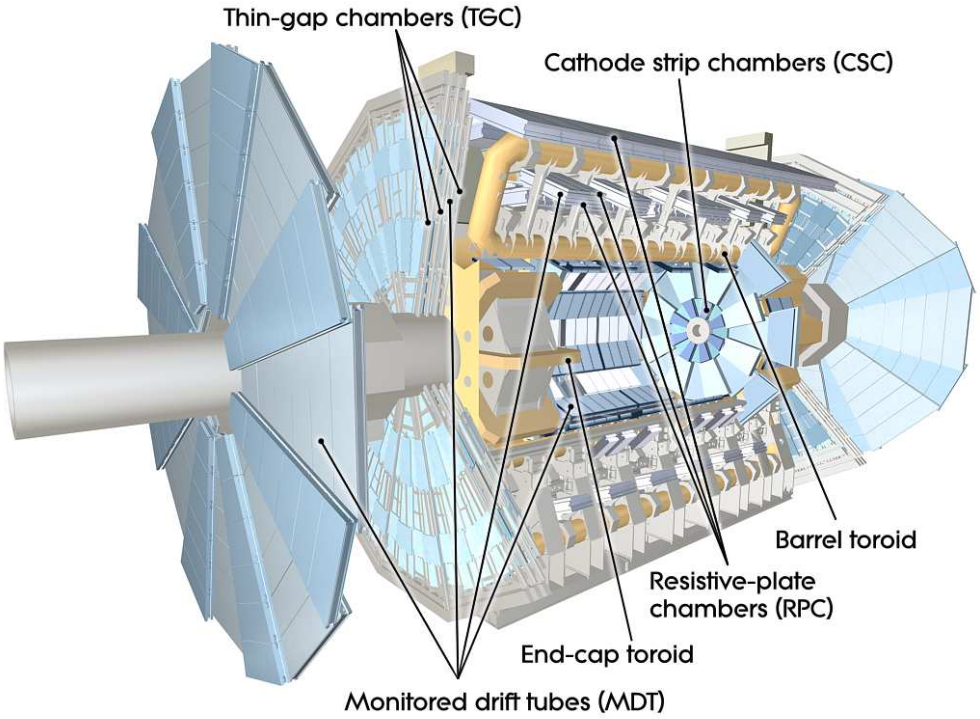

Figure 1.4: Cut-away view of the ATLAS muon system.

The overall length of the muon system is 44 m and total height equals to 25 m.

The muon spectrometer is used for the detection of the charged particles (high p_T muons) exiting the calorimeter system, their momentum measurement and their track reconstruction. The muon tracks are deflected by the magnetic field formed by the large superconducting toroid magnets. The muon spectrometer covers the pseudorapidity range $|\eta| < 2.7$. The stand-alone transverse momentum resolution of the muon spectrometer is ≈10 % for the 1 TeV tracks and it can be translated into the sagitta (along the z-axis of about 500 μm) measurement resolution of ≈50 μm [6]. Due to the large dimensions of the muon system it is critical to have correct/precise alignment for the system components (muon chambers). For this purpose the optical alignment system is used and offline calculations/corrections are done to reach the design precision of 30 μm on the relative alignment of the chambers.

The muon system consists of the Monitored Drift Tube (MDT) chambers and the Cathode Strip Chambers (CSCs) used for the precise measurements in η and the Thin Gap Chambers (TGCs) and Resistive Plate Chambers (RPCs) used for the triggering purpose, for the fast but lower resolution η measurements and a second coordinate measurement. (See Figure 1.4).

The Monitored Drift Tube (MDT) chambers consist of the pressurized aluminum tubes (Cathode tube) with the diameter of ≈30 mm operating with the Ar/CO_2 gas mixture at 3 bar pressure and a central 50 μm diameter tungsten-rhenium wire (Anode wire) at a potential of 3.08 kV. A muon crossing the tube excites the electrons (ionization) and they start to drift to the wire. To calculate the distance between the wire and the muon track the drift time of the first electron reaching the wire is used. The maximum drift time is about 700 ns and the resolution of the drift distance is around 80 μm.

The MDT chambers are installed in the both barrel and end-cap regions of the muon system. In the barrel region, which covers the pseudorapidity range of $|\eta| < 1.05$, the MDT chambers are positioned in three concentric layers at

the radii of 5 m, 7.5 m and 10 m from the beam axis. In the end-cap region the MDT chambers, representing the assembly of the three (per side) perpendicular to the Z axis end-cap wheels, are located at ≈7.5 m, ≈13 m and ≈20 m from the interaction point. In the end-cap region MDT end-cap wheels cover the pseudorapidity region of $1.05 < |\eta| < 2.7$ (except in the innermost layer, where $|\eta| < 2.0$).

The Cathode Strip Chambers (CSC) are installed in the inner-most end-cap ring perpendicular to the Z axis and cover the pseudorapidity region of $2 < |\eta| < 2.7$. Two CSC end-cap wheels (one per side) are segmented into the eight large and eight small chambers and each chamber consists of four CSC planes providing the four independent measurements in η and ϕ for each track. The CSC chambers have high spatial resolution and very short electron drift time <30 ns giving the possibility of the precise measurements in the high background forward region. The CSC chambers are multi-wire proportional chambers with operation method based on the use of the cathode strip readout. In the chamber the Anode wires are oriented in the radial direction and the strips (Cathode) are segmented perpendicular to the wires (for the precision coordinate measurement) and parallel (providing the transverse coordinate). The CSCs are fiiled with the Ar/CO_2 gas mixture. Electrodes are at a potential of 1.9 kV. For the CSC precision coordinate resolution is ≈60 μm and the second coordinate resolution is ≈5 mm.

The Resistive Plate Chambers (RPC) are placed in all three MDT barrel layers covering each MDT barrel chamber from the top and the bottom (See Figure 1.4). In the RPC chamber there is a 2 mm gap between the two parallel plates (electrodes at a potential of 4.9 kV) filled with a $C_2H_2F_4$/Iso-C_4H_{10}/SF_6 gas mixture. In the gas ionization occurs by the passage of charged muons and the created electrons drift towards the anode. The signal is read by the capacitive coupling strips fixed to the outer face of the plates. The η strips used to provide the fast p_T estimate for the trigger are parallel to the MDT wires and the ϕ strips,

providing position measurement, are orthogonal to the MDT wires. The electron drifting time between the plates (electrodes) in the RPC is $\leq$10 ns and the pitch of the η strips equals to 23 mm and for the ϕ strips equals to 35 mm.

The thin-gap chambers (TGC) are used for the triggering and for the second coordinate measurements in the end-cap part of the muon system. The TGCs represent the multi-wire proportional chambers with the operation method based on the use of the array of the anode wires and cathode strips at a potential of 2.9 kV. In the TGC chambers thin gap between the plates is filled with a CO_2/n-C_5H_{12} gas mixture where the ionization occurs. The signal from the anode wires (parallel to the MDT EC wires) is used for triggering and the signal from the cathode strips (orthogonal to the wires) is used for the second coordinate measurement. The distance between the anode wires equals 1.4 mm and the distance from the wire to the cathode is 1.8 mm. The TGC provides fast signal in $\leq$25 ns time window.

The main parameters of the muon spectrometer (muon chambers) are summarised in Table 1.4 [6].

Monitored drift tubes	**MDT**
Coverage	$\|\eta\| < 2.7$ (innermost layer: $\|\eta\| < 2.0$)
Number of chambers	1150
Number of channels	354000
Function	Precision tracking
Cathode strip chambers	**CSC**
Coverage	$2.0 < \|\eta\| < 2.7$
Number of chambers	32
Number of channels	31000
Function	Precision tracking
Resistive plate chambers	**RPC**
Coverage	$\|\eta\| < 1.05$
Number of chambers	606
Number of channels	373000
Function	Triggering, second coordinate
Thin gap chambers	**TGC**
Coverage	$1.05 < \|\eta\| < 2.7$ (2.4 for triggering)
Number of chambers	3588
Number of channels	318000
Function	Triggering, second coordinate

Table 1.4: The main parameters of the muon spectrometer.

1.2.3 Trigger System, Data Acquisition and Control

Due to the high bunch crossing rate (40 MHz) in the LHC and several megabits of generated data for each bunch crossing it is obvious that the data set measured in the ATLAS detector is too large to be recorded on physical storage for each event. The purpose of the trigger system is to reduce the total data flow by distinguishing only the interesting physics events. The ATLAS trigger system consists of three main levels: Level 1 trigger where the triggering logic is based on the use of dedicated electronics, Level 2 trigger and Event Filtering levels using software algorithms. In each level the decision made in the previous level is refined and additional selection criteria are applied if necessary. A schematic view of the ATLAS trigger system is illustrated in Figure 1.5 [13].

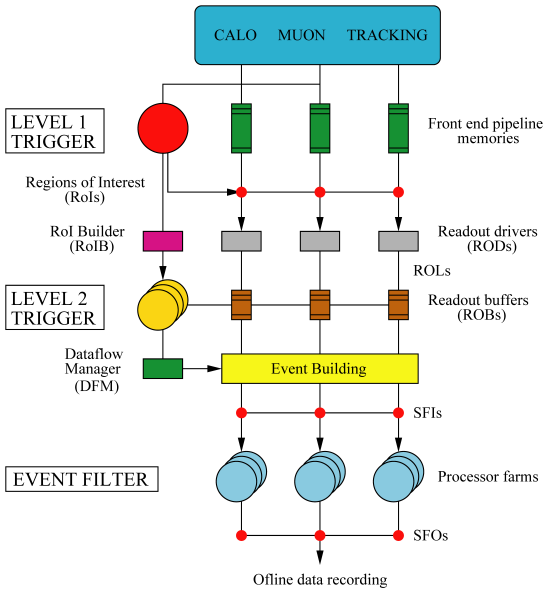

Figure 1.5: The ATLAS trigger system.

Level 1 trigger represents the hardware based trigger which reduces the LHC bunch crossing rate of 40 MHz to a data rate of interesting events of approximately 75 kHz (event processing time $\approx$2.5 μs). The Level 1 trigger uses the information from the electromagnetic and hadronic calorimeters and from the muon system (RPC and TGC chambers) to identify the electrons, photons,

high p_T muons, τ leptons decaying into hadrons and products with large missing transverse energy (E_T^{miss}) produced from the proton-proton collisions. In addition the Level 1 trigger defines the Regions of Interest (RoI) (the region where the interesting feature was detected) in each event giving the geographical coordinates of this regions in η and ϕ and including the information about the type of the feature and the selection criteria of this region. All this information is transferred to the Level 2 trigger.

Level 2 trigger is a software based trigger using algorithms to analyse the data from the Level 1 trigger and it further reduces the data rate to approximately 2 kHz (event processing time ≈40 ms). Level 2 trigger uses in addition data from the precise MDT and CSC muon chambers for better momentum estimation and information from the inner detector about the reconstructed track.

Event Filter uses more complicated and complex software algorithms to do the event identification. All events passing this final stage are then recorded to the data storage and are available for the offline physics analyses. In this stage the event rate is reduced to approximately 200 Hz with the event processing time ≈4 s, this corresponds to a stored data rate of ≈100 Mbs^{-1}. Since this stage of analysis requires large computing resources event filter runs on several computers located in the CERN computer farm.

Readout and Data Acquisition. Events accepted by the Level 1 trigger are transfered from the front-end electronics into the Readout Drivers (RODs) [13] and afterwards to the Readout Buffers (ROBs) [13], where they are analysed and stored until the Level 2 trigger accepts or rejects the event. These digital signals represent specially formated raw data ready to be transfered to the Data Acquisition (DAQ) system. On the first stage of the DAQ data received and stored in RODs and temporary ROB buffers is analysed by the Level 2 trigger, with the additional information about the RoIs, and accepted events are transferred to the event building system. Afterwards the data is sent to the event filter stage for the final event selection. Events selected by the final stage event filter are transfered

to the CERN computer center and are stored permanently and are available for physics analyses. For the data flow in the ATLAS trigger and DAQ system see Figure 1.5 [13].

The Detector Control System (DCS) is used to ensure logical and safe operation of the ATLAS detector. The DCS allows control, monitor and archive of the different operation parameters for the ATLAS sub-detectors and the technical infrastructure of the experiment. This allows the diagnostic and error recovery of the system, which is implemented through the software platform PVSSII [14] based user interface (Finite State Machine (FSM) [15] panel). The DCS also controls the detector operation experts and the detector operation monitoring shifters systems; enables the communication between the detector and the data acquisition system, allowing synchronisation between the data-taking and the detector state and manages the communication between ATLAS and the independently controlled systems like LHC accelerator, technical services and the detector safety system (DSS). The block diagram of the DCS architecture is presented in Figure 1.6 [6].

The screen shot of the ATLAS FSM control panel (the main branch) is presented in Figure 1.7.

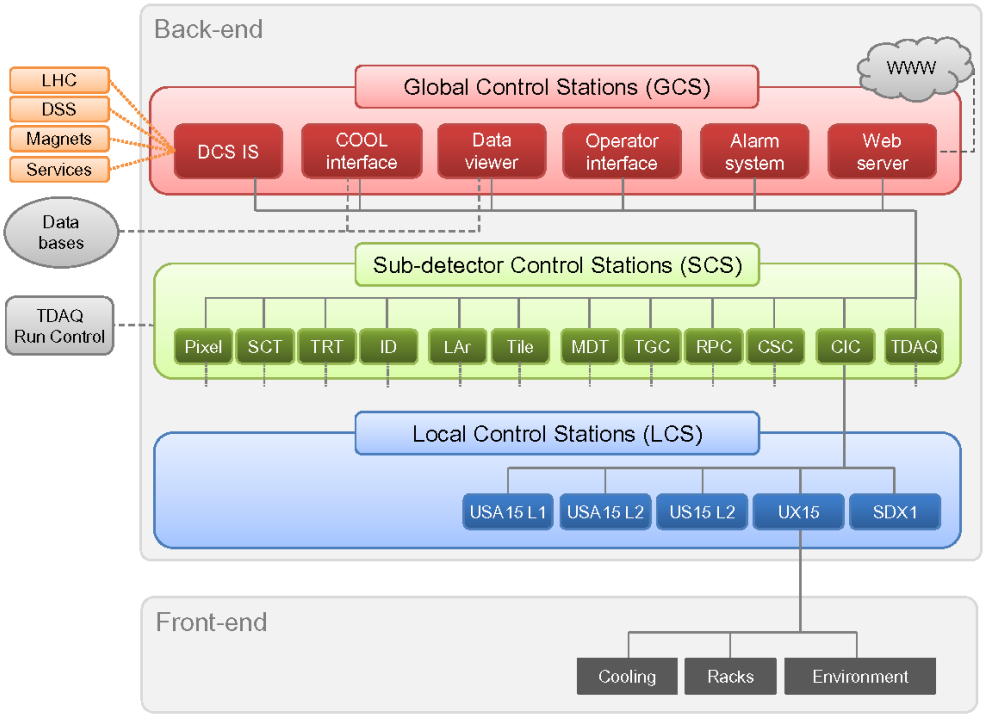

Figure 1.6: Architecture of the DCS.

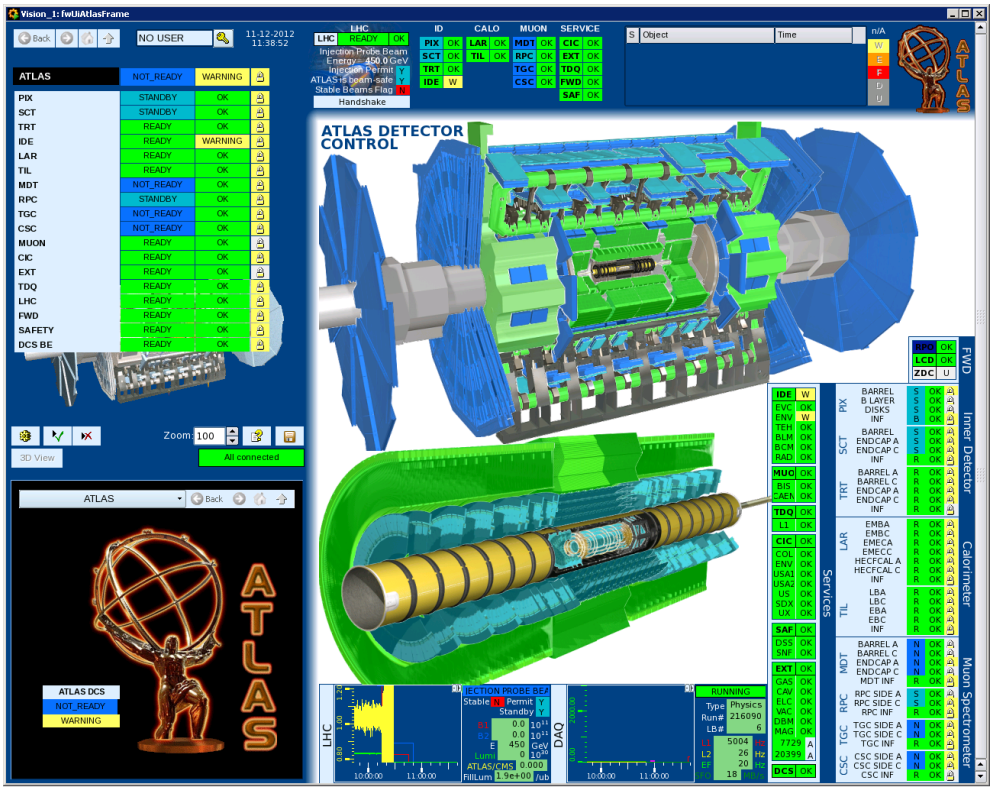

Figure 1.7: The screen shot of the ATLAS FSM control panel.

The Off-line framework. The software framework called Athena [16] is used to analyse the huge amount of recorded data from the ATLAS detector. This framework is designed for the reconstruction of the events from the recorded data and for the simulation of collision events in the ATLAS detector. For these purposes the software framework uses special software packages such as Pythia [17] and GEANT4 [18]. For both the reconstruction and the simulation processes huge amounts of additional information is needed, for example the detailed description of the detector; material description of the sub-detectors, calorimeter and muon system; alignment of the muon structure; state of the magnets and magnetic field; condition of the beam and much more. This kind of information is stored in the on-line database and is updated regularly. The event simulation process consists of several steps including: the simulation of the collision itself, the simulation of the generated particles interacting with the detector material and the simulation of the response of the detector. The various algorithms are employed for the event reconstruction process using the detector response data; both the real (recorded) or the specially simulated data.

1.3 Inner Detector

The purpose of the Inner Detector (ID) [19] [20] tracker is the highly efficient reconstruction of the tracks and vertexes for the events and with the calorimeter and the muon system, the detection and recognition of the particles produced from the collisions (electrons, photons, muons...).

The ATLAS Inner Detector consists of the three separate sub-detectors: the **Pixel Detector**, the **Semiconductor Tracker (SCT)** and the **Transition Radiation Tracker (TRT)**. The schematic drawing of the inner detector layout showing the position of the sub-detectors and their dimensions is presented in Figure 1.8 [12] (the figure shows one quadrant of the ID) and the cut-away view of the inner detector 3D model is presented in Figure 1.9 [6] [3].

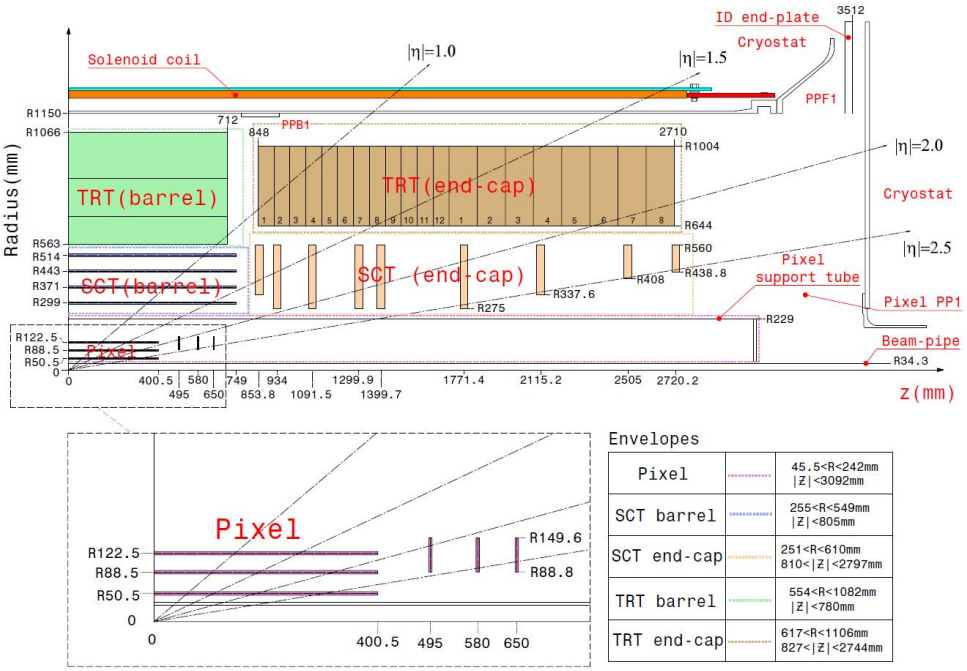

Figure 1.8: Schematic drawing of quarter-section of the ATLAS inner detector showing major detector elements with its active dimensions and envelopes.

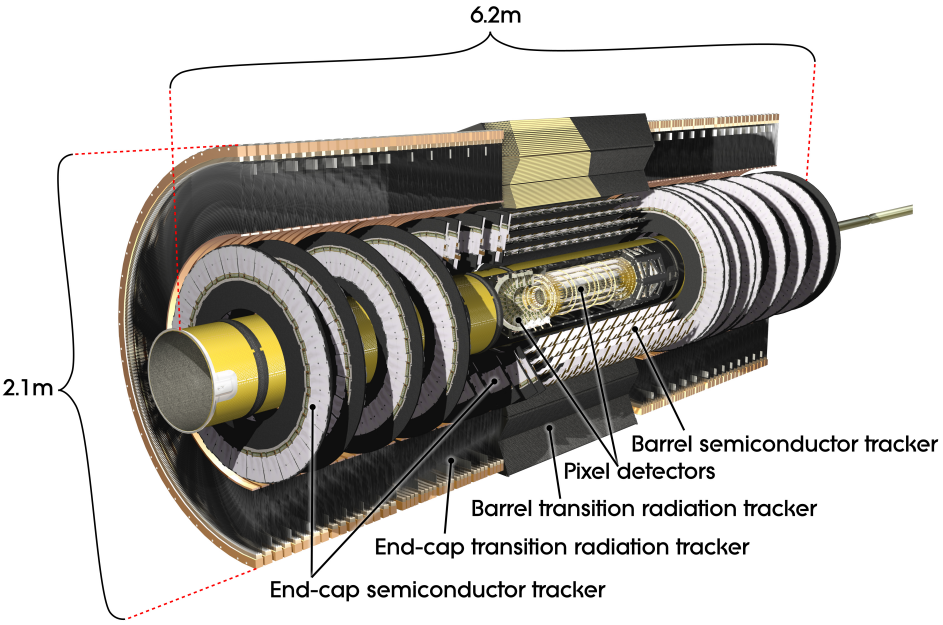

Figure 1.9: Cut-away view of the ATLAS inner detector.

Detector elements are identified as side A and side C for the sections on the +z side of the interaction point and -z side respectively. Each sub-detector consists of the barrel and two endcap sections and in total the ID covers the pseudorapidity range of $|\eta|$ <2.5. The momentum resolution for the inner detector is $\Delta p_T/p_T = 0.04\% \times p_T \oplus 2\%$ (p_T in GeV). The inner detector is surrounded by a solenoid magnet providing 2 T magnetic field, with the field direction parallel to the beam axis, necessary for the bending of the charged particle tracks [6].

Since the particle density is highest close to the interaction point, where the pixel sub-detector is located, high granularity of the innermost detector is essential. The pixel sub-detector consists of three horizontal concentric cylindrical barrel layers and the end-cap region with three discs per side perpendicular to the beam axes. The pixel sub-detector modules (Subsection 1.3.3) with the silicon sensors (Subsection 1.3.1) segmented in small rectangles (pixels) are mounted on the barrel layers and the end-cap discs. The smallest pixel size is $50\times400\mu m^2$ and in total there are 67 million pixels in the barrel region and 13 million pixels in the end-cap discs. The layout parameters of the pixel sub-detector are summarised in Table 1.5 [12].

	Barrel	**End-caps**
silicon area [m^2]	1.45	0.28
number of layers	3 barrels	3 discs (per endcap)
number of pixels [10^6]	67	13
number of modules	1456	288
r-ϕ resolution [μm]	12	12
z resolution [μm]	110	110
pseudorapidity coverage	$\|\eta\| \leq 2.5$	$2.0 \leq \|\eta\| < 2.5$
radial coverage [mm]	50.5 < r < 122.5	88.8 <r< 149.6

Table 1.5: Layout parameters of the pixel detector.

The SCT detector is located around the pixel detector and it consists of the barrel region with four concentric horizontal layers and the end-cap region with nine discs (per side) perpendicular to the beam axis. Since the particle density in this region is low enough detector modules with silicon strip sensors

	Barrel	**End-caps**
silicon area [m^2]	34.4	26.7
number of layers	4 barrels	9 discs (per endcap)
number of channels [10^6]	3.2	3.0
number of modules	2112	1976
r-ϕ resolution [μm]	17	17
z resolution [μm]	580	580
pseudorapidity coverage	$\|\eta\| \leq 1.2$	$1.2 \leq \|\eta\| < 2.5$
radial coverage [mm]	$299 < r < 514$	$300 < r < 520$

Table 1.6: Layout parameters of the SCT detector.

are used to reduce the number of the readout channels. In the barrel region the strip direction is parallel the solenoid field (beam axis) and in the end-cap region radially outwards and perpendicular to the magnetic field. The barrel sensors have a constant pitch of 80 μm and the end-cap sensors have variable pitch widening towards the larger radii. The strips are read out by the radiation hard ABCD3TA [21] front-end chips. The readout of the SCT modules is binary (i.e. a "1" if a strip was hit and a "0" otherwise) giving the information about the hit strip channel address. The layout parameters of the SCT sub-detector are summarised in Table 1.6 [12].

The Transition Radiation Tracker (TRT) is assembled around the SCT and as well consists of a barrel and two end-cap regions. The TRT is based on straw tube detectors (Subsection 1.3.2): 4 mm inner diameter tubes filled with a $Xe/CO_2/O_2$ gas mixture and having an Anode wire in the center. The TRT barrel region contains 50000 straw tubes oriented parallel to the beam axis while the end-cap region, 20 end-cap wheels per side, contains 320000 tubes pointing to the beam axis. The TRT covers the pseudorapidity range up to $|\eta| < 2.0$ and the tracker geometry guarantees that approximately 40 straw tubes are crossed by each charged particle. This gives the precise tracking possibility at the large radii of the inner detector and increases the pattern recognition ability. When the charged particle passes the TRT straw tube ionization occurs in the gas mixture and electrons drift to the wire (Anode). The wire in each tube is split in half

and read out every 75 ns at each end providing the information about the drift time. The distance from the wire to the track is determined by converting the drift time into the distance. In the TRT straw tube track position measurement accuracy is ≈170 μm. The transition radiation measurement in the TRT is based on use of the polypropylene radiator material [22] [23] which fills the space between the straw tubes. The transition radiation (X-rays) is produced when the charged particle cross the boundary between the two materials having different dielectric constants. The transition radiation depends on the Lorentz factor (γ) and the mass and momentum of the particle. The gas mixture in the straw tubes absorbs X-rays and a large amount of charge is produced. The TRT readout has two thresholds: the low threshold for the ionization detection and the high threshold for the X-ray energy deposit detection, rendering the TRT capable of identifying the electrons. Electron identification efficiency in the ATLAS TRT is ≈90% (for energies ≥2 GeV) [6].

The layout parameters of the TRT tracker are summarised in Table 1.7 [12].

	Barrel	**End-caps**
number of straw layers	73	2×160
number of readout channel	105088	2×122880
drift time resolution Xe [μm]	130	130
drift time resolution Ar [μm]	190	190
pseudorapidity coverage	$\lvert\eta\rvert \leq 1.0$	$1.0 \leq \lvert\eta\rvert < 2.0$
radial coverage [mm]	$563 < r < 1066$	$644 < r < 1004$

Table 1.7: Layout parameters of the TRT detector.

The heat dissipated from the TRT straw tubes (produced by the ionisation current in the gas mixture) is removed in different ways in the TRT barrel and end-cap regions and the temperature along each straw tube is kept $< 10\,^{\circ}$C. In the barrel heat is evacuated through the module shells; the high thermally conductive structure is made of 400μm thick carbon fibers and being part of the support structure for the straw tube matrix and the radiator material. The heat from the straw tubes is transfered to the module shells by conduction through

the CO_2 gas envelope surrounding the TRT structure. Module shells are cooled by the mono-phase cooling circuits (two cooling pipes located in the corners of each module shell) running C_6F_{14} refrigerant. These cooling circuits as well serve to cool the front-end electronics. In the TRT end-cap region the heat dissipated from the straw tubes is evacuated through the CO_2 gas envelope; each end-cap wheel has a separate CO_2 cooling envelope where gas flows continuously with a flow rate of $\approx 50\,m^3h^{-1}$ and the heat from the gas is removed by the external heat exchanger cooled with C_6F_{14} refrigerant.

1.3.1 Pixel and SCT detector sensors

The general operational principle of silicon sensors is based on use of the p-n junction [24]; connection of the two doped silicon regions with different concentration of free electrons and holes. The n-doped region represents an area (usually doped with Arsenic, As) with free electrons and the p-doped region represents an area (usually doped with Boron, B) with free holes, thus a bipolar diode is created. Simple schematic is presented in Figure 1.10.

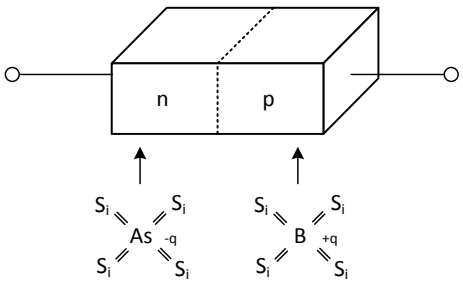

Figure 1.10: p-n junction.

Since the sides of the junction contain excess of electrons or holes a diffusion current flows in both direction; electrons and holes are diffusing leaving behind a region of fixed ions. This region is called the Depletion Region. To extend the depletion region of the sensor an external electrical potential is applied to the junction. See schematic in Figure 1.11.

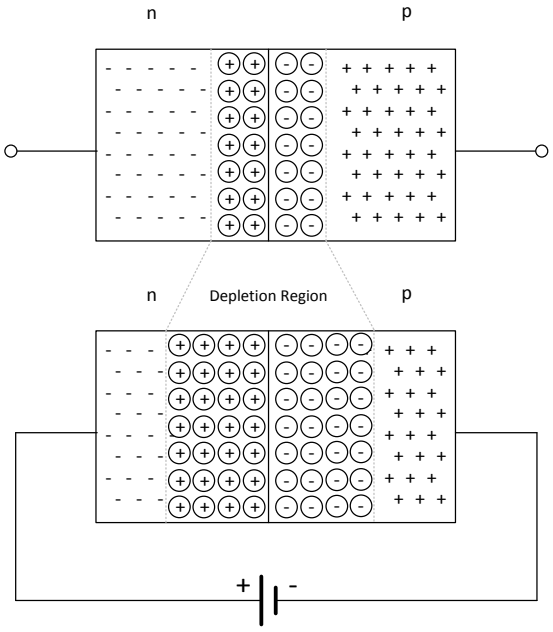

Figure 1.11: Depletion region.

The voltage necessary to increase the width of the depleted region (sensitive region of the sensor) is called the Bias Voltage. The depleted region of the sensor is used for particle detection; electrical charges created by the passage of an ionizing particle through the silicon are drifting to the respective electrodes (electrons into n direction and holes into p direction) forced by the electrical field formed in this area and are detected by the readout electronics connected to the silicon sensor. The advantage of the silicon technology is that energy necessary for the electron-hole pair production in silicon is much less ($\approx$3.6 eV) than in ionizing gases ($\approx$30 eV) or diamond ($\approx$13 eV) therefore giving bigger readout signal directly proportional to the released energy and allowing lower energy particle detection. From the other hand diamonds are more resistive to the radiation damage but their production is much more difficult and expensive.

High luminosity in the LHC (integrated radiation dose in the ATLAS ID) has significant effect on the performance of the Pixel and SCT silicon sensors: displacement of the atoms in the silicon lattice changes effective doping concentration therefore increases the depletion (bias) voltage for the sensors; The

leakage current of the silicon sensor as well increases with the radiation causing an overall increase in the dissipated power from the sensor affecting the subsequent change in the silicon doping concentration and the increase in the required operation voltage (depletion voltage); The Pixel [25] and SCT [26] silicon sensors are designed to cope with these requirements. In the ATLAS inner detector they are operated in the temperature range -5 °C to -10 °C (Section 2.2) to minimise the change in the effective doping concentration and lower the leakage current and can guarantee adequate signal performance over the entire inner detector operation period with the given LHC luminosity.

The pixel silicon sensor represents the 250μm thick detector; the array (pixels) of the bipolar diodes implanted into the n-type bulk. High positive (p^+) and negative (n^+) doped regions are implanted on both sides of the wafer. This allows good charge collection efficiency even after the p-n type inversion caused by the radiation damage [25] . On each sensor 47232 pixel implants with the nominal size of $400\times50\,\mu m^2$ are arranged in 144 columns and 328 rows and in each column eight pairs of pixel implant are ganged resulting in 46080 pixel read-out channels, or 320 independent read-out rows, allowing connection of the sensor tile to the 16 read-out electronic front-end chips. For the quality assurance tests all read-out channels were connected to the common bias grid but in normal operation biasing for each individual pixel is provided by the bump-bond technique [25] through the openings in the passivation layer of the sensor. The nominal bias voltage required for the sensor operation is ≈150 V and the maximum predicted bias voltage, after the maximum expected irradiation with respect of the integrated luminosity and the expected operating temperature profile is ≈600 V. The Pixel sensor design guarantees each pixel isolation and a special p-spray isolation technology [25] was used to allow small feature size and good performance of the sensor after the irradiation.

The SCT sensors are 285±15μm thick silicon detectors with the standard single sided p-n technology, the p-strips on the high resistive n-bulk, with the

AC-coupled readout strips. In total there are 15912 silicon sensors used in the SCT sub-detector. For the SCT barrel sensors 768 readout strips are positioned with 80μm pitch but for the EC sensors are not at a constant pitch since the EC sensors have a wedge-shaped geometry in contrast to the barrel rectangular sensors [26]. The complicated sensor geometry was adopted because of their layout on the EC discs. The different type (geometry) EC sensors are grouped in five and named W12, W21, W22, W31 and W32 to form the sub-detector modules [26]. Each sensor of both the SCT barrel and EC modules are read out by six 128-channel ABCD3TA ASICs [27]. The nominal bias voltage required for the SCT sensor operation, as it was proposed in the ATLAS TDR [6], is ≈150 V and the predicted bias voltage range after the irradiation at the end of the ATLAS inner detector operation period is between 350 V and 450 V depending on the position of the sensor, integrated luminosity and the expected operational temperature profile. These values were revised later in this work in Chapter 3.

1.3.2 TRT straw tubes

The basic elements of the TRT are the 4 mm inner diameter thin-walled proportional drift tubes with the gold plated tungsten anode wire located in the center with the tubes filled with a $Xe/CO_2/O_2$ gas mixture. They are called "straw tubes" [22]. The length of the straw tubes for the TRT barrel equals to 144 cm and for the TRT end-cap to 37 cm. To obtain the necessary mechanical and electrical properties of the tubes a special film coating technology is used; the wall of the straw tubes is formed from the two layers of the 35μm thick multilayer films. These films themself are made of 25μm thick Kapton 100 VN film. On the one side of the Kapton film 0.2μm thick Aluminum (Al) (protected with the 5-6μm thick graphite-polyimide layer) is deposited and the other side of the film is coated with the 4-5μm polyurethane layer used as a sealant. Aluminum provides good electrical conductivity and the graphite-polyimide layer provides good protection of the aluminum layer against damage from the cath-

ode etching effects. To protect the straw tubes against environmental factors like humidity and temperature they are reinforced by carbon fibers. The anode wire for the TRT straw tube is a 31μm thin Tungsten (Wolfram W) wire which is plated with a 0.5-0.7μm layer of gold . The wire is centered in the straw tube and is supported by the end plugs. The electrodes (wire-anode, aluminum tube-cathode) in the straw tube are at a potential of 1530 V. The anode wire in the tube is electrically split in two and is continuously read from the both ends by the front-end electronics. Straw tubes are filed (5-10 mbar over-pressured) with the 70%Xe + 27%CO_2 + 3%O_2 gas mixture which is continuously re-circulated and the mixture composition is continuously monitored. The maximum electron collection time in the straw tubes, in case of the standard conditions, is ≈48 ns and the drift time accuracy is ≈130μm. The charged particle passing through the straw tube causes the ionisation in the gas mixture and free electrons drift to the anode wire (forming an avalanche) and signal is read-out by the front-end electronics. In the space between the straw tubes, filled by the radiator material, transition radiation photons (X-rays) are produced and they are absorbed by the gas mixture in the straw tube, leading to the large charge deposit on the anode wire therefore producing higher signal. In the TRT particle identification is obtained through the two readout signal thresholds; low for the ionization and high for the X-rays absorption. Since the produced transition radiation is different for the particles with the same momentum but different mass (electrons produce the transition radiation if their momentum is above 1 GeV/c, but pions produce the transition radiation if their momentum is ≈100 GeV/c) electron identification (pion rejection) is possible with the TRT (with the identification efficiency of ≈90% for the energies ≥2 GeV [6]).

1.3.3 Inner Detector (Pixel, SCT and TRT) Modules

In total 1744 identical modules cover the barrel and end-cap regions of the pixel detector. Each pixel module represents the assembly of the pixel silicon sensor

containing 47232 pixels; the sixteen 180μm thick front-end electronics chips (FE) each with 2880 electronic channels with amplifying circuitry; fine-pitch bump bonds connecting the electronics channels to the silicon sensor; 100μm thick double sided flexible polyimide printed-circuit board (flex-hybrid) used for the signal and power routing and the module control chip (MCC) glued on it. For the barrel modules, to provide the connection to the electrical services through the microcable, the flexible foil (pigtail) with the Type0 connector is attached, while for the end-cap modules microcables are attached without this pigtail connection. The image of the pixel module (barrel) assembly is presented in Figure 1.12 [25].

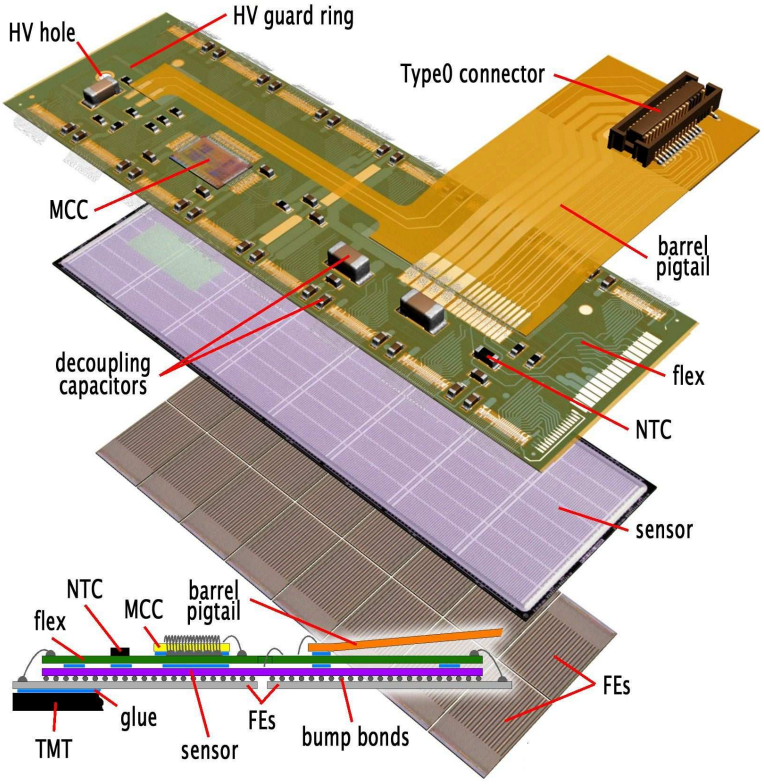

Figure 1.12: The elements of a pixel barrel module.

Signal from the silicon sensor is routed through the copper traces on the flex hybrid to the module control chip and the MCC transmits the digital data to the electrical services out of the module. The low voltages (decoupled) to the chips are distributed through the channels on the flex and the back side of the flex is

pinhole free to guarantee the safe connection to the high voltage side of the silicon sensor. Temperature of the module is monitored by the Negative Temperature Coefficient (NTC) sensor fixed on the flex and in case of module overheat the power to the module is switched off by the fast interlock system.

At the end of the module operation period (with respect to the inner detector integrated luminosity and the temperature profile) it is predicted that pixel module will draw 1.3 A at 1.7 V (analog supply) and 0.9 A at 2.1 V (digital supply) including the voltage drops from the pigtail and the flex, plus voltage drops from the microcables and in addition 1 mA at 600 V for the silicon sensor bias. These yield a total power consumption (dissipated power) for the pixel module of 4.7 W. Since it might be necessary to increase the analog or digital supply voltages for a better performance it was assumed that maximum power consumption per pixel module at the end of the operation period will be ≈6 W [25]. The pixel barrel modules are glued on the Thermal Management Tile (TMT) which itself is attached to the pixel cooling stave (D-shaped Aluminum (Al) tube) by the carbon fiber reinforced plastic (see Section 2.5.1). The pixel end-cap modules are directly mounted on the cooling sectors of the pixel end-cap wheels. Each cooling sector represents the W-shaped Aluminum (Al) tube trapped between the carbon composite sheets and the carbon foam in between the sheets with the thermally conducting adhesive (see Section 2.5.1).

The SCT barrel consists of 2112 modules. Each SCT barrel module represents the assembly of the four SCT barrel silicon sensors (80μm pitch micro-strip sensor) connected to the binary signal readout chips located on the polyimide hybrid which has 12 (6 per side) identical 128 channel ASICs (chips) and bridges the silicon sensors from both sides. The image of the SCT barrel module assembly is presented in Figure 1.13 [28] [6].

These four silicon sensors two on the top and two on the bottom side are positioned back to back in pairs and these pairs are positioned at the stereo rotation angle of 40 mrad. The silicon sensors are glued on a 380μm thick base

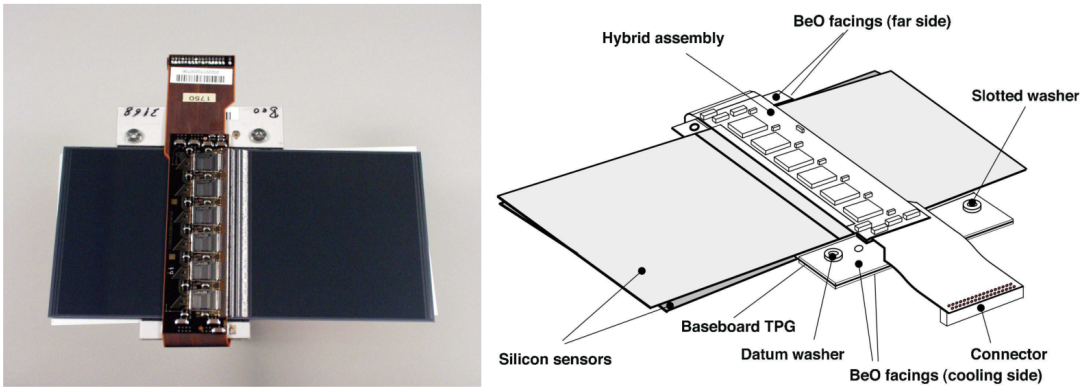

Figure 1.13: Assembly of the SCT Barrel Module.

board made of thermal pyrolitic graphite (TPG) which represents the thermal and mechanical structure of the module. It is extended on both sides and includes beryllia (BeO) facings. High voltage bias supply to the silicon sensors is delivered through the conductive lines on the base board. Cooling of the SCT barrel modules is provided by the SCT barrel cooling stave (see Section 2.5.1).

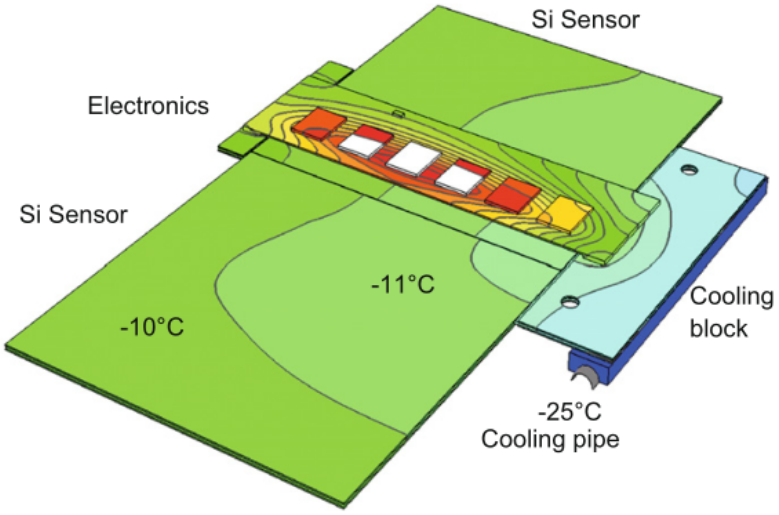

Figure 1.14: Thermal FEA of ATLAS barrel SCT Silicon strip module (top plane with two $6 \times 6\,\mathrm{cm}^2$ sensors visible) with a hybrid power of 6W and a sensor leakage power of $120\mu\mathrm{W/mm}^2$ at 0 °C. Temperatures range from -25 °C (coolant) to 6 °C (electronics maximum). Contours are shown at 1 °C intervals between -20 °C and 4 °C. Note the small variation of temperature (labelled contours) over the sensor surface.

The modules are fixed on the Aluminum (Al) cooling blocks with the layer of the thermal grease and a copper-polyimide capacitive shunt shield. These cooling blocks are soldered on the barrel stave pipe. Heat from the silicon sensor and the hybrid is evacuated through the base board and the hybrid substrate to the beryllia facing which is in direct contact with the cooling block surface. Several calculations were done to predict the thermal behaviour of the SCT barrel modules [29]. Thermal FEA image of the SCT barrel module is presented in Figure 1.14 [29]. Heat propagation over the module and thermal runaway problems are discussed in detail in the following chapters 3, 4, 5.

In total SCT end-cap region consists of 1976 modules. Unlike the barrel in the end-cap there are three different module types; Outer, Middle and Inner depending on the position on the end-cap wheel therefore having the different type of the silicon sensors (W12, W21, W22, W31 and W32 see Subsection 1.3.1) in the assembly. The image of the different type of SCT end-cap modules and module components is presented in Figure 1.15 [30].

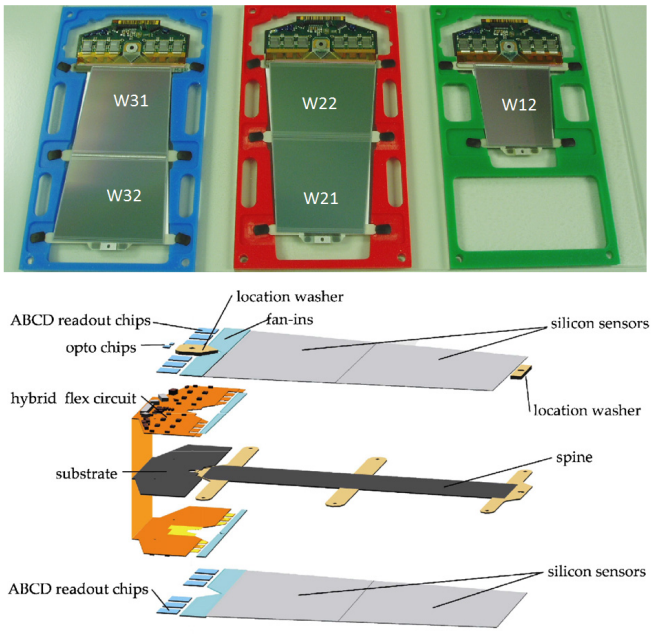

Figure 1.15: Types (outer, middle and inner from left to right) and Components of SCT End-Cap Modules (middle module).

Each SCT end-cap module has the set of the silicon sensors (two or four) glued back to back on a thermal pyrolitic graphite spine and they are positioned at the stereo rotation angle of 40 mrad to achieve the required space point resolution for the SCT. The spine is used as the thermal conductor to the cooling pipe and as a contact for the high voltage bias to the silicon sensors. From the one side it is attached to the carbon substrate plate by the glass fan-ins and there is a polyimide flex hybrid glued on the substrate. Signal from the silicon sensors is read by the ABCD readout ASIC [31] chips connected to the flex hybrid. Cooling of the SCT end-cap modules is provided by the SCT end-cap cooling stave (see Section 2.5.1); The modules are attached to the carbon-carbon cooling blocks which are soldered to the cooling pipe. There is a layer of thermal grease used between the cooling block and the module. Heat from the silicon sensor is evacuated through the spine and from the hybrid through the hybrid substrate. Outer and middle modules are cooled by two cooling blocks (main block cools the hybrid and the spine and far block cools only the spine), while the inner modules are cooled only by the main block and the far block serves as a mechanical support.

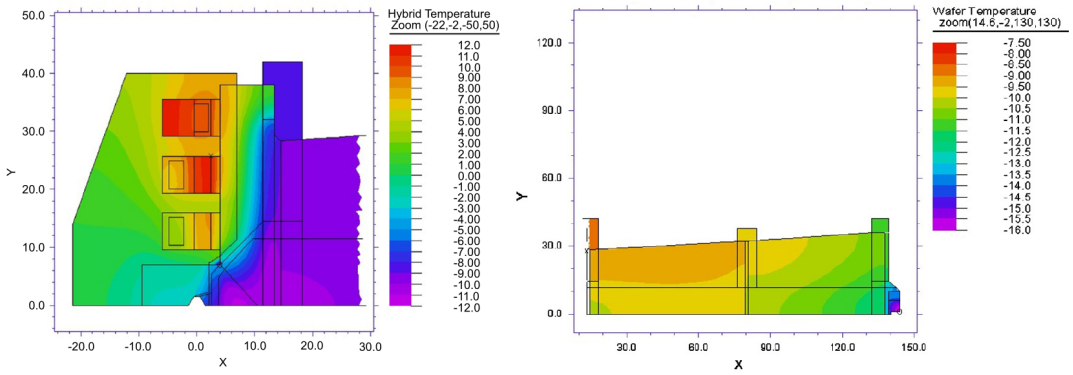

Figure 1.16: The FEA simulation of an outer SCT end-cap module; the hybrid end of a module on the left and the sensor part of a module on the right. Simulated at 7W power and with the coolant at -20 °C. The simulation has a 2-fold symmetry (zero stereo angle) so only half of the module is shown.

Several calculations were done to predict the thermal behaviour of the SCT end-cap modules [30]. Thermal FEA image of the SCT end-cap module is presented in Figure 1.16 [30]. Heat propagation over the module and thermal runaway problems are discussed in detail in the following chapters 3, 4, 5.

Both the SCT barrel and end-cap modules (the silicon sensor part) were specified to be operated at or below $-7\,^{\circ}\mathrm{C}$. The nominal hybrid power per module, as specified in the ATLAS TDR [6], is 5.5 W and after irradiation at the end of the operation period will reach 7.5 W. The silicon sensor power load was expected to reach ≈1W per module after ten years of operation. The convective heat load for the modules at the top part of the barrel and end-cap discs was expected to reach ≈0.8W per module. This leads to a total of ≈9.5W power dissipated per module at the end of the ATLAS inner detector operation period and with the safety margin defined for the cooling system to ≈10.5W. These values defined in the ATLAS TDR are revised in Chapter 3.

In the TRT 96 modules supported by the space frame create the three layers of the barrel assembly. Each module represents the transition radiation material (polypropylene radiator material called the radiator) and an array of the straw tubes (see Subsection 1.3.2) with the average spacing of ≈7 mm [22][6]. The module shell made of 400μm thick carbon fiber serves as a support structure and as a gas manifold for the CO_2 circulated in the TRT barrel envelope. CO_2 is used to prevent HV discharges and accumulation of the Xenon (Xe) leaking from the straw tubes. The tension plate and the HV plate covering the modules are used to close the active gas volume (envelope) and serve as a support (precise position and wire tension) for the straw tube wires and for the HV supply lines. As described previously in this chapter, heat dissipated by the straw tubes and conducted by CO_2 is evacuated thought the module shells when module shells are cooled by the monphase cooling circuits circulating the C_6F_{14} refrigerant.

In the TRT end-cap wheels straw tubes are located perpendicular to the beam axes in a matrix embed into the transition radiation material and they are not

grouped (or addressed) as modules. High voltage and signal connection to the TRT end-cap wheels is provided by the flex-rigid printed-circuit boards [23]. The heat dissipated from the straw tubes is evacuated through the CO_2 gas envelope and the heat from the gas is removed by the external heat exchanger cooled by the C_6F_{14} refrigerant.

Chapter 2

Evaporative Cooling

In general, there are different approaches used to cool particle detectors such as the ATLAS Inner Detector. Due to the complexity of the ATLAS inner detector and the many special requirements for the SCT and Pixel sub-detectors, the ATLAS inner detector cooling system is custom designed. This chapter starts with a discussion of the different approaches used to cool particle detectors and their advantages and disadvantages. Following this is a detailed description of the custom designed C_3F_8 based evaporative cooling system used in the ATLAS inner detector.

Cooling by Cold Gas

The simplest solution in terms of construction is cooling by a stream of cold gas, usually Nitrogen, CO_2 or Air is used for this purpose. In this case the cooling gas is in direct contact with the device to be cooled, therefore the heat transfer surfaces are larger compared to small cooling tubs used for liquid based cooling systems. There are several disadvantages of this type of cooling system. The first is that the cooling relies only on the heat capacity of the gas and not on the latent heat associated with a change of state. The heat capacity of gases are lower than for liquids and heat capacities are lower than latent heats. Therefore cold gas

cooling systems require a larger mass flow compared to liquid systems or phase change based systems (for example an evaporative cooling systems). The second disadvantage is the low heat transfer coefficient between the object to be cooled and the cooling gas compared to the heat transfer coefficient for a liquid. This is compounded by the requirement to use low mass flows to reduce vibrations in the system which reduce the heat transfer coefficient still further. Finally, it is very difficult and challenging to assemble a cooling structure to uniformly distribute gas for a complex detector system like the ATLAS inner detector. Therefore, this approach is not the best choice for the ATLAS Inner Detector.

Mono Phase Cooling

In a mono-phase liquid cooling system cold liquid runs through the cooling pipes, which are in thermal contact with the detector modules to be cooled, and removes heat from these modules via the heat capacity of the liquid. The simplicity of the system is the big advantage; it does not require complicated theoretical calculations, the cooling circuit does not need throttling elements and the pressure drop in system does not have a significant effect on the system's cooling ability.

There are several disadvantages to mono-phase liquid cooling. The first is that as the system relies only on the heat capacity of the liquid and no phase change, higher coolant mass flows are therefore required compared to phase change cooling systems. The second is that the coolant will be cold throughout the entire cooling circuit. The inlet cooling pipes require thermal isolation to prevent premature warming of the cooling fluid, and if the coolant is below the dew point in the experimental cavern the cooling pipes demand thermal isolation on their return as well. This implies a larger volume of the detector is occupied by the cooling services than for a non-isolated system. Finally, the cooling liquid should be chosen carefully in respect to possible leaks (only non-corrosive, non-electrically conductive, non-toxic). It is preferable to use a volatile and non-conductive liquid, which are available. If possible the cooling circuit should run at below

atmospheric pressure to avoid leaks into the detector system in the first place.

Mono-phase Cooling is used as the cooling system for the electronics in the ATLAS Transition Radiation Tracker [23]. In that system, the fluorocarbon C_6F_{14} is used as a coolant. It is a very reliable and simple to use system, but because of disadvantages listed above,this approach was not chose for the ATLAS SCT and Pixel sub-detectors.

Binary Ice

Binary Ice is a mixture of microscopic ice crystals in water or in a mixture of water and a freezing point depressant. It has some advantages for example it's simplicity in design and construction, for example; the absence of throttling elements, simple theoretical calculations and predictions, heat removal at almost constant temperature, increased heat transfer with respect to gas cooling and lower mass flow than for mono-phase liquid system. However, there are many disadvantages which include; the necessity to thermally isolate pipes everywhere in the detector to avoid condensation, as the coolant is cold in the feed and return pipes, it is necessary to run the fluid in the cooling circuit below atmospheric pressure to prevent water escaping into the detector in case of leaks (this can cause serious damage to detector). The approach was studied for the ATLAS inner detector, but after some investigation it was not chosen.

2.1 Evaporative Cooling

The general principle of an evaporative cooling system is based on the use of the coolant's (refrigerant's) latent heat of vaporization. The refrigerant, circulating in the cooling system, vaporizes in the detector structure, absorbing latent heat removed from detector modules. Then in vapour phase, it is compressed by a compressor and delivered to a condenser, which is cooled by another substance (refrigerant, water, etc.), and now returned to the liquid phase and at

high pressure, the refrigerant circulates back to the detector structure. Normally, additional sub-cooling, via a counter flow heat exchanger, is used to increase the efficiency of the cooling circuit by increasing the available enthalpy of the refrigerant.

Advantages of an evaporative cooling system are: it allows heat to be removed at a constant temperature, as long as the pressure drops along the cooling structure are low; a significant increase in heat removal capacity compared to a mono-phase based system, the same amount of refrigerant can remove a few orders of magnitude more heat [32] when it evaporates, than when it remains in liquid state; significantly lower mass flow compared to other approaches; the refrigerant can be at room temperature up to the evaporator (detector), so no thermal isolation is needed for circuit pipes. If an additional evaporator is housed in the detector volume, after the detector structure to be cooled, such that all the liquid is evaporated and heated to above the experimental cavern dew point then the return pipes do not need to be thermally isolated. This gives the advantage of using less material inside the tracking detector (one of the requirements for the precise reconstruction of the particle momentum and in order to minimize the production of secondary particles [6]), and since the ATLAS detector is designed to be hermetic, gaps in the detector structure due to the services should be minimized [33].

Because of the many advantages mentioned above, an oil free Evaporative Cooling System using C_3F_8 (Section 2.3) refrigerant was chosen for the ATLAS ID SCT and Pixel sub-detectors.

2.2 Requirements for the SCT and Pixel Sub-detectors

The ATLAS inner detector evaporative cooling system was specified to be efficient enough to protect the SCT and Pixel sub-detectors against overheating

with a design target of keeping the maximum silicon sensor temperature of the detector modules at or below -7 °C for the SCT [26], -7 °C for the Pixel and 0 °C for the Pixel optoloops [25], during normal running conditions. Later, instead of having a constant sensor temperature, a constant coolant temperature approach was adopted. Because of the overall thermal resistance between the silicon and the cooling fluid; formed by the silicon module's internal thermal resistance, the thermal resistance between the silicon module and it's mounting point to the cooling stave and the heat transfer inside the cooling pipe to the fluid, the refrigerant's temperature was defined to be -25 °C or less [33] [28]. Later calculations (see Chapter 3) showed that with updated operation scenarios, updated values for the predicted luminosity, depletion voltage and leakage current and based on the thermal runway limits it is possible to guarantee the inner detector's thermal stability with the coolant's evaporation temperature below or at -15 °C .

To avoid condensate on detector parts, sub-detectors must be kept inside a dry environment flushed with cold dry nitrogen. With respect to the rest of the experiment, the ATLAS SCT and Pixel sub-detectors must be kept thermally neutral. To achieve these goals the sub-detectors are housed in thermally insulated enclosures which have heating pads on the exterior to maintain an external temperature of 20 °C. Only non-corrosive, non-electrically conductive, non-toxic, radiation hard and non-flammable refrigerants can be used as a coolant in the system.

All materials used in ATLAS inner detector must be non-magnetic, radiation hard and minimize the amount of extra material in sub-detectors, to achieve this the size of pipes and all other parts of the detector structure of the cooling system must be as small as possible.

Originally the predicted total integrated luminosity for LHC was 730 fb^{-1} [6] over the 10 years operational period. In Phase 0, it was assumed to operate the LHC at low instantaneous luminosity of approximately $10^{33}\,\mathrm{cm}^{-2}\mathrm{s}^{-1}$ and after the upgrade to LHC Phase 1 operation, the luminosity to approximately

$10^{34}\,\mathrm{cm}^{-2}\mathrm{s}^{-1}$. Therefore radiation will cause ageing of the silicon modules (depletion voltage and leakage current), so the ID evaporative cooling system must be able to remove much more heat from detector modules at the end of the LHC running period (see Chapter 3).

2.3 Refrigerant Choice

Several studies were performed, to choose the most suitable refrigerant for the desired evaporation temperature of -25 °C. [34] [32] [35]

Table 2.1 [34] shows a comparison of the C_3F_8 refrigerant with other common industrial and commercial refrigerants having similar evaporation temperatures.

	R218 (C_3F_8)	**HFC-134a**	**HFC-143a**	**R-404a**	**R-407c**	**R717 (NH_3)**	**R116 (C_2F_6)**
Boiling point at 1 bar_{abs}[°C]	-36.8	-26.1	-47.3	-46.8	-43.6	-31.6	-78.2
at -25 °C							
Saturated Vapour Pressure P_{sat}[bar_a]	1.67	1.07	2.62	2.47	1.72	1.52	9.01
Latent Heat of Vaporization L [kJ×kg^{-1}]	102	216	209	190	236	1345	86.4
Liquid Phase Density $P^{'}$ [kg×m^{-3}]	1565	1371	1104	1243	1321	672	1332
Vapour Phase Density $P^{''}$ [kg×m^{-3}]	16.4	5.53	11.8	12.8	7.64	1.28	77.2
Liquid Phase Viscosity $\mu^{'}$ [μPa×s]	268	373	216	246	284	240	172
Vapour Phase Viscosity $\mu^{''}$ [μPa×s]	10.3	9.82	10.4	9.88	9.88	9.2	11.8
Critical Temperature t_{crit} [°C]	72	101.1	72.7	72	85.6	132.3	19.9
Critical Pressure P_{crit} [bar_a]	26.7	40.6	37.6	37.2	46.1	113	30.0

Table 2.1: Comparison of Refrigerants.

Since C_3F_8 has the lowest latent heat of vaporization, although having the highest density compare to other refrigerants (excluding C_2F_6), C_3F_8 has to have the highest mass flow to cope with the SCT and Pixel sub-detector cooling system requirements. Therefore C_3F_8 is not the best choice, but other commercial or industrial refrigerants (listed in table) contain both fluorine and hydrogen. Under ionizing radiation fluorine can create corrosive and toxic hydrofluoric acid by reacting with contained hydrogen, therefore increasing risk of serious damage to the detector; and ammonia (NH_3) is toxic so can not be used in ATLAS underground areas because of safety reasons. On the other hand C_2F_6 has even lower latent heat of vaporization than C_3F_8, lower boiling point at 1 bar_{abs}, very low

critical temperature and most importantly very high saturated vapour pressure making it not suitable for use in the inner detector cooling system because of safety reasons.

As an advantage, C_3F_8 has a good heat transfer coefficient, low saturated vapour pressure, which is still above the atmospheric pressure, therefore securing the system against influence of N_2, CO_2 or Air from surrounding environment. and most of all, C_3F_8 gives lower pressure drops in return pipes allowing their comparably small size and relatively bigger overall pressure drop budget in system [34] [32].

Therefore, C_3F_8 was chosen as the refrigerant for SCT and Pixel sub-detector Evaporative Cooling System.

2.4 System Design and Architecture

In the ATLAS inner detector evaporative cooling system the C_3F_8 refrigerant is recirculated through the on-detector cooling system and the off-detector cooling plant. Schematic of the ATLAS inner detector evaporative cooling system is presented in Figure 2.1 [33].

The evaporative cooling system has been built to guarantee a total cooling capacity of 70 kW with a target temperature on the detector structure of -25 °C and be capable to supply the refrigerant's total mass flow rate of $1130\,\mathrm{gs}^{-1}$ [33].

A constant flow system is adopted over the varied flow system since it has several advantages and conforms to the ATLAS sub-detector's cooling requirements. With the constant flow approach (where the flow in each cooling circuit is fixed by the corresponding throttling element), regardless of the heat load on the detector modules, the pressure for each circuit is regulated at a constant value by the pressure regulator, keeping the refrigerant fluid inside the inlet lines above the saturation point at room temperature. This guaranties that refrigerant delivered to the detector structure is in liquid phase and the full enthalpy budget

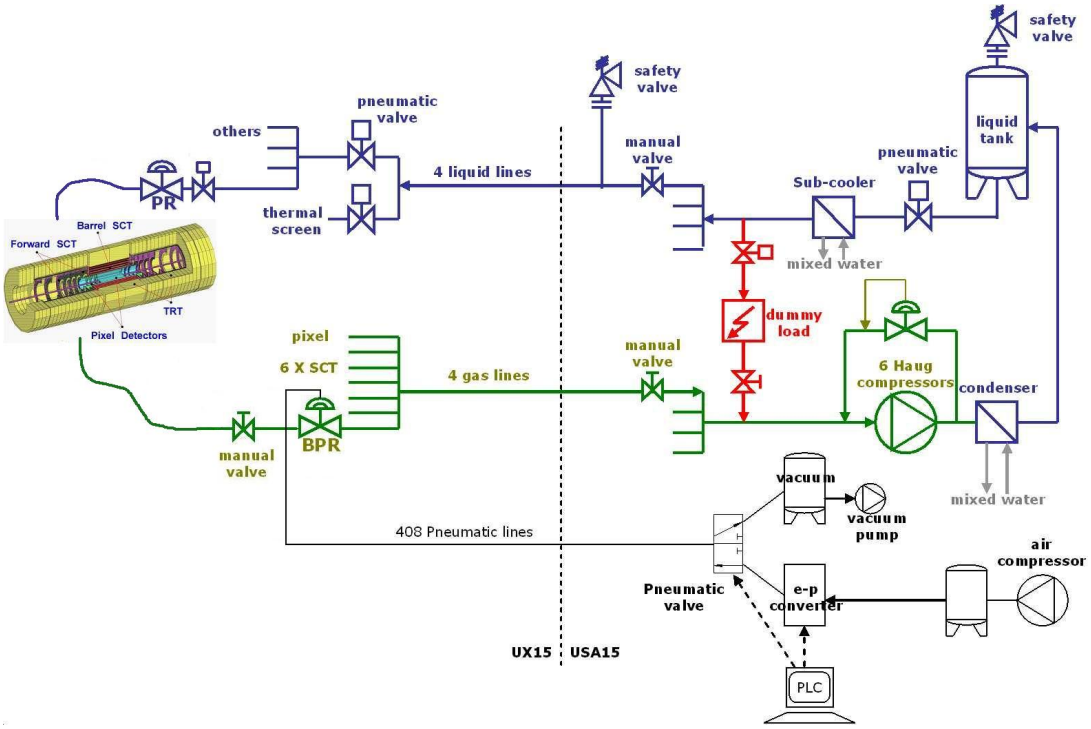

Figure 2.1: Schematic of the evaporative cooling system main plant.

can be used for cooling the modules. Pressure in the refrigerant return line for each circuit is also controlled to be a fixed value by back pressure regulator and the custom made inline heater allows the remaining liquid to be boiled and the vapour to be heated up above the cavern dew point. Therefore fixed flow system allows liquid supply lines that are not thermally isolated from the distribution racks to the detector structure and vapour return lines that are not thermally isolated from the detector structure up to the racks in the ATLAS underground cavern. A varied flow system would require an additional sub-cooling of the liquid supply lines outside the detector structure. This would be necessary to keep the inlet fluid temperature below the saturation temperature over the full range of mass flow changing according to the heat load on the detector modules. This would demand the thermal isolation on the inlet lines from the distribution racks down to the detector structure and that would be an obvious disadvantage of the system as described above in Section 2.1. The fixed flow system is also a simpler system from the control point of view compared to the varied flow sys-

tem. The control of the varied flow system requires feedback of the temperature at the exhaust of the detector structure cooling circuits to vary the flow in the system as a function of the heat load on the detector modules, but in the fixed flow system control is provided only for the inline exhaust heaters on each cooling circuit line therefore making it simple to manipulate each cooling line when the overall system is running in a steady state. It is also possible to have variable flow system where the flow rate is changed by the needle valves instead of capillaries and inlet and outlet pressure for each circuit is regulated at a constant value by the pressure regulator. Disadvantages of this kind of variable flow system are: having extra material introduced in the inner detector volume since the variable flow needle valve is more massive than a capillary; system is less reliable since it has more complex parts than a simple capillary; complex control system and additional cables for control and power to the needle valve. With respect to all of these advantages described above the constant flow system was chosen over the varied flow system for the cooling of the ATLAS inner detector.

The cooling cycle of the ATLAS inner detector evaporative cooling system is explained starting at an arbitrary point in the cooling cycle. The refrigerant (C_3F_8) in liquid phase from the storage tank is transferred in non-thermally isolated, warm (above the cavern dew point) feed lines to the four distribution racks located in the ATLAS UX15 cavern. The four distribution racks, each corresponding to an inner detector quadrant, are located on the support structure surrounding the ATLAS detector. These structure/platforms called "HS platforms" [10] are used for the access of the personnel to the detector and for the support of all the equipment that should be located close to the detector. The layout of one of the distribution racks is presented in Figure 2.2 [33].

Distribution racks are places two on either side of the experiment with one on a side at ≈10 meters above and one at ≈10 meters below the beam interaction point. After these racks, the feed lines are split into 204 independent liquid inlet lines (116 of the SCT and 88 of the Pixel system). Through these

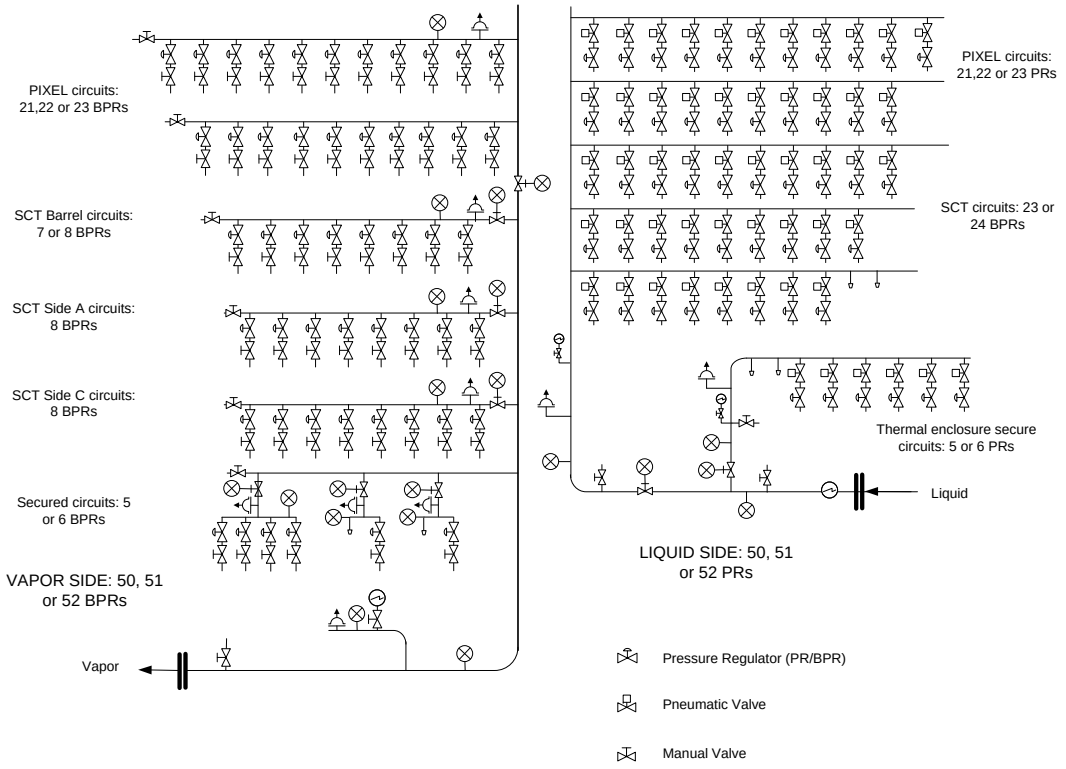

Figure 2.2: The layout of the distribution rack

lines liquid is delivered to the detector structure. In the inner detector structure the coolant is sub-cooled in the inline recuperative heat exchangers (HEX) (Subsection 2.5.3) by the return fluid of the same circuit. After the throttling elements (capillaries) (Subsection 2.5.2), the coolant pressure is significantly reduced defining the coolant's evaporation temperature. This pressure is controlled by a back pressure regulator in the return lines in the distribution racks. After the evaporator (the cooling pipes attached to the SCT or Pixel modules), any remaining return liquid needs to be boiled off, therefore custom made Heaters (Subsection 2.5.4) are installed on the return lines in the inner detector volume to boil any remaining liquid in the system and heat up the vapour above the cavern dew point to allow warm, non thermally isolated, return lines. Warm vapour is then delivered back to compressors in USA15, where it is compressed

to 17 bar_{abs} and increases in temperature to 90 °C. The minimum suction pressure of the compressors is 0.8 bar_{abs}; this defines the minimum back pressure in the system measured at the end of the vapour return pipe at the distribution rack on the detector side of the back pressure regulator to be ≈1.2 bar_{abs}; given by the 0.8 bar_{abs}, plus 200 mbar_{abs} safety level for the PLC control system (Section 2.6), plus 150 mbar_{abs} pressure drop in the return pipes from the compressor to the distribution rack and plus 50 mbar_{abs} pressure drop over the back pressure regulator. Then the hot vapour is transferred to the condenser where it condenses from 90 °C to 52 °C and in liquid phase is delivered to the storage tank. Just after the storage tank liquid refrigerant is cooled by the station's sub-cooling to 17 °C at 16 bar_{abs} pressure and is delivered to the distribution racks for the continuous running cycle.

The overall thermodynamic behavior of the system is shown on the Pressure-Enthalpy diagram in Figure 2.3.

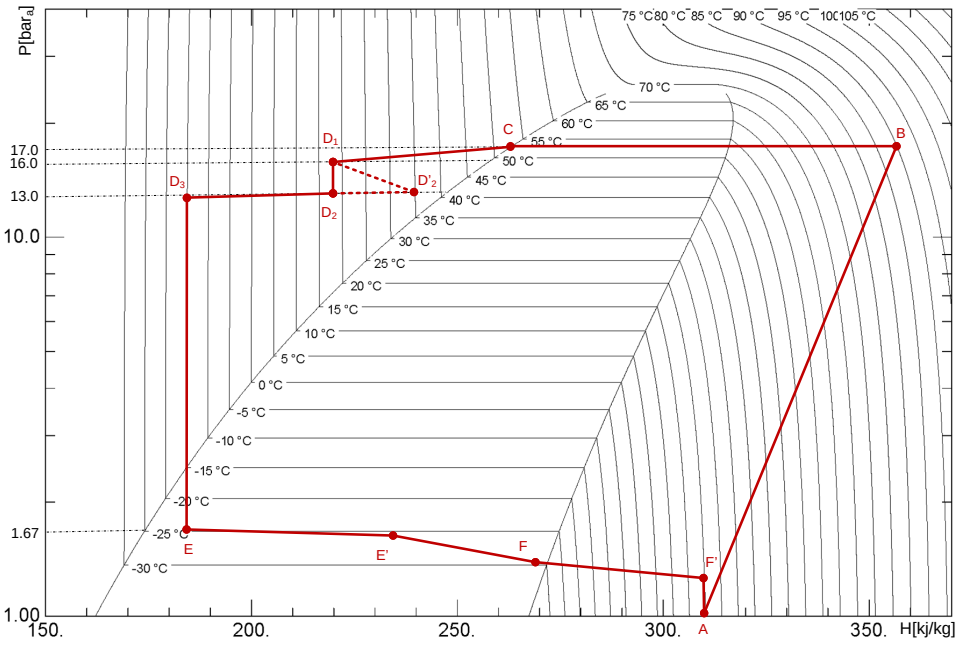

Figure 2.3: Phase Diagram of the ATLAS Inner Detector Evaporative Cooling System.

Each of the stages described above can be seen on the P-H diagram and are given below:

From point C to point D_1 refrigerant in liquid state from the storage tank is sub-cooled by the plant's additional sub-cooling system from 53 °C to 17 °C at 16 bar_{abs} and is delivered to the distribution racks. The line from point D_1 to point D_2 corresponds to the pressure drop over the pressure regulator in distribution rack when pressure value on the pressure regulator is set to 14 bar_{abs} or 12 bar_{abs}. This is necessary to cope with the hydrostatic pressure in the inlet liquid lines formed by the top and the bottom position of the distribution racks relative to the inner detector position as it is described above, and to ensure the inlet liquid pressure on the detector side (before the heat exchanger) is equal to 13 bar_{abs} for each cooling circuit. Point D_2 to point D_3 corresponds to the detector's sub-cooling system (Heat exchanger) (Subsection 2.5.3) where inlet liquid is sub-cooled to -15 °C by the counter flow liquid remaining in exhaust line to provide as big an enthalpy budget as possible. Point D'_2 corresponds to the temperature safety margin; expected temperature rise in the ATLAS UX15 cavern is unknown, therefore worst scenario prediction was assuming inlet liquid temperature to be $\approx$35 °C therefore rising the sub-cooled inlet liquid temperature to $\approx$0 °C, but this effect never been observed over the operation period since the room temperature in the ATLAS UX15 cavern did not change. The line from point D_3 to point E corresponds to the significant pressure drop over the throttling element (Capillary) (Subsection 2.5.2); In this figure a pressure drop to 1.67 bar_{abs} is shown, which corresponds to an evaporation temperature of -25 °C. The part between the points E and E' corresponds to the coolants's evaporation process in the detector structure. The silicon modules of the detector are cooled down by latent heat of the coolant. High efficiency of the heat exchanger leads to the lower input liquid temperature to the capillary, therefore to the lower input vapour quality at the entrance of the detector cooling structure (Cooling Stave)(Subsection 2.5.1), giving bigger enthalpy budget and increasing

cooling capacity of the system for a given mass flow and back pressure in the system. Expected vapour quality at a nominal detector power and a nominal inlet and outlet pressure set point for the inlet liquid is 0.15 and for the exhaust is 0.78 [33]. Point E' to point F corresponds to the amount of the enthalpy used in the heat exchanger to cool down the inlet liquid. From points F to F' refrigerant vapour is warmed up by the heater to 20 °C. Vapour at room temperature is therefore returned to the compressor. The section from F' to A corresponds to the pressure drops over the return lines, from the exit of the heater to the front of the compressor; including pressure drop over the 30 m pipes from the detector structure to the distribution racks, over the back pressure regulator and over the return lines from rack to the compressors in USA15. Between points A to B vapour is compressed at 17 bar_{abs} and 90 °C and is delivered to the condenser. From point B to point C the vapour condenses inside the condenser into liquid at 53 °C and is delivered to the storage tank for for the continuous running cycle.

As mentioned above, the overall pressure drop over the system must be able to maintain an evaporation pressure over the detector structure (cooling stave) $\approx$1.67 bar_{abs}, to be able to reach a stable -25 °C as a coolant temperature, in the case of minimum possible back pressure in system of 1.2 bar_{abs} measured on the detector side of the back pressure regulator. This requirement gives a pressure drop budget limit of only 470 $mbar_a$ from the detector structure (stave) to the back pressure regulator.

The pressure drop budget for inlet line is less critical, because it is driven by minimum pressure in the condenser and minimum pressure before capillaries, and is set to 1 bar. The system allows a maximum inlet pressure of the liquid to be 16 bar_{abs} on the off-detector cooling plant side of the pressure regulator for each cooling circuit (pressure regulator on the distribution rack). Therefore, inlet pressure value on the on-detector side of the pressure regulator (pressure from the distribution rack to the entrance of the capillaries) can be set to 12 bar_{abs} and/or 14 bar_{abs} in respect of the atmospheric pressure difference for upper and lower

racks; Since distribution racks for the top quadrants of the detector (quadrant 1 and quadrant 2) are placed ≈10 meters above and for the bottom quadrants of the detector (quadrant 3 and quadrant 4) ≈10 meters below the beam interaction point, the hydrostatic pressure difference in liquid line must be taken into account to ensure stable 13 bar_{abs} pressure before the entrance of the capillaries for each cooling circuit. Calculation of the hydrostatic pressure in the liquid line is presented below:

$$P = \rho \times g \times h$$
$$P = 1358.9 \times 9.8 \times 10$$
$$P = 133172.2\text{Nm}^{-2}[\text{Pa}]$$
$$P = 1.331722[\text{bar}]$$

Where:

P - Hydrostatic pressure [Pa or bar].

ρ - Density of fluid C_3F_8 (at 12 bar_{abs} and 20 °C) [kgm^{-3}].

g - Gravitational acceleration [Nkg^{-1}].

h - Hydrostatic head [m].

Of course this is a very academic way of calculation. In reality it is difficult to precisely calculate the hydrostatic pressure since the routing of the inlet liquid pipes is very complicated; distance between location of the top and the bottom distribution racks and location of the heat exchange and the capillaries mounted on the detector structure is approximately measured to be 10 m; value of the fluid density used in the formula is defined for 20 °C, when temperature of the environment around the inlet liquid pipes in ATLAS underground cavern changes depending on the place and in worst case scenario expected temperature rise can be up to ≈ 35 °C. Therefore pressure values set on the pressure regulators for each cooling loop or each quadrant are empirically adjusted, based on the return vapour temperature and silicon sensor temperature.

For the ATLAS inner detector evaporative cooling system inlet pressure value of 13 bar_{abs} has been chosen to prevent the fluid from boiling in the inlet supply lines and keep the delivered refrigerant's vapour quality close to zero; Saturation temperature of C_3F_8 at 12 bar_{abs} (with respect of the hydrostatic pressure as described above) equals 37.5 °C and is still above the maximum expected temperature in system 35 °C.

2.5 On-Detector parts of the System

The cooling Stave, throttling element (Capillary), Heat Exchanger and exhaust vapour Heater are called the "on -detector" parts of the ATLAS inner detector cooling system. These parts, for each cooling circuit, are mounted into the inner detector structure itself and therefore they are not accessible and cannot be changed. Each item is discussed in detail in the following sub-sections.

2.5.1 Cooling Stave

The stave is the part of the cooling system where evaporation occurs. As described above, by dropping the refrigerant's pressure after the capillary, the coolant changes state (from liquid to vapour) and starts evaporating, removing heat from the detector modules.

The SCT Barrel Stave is an assembly of eight straight Copper-Nickel (Cu-Ni) tubes. Pairs of tubes are connected together by an insulated pipe joint to form an electrical break in the cooling tube. Two sets of "U" shaped pipes are formed by connecting together two of these longer tubes by a short "U" shaped tube. These two long "U" shaped pipes are connected together by a manifold. The stave therefore has two inlets, one per "U"-shaped tube and one outlet, which is the manifold outlet. A detailed drawing of SCT Barrel stave is presented in Figure 2.4. The inner diameter of the stave tube is 4 mm and wall thickness equals to 70 μm. 48 special mounting blocks are soft-soldered to the straight

parts of the tube, 12 per leg of each "U", and detector modules are fixed to these blocks. Two Capillaries are connected to each stave by an inlet connector, one for each "U"-section, forming "double flow" of coolant in the stave structure.

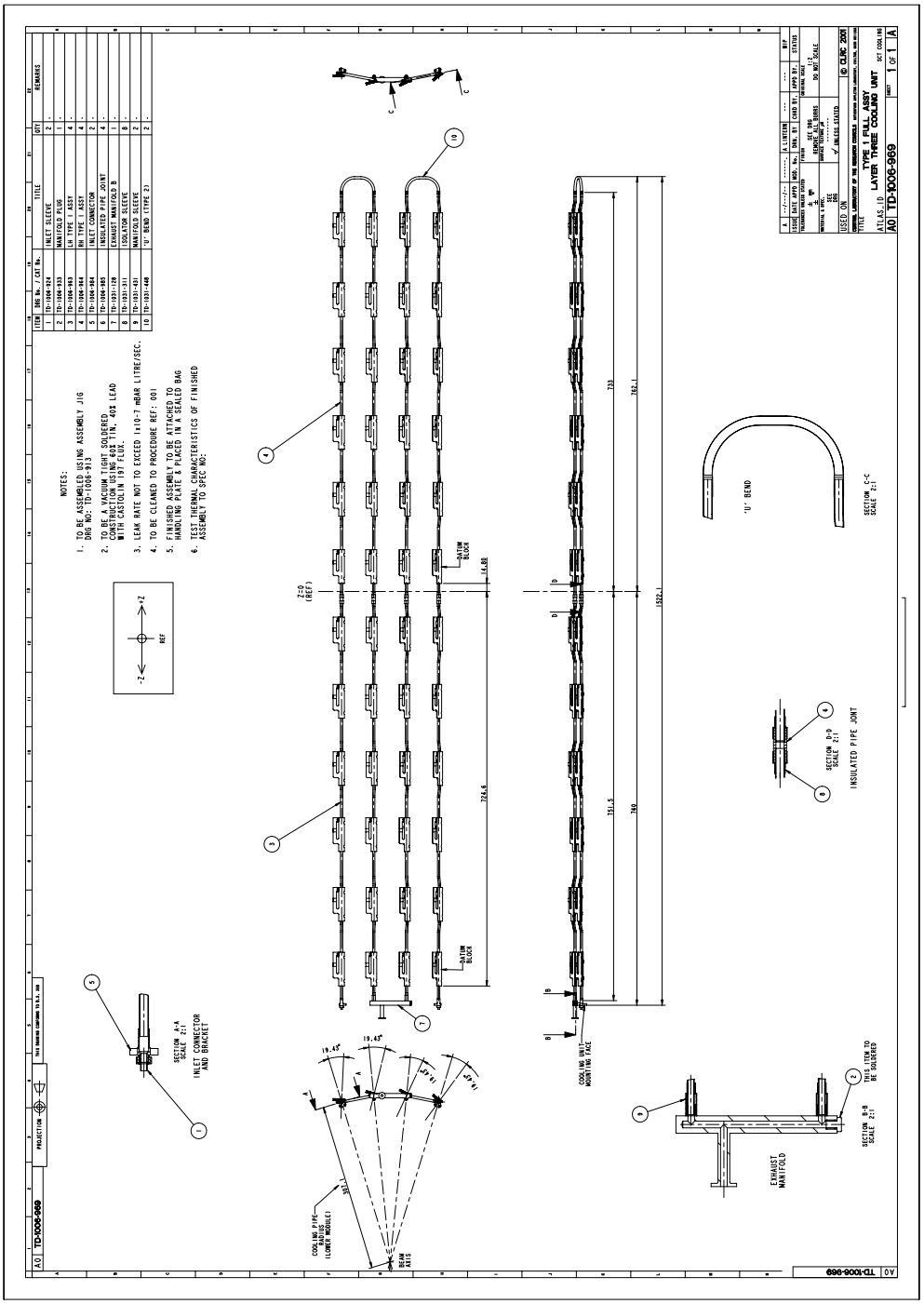

Figure 2.4: SCT Barrel Stave

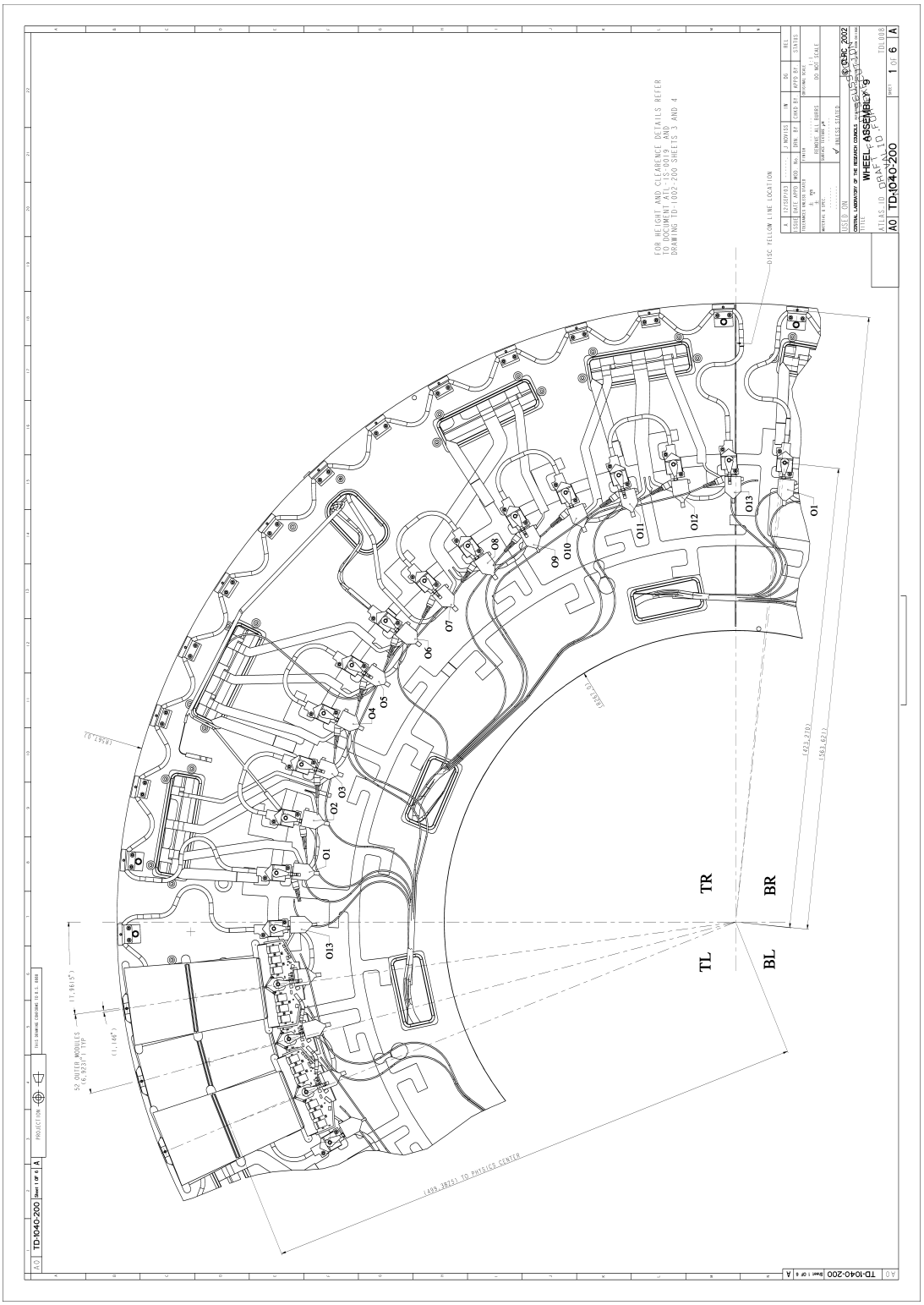

Figure 2.5: SCT End-Cap Stave

The SCT End-Cap Stave is manufactured from copper-nickel (Cu-Ni) pipes with 70 μm wall thickness and 3.74 mm outer diameter. An example drawing of the SCT End-Cap disc with one cooling circuit and several modules mounted on it, is presented in Figure 2.5. Cooling circuits are manifolded together on the exhaust side to form four quadrants on each disc. A typical disc quadrant has three cooling circuits; outer, middle and inner cooling loops. Different numbers of modules are mounted per loop (outer = 52; middle = 40; inner = 40;), therefore forming a different heat load per loop and requiring different coolant mass flow. To cope with this, two separate types of capillaries (one capillary per cooling loop) were chosen; one type for the inner and middle loops and another type for the outer cooling loops (Subsection 2.5.2). Cooling is supplied to the modules via "main" and "secondary" carbon-carbon cooling blocks soft soldered to the cooling circuit.

Pixel Barrel stave is comprised of a D-shaped Aluminum (Al) tube with a Hydraulic diameter of 4.17 mm and the wall thickness of 0.2 mm. 112 stave tubes form the three cylindrical layers of the barrel part of the pixel detector cooling structure. 13 sensor modules per tube are glued on the Carbon-Carbon Thermal Management Tile which is fixed to the Aluminum pipe by 0.3 mm thick carbon fiber reinforced plastic. Neighbouring pairs of these stave tubes are connected to each other by a custom made "U-shape" connector to form what is known as the "Bi-Stave" [36]. Inlet and exhaust of a single "Bi-Stave" are always on the same side; 56 Bi-Stave assemblies correspond to the 56 Pixel Barrel cooling loops; A picture of a pixel Barrel Bi-Stave with U-shape connector and mounted detector modules is shown in Figure 2.6 and the pixel Barrel stave profile is illustrated in Figure 2.7

The Pixel Disc (endcap) stave is an Aluminum (Al) tube bent into a W-like shape and is trapped between the carbon composite sheets and the carbon foam in between the sheets with the thermally conducting adhesive [37]. There are three discs on each side of the forward regions. One disc consists of 8 sectors

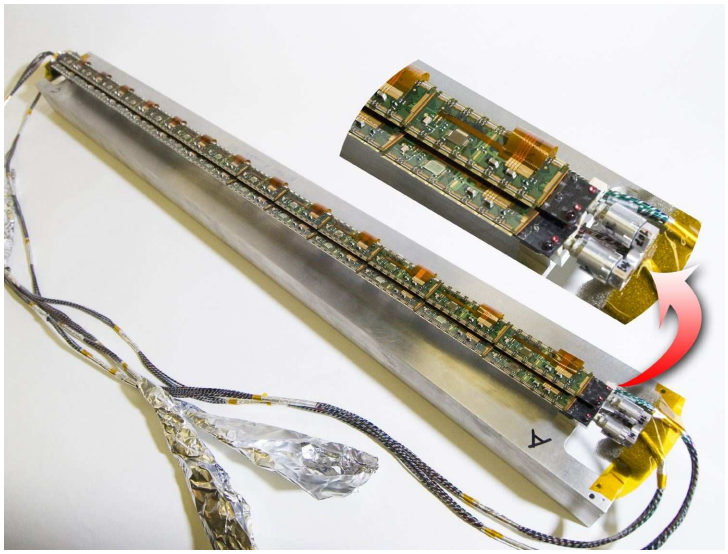

Figure 2.6: Pixel Bi-Stave

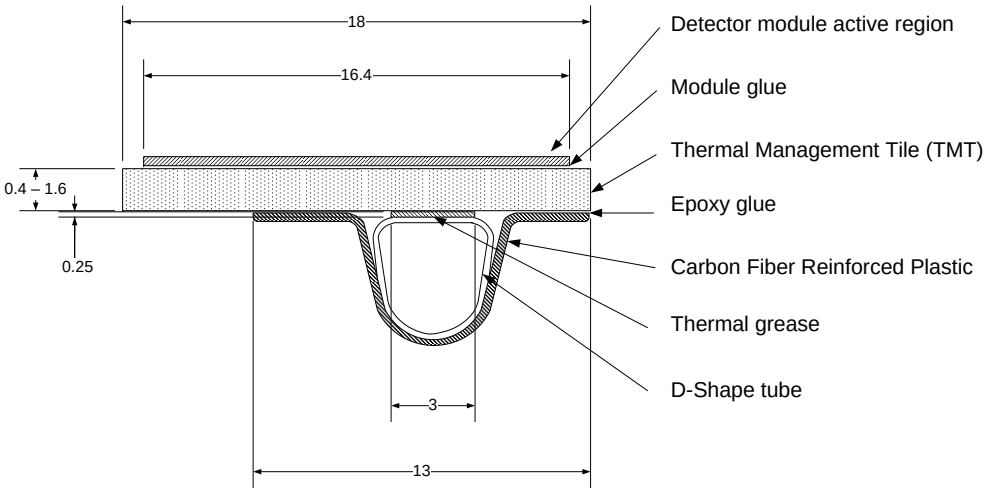

Figure 2.7: Pixel Stave Profile

with 6 modules mounted in each sector. Disc and barrel modules are identical except for the power cable connection. Stave tubes in the two neighboring sectors are connected to each other having one inlet and one exhaust and forming one quadrant of the Pixel disc cooling structure. Therefore each cooling circuit in the disc region serves two sectors (one quadrant). In total 24 cooling loops are used for the cooling of six Pixel Discs (endcap) on the both sides of the detector structure.

The remaining 8 cooling loops (out of 88 Pixel circuits) provide the cooling of the opto-boards by running the refrigerant through the cooling pipe attached to the bottom of the opto-board and keeping board temperature below 20 °C. Opto-boards are located inside the four per side of the detector structure services quarter panel boxes [38].

2.5.2 Capillaries

Capillaries (throttling elements) are used to control the refrigerant mass flow in the cooling circuits. Due to the different number of modules per loop and different heat load per loop for SCT barrel, End-Cap and Pixel circuits, different mass flow is delivered by using five different types of capillaries. Mass flow through the capillary depends on the inner diameter and length of the capillaries. It increases with inner diameter and decreases with length, as well increasing with pressure drop over the capillary and decreasing with rising liquid temperature before capillary. But, as described above, the pressure drop over the cooling circuit is fixed by inlet liquid pressure and outlet vapour back-pressure regulators and the temperature before the capillary is fixed by the Heat Exchanger's efficiency, therefore only by changing capillary length and inner diameter a different mass flow can be set for each group of cooling circuits. Because it is very difficult to do predictions and exact calculations in the case of two phase flow, an empirical approach was chosen to determine the required length and inner diameter of the capillaries for different flow settings. Several measurements were done on a test station [33] to define the necessary parameters and they were tuned individually for each capillary. Table 2.2 represents the **nominal** design parameters for five different groups (type) of capillaries.

The capillaries are annealed copper nickel (Cu/Ni30Mn1Fe) tubes, with wall thickness of 0.2 mm.

In the ATLAS ID evaporative cooling system different capillaries are used for the different sub-detector cooling loops depending on the required mass flow. For

CIRCUIT	MASS FLOW (g/s)	ID (mm)	Length (mm)
Barrel SCT	3.9	0.75	500
EC SCT (inner and mid sector)	1.6	0.75	2500
EC SCT (outer sector)	2.1	0.68	2500
Pixel barrel and opto-boards	4.1	0.8	1200
Pixel discs	2.1	0.55	1250

Table 2.2: The capillary nominal design parameters.

the SCT Barrel loops there are two capillaries connected to the stave pipe forming double flow in it. For the SCT endcap cooling loops there are 2 or 3 capillaries used depending on the disc (number of modules mounted on the disc) that is served; as described above in Subsection 2.5.1, one SCT endcap cooling circuit serves one quadrant of each disc; out of 72 SCT endcap cooling circuits 64 have 3 capillaries and 8 have 2 capillaries (since the two most outer discs have only outer modules mounted on them). The remaining cooling capacity (extra third line) of these 8 cooling circuits is used to supply cooling for the low mass tapes of the endcap. These cooling lines are routed on the outside of the endcap (inside the thermal enclosure) to cool the tapes that supply power to the modules. In the Pixel cooling loops regardless the Barrel, Disc (endcap), or opto-board cooling, only one capillary is used per cooling loop.

2.5.3 Heat Exchanger

The Heat Exchanger (HEX) is a counter flow devices which uses the returning refrigerant's entropy, from the detector cooling structure, to cool down the incoming liquid. The efficiency of the HEX defines the coolant temperature before the capillaries, so lowers the input vapour quality and gives bigger budget for refrigerant's enthalpy to cool the detector structure. Therefore by increasing the HEX efficiency the cooling capacity of the system can be increased. The efficiency of the heat exchanger can be calculated according to the following equation [33]:

$$\eta = \frac{T_0 - T_1}{T_0 - T_2}$$

Where:

η - Efficiency of the heat exchanger.

T_0 - Inlet liquid temperature [°C].

T_1 - Inlet liquid temperature after the sub-cooling [°C].

T_2 - Evaporation temperature in the cooling stave [°C].

The functionality of the SCT Barrel, SCT End-Cap and Pixel Heat Exchanger's is absolutely similar, but because of geometrical limitations, the design of HEXs was done in different way, to match requirements for each sub-detector's cooling performance (Section 2.2).

The inlet line for each HEX is equipped with a "Screen" type filter, having 264 0.5 mm diameter holes, to prevent the passage of small items and protect capillaries from blocking. Heat exchanger's inlet line (at the inlet liquid connector) and outlet line (at the return vapour connector) are connected to the off-detector structure via a peek based electrical break to electrically isolate the detector structures from the rest of the ATLAS experiment (see HEX schematics below). The SCT HEXs are made from Cu and CuNi pipes and Pixel HEXs are made in Aluminum.

For SCT Barrel HEX, the inlet line is split before the HEX into two straight tubes, passing inside, all over the 150 cm length of HEX. A schematic drawing for SCT Barrel Heat Exchanger is presented in Figure 2.8.

Because of space limitations for SCT End-Cap Heat Exchanger, it was decided to make it much shorter (37 cm), but with inlet pipe coiled inside the HEX, so it's efficiency is increased by increasing inlet line's contact surface area with vapour return line. A schematic drawing for SCT End-Cap Heat Exchanger is presented in Figure 2.9.

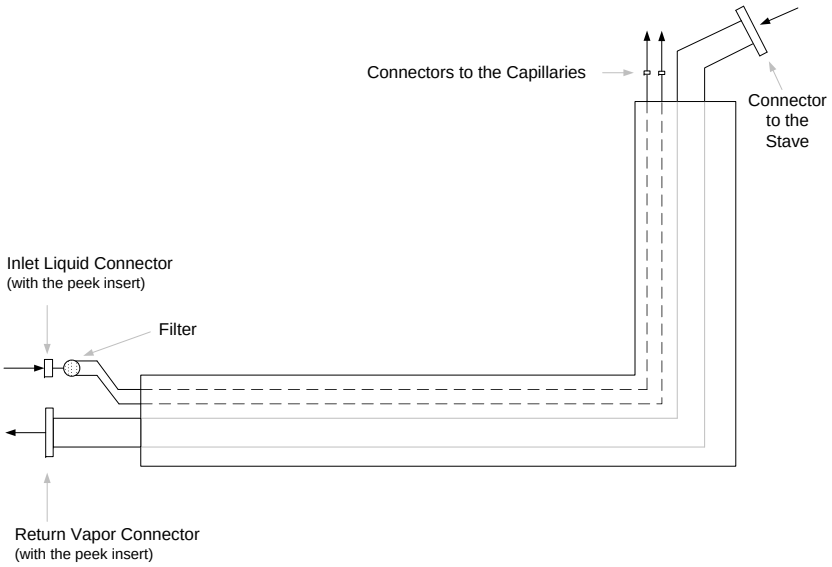

Figure 2.8: Schematic Drawing of SCT Barrel Heat Exchanger

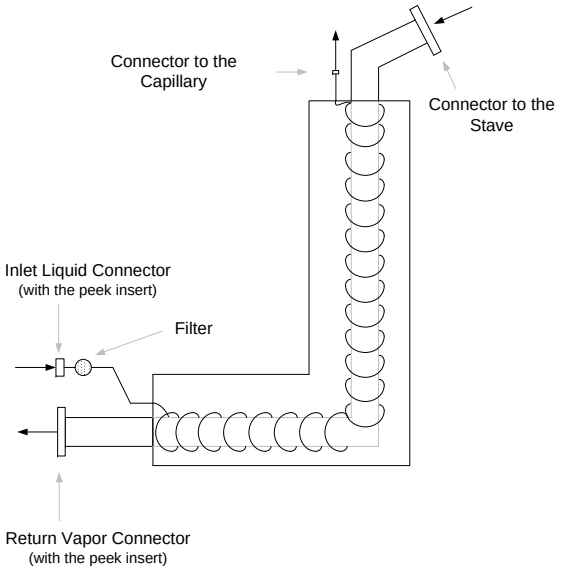

Figure 2.9: Schematic Drawing of SCT End-Cap Heat Exchanger

A simpler approach was adopted in the construction of the Pixel Heat Exchangers. Because of the sufficient possible length of HEX (1500 cm), the required heat transfer efficiency was achieved just by gluing the inlet line to the outside surface of the vapour return line. A schematic drawing for the Pixel Heat Exchanger is presented in Figure 2.10.

Figure 2.10: Schematic Drawing of Pixel Heat Exchanger

In case of a sudden change of heat load on the detector cooling structure, or in case of different operation modes (Section 2.6) causing quick change of return vapour quality the Heat Exchangers are still able to function properly and return to stable running conditions in a short time.

2.5.4 Heater

Heaters mounted on each return line of the evaporative cooling circuit are used to evaporate any remaining liquid coming from the cooling stave back to the compressor, and keep the refrigerant's temperature above the cavern dew point, to avoid condensation on non-thermally isolated long exhaust pipes from detector to compressor room. Heaters for the SCT Barrel, End-Cap and Pixel sub-detector's cooling circuits have a simple design, but are very efficient. A coiled heating element is placed inside of the heater's body (tube) and is in touch with tube's wall. Since the heating element is in direct contact with the coolant, with the given geometrical limitation of heater's length and diameter, the present heaters are efficient enough to boil all the liquid and to raise the temperature of the refrigerant at the exhaust above the 20 °C. Design parameters of the heaters have been selected in order not to exceed a safety/maximum temperature of the heating element of 100 °C and at the same time keep the pressure drops across the heater within a budget of 50 mbar. This was achieved by keeping the free internal di-

ameter of the heater sufficiently large, shown in Table 2.4. Measurements of the pressure drops over the heaters were performed for the design massflows and a range of detector power loads to confirm the pressure drops over the heaters. Design parameters of Heaters (and Heating elements), used in SCT Barrel, End-Cap and Pixel sub-detectors' cooling circuits, are presented in Table 2.3 and 2.4 [33].

CIRCUIT	**Nominal Power Load on The Detector**	**Heater Design Power**	**Design current**	**Resistance of hot wire**	**Material of hot wire**
	W	W	A	Ω	
SCT Barrel	504	960	9.6	10.27	Ni 80/20
SCT EC	346	650	6.5	14.93	Constantan
Pixel barrel/opto-boards	220	480	4.8	20.23	Constantan
Pixel discs	110	260	2.6	38.01	Ni 80/20

Table 2.3: Design Parameters of Heater.

CIRCUIT	**Heater Tube ID/OD**	**Heating Wire OD**	**Hot length**	**Coil length**	**Coil pitch**	**Free diameter**	**Heat transfer area**	**Specific heat flux**
	mm	mm	cm	mm	mm	mm	mm^2	W/cm^2
SCT Barrel	14/16	2	331	397	4.6	10	208	4.55
SCT EC	11/13	1	363	390	3.3	8.7	131	4.81
Pixel barrel/opto-boards	11/13	1.15	373	390	3.3	9	117	3.98
Pixel discs	11/13	1.15	402	390	3.0	8.7	145	1.77

Table 2.4: Design Parameters of Heater (Heating Element).

Because of the requirement of non magnetic materials in ATLAS, all the metallic parts (except heating wire) of the heater are made in stainless steel AISI 304L/316L. The joints between the sections of tubes and the fittings are orbital welded. Power cables from heating element (ceramic insulated custom made connectors) to LEMO connectors are kapton insulated. Cable's outer diameters are approximately 2.4 mm for the thermocouples and 1.6 mm for the power.

Heating element is a heating wire, electrically isolated by compressed electrical insulating powder (Magnesium oxide) and is divided in "hot" and "cold"

parts. The hot part, made in Constantan (copper-nickel alloy) or Ni80/20, is the electrically resistive section and is part located inside the heater body and the cold part, made in copper with low electrical resistance, is the part outside the heater body up to the ceramic insulated custom made connectors. This cold section also goes into the heater a little such that the hot part is truly inside the heater body.

DC high voltage power supplies are used for the heaters power source. This minimizes the injection of noise to the ID from the heaters during operation, and minimizes the size, occupancy and cost of cables. Heaters are powered with a fixed voltage of 110 V, to respect safety requirements. To provide the required power to boil the fluid in the heater and warm it to 20 °C, and no more, the heaters are switched on and off in accordance with the temperature of the outside of the copper pipe just after the heater. The copper pipe temperature is assumed to follow the fluid temperature.

The Distributed Power Supply (DPS) system, delivering total 160 kW of power to the heaters, is divided into four racks and distributed on both sides of the experimental cavern. Half of the racks are located in the USA15 and half in the US15 caverns. This is done to minimize the length of the power cables from racks to the detector.

To prevent the C_3F_8 refrigerant from excessive temperature the hottest point (in line with the end of the hot section of the heating wire at the outlet of the heater) of the outside of the heater is measured. If this temperature goes above 100 °C (sufficient safety margin with a C_3F_8 decomposition temperature of 200 °C) the power to the heater is turned off (interlock). The control of the power to the heater is preformed by four 64-channel Programmable Logic Controllers (PLC) which are located in USA15 service cavern. They are used to control all 204 heaters of the evaporative cooling system. As explained in Section 2.6, to control power delivered to the heater and monitor heater temperature (interlock to protect against overheating of the heating element), each heater is equipped

with two (main) temperature sensors. The PLC takes readings of the control temperature signal and turns on and off the heater as required to maintain the vapour temperature close to 20 °C with the use of metal-oxide-semiconductor transistors in DPS racks. The PLC can also completely switch off the supply to the heater in case of interlock signal. Remote control (switching ON or OFF) of DPS power supply racks in US15 and USA15 cavern is also provided by PLC.

From the point of mechanical design, there are two types of heaters for each sub-detector groups, "Short" and "Long". Drawing of SCT Barrel Heater (Long) is presented in Figure 2.11. For "Short" type of heater, the only difference is the length of pipe, on both sides of heater's main body, to connectors. (For SCT Barrel heater it is 20 mm and 18 mm, instead of 65 mm and 94 mm).

Originally it was planned to install the Heaters inside the inner detector volume, but for safety reasons and the opportunity to have better access, in case of malfunctioning, the Heaters were installed on the inner detector cryostat flange. This required mechanical modifications for Heaters, return pipes and cables. Modification done to SCT Barrel, End-Cap and Pixel Heaters are shown on drawings Figure 2.12 and Figure 2.13.

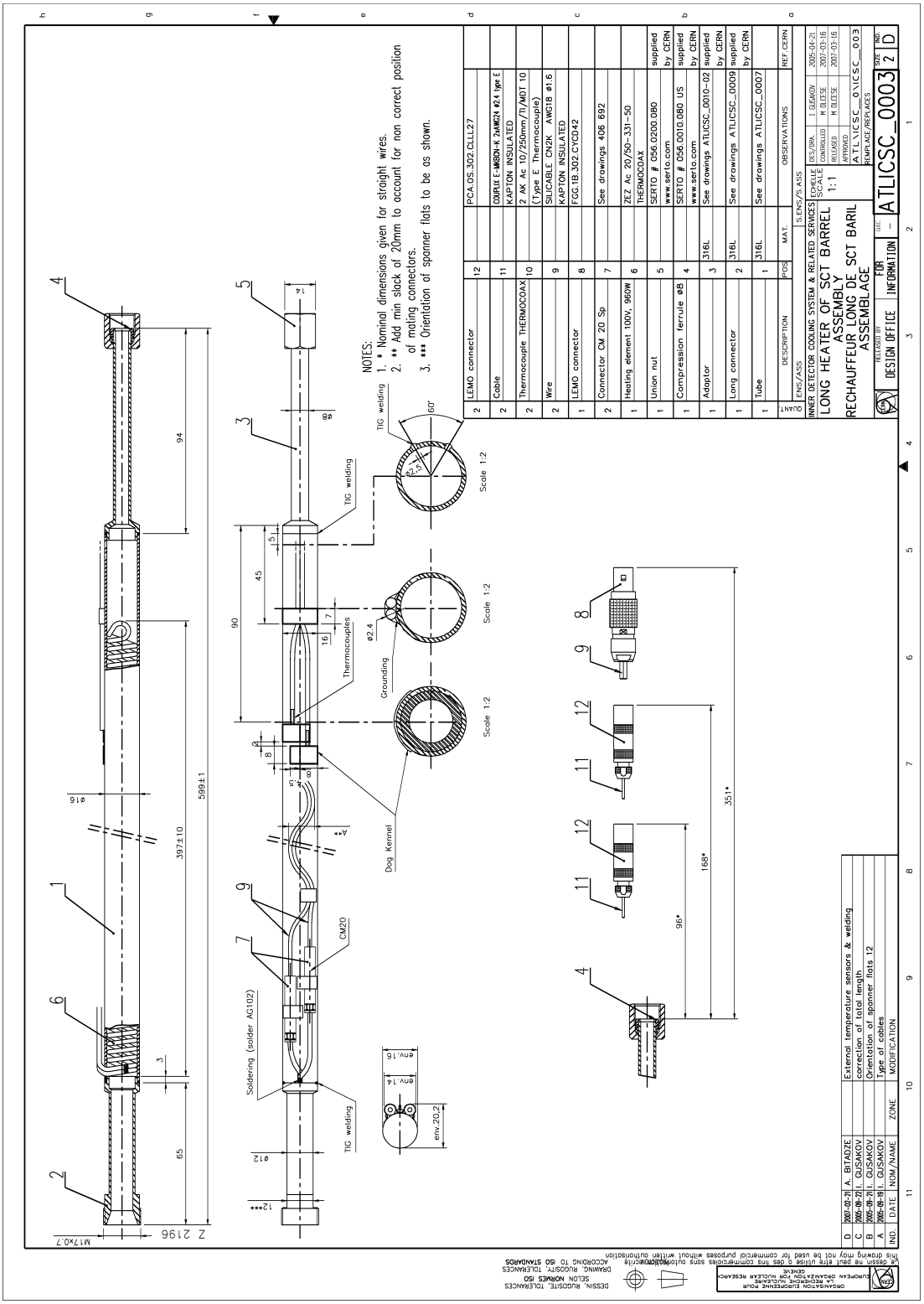

Figure 2.11: SCT Barrel Heater (Long)

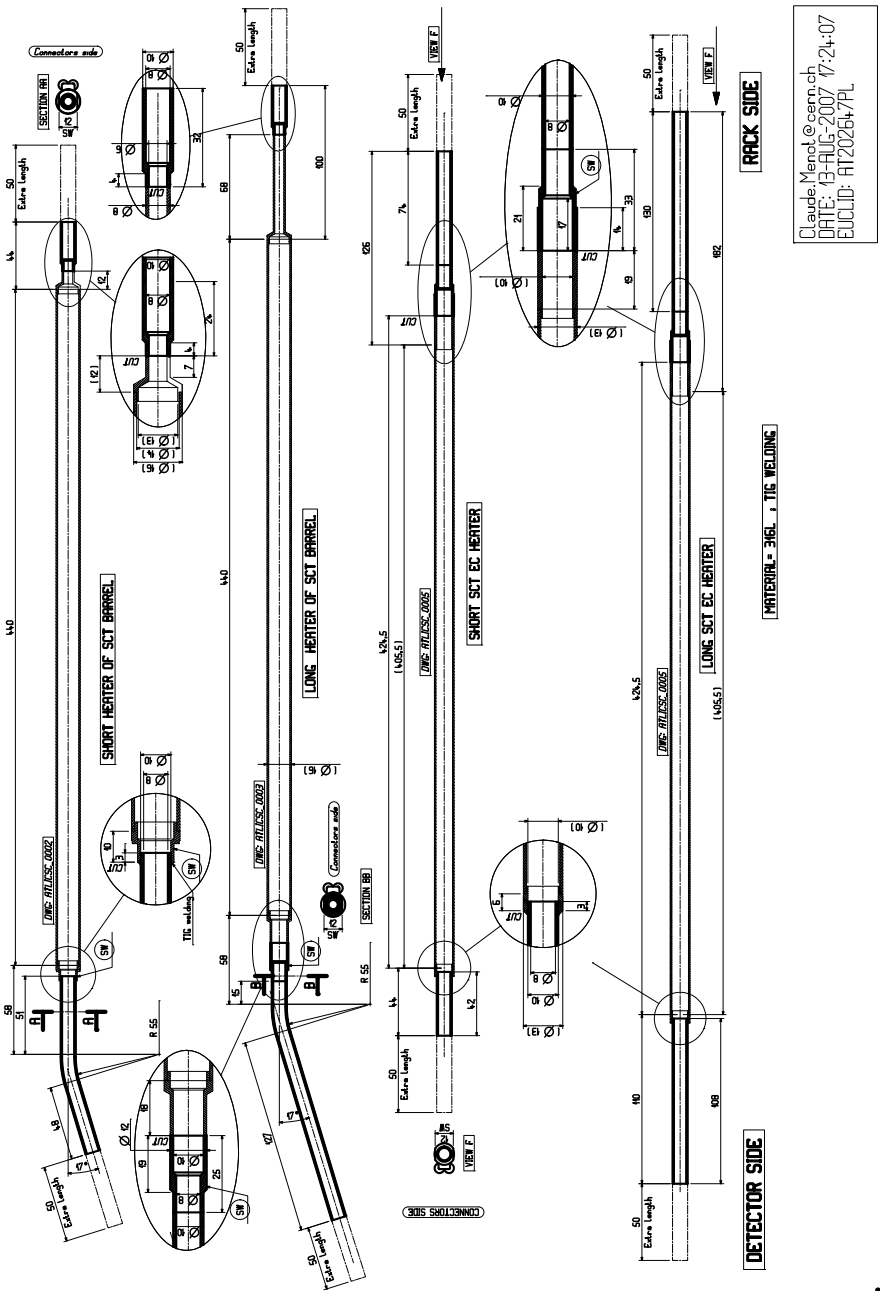

Figure 2.12: Modifications for SCT Barrel and EC Heaters

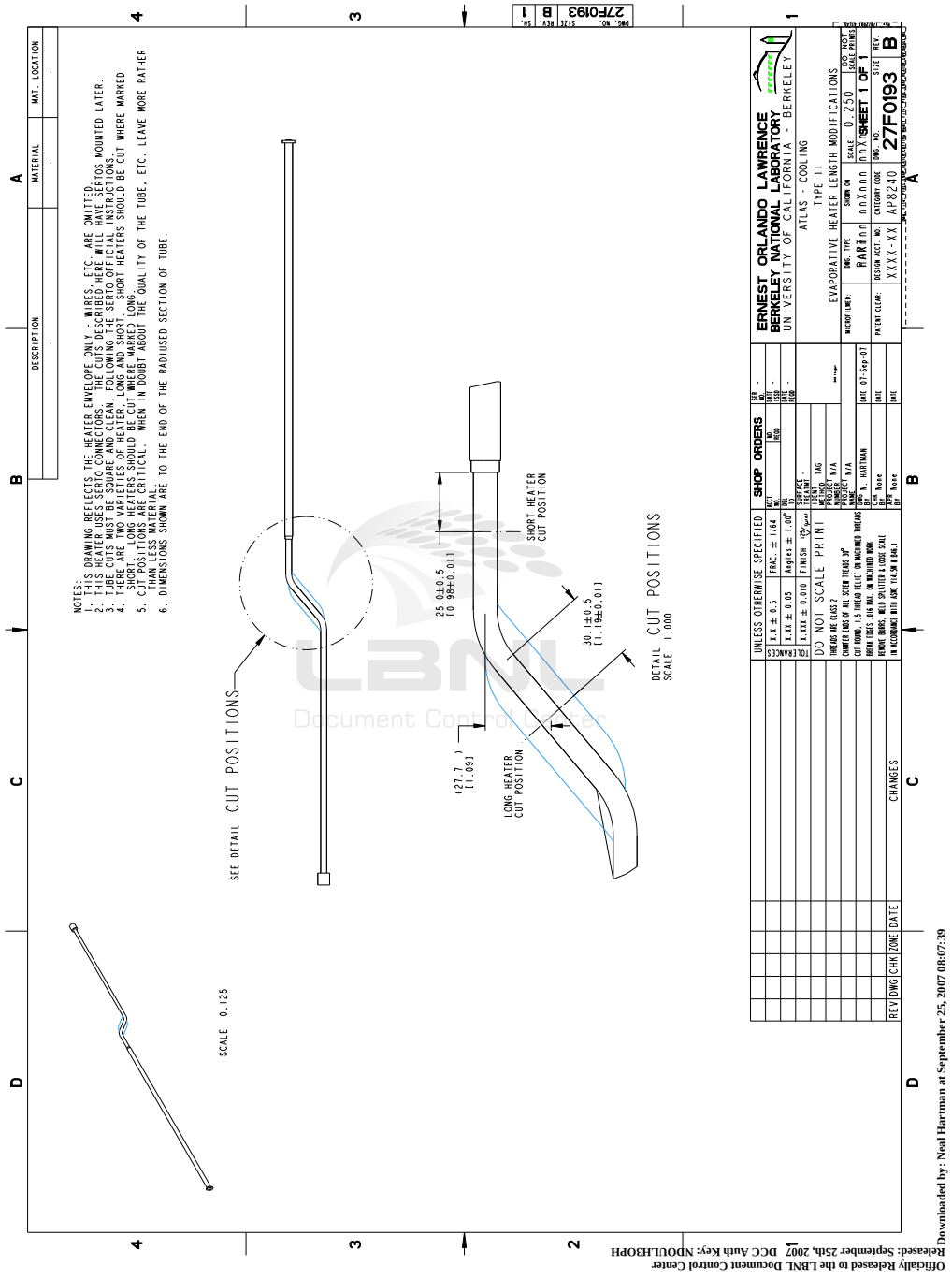

Figure 2.13: Modifications for Pixel Heaters

2.5.5 Heater Pads

Since the Semiconductor Tracker (SCT) operates at a cold temperature, lower than the Transition Radiation Tracker (TRT) which surrounds it, an abrupt thermal transition must be provided by heating the exterior of the SCT thermal enclosure. This is achieved using "Heater Pads" attached to the outside of the SCT thermal enclosures. The soft thermal transition prevents the TRT (operating on room temperature) from damage and prevents the SCT from forming condensate in time of service maintenance. Thermal enclosures as well contribute to structural integrity and prevent mixing of gases between different sections of the ID.

Heater pad represents a single physical piece of polyimide sheet with one or more Heated Areas, heated by spirally shaped heating elements (resistor). The supply of electrical power to the heater pads and monitor of their temperature is provided by 48 volt Heater Pad Control System [39]. Control parameters are set and status information like temperatures, alarms and ON/OFF statuses are monitored by the Detector Control System (DCS) from FSM panel (Section 2.6). A simple schematic of the Heater Pad Control System is presented in Figure 2.14 [39].

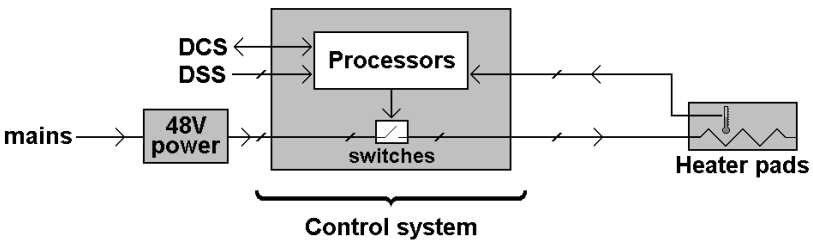

Figure 2.14: Simple schematic of the Heater Pad Control System.

All main electrical parts of 48 V Heater Pad Control System are mounted on two racks, separately located in US15 and USA15 service caverns. Communication to the DCS is provided through the CANBus connection. 48 V power is delivered to heater pads through Switching Cards. Controlled by ELMB pro-

cessor, Switching card sends power pulses to resistive heating elements of each Heater Pad separately. The cycle time is about two seconds. One custom made Controller card is installed separately into each system racks, used to control the Request (REQ) and external Enable (EN) input or Reset signals to the Switching Card sent from Detector Safety System (DSS) and monitoring signals sent to the DCS. For safety reasons and for high reliability each Controller Card is powered by two separate and independent 24 volt power supplies. Switching Cards and Controller Cards are installed and connected into the crates (mounted into rack) using the AMP connectors and Positronic connectors. 1.6 A self-resetting fuses are used to individually protect each switching element. For system safety, DSS is able to cut power to heater pads regardless of any state or condition of software or any ELMB card.

2.6 Control System

For the ATLAS ID different operation modes are foreseen, meaning different running conditions for the SCT and Pixel sub-detectors, different thermal conditions for sub-detector layers and different thermal conditions for "'Start Up", "Normal Run" and "Shut Down" procedures. Therefore, a reliable Control System is necessary to monitor and maintain the control set-points of the evaporative systems, namely; inlet/outlet pressure, heat load, different evaporation temperature (pressure), separately for each cooling circuit. The control System of the inner detector evaporative cooling system is part of the overall ATLAS Detector Control System (DCS) [15], which is responsible for the control and monitor of the supply of powering, cooling and other necessary control signals. DCS as well ensures the full protection of the detector from any failure or error conditions, by rapid software actions or by direct hardware interlocks. The DCS also supplies safe communication between the subsystems and data acquisition system (DAQ) [40].

All parameters and values of the inner detector evaporative cooling system are defined and monitored from a Finite State Machine (FSM) [15] panel, which is based on the software platform PVSSII [14]. FSM is a framework, which controls and monitors the behavior of a system, based on logical connections/links between system status, working state, actions and events.

The FSM of the Inner Detector infrastructure is hierarchically structured, reflecting the sub-systems, sub-detectors and their quadrants ("Q1", "Q2", "Q3", "Q4"), as well as each cooling loop. Screen shot of the general view of the FSM control panel is presented in Figure 2.15.

The control of the main plant is based on a standard Programmable Logic Controller (PLC). Set parameters (values), temperature and pressure values, all warnings and alarms are transfered to the PLC (located into the USA15 cavern), so it takes necessary actions to maintain detector cooling and keep detector in safe state.

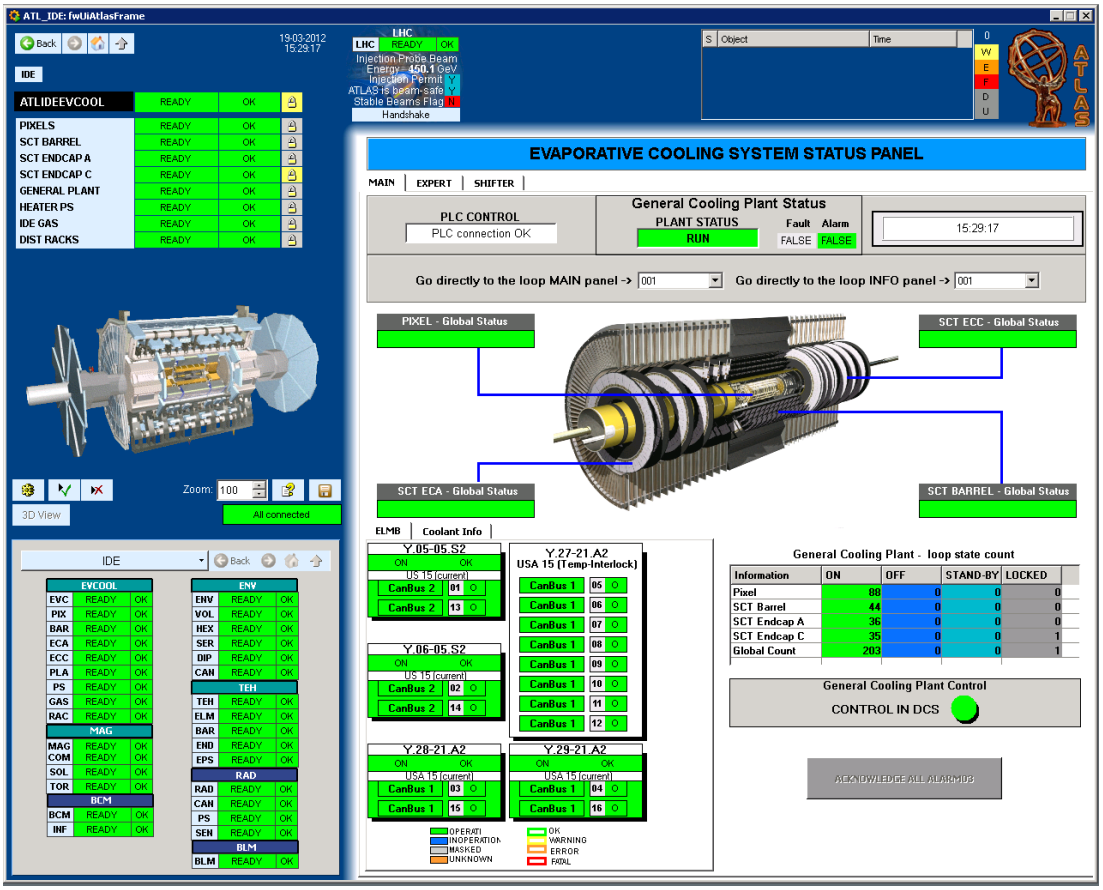

Figure 2.15: Control System FSM Panel

As mentioned above, the control system is able to maintain and monitor general performance of evaporative cooling system as well as all parameters for each cooling circuit. Figure 2.16 represents the screen shot of the FSM control panel for the one cooling circuit.

Each cooling loop is supplied with several temperature and pressure sensors. "S1" and "S2" sensors (one of which is redundant), located on the exhaust part of the detector structure, are used to monitor refrigerant temperature on exit of detector and serve as interlock in case of cooling malfunctioning. There is one more sensor, attached to the detector structure, to monitor the detector temperature and serves as an interlock as well. The "C1" temperature sensor is located on the inlet liquid line after the recuperative heat exchanger, and is used to monitor the inlet liquid temperature before the capillaries. The "C2"

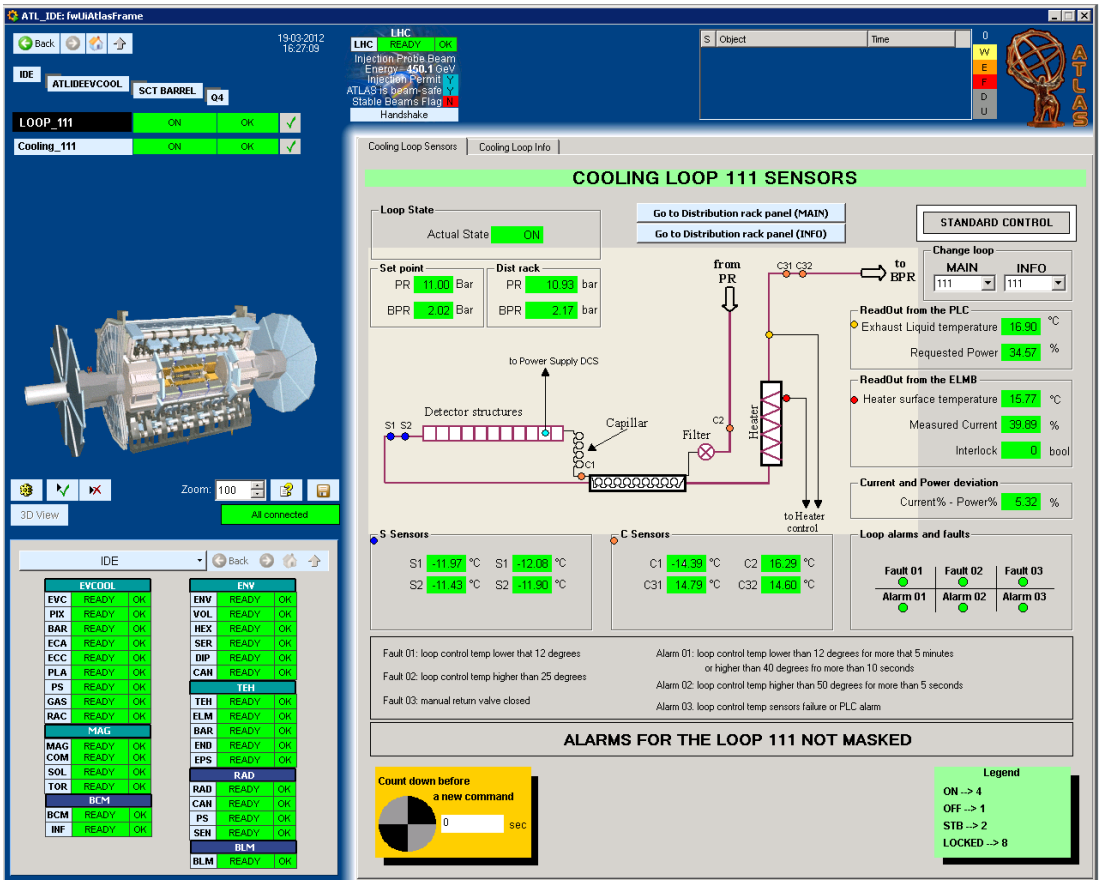

Figure 2.16: Control System FSM Panel (for the one cooling circuit)

sensor, located on inlet pipe before the HEX, serves as an inlet liquid temperature indicator. By comparing temperature difference between these two sensors, the Heat Exchanger's efficiency can be calculated (see Subsection 2.5.3). There are two (one redundant) temperature sensor attached to the Heater's surface, serving as an interlock signal, to ensure that the power is cut from the Heater, in case of overheating. Two temperature sensors (one of which is redundant), located on exhaust pipe immediately after the Heater, are used as a "control" temperature by the PLC supplying power to the Heater (Subsection 2.5.4). "C31" and "C32" temperature sensors are installed on the distribution rack branches to monitor coolant vapour temperature and be sure it is above the ATLAS UX15 cavern dew point (to avoid condensation on non thermally isolated pipes).

In each circuit the Inlet and Outlet coolant pressures are monitored by pres-

sure transmitters mounted on the distribution rack branches, before the inlet-pressure (PR) and the back-pressure (BPR) regulators.

In case of cooling malfunctioning, "warning" and/or "alarm" signals appear on the FSM panel and the DCS sends the necessary action commands to the PLC, which takes the required action, for example; putting the cooling circuit, or entire system, into different operation modes.

Operation modes

Pressure and Temperature parameters of each cooling circuit, or entire system, can be changed (adjusted) from the FSM panel (DCS), but in general there are four predefined operation modes for the ID Evaporative cooling system:

ON mode. This is the standard run mode, when refrigerant circulates in the cooling circuit and removes heat from the detector structure (modules). By putting loops in ON mode, from the FSM panel, the DCS sends necessary action commands to PLC: Inlet pressure and back pressure regulators are open (set to nominal pressure and back pressure values), Heater power is on. Coolant in liquid state is injected into circuit and PLC controls supplied heater power.

ON mode can be split into two different run modes, the **"Cold"** and the **"Warm"** operation modes. The "cold" mode is standard/normal operation mode for the detector, when back pressure is set to the value obtaining refrigerant's evaporation temperature necessary to cool the silicon sensors, while the "warm" mode is used only for the commissioning of the detector, allowing safe running conditions, but keeping evaporation temperature and silicon module temperature above the nominal value. Pressure set point values for "cold" and "warm" run are presented in Table 2.5:

STB mode. This mode is used to safely turn off cooling circuits. In case of planned turn off, or cooling system problems, the PLC receives a signal from the DCS and closes the pneumatic operated valve installed in front of the inlet pressure regulator (PR) as well closing Pressure Regulator, by applying vac-

Cold Run	
SCT Barrel	
BPR	$1.4\,\mathrm{bar}_a$
PR loops in Q1 and Q2	$12\,\mathrm{bar}_a$
PR loops in Q3 and Q4	$14\,\mathrm{bar}_a$
SCT EndCap	
BPR	$1.4\,\mathrm{bar}_a$
PR loops in Q1 and Q2	$12\,\mathrm{bar}_a$
PR loops in Q3 and Q4	$14\,\mathrm{bar}_a$
SCT Pixel	
BPR	$1.4\,\mathrm{bar}_a$
PR loops in Q1 and Q2	$12\,\mathrm{bar}_a$
PR loops in Q3 and Q4	$14\,\mathrm{bar}_a$
Warm Run	
SCT Barrel	
BPR	$6.3\,\mathrm{bar}_a$
PR loops in Q1 and Q2	$13\,\mathrm{bar}_a$
PR loops in Q3 and Q4	$15\,\mathrm{bar}_a$
SCT EndCap	
BPR	$4.0\,\mathrm{bar}_a$
PR loops in Q1 and Q2	$13\,\mathrm{bar}_a$
PR loops in Q3 and Q4	$15\,\mathrm{bar}_a$
SCT Pixel	
BPR	$1.4\,\mathrm{bar}_a$
PR loops in Q1 and Q2	$12\,\mathrm{bar}_a$
PR loops in Q3 and Q4	$14\,\mathrm{bar}_a$

Table 2.5: Nominal Pressure Set Points for "cold" and "warm" run.

uum. Therefore refrigerant delivery to the detector cooling circuit in question is stopped. The back pressure regulator stays open (is kept at its set-point) letting the remaining liquid evaporate and expel from the circuit. In this case, temperature of the cooling circuit does not fall to a value lower than the operating value, securing the detector against thermal shock. Heater power is still on, but required power is slowly reducing with the flow. When refrigerant flow in circuit equals to zero and requested power for heater is also zero, loop can/should be turned to OFF mode.

OFF mode. Turning the loop OFF will fully open the BPR (by applying vacuum to the dome) to allow the remaining vapour to return to the plant. This would imply very low evaporation temperature in the cooling circuit, but because only a small amount of vapour is left in the return lines the cooling effect will be insignificant. PR and pneumatic operated valve stays closed and PLC still controls power applied to heater, which normally equals to zero.

OFF state should never be applied to a loop which is full of liquid, to avoid very low evaporation temperature (because of open BPR). Therefore it is not recommended to move from ON mode directly to OFF mode.

LOCK mode. This mode is used for keeping unused loop(s) in safely closed condition. In this mode, BPR is closed by applying high pressure on dome ($\approx 7\,\mathrm{bar}_a$), manual valve after the BPR is also closed due to the risk that the BPR might leak. PR and pneumatic valve stay closed. Manual valves on each of the liquid feed lines for the distribution racks are closed as well, due to the risk that the PR or pneumatic valve might leak. Power supply for Heater is off.

Control of the Heater Pads

Control and monitoring of the Heater Pads (Subsection 2.5.5) is also maintained from the Finite State Machine (FSM) panel. A screen shot of the FSM panel is presented in Figure 2.17.

The heater pad branch of the FSM panel gives possibility to set the status of the Control cards and the Crates (Enable or Disable); change or check the status of each heater pad; monitor temperature over the each heater pad; monitor temperature in the different ares of the SCT sub-detector (over the heater pad area);

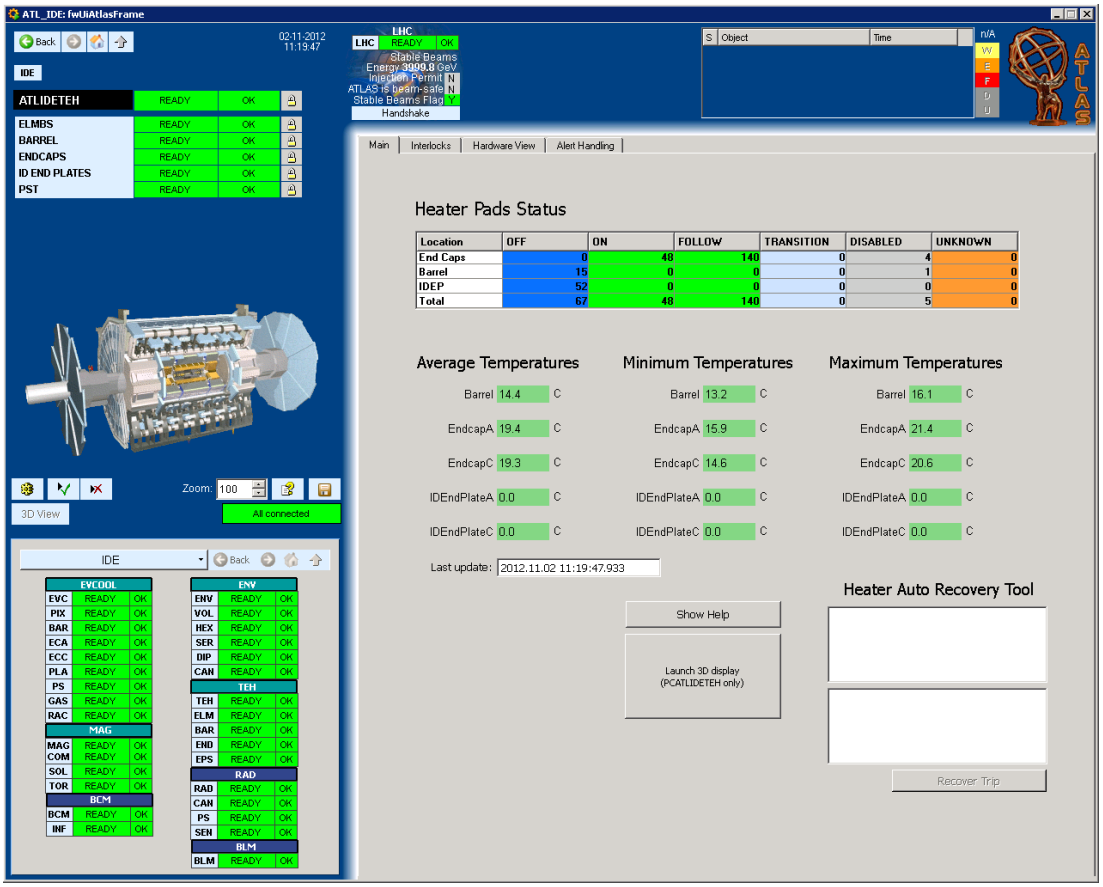

Figure 2.17: Control System FSM Panel (for the Heater pad control)

Chapter 3

The problem statement

The Evaporative Cooling System for the ATLAS Inner Detector is the largest evaporative cooling system used in particle physics detectors to date. The large system structure is custom made and is very complicated. As described in previous chapters, it consists of many different devices, piping structures, and control systems and the proper operation of each part or device is critical for normal running of the ATLAS Inner Detector.

After assembly, installation and commissioning of the system there were some concerns raised about the consistency of system's performance and working parameters, with reference to the requirements made in ATLAS Inner Detector Technical Design Report [41]. These concerns were related to two major subjects, firstly; the LHC and ID luminosity profile, depletion voltage and leakage current (over the ID silicon sensor) predictions, and secondly; the pressure drop predictions for the evaporative cooling system (piping structure).

3.1 Luminosity, Depletion Voltage and Leakage Current reassessment.

Obviously, it is very difficult to exactly predict the LHC luminosity, but originally in the TDR it was assumed, that for the first three years of operation the average instantaneous luminosity would be $10^{33}\,\mathrm{cm}^{-2}\,\mathrm{s}^{-1}$ and for the next seven years would be $10^{34}\,\mathrm{cm}^{-2}\,\mathrm{s}^{-1}$. This would make a total integrated luminosity of approximately $730\,\mathrm{fb}^{-1}$ over the 10 years of LHC operation period, assuming 116 operational days per year. After the first year of operation, these values were recalculated in respect of existing data and future plans for high luminosity modifications leading to the high luminosity (HL-LHC) upgrade to the LHC (known as Phase II operation of the LHC) [42]. For the new calculations of the depletion voltage and leakage current of the ID silicon sensors the revised LHC luminosity profile given in Table 3.1 was used. The HL-LHC upgrade is planned after 10 years of LHC operation, however to be conservative the luminosity predictions used includes an extra 2 years of operation at Phase I instantaneous luminosity levels.

N:	Year	Integrated luminosity $\mathrm{fb}^{-1}\mathrm{y}^{-1}$	Total integrated luminosity fb^{-1}
1	2010	0.5	0.5
2	2011	3.3	3.8
3	2012	15	19
4	2013	19	38
5	2014	41	79
6	2015	42	121
7	2016	99	220
8	2017	132	352
9	2018	132	484
10	2019	145	629
11	2020	193	822
12	2021	242	1064

Table 3.1: Revised LHC Luminosity Profile

In comparison to the shutdown and temperature scenario predicted in the TDR, given in Table 3.2, a set of updated and more detailed operational scenarios, presented in Table 3.3, based on the operational experience of the ID system to

date, were examined to have more detailed understanding of the ID sub-detector's cooling performance.

Attention was paid to the SCT barrel sub-detector, because it requires the most cooling power and has the largest pressure drops due to system design and coolant massflow.

Based on these scenarios (revised operation time and silicon module temperatures), calculations were done to predict the change to the full depletion voltage, leakage current and power dissipated by the silicon sensors as a function of luminosity, which is due to radiation damage.

Days	Experiment Status	Sensor temperature [°C]
116	Beam on	-7
100	Beam off	-7
2	Access	+20
14	Maintenance	+17
133	Beam off	-7

Table 3.2: Operation Scenario. Prediction from TDR.

Scenario	T_{sensor} for first 3 years					T_{sensor} for next 9 years				
	Beam off SCT on	Bam on SCT on	Beam off SCT on	Maintenance	Beam off SCT off	Beam off SCT on	Beam on SCT on	Beam off SCT on	Maintenance	Beam off SCT off
	50d	116d	50d	23d	126d	50d	116d	50d	23d	126d
A	-7°C	-7°C	-7°C	20°C	-22°C					
B	0°C	0°C	0°C	20°C	-15°C					
C	7°C	7°C	7°C	20°C	-8°C	-7°C	-7°C	-7°C	20°C	-22°C
D	15°C	15°C	15°C	20°C	0°C					
E	25°C	25°C	25°C	20°C	10°C					
F						-15°C	-15°C	-15°C	20°C	-30°C
G						-10°C	-10°C	-10°C	20°C	-25°C
(B)	0°C	0°C	0°C	20°C	-7°C	-7°C	-7°C	-7°C	20°C	-22°C
H						-5°C	-5°C	-5°C	20°C	-20°C
I						-0°C	-0°C	-0°C	20°C	-15°C
J	5°C	5°C	5°C	20°C	5°C	5°C	5°C	5°C	20°C	5°C

Table 3.3: Updated possible operation scenarios.

Depletion Voltage and **Leakage Current** are indirect indicators of a silicon sensor's radiation damage (ageing process). Sensor ageing is a long term effect, caused by several parameters [24]:

- High energy particles, from LHC interactions, causing displacements of atoms in the silicon lattice, therefore changing effective doping concentration of near intrinsic silicon in p-i-n diode structure.
- Change in doping concentration causing rise of the voltage required to fully deplete the p-i-n diode structure (full depletion voltage) (bias voltage applied to silicon sensor to form depletion region). For the sensor technology used in the SCT the sensor must be fully depleted to give correct operation and high resolution space points.
- Damage of atomic lattice and change in doping concentration causing rise of leakage current for a given applied bias from the silicon sensor.
- The increase in the applied bias and the associated current gives rise to an increase in the dissipate power from the sensor. If the cooling system is not sufficient, this results in a rise in the silicon sensor's temperature and causes an additional rise in the leakage current and dissipated power.

The feedback process between a rise in leakage current and a rise in the temperature of the sensor can lead to an uncontrolled rise in sensor temperature, known as thermal run-away, if the cooling system is not sufficient. Therefore proper understanding and control of the cooling system is crucial as the integrated luminosity increases to protect against thermal run-away.

The sensor full depletion voltage (V_{dep}), as a function of received particle fluence, was calculated based on the "Hamburg model" [43]. Parameters and formulas used in calculation are presented in Table 3.4 [42].

$\Delta N_{eff}(\Phi,t) = N_a(\Phi,t,T) + N_C(\Phi) + N_Y(\Phi,t,T)$	
Donor removal & stable acceptor	$N_C(\Phi) = -N_{C0}(1-\exp(-c\Phi)) - g_C\Phi$
Unstable acceptor	$N_a(\Phi,t,T) = -g_a\Phi\exp(-\Theta_a(T)t/\tau_a)$ $\Theta_a(T) = \exp(E_a(1/T_R - 1/T)/k_B)$
Reverse annealing	$N_Y(\Phi,t,T) = -g_Y\Phi\left(1-\frac{1}{(1+\Theta_Y(T)t/\tau_Y)}\right)$ $\Theta_Y(T) = \exp(E_Y(1/T_R - 1/T)/k_B)$
$N_{eff,0}$ = 1.026×10^{12} cm^{-3}	E_a = 1.09 eV
$N_{C0} = 0.7N_{eff,0}$	g_C = 0.017 cm^{-1}
c = 0.075cm^{-1}/N_{C0}	g_Y = 0.059 cm^{-1}
g_a = 0.018 cm^{-1}	τ_Y = 480d (T_R=20°C)
τ_a = 55h (T_R=20°C)	E_Y = 1.33 eV

Table 3.4: Change in effective doping concentration and Depletion Voltage Calculation.

where:

ΔN_{eff} - Change in efficient doping concentration;

N_a - Beneficial annealing component;

N_C - Stable annealing component;

N_Y - Reverse annealing component;

N_{eff0} - Efficient doping concentration before irradiation;

N_{C0} - Final donor concentration after Beneficial annealing stage;

c - Removal constant for radiation induced removal of donors;

Φ - Fluence;

$g_{(a,C,Y)}$ - Introduction rate for the given process;

$\tau_{(a,Y)}$ - Annealing time constant for the given process;

t - Time;

T - Temperature;

T_R - Reference Temperature;

$E_{(a,C,Y)}$ - Activation energy for the given process;

$\Theta_{(a,Y)}$ - Temperature scaling factor for a particular process;

Depletion voltage is calculated based on the following equation:

$$V_{dep} + V_b = \frac{q_0}{2\epsilon\epsilon_0}|N_{eff}|d^2$$

where:

V_{dep} - Depletion voltage;

V_b - Bias voltage;

$\epsilon\epsilon_0$ - Permittivity of silicon;

q_0 - Charge on an electron;

d - Thickness of the depletion layer (physical thickness of the detector at full depletion);

Results for predicted depletion voltage, for a sub-set of the different operation scenarios given in Table 3.3, are presented in Figure 3.1 [42].

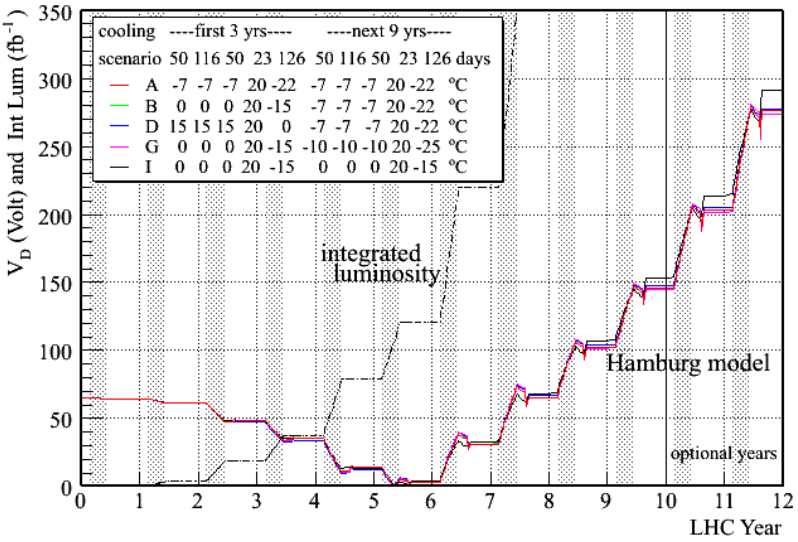

Figure 3.1: Predicted Depletion Voltage.

Equations used to calculate leakage current (I_{leak}) are presented in Table 3.5 [42] and results, for a sub-set of the different operation scenarios of Table 3.3, are presented on Figure 3.2 and Figure 3.3 [42]

$$I = g\left(\Theta(T_A)t_{ir}, \Theta(T_A)t'\right)\alpha\Phi V$$

$$g\left(\Theta(T_A)t_{ir}, \Theta(T_A)t'\right) = \sum_{i=1}^{n}\left\{A_i \frac{\tau_i}{\Theta(t_a)t_{ir}}\left[1-\exp\left(-\frac{\Theta(T_A)t_{ir}}{\tau_i}\right)\right]\exp\left(-\frac{\Theta(T_A)t'}{\tau_i}\right)\right\}$$

$$\Theta(T_A) = \exp\left(\frac{E_I}{k_B}\left[\frac{1}{T_R}-\frac{1}{T_A}\right]\right)$$

$$E_I = 1.09eV$$

$$\alpha_{eq}(-7°C) = 6.90\times10^{-18}\,\mathrm{Acm}^{-1}$$

i	1	2	3	4	5
$\tau_{i(\min)}$	1.2×10^6	4.1×10^4	3.7×10^3	124	8
A_i	0.42	0.10	0.23	0.21	0.04

Table 3.5: Leakage Current Calculation.

where:

i - The term in the sum of exponentials;

g - Introduction rate;

Θ - Temperature scaling factor;

T_A - Annealing temperature;

T_R - Reference temperature;

t_{ir} - Irradiation time;

t' - Time after irradiation;

E_i - Activation energy;

α - Current-related damage constant;

A_i - Normalisation factor for each exponential factor in the exponential sum;

τ_i - Time constant for each term in the exponential sum;

k_B - Boltzmann's constant;

Φ - Fluence;

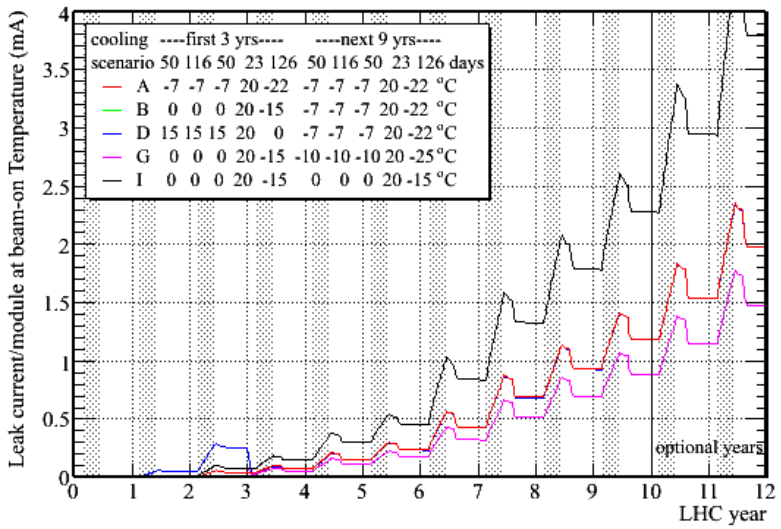

Figure 3.2: Predicted Leakage Current at the operating temperature

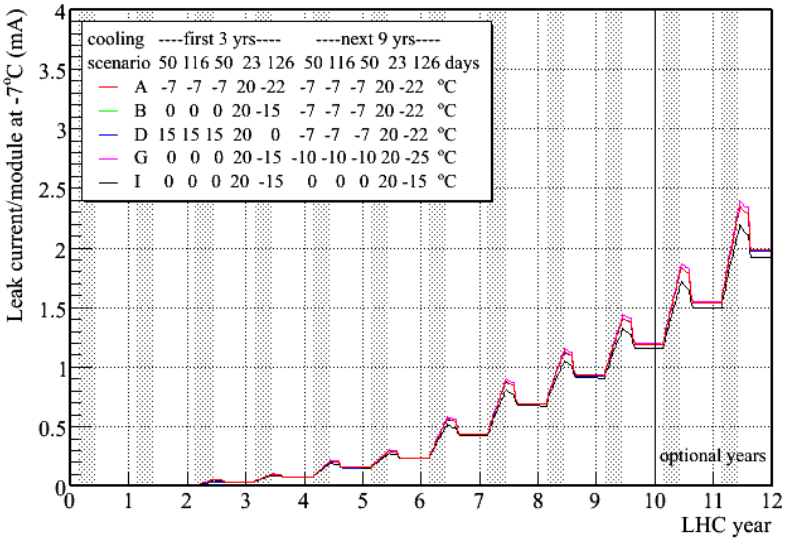

Figure 3.3: Predicted Leakage Current normalised at -7°C

Results show that values are lower then predicted in the TDR; LHC luminosity 629 fb^{-1} instead of 730 fb^{-1}, depletion voltage 250 V instead of 450 V, leakage current 1.5 mA instead of 2.0 mA. Based on the recent calculations, depletion voltage level will reach 250 V (150 bias voltage + 100 over-depletion voltage) and leakage current level will reach 1.5 mA over the ten years of the LHC operation period, resulting in total dissipated power from the silicon sensor of 0.375 W. Based on these predictions, by using the thermal simulation (FEA) and theoretical model (see Figure 3.4) [44], thermal stability of the detector was recalculated [42]. The thermal runaway time was calculated based on the thermal runaway critical point; at a chosen coolant temperature (-22°C) the thermal runaway critical point is equivalent to 150μWmm^{-2} and with a safety factor of 2 equals 75μWmm^{-2}. Time to reach this thermal runaway critical point was calculated and results are presented in Figure 3.5. It can be concluded that coolant temperature should be -15°C to achieve the thermal stability of ID over the ten years of operation period (with a safety factor of 2).

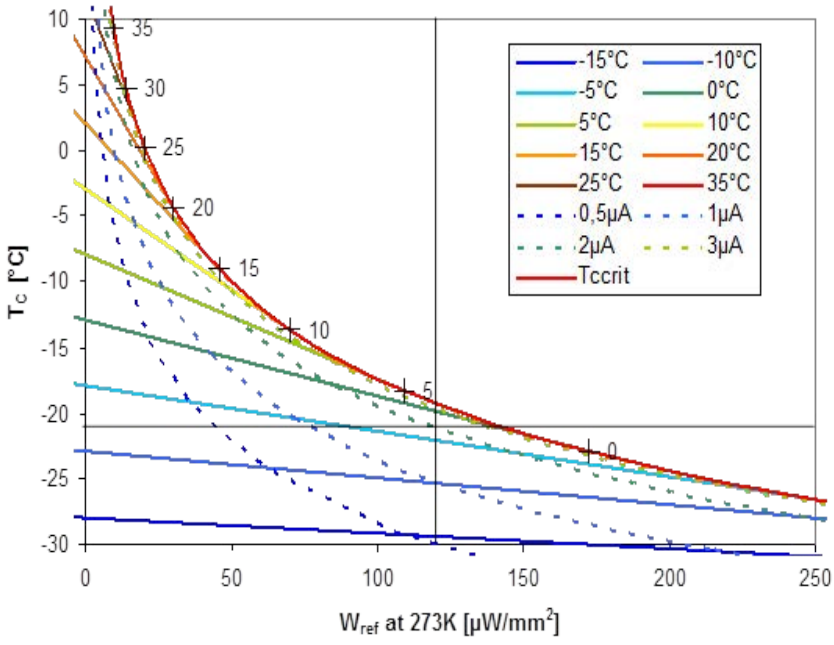

Figure 3.4: Thermal runaway limits

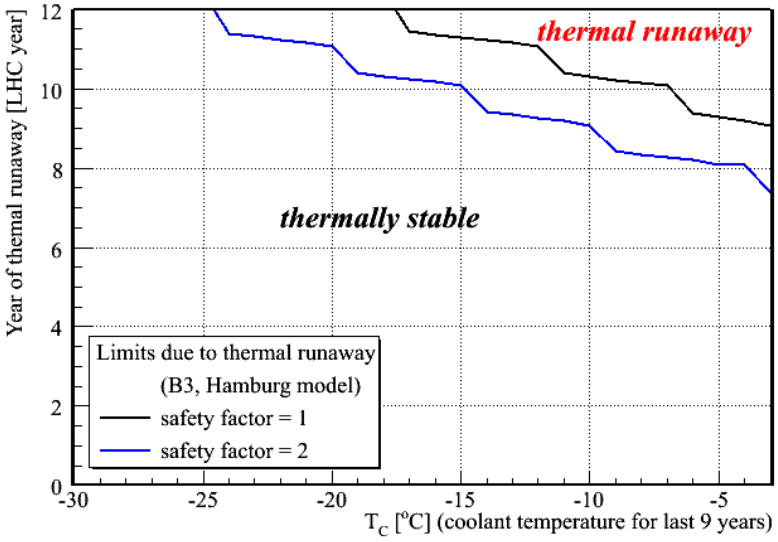

Figure 3.5: The runaway year as a function of coolant temperature

Reassessment of the luminosity profile, depletion voltage, leakage current and the thermal runaway critical points, presented above, shows that the ATLAS inner detector evaporative cooling system must be able to provide the coolant temperature in the cooling stave at -15°C to be capable to remove the heat from the irradiated modules; the maximum predicted power dissipated from each module at the end of the operation period is ≈10.5 W (silicon sensor 250 V×1.5 mA = 0.375 W + module hybrid power 7.5 W + expected convective heat load for top modules 0.8 W + safety margin for the cooling system 1.8 W). This will guarantee the thermal stability of the inner detector over the ten years of operation.

3.2 Pressure drops over the cooling structure

Bigger concerns were raised about the pressure drops in the vapour side of the cooling system, between the detector structure and the BPR, affecting the temperature of the coolant and questioning the possibility of having the design -25°C or necessary -15°C evaporation temperature in the cooling stave.

The original design plan of the evaporative cooling system [33] assumed 470 mbar pressure drop budget, over the coolant return pipes, from the detector structure (end of stave) to the back pressure regulator. This gave the possibility of having an evaporation pressure of 1.67 bar_{abs} in the stave cooling pipe (C_3F_8 refrigerant's temperature of -25°C corresponding pressure), in case of the minimum possible back pressure at the distribution rack before the BPR of 1.2 bar_{abs} (Section 2.4).

After the installation of the piping system, especially after the necessary modifications for the Heater's design and position (Subsection 2.5.4), it became doubtful if it was possible to have such a small pressure drop budget over the modified piping structure.

Tests were performed on the installed in ATLAS SCT Barrel loops, to check the cooling circuit temperature (S1 and S2 sensors at the exit of the Stave)(Section 2.6) in case of minimum possible back pressure in the system.

The liquid inlet pressure on PR was set to 12 bar_{abs} and 14 bar_{abs} leading to the 13 bar_{abs} pressure before the capillaries at the detector (the difference being caused by the hydrostatic head for top and bottom quadrants). The system back pressure was varied by changing the value set on the BPR. The BPR was set to the minimum value of 1.2 bar_{abs} and to 1.5 bar_{abs}, 2.0 bar_{abs} and 3.0 bar_{abs}. SCT Barrel modules were turned ON (fully powered) with the power dissipated per module of ≈6 W, which is the power load for the unirradiated SCT Barrel module. Measurement of the cooling circuit temperature (average of S1 and S2 sensor values) as a function of the back pressure in the system (vapour pressure measured before the BPR) shown as an averaged of the SCT Barrel cooling loops in a quadrant, are presented in Figure 3.6.

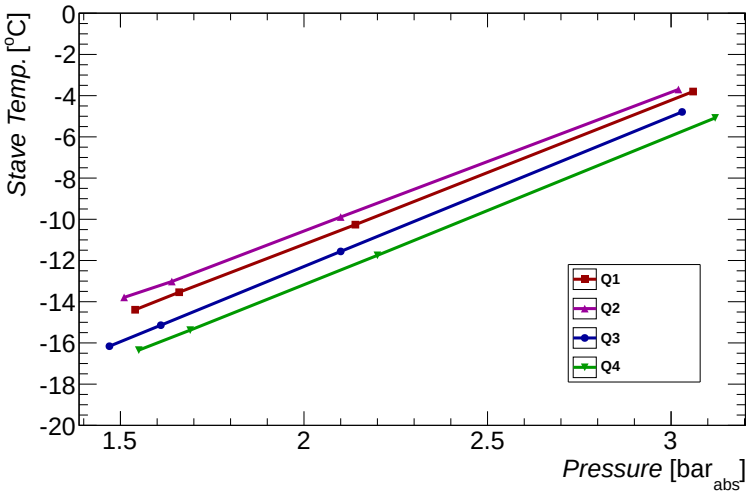

Figure 3.6: SCT barrel cooling circuit temperatures (averaged by quadrant) as a function of vapour back pressure.

The small difference in temperature for top (Q1,Q2) and bottom (Q3,Q4) quadrants is caused by a small difference in massflow which depends on hydrostatic pressure in inlet lines and set points (See Section 2.4).

The measured temperature of the SCT Barrel staves clearly show that with the existing system it is impossible to reach the design evaporation temperature of -25°C or necessary -15°C (for top quadrants) even in case of unirradiated modules. Therefore it is impossible to guarantee thermal stability of the inner detector, especially at the end of the operation period, when modules will be irradiated and work at "full power" (10.5 W).

To study this problem in detail it was decided to assemble a new test setup in the CERN SR1 Laboratory. This test structure duplicates the in-pit installation as much as possible and has been used to perform extensive tests to study the cooling performance of the ATLAS Inner Detector Evaporative Cooling System.

Chapter 4

Laboratory Measurements, Analysis and Results.

As the main part of this PhD work, I had a leading role in the design and construction of a test station in the CERN SR1 laboratory. This was used for extensive studies of the thermal behavior of the ATLAS inner detector cooling system; the results from which were used to make predictions of the performance of the ATLAS ID cooling system at the end of life of Phase I of LHC operation. This work included measurements of pressure drops in the system, measurements of temperature over the stave pipe, study of flow and other parameters. Based on results (presented below) we were convinced that the existing cooling system cannot reach the design evaporation temperature, therefore a new approach was proposed. I studied the thermal behavior of the evaporative cooling system with C_3F_8/C_2F_6 refrigerant mixture. To achieve this a machine to blend C_2F_6 and C_3F_8 was designed and produced. A sonar based mixture analyzer was designed and developed to enable online real time measurements of the blend ratio. I proved that with the correct blend mixture it is possible to achieve the necessary evaporation temperature (-15°C) for the ATLAS inner detector and it should maintain the inner detector's thermal stability even at the end of the 10 years

operation period. The work relating to the design of the test system and the results and interpretation from the C_3F_8 coolant measurements are presented in this chapter. The work performed on the blend station, sonar analyzer and C_3F_8/C_2F_6 blends are presented in the next chapter.

4.1 SR1 Test Station

The laboratory mock-up is an as close as possible duplicate of one of the ATLAS ID SCT Barrel cooling loops. Only spare parts from the in-pit installation were used in this assembly to reproduce the cooling loop's geometry, technical specifications and thermal performance as close as possible to the working ID evaporative cooling structure. A general view of cooling system assembly is presented in Figure 4.1 and a schematic view is presented in Figure 4.2.

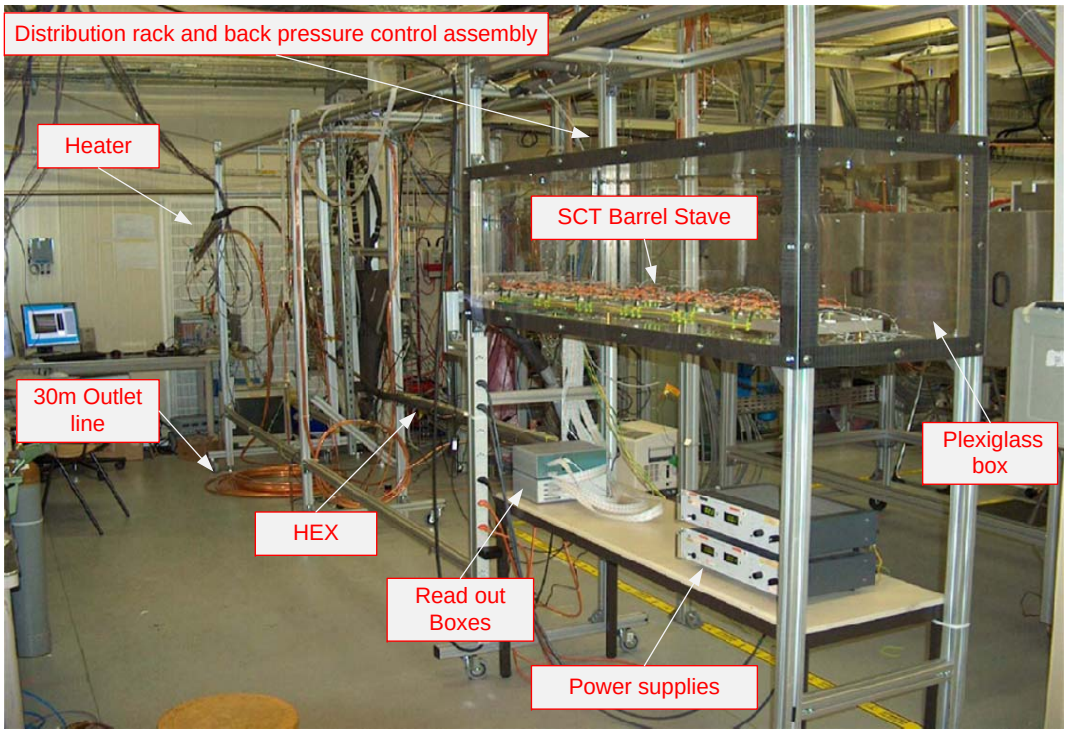

Figure 4.1: General view of SR1 Test Station.

The understanding of the system depends on the accurate measurement of the fluid temperature and pressure at various points throughout the system

and the massflow through it. The pressure in the system was measured with KELLER Type PAA-33X [45] pressure transducers and for temperature measurements NTC thermistors Type 104JT [46] were used. These were mounted at points of interest over the system. For pressure and temperature sensor code-naming and functionality see Table 4.1 and Table 4.2. For the measurements of the flow in the system a Bronkhorst® model F-113AC-AAD-99-V [47] volume flow meter was installed after the back pressure regulator on the vapour return line. The measured volume flow values were converted into mass flow values. For the calculation formulas and error estimation see Appendix D. For the mounting positions of the pressure and temperature transducers and flow meter see schematic in Figure 4.2.

N:	Name	Description
1	P_INPUT	Input Liquid Pressure
2	P_A1	Input Liquid Pressure after the capillary (A)
3	P_B1	Input Liquid Pressure after the capillary (B)
4	P_A2	Pressure in the middle of Stave (A)
5	P_B2	Pressure in the middle of Stave (B)
6	P_A3	Pressure at the end of Stave (A)
7	P_B3	Pressure at the end of Stave (B)
8	P_VAM	Vapour pressure after the Manifold
9	P_BH	Pressure Before the Heater
10	P_AH	Pressure After the Heater
11	P_BBPR	Pressure Before Back Pressure Regulator
12	P_BFM	Pressure Before Flow Meter
13	P_DOME	Dome Pressure

Table 4.1: Pressure transducer naming and functionality.

N:	Name	Description
1	T_LIN	Input Liquid Temperature
2	T_C2	Temperature before Heat Exchanger
3	T_C1	Temperature before Capillary
4	T_PLC	Heater Control Temperature (PLC)
5	T_Heater	Heater Temperature (Interlock Temperature)
6	T_A1 to T_A25	Temperature on Stave (A)
7	T_B1 to T_B25	Temperature on Stave (B)

Table 4.2: Temperature transducer naming and functionality.

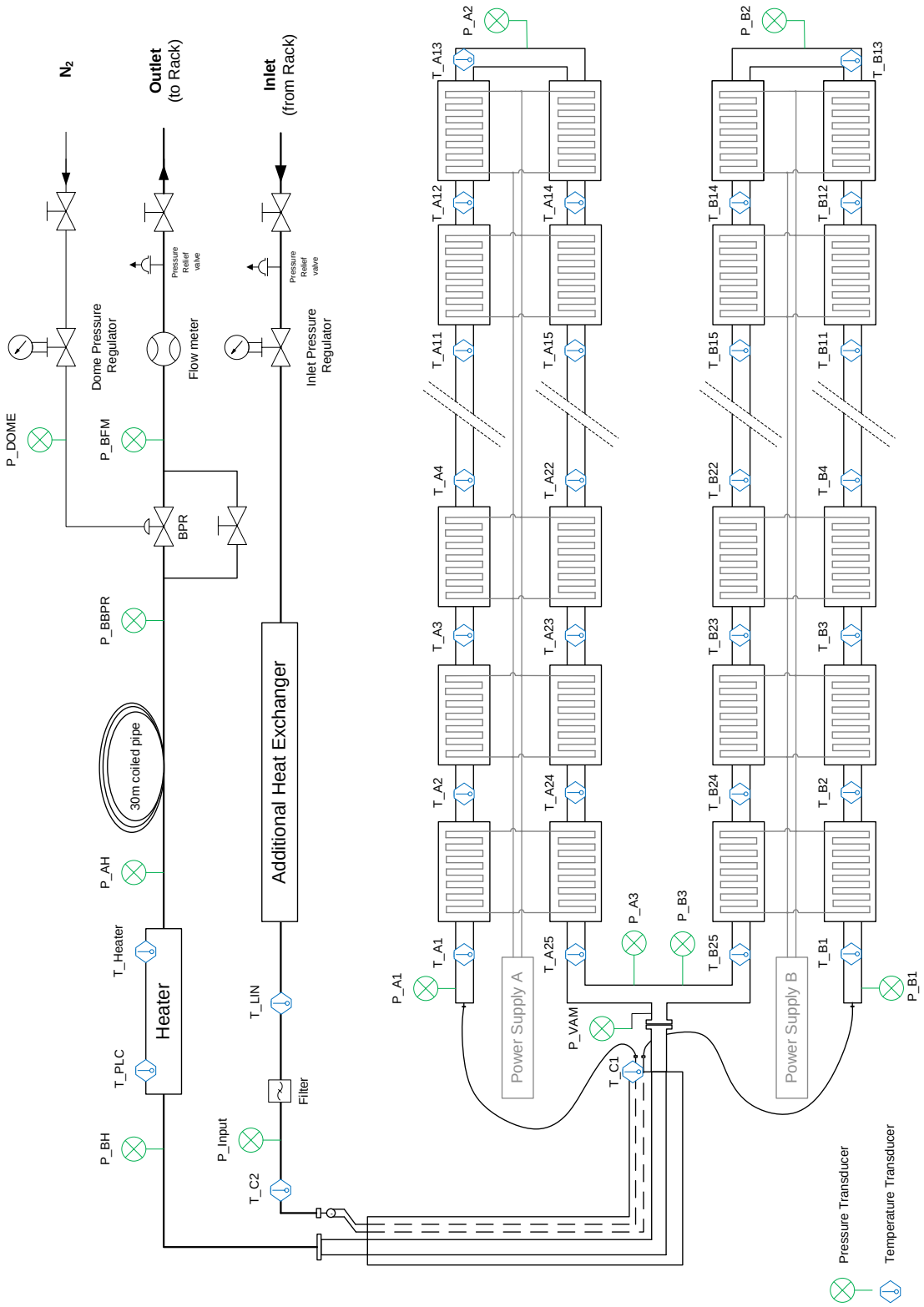

Figure 4.2: Schematic view of SR1 Test Station.

The refrigerant's circulation cycle in the laboratory station is similar to the real ID evaporative cooling system cycle (Section 2.4). A HAUG (model QTOGX 160/80 LM) two-stage oil free compressor was used to circulate refrigerant in the system. The compressor, located outside the SR1 clean laboratory room, compresses the refrigerant (in vapour phase) from 1.2 bar_{abs} at the compressors inlet to 17 bar_{abs} at the compressor's exhaust, and delivers it to a condenser which also acts as the liquid storage tank. Then coolant in the liquid phase (condensed in condenser) is delivered to the distribution rack located in the SR1 clean room. To match the operation conditions of the system as they are in the ATLAS cavern a sub-cooling system with the standard heat exchanger (spare SCT Barrel heat exchanger) is used to keep the delivered inlet liquid temperature ≈17°C. A picture of the thermally isolated heat exchanger, which is connected to a small laboratory chiller (Huber model ICO-12W), is presented in Figure 4.3. The Huber chiller uses standard thermo-regulation liquid (ethanol) and has a working temperature range from -25°C to 40°C.

Figure 4.3: Sub-cooling system (Heat Exchanger).

The liquid inlet pressure is controlled by a standard manual pressure regulator. The inlet line (6 mm CU pipe) with manual pressure regulator and pressure sensor P_{INPUT} is presented in Figure 4.4.

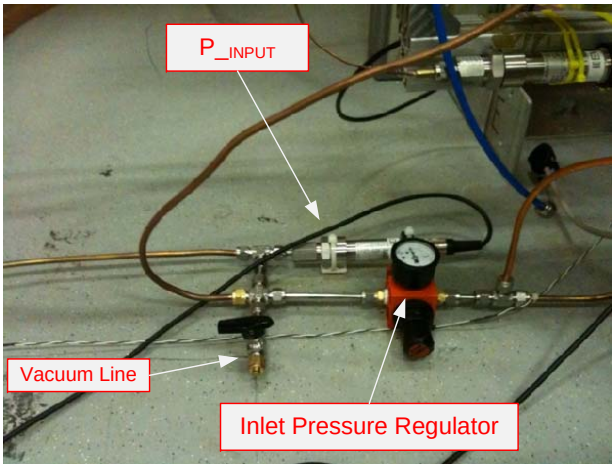

Figure 4.4: Inlet line with pressure sensor (P_{INPUT}) and manual pressure regulator.

The inlet line is connected to an SCT barrel heat exchanger (spare HEX from ATLAS ID installation) (subsection 2.5.3). The geometrical orientation of the HEX is the same as the pit installation for the HEX that serves the barrel cooling loops at the bottom of the tracker (The HEXs in the pit installation have rotational symmetry around the beam axis). A picture of the thermally isolated Heat Exchanger is presented in Figure 4.5. The temperature of refrigerant before and after the HEX is monitored by NTC transducers T_C2 and T_C1.

Two SCT Barrel capillaries (subsection 2.5.2), corresponding to each side of a stave, are mounted between the HEX and the inlet connectors of the stave pipe. SCT Barrel stave (subsection 2.5.1) is located in a Plexiglass® box. This box is thermally isolated with 5 cm thick Armaflex® insulation to avoid external heat penetrating into the box and affecting temperature measurements. A picture of the SCT barrel stave mounted into the box (not insulated on picture) is presented in Figure 4.6.

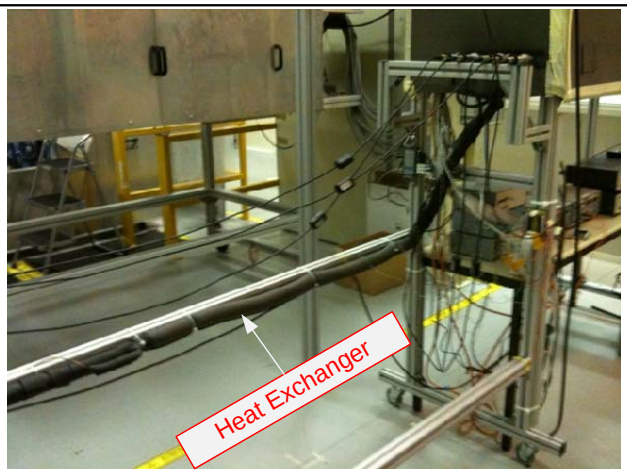

Figure 4.5: Heat Exchanger (HEX).

Figure 4.6: SCT Barrel Stave located into Plexiglass® box.

The stave pipe is instrumented with NTC thermistors (T_A1 to T_A25 and T_B1 to T_B25) along its length and with pressure sensors at the beginning (P_A1 and P_B1), middle (P_A2 and P_B2) and end (P_A3 and P_B3) of the loop. NTC temperature sensors are fixed to the stave pipe with a special plastic ring, assuring tight connection. Thermal grease, GC-ELECTRONICS® 10-8108, is used between the sensors and pipe. Temperature sensors are thermally insulated from the surrounding air with 5 cm thick Armaflex®.

48 "dummy heaters" (ceramic plate with resistive trace on the top surface) are installed in place of the silicon modules. A picture of the stave with mounted ce-

Figure 4.7: SCT Barrel Stave with mounted "dummy heaters" and NTC sensors.

ramic plates and temperature sensors is presented in Figure 4.7. To apply power to the "dummy heaters" (resistors connected in parallel) two Delta Elektronika® SM7020-D type power supplies are used (one per half side of the stave). Electrical circuit parameters are presented in Table 4.3.

Parameter	**Value**
Resistance of one dummy heater R [Ω]	161
Max.Power applied to one dummy heater P [W]	10.5
Current in one dummy heater I [A] ($I = \sqrt{P/R} = \sqrt{10.5/161}$)	0.26
Current for one circuit I [A] (I= 0.26 ×24)	6.24
Voltage in one dummy heater and for one circuit U [V] (U=I ×R=0.26 ×161)	41.9

Table 4.3: Electrical circuit parameters.

The exit of stave pipe (after the manifold joining two sides of stave) is connected to the heat exchanger's return line with custom made connector. Pressure transducer P_VAM is installed after the manifold to measure the refrigerant's pressure at the exit of the stave. The other side of the heat exchanger is connected to a standard ATLAS SCT barrel Heater by a 3 m long, 12 mm internal diameter, thermally isolated stainless steel pipe. This SCT Barrel Heater (Subsection 2.5.4) is positioned to match the in pit installation position for lower quadrant heaters.

A picture of the Heater mounted in the test station is presented in Figure 4.8. Two pressure transducers (P_BH and P_AH) are installed before and after the heater to measure the pressure drop over this region. A Programmable logic controller (PLC) is used to monitor Heater control temperature, interlock temperature and depending on the heater power adjust the delivered power to the heater in order to maintain the heater's standard operation temperature ≈18°C as measured on the outside of the copper pipe 10 cm down flow after the exit of the heater.

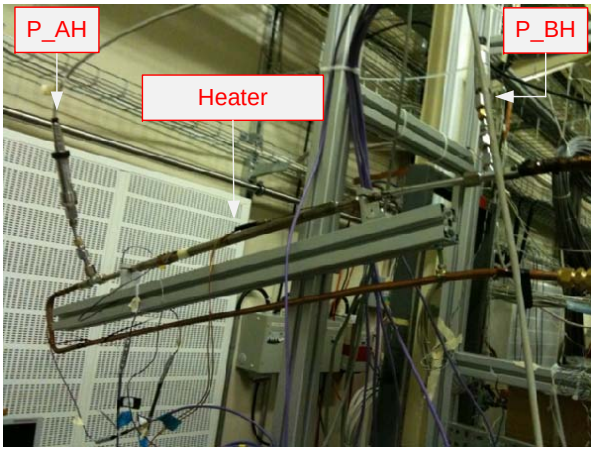

Figure 4.8: SCT Barrel Heater.

Since it was impossible to replicate the complex pipe rooting and the 10 m height difference, as it is in pit, the return copper pipe (30 m in length with an internal diameter of 14 mm) (Figure 4.9) was coiled on the floor of the experimental room. The pipe connected the outlet of the Heater to the distribution rack to reproduce the vapour return line in the ATLAS experiment. This arrangement of the vapour return pipe reproduces the frictional pressure drop in the vapour return pipe. It does not, however, reproduce the hydrostatic head in the system, but calculated hydrostatic pressure for the vapour line (≈0.008 bar) is too small compared to the pressure drops in this region.

To control back pressure in the test assembly, a standard ATLAS SCT Barrel cooling loop back pressure regulator (spare from the ATLAS build) is mounted

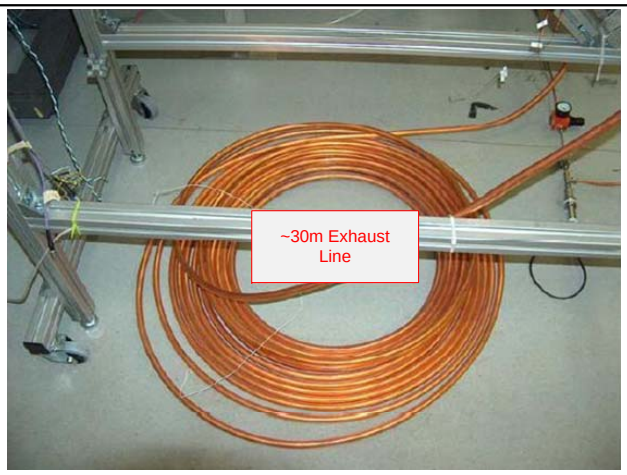

Figure 4.9: Vapour return line.

on the vapour return line in front of the distribution rack. The dome pressure for this BPR is controlled by a small assembly containing a N_2 bottle with pressure regulator. The dome pressure is monitored by pressure transducer P_DOME. Two pressure transducers are installed before (P_BBPR) and after (P_BFM) the back pressure regulator to monitor the pressure before the BPR and the pressure drop over this region. A by-pass line with manual valve is assembled around the BPR which allows the minimum possible back pressure to be obtained.

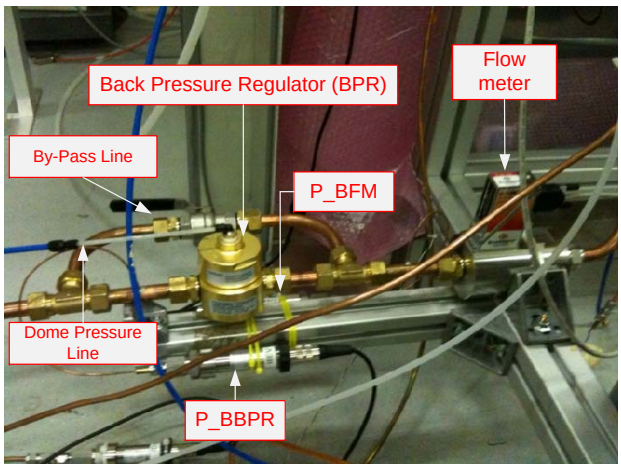

Figure 4.10: Back pressure regulator, pressure transducers, by-pass line and flow meter.

A picture of the back pressure regulator with pressure transducers, by-pass

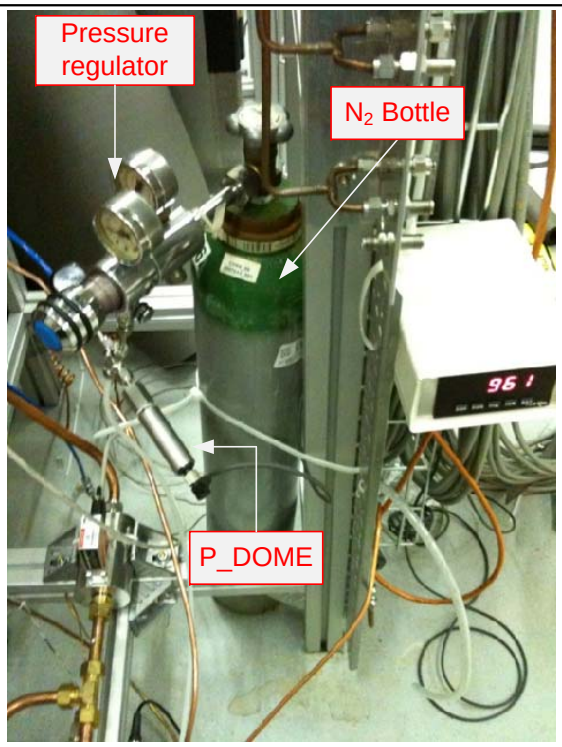

Figure 4.11: Dome pressure control system.

line and a Bronkhorst® model F-113AC-AAD-99-V flow meter is presented in Figure 4.10 and dome pressure control assembly is shown in Figure 4.11.

A custom made Read-Out system was assembled to monitor and record the temperature, pressure and flow values in points of interest all over the test structure. Each of the two Read-Out boxes consists of one Microcontroller, a 24-bit Analog-to-digital converter (ADC) and a 32-channel multiplexer. Temperature sensors are connected to the Read-Out boxes through custom made patch panels and flat flexible cables. Read-Out boxes (Microcontroller) are connected to a PC using standard a USB cable. Pressure sensors and flow meter are connected directly to the PC through the USB interface.

Based on the National Instruments LabVIEW® software development environment, a custom made software application is used for data recording. The recording time and frequency is set from application. Data is stored in *.txt file format.

A picture of Read-Out boxes and the LabVIEW application panel is presented in Figure 4.12.

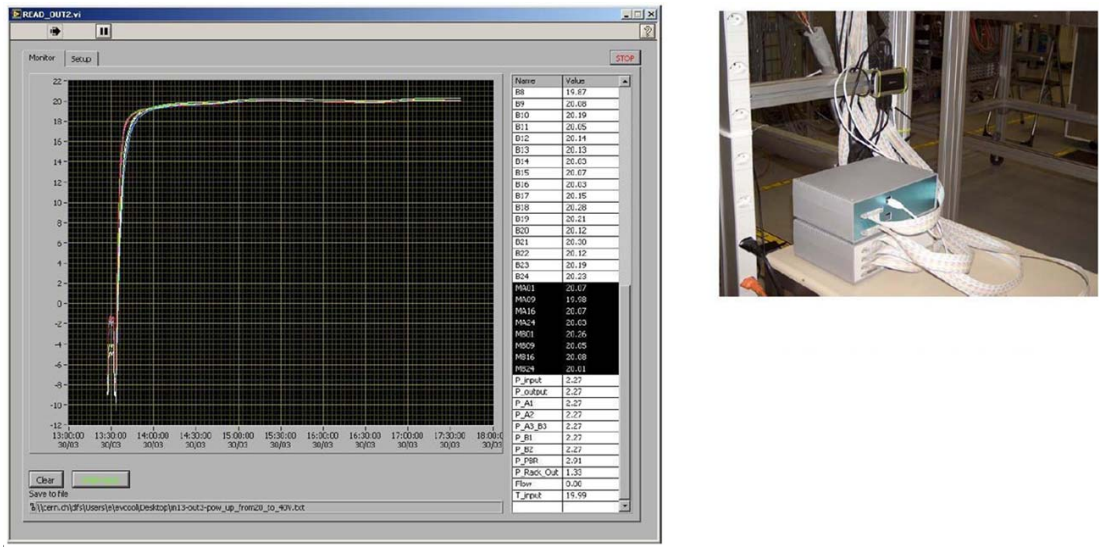

Figure 4.12: Read-out system. LabVIEW® application.

4.2 Measurement Results for C_3F_8

On the laboratory Test Station, measurements were performed with different input liquid pressures (10 bar_{abs}, 11 bar_{abs}, 12 bar_{abs}, 13 bar_{abs}), with different power loads on modules (0 W, 3 W, 6 W, 9 W, 10.5 W) and different back pressures (dome pressure): "Open By-pass" (1.3 bar_{abs}) [1], 1.6 bar_{abs}, 2 bar_{abs}, 2.5 bar_{abs}, 3 bar_{abs}, 4 bar_{abs}, 5 bar_{abs}, 6 bar_{abs} .

As described above in Section 2.4, at the time of construction the design inlet liquid pressure and vapour return back pressure in the system was chosen to guarantee the necessary cooling capacity of the ATLAS ID evaporative cooling system. The input liquid pressure in the system was defined to ensure that the inlet liquid remained above the saturation pressure, resulting in a bigger enthalpy budget over the detector structure and the back pressure was defined to ensure the necessary evaporation temperature over the cooling stave. Therefore a range of input liquid pressures and vapour back pressures was investigated over the laboratory test to study the effects on the massflow and pressure drops in the system. The effect of varying the power load on the module is of interest as well; as described above in Section 3.1, nominal power dissipated from the unirradiated modules is ≈6 W and after the irradiation at the end of the lifetime will rise to ≈10.5 W.

The matrix of measurement parameters is presented in Table 4.4. Some tests "Failed" because of the thermal runaway caused by inadequate cooling capacity. As an additional information, requested power on the exhaust Heater (% value of heater design maximum power, as delivered by the PLC system) is presented as well, just to show the heaters working behaviour as a function of different pressure in system and power per module, therefore different massflow in the system.

[1] In laboratory test station it was impossible to replicate minimum back pressure of 1.2 bar_{abs} because of a bit higher pressure drop over the return pipes from distribution rack to compressor.

Inlet P 10 Bar_{abs}	Power				
	0W	**3W**	**6W**	**9W**	**10.5W**
Open	52%	40%	26%	17%	11%
1.6	51%	39%	25%	16%	9%
2	51%	39%	25%	14%	Failed
2.5	51%	39%	24%	13%	Failed
3	51%	38%	24%	12%	Failed
4	51%	38%	21%	10%	Failed
5	51%	35%	19%	8%	Failed
6	Failed	Failed	Failed	Failed	Failed

Inlet P 11 Bar_{abs}	Power				
	0W	**3W**	**6W**	**9W**	**10.5W**
Open	56%	43%	30%	18%	12%
1.6	56%	43%	30%	17%	10%
2	55%	43%	30%	17%	10%
2.5	55%	43%	30%	17%	10%
3	56%	42.5%	29.5%	16.5%	11%
4	56%	41.5%	26%	13%	8%
5	56%	38.5%	23%	10%	4%
6	55%	36.5%	21%	6%	Failed

Inlet P 12 Bar_{abs}	Power				
	0W	**3W**	**6W**	**9W**	**10.5W**
Open	65%	55%	35%	24%	18%
1.6	61%	47%	35%	21%	19%
2	62%	48%	35%	21%	17%
2.5	61%	48%	35%	21%	15%
3	61%	47.5%	34%	21%	15%
4	62%	46.5%	33%	19%	14%
5	62.5%	44.5%	29%	16%	8%
6	63%	44%	27%	12%	5%

Inlet P 13 Bar_{abs}	Power				
	0W	**3W**	**6W**	**9W**	**10.5W**
Open	66%	55%	41%	27%	22%
1.6	65%	52%	40%	27%	20%
2	65%	52%	39%	26%	20%
2.5	65%	52%	39%	26%	20%
3	65%	51.5%	39%	25%	19%
4	65%	50.0%	37%	23%	17%
5	65.0%	50.0%	35%	21%	15%
6	64%	49%	34%	20%	13%

Table 4.4: Matrix of measurements.

The total pressure drop over the test cooling system, from the exit of the capillary to the entrance of the BPR, was measured as a function of inlet liquid pressure for different module power loads, with the minimum obtainable back pressure before the BPR of 1.3 bar_{abs}. Results are presented in Figure 4.13. For pressure values in different parts of the test structure, see Appendix C. Pressure drops were measured as well in the most interesting parts of system: Over the Stave pipe ("On-detector" part of system) and for piping structure from Stave to Back Pressure regulator ("Off-detector" part of system). Results for pressure drops over the Stave pipe are presented in Figure 4.14 and results for pressure drop over the "Off-detector" part of system are presented in Figure 4.15.

Error estimation was done for measured pressure values (see Appendix D). Total measurement error for the inlet pressure ($\sigma_{P.tot.In} = 19.5\,\text{mbar}$) and total measurement error for the outlet pressure ($\sigma_{P.tot.Out} = 9.86\,\text{mbar}$) are too small to be visible as an error bars on the plots therefore error values are presented in figure caption.

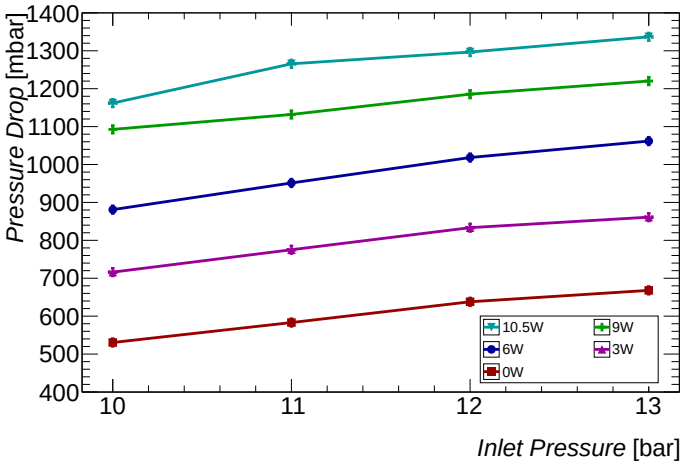

Figure 4.13: The total pressure drop over the system, from the exit of the capillary to the entrance of the BPR, as a function of inlet liquid pressure for different module power loads, with the minimum obtainable pressure before the BPR of 1.3 bar_{abs}.($\sigma_{P.tot.In} = 19.5\,\text{mbar}$, $\sigma_{P.tot.Out} = 9.86\,\text{mbar}$)

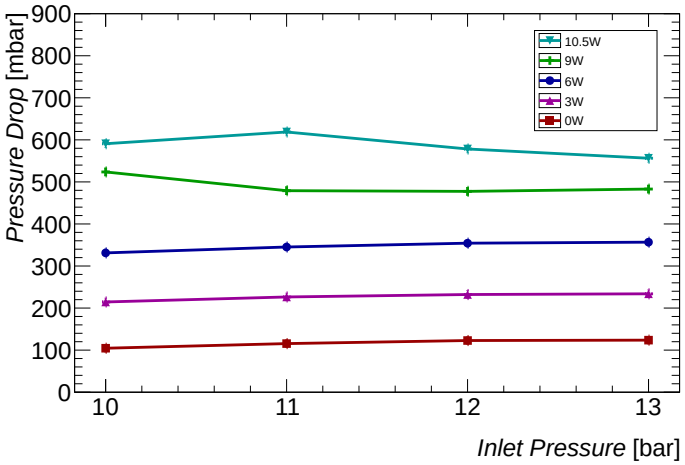

Figure 4.14: The pressure drop over the "On-detector" part of system (over the Stave pipe), as a function of inlet liquid pressure for different module power loads, with the minimum obtainable pressure before the BPR of 1.3 bar_{abs}.($\sigma_{P.tot.In} = 19.5\,\text{mbar}$, $\sigma_{P.tot.Out} = 9.86\,\text{mbar}$)

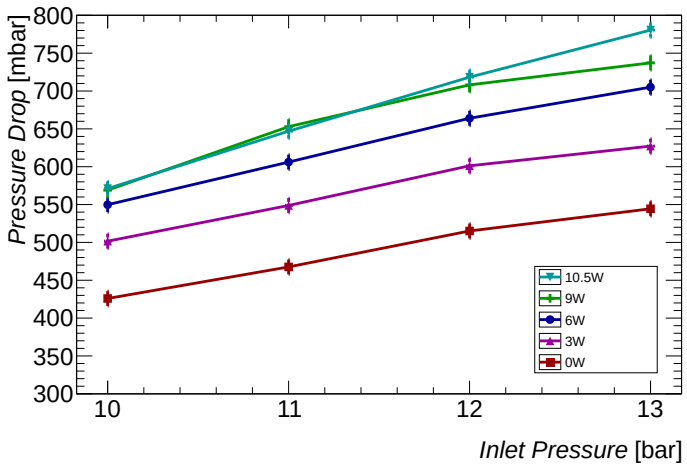

Figure 4.15: The pressure drop over the "Off-detector" part of system, from the exit of the Stave to the entrance of the BPR, as a function of inlet liquid pressure for different module power loads, with the minimum obtainable pressure before the BPR of 1.3 bar_{abs}.($\sigma_{P.tot.In}$ = 19.5 mbar, $\sigma_{P.tot.Out}$ = 9.86 mbar)

Measurement results clearly show that, pressure drop over the "Off-detector" part of system, from the end of the stave to the entrance of BPR, is almost twice the predicted value in the TDR pressure drop budget for SCT barrel cooling loops (470 $mbar_{abs}$) (Section 2.4 and Section 3.2).

This problem leads to higher pressure over the stave, leading to a higher cooling temperature. The design evaporation pressure of ≈1.67 bar_a, the pressure measured at the exit of the stave equals to ≈2.15 bar_{abs} (1300 $mbar_{abs}$ back pressure + 705 $mbar_{abs}$ ΔP over the "Off-detector" part of the system + 144 $mbar_{abs}$ ΔP over the manifold) in the case of nominal 13 bar_{abs} inlet pressure, 1.3 bar_{abs} back pressure and nominal 6 W power per module and in the case of 10.5 W (power for irradiated module) measured pressure at the exit of the stave equals to ≈2.23 bar_{abs} (1300 $mbar_{abs}$ back pressure + 737 $mbar_{abs}$ ΔP over the "Off-detector" part of the system + 195 $mbar_{abs}$ ΔP over the manifold).

The overall thermodynamic behavior of the system is shown on the Pressure-Enthalpy diagram in Figure 4.16. Each of the stages are described in Table 4.5.

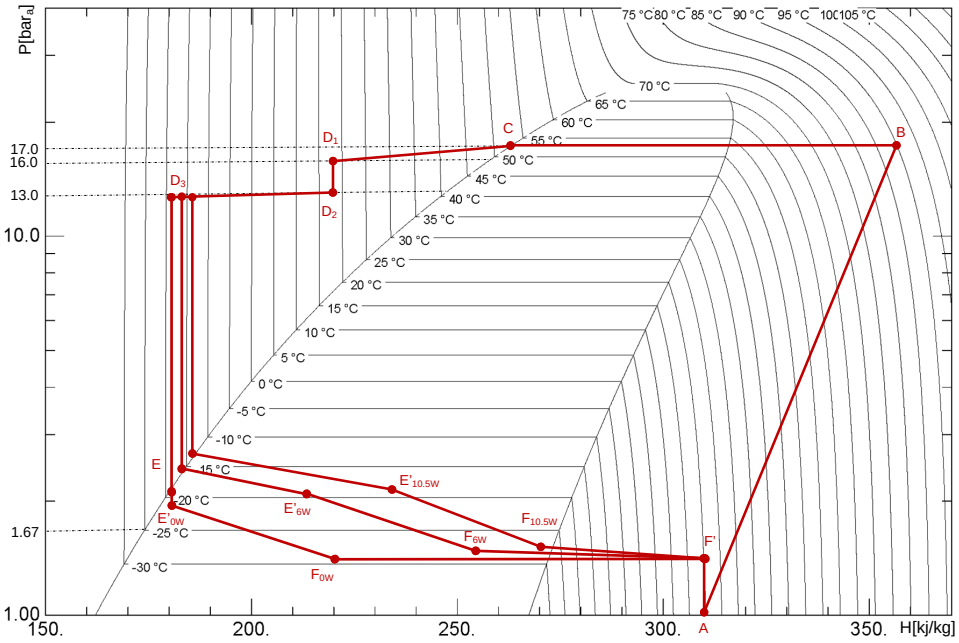

Figure 4.16: Phase Diagram of the SR1 laboratory test station.

Between Points	Description
A to B	refrigerant vapour is compressed at 17 bar_{abs} and 90°C and is delivered to the condenser.
B to C	refrigerant vapour condenses inside the condenser into liquid at 53°C and is delivered to the storage tank for the continuous running cycle.
C to D_1	refrigerant in liquid state from the storage tank is sub-cooled by the plants additional sub-cooling system from 53°C to 17°C at 16 bar_{abs} and is delivered to the distribution rack.
D_1 to D_2	the pressure drop over the pressure regulator in the distribution rack where the pressure value on the pressure regulator is set to 13 bar_{abs}.
D_2 to D_3	sub-cooling system (heat exchanger) where inlet liquid is sub-cooled to -15°C by the counter flow vapour/liquid remaining in the exhaust line to provide as big an enthalpy budget as possible. Note: sub-cooling temperature (position of point D_3) changes depending on heat load on the modules.
D_3 to E	the pressure drop over the throttling element (Capillary). Note: position of point E changes depending on heat load on the modules.
E to E′	refrigerant evaporates inside the cooling stave removing heat from the modules. Note: on the diagram there are presented three different positions corresponding to the different power load on the modules (0 W, 6 W, 10.5 W).
E′ to F	the amount of the enthalpy used in the heat exchanger to cool down the inlet liquid (corresponding to D_2 to D_3). Note: different positions for 0 W, 6 W, 10.5 W.
F to F′	the heater evaporates the remaining liquid and the vapour is warmed up to 20°C (above the dew point). Note: different positions for 0 W, 6 W, 10.5 W.
F to A	the pressure drops over the return lines, from the exit of the heater to the front of the compressor; including pressure drop over the back pressure regulator and over the return lines from rack to the compressors.

Table 4.5: Description of the thermodynamic stages in the SR1 laboratory test station Phase Diagram.

The thermal profile of the cooling Stave was studied in detail with different inlet and outlet pressure in the system and different power applied to the modules, to define possible evaporation temperature in respect to new pressure drop measurement results. Maximum cooling loop temperature over the stave was measured as a function of inlet liquid pressure for different module power loads. Results are presented in Figure 4.17.

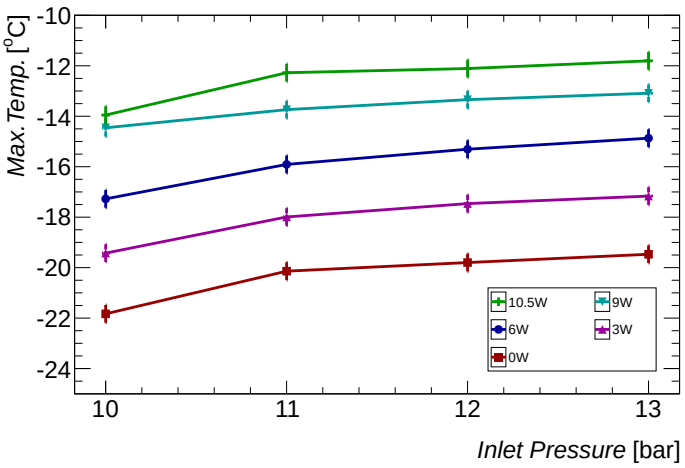

Figure 4.17: Max.Temp. as a function of inlet liquid pressure for different module power loads, with the minimum obtainable pressure before the BPR of 1.3 bar_{abs}. ($\sigma_{P.tot.In} = 19.5\,\text{mbar}$, $\sigma_{T.tot} = 0.35°\text{C}$)

Maximum cooling loop temperature (Max.Temp.) is defined as a measured maximum temperature value by NTC thermistors mounted all over the stave pipe (T_A1 to T_A25 and T_B1 to T_B25) (See Figure 4.2 and Table 4.2), the maximum value measured over the full test time (5 min).

Error estimation was done for measured temperature values (see Appendix D). Total measurement error ($\sigma_{T.tot} = 0.35°\text{C}$) for the temperature values are presented as an error bars on the plots. In some figures they are too small to be visible therefore error values are presented in figure caption.

Max.Temp. over the Stave as a function of Dome pressure (pressure applied to BPR) for different power loads on modules, in case of 13 bar_{abs} input liquid pressure, is presented in Figure 4.18 and as a function of real Back pressure (pressure measured before the BPR), is presented in Figure 4.19. Measured temperature values are presented in Table 4.6. The saturation temperature of C_3F_8 is also plotted as a guide indicating the minimum possible temperature for a given pressure. (Max.Temp. values for 1.3 bar_{abs} are not presented on Figure 4.18, because measurements were done with "Open By-pass", therefore no dome pressure was applied to BPR and minimum back pressure was maintained

by compressor).

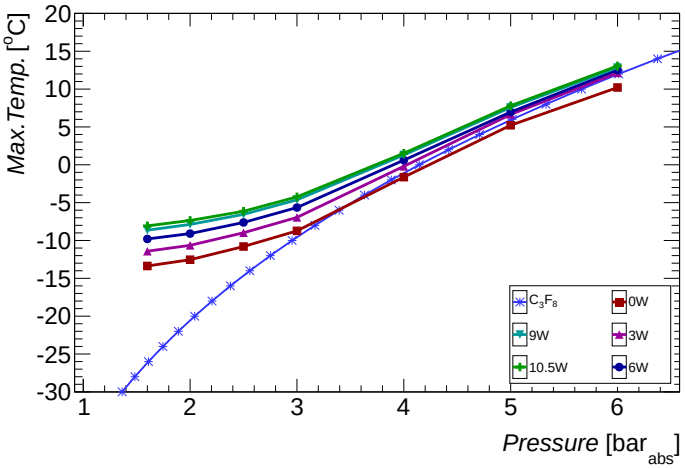

Figure 4.18: Max.Temp. as a function of *Dome pressure* for different module power loads, with C_3F_8 saturation temperature line, in case of 13 bar_{abs} input liquid pressure. ($\sigma_{P.tot.Out} = 9.86$ mbar, $\sigma_{T.tot} = 0.35$°C)

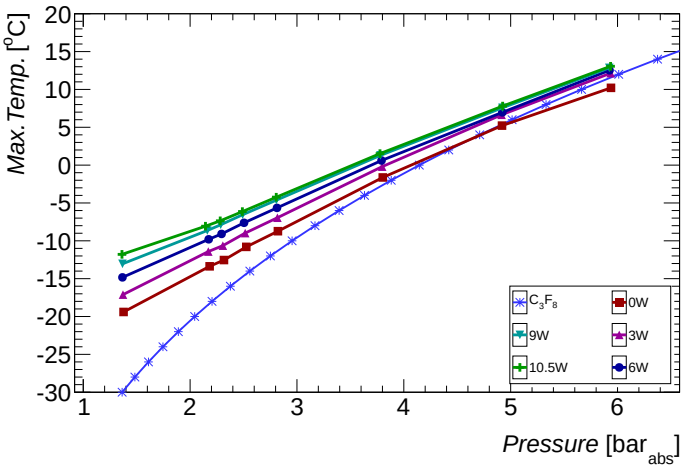

Figure 4.19: Max.Temp. as a function of *Back pressure* for different module power loads, with C_3F_8 saturation temperature line, in case of 13 bar_{abs} input liquid pressure. ($\sigma_{P.tot.Out} = 9.86$ mbar, $\sigma_{T.tot} = 0.35$°C)

Vapour pressure before the BPR [bar_{abs}]	Maximum temperature on the cooling loop [C] Module power				
	0W	3W	6W	9W	10.5W
1.3	-19.5	-17.2	-14.9	-13.7	-11.8
2.2	-13.4	-11.4	-9.8	-8.7	-8.1
2.3	-12.6	-10.7	-9.1	-7.9	-7.3
2.5	-10.8	-9.0	-7.7	-6.6	-6.2
2.8	-8.8	-7.0	-5.7	-4.7	-4.3
3.8	-1.7	-0.2	0.6	1.3	1.5
4.9	5.2	6.6	6.9	7.5	7.8
5.9	10.2	12.1	12.5	12.8	12.9

Table 4.6: Max.Temp. measured for different power load on modules, in case of 13 bar_{abs} inlet pressure and different back pressure in system.

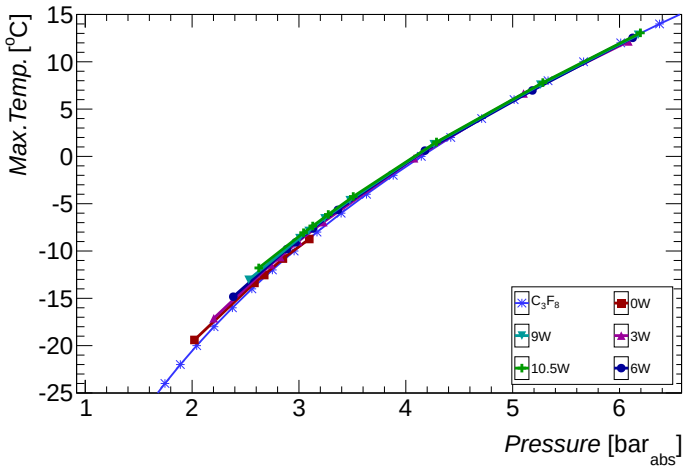

Figure 4.20: Max.Temp. as a function of measured pressure in the middle of the Stave (P_A2) for different power load on modules , with C_3F_8 saturation temperature line, in case of 13 bar_{abs} inlet pressure and different back pressure in system. ($\sigma_{P.tot.Out} = 9.86$ mbar, $\sigma_{T.tot} = 0.35°C$)

Max.Temp. as a function of measured pressure in the middle of the Stave for different power loads on modules is presented in Figure 4.20. Pressure was measured by pressure transducer mounted at the middle of the Stave pipe (P_A2) (See Figure 4.2 and Table 4.1).

To have clear picture of temperature propagation over the Stave pipe, maximum temperature for each separate NTC transducers (the maximum value recorded over the full test time of 5 min) are presented in Figure 4.21. The thermal profile of second (symmetrical) part of the stave is identical.

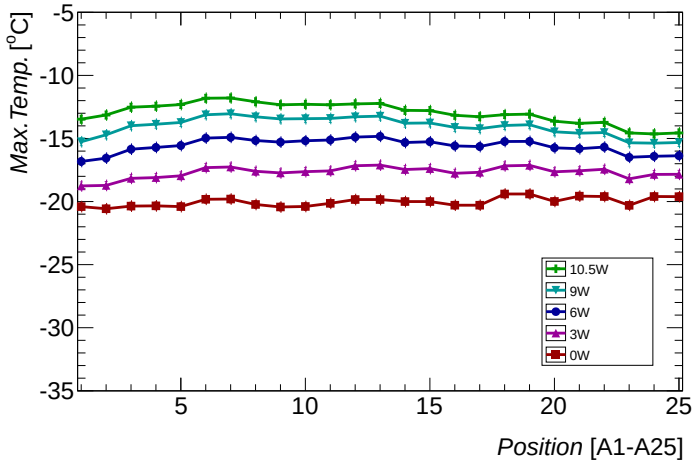

Figure 4.21: Max.Temp. for each temperature transducers for different power load on modules, in case of 13 bar_{abs} inlet pressure and 1.3 bar_{abs} back pressure in system. ($\sigma_{T.tot} = 0.35°\text{C}$)

The mass flow in the system was measured as a function of inlet liquid pressures, for different power loads on modules (presented on Figure 4.22) and as a function of power applied to modules for different inlet liquid pressure (presented on Figure 4.23). For mass flow measured values see appendix Table C.9.

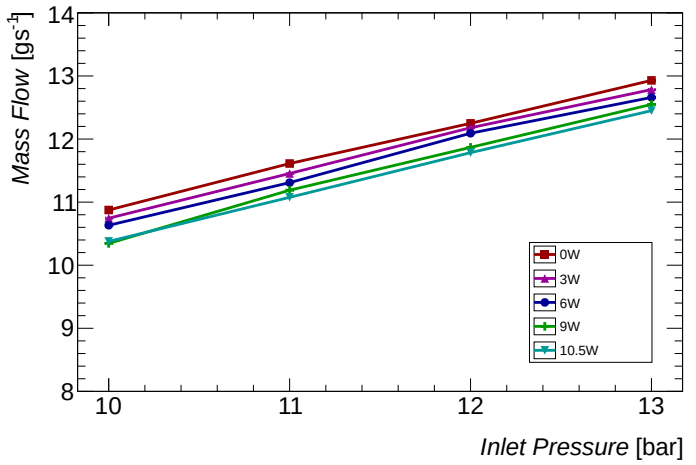

Figure 4.22: Mass Flow in system as a function of inlet pressure for different power load on modules in case of minimum possible back pressure in system 1.3 bar_{abs}. ($\sigma_{P.tot.In} = 19.5\,\text{mbar}$, $\sigma_{Flow} = 0.049\,\text{gs}^{-1}$)

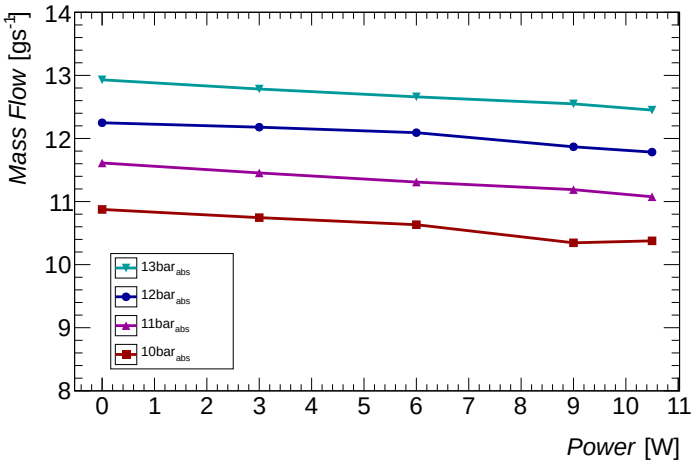

Figure 4.23: Mass Flow in system as a function of power load on modules for different inlet pressure in case of minimum possible back pressure in system 1.3 bar_{abs}. ($\sigma_{Flow} = 0.049\,\text{gs}^{-1}$)

Error estimation was done for measured flow values (see Appendix D). Measurement error ($\sigma_{Flow} = 0.235\,\text{lmin}^{-1}$ / $\sigma_{Flow} = 0.049\,\text{gs}^{-1}$) is too small to be visible as an error bars on the plots.

Measurement results from SR1 laboratory test station, for thermal behavior of the SCT Barrel cooling loop, clearly show that the cooling system can not achieve the design evaporation temperature of -25°C (from TDR) nor the necessary -15°C (Section 3.1) in the Stave. According to test results (See Figures 4.18, 4.19, 4.21), with a nominal inlet pressure in system of 13 bar_{abs}, minimum possible back pressure in system of 1.3 bar_{abs} and maximum heat load per module 10.5 W (at the end of lifetime), C_3F_8 coolant's evaporation temperature over the Stave is higher (-11.8 °C) than necessary -15°C, therefore the thermal stability of the Inner Detector can not be guaranteed.

Because of access limitation for the ID Evaporative Cooling System (it is impossible to reach or change mechanical parts of the system in the ATLAS cavern) the only possible way of improving the cooling efficiency, is to use different mixtures of refrigerants which have lower saturation temperatures.

By adding a certain amount of more volatile Hexafluoroethane (R116) C_2F_6 into Octafluoropropane (R218) C_3F_8, the evaporation pressure for the same evaporation temperature can be raised. This will allow the pressure drop limitation over the "Off-detector" part of the system to be overcome and will give the possibility of having lower coolant temperature in the Stave.

Fluorocarbon Coolant	Average Evaporation Pressure at -25°C [bar_{abs}]	Minimum Evaporation Pressure at -25°C [bar_{abs}]
C_3F_8	1.7	1.7
$90\%C_3F_8/10\%C_2F_6$	2.3	1.8
$80\%C_3F_8/20\%C_2F_6$	2.7	2.1
$70\%C_3F_8/30\%C_2F_6$	3.2	2.3

Table 4.7: Predicted evaporation pressure at -25°C for C_3F_8/C_2F_6 coolant blends.

Predictions of evaporation pressure, from NIST REFPROP [1], at -25°C evaporation temperature in binary C_3F_8/C_2F_6 coolant blends, are presented in Table 4.7. At minimum evaporation pressure 100% of injected coolant is evaporated and at average evaporation pressure 50% respectively.

Chapter 5

Laboratory Measurements for the Fluorocarbon Mixtures.

5.1 Blending Machine

In the SR1 laboratory, outside the clean room, a new device the blend recirculation machine "Blending Machine" (BM) was assembled. This machine is used to mix different concentration of the C_3F_8 and C_2F_6 to make the coolant blends, and for delivering this binary coolant to the Test Station in the clean room for the continuous circulation cycle. The general view of the Blending Machine is presented in Figure 5.1 and the schematic view is presented in Figure 5.2.

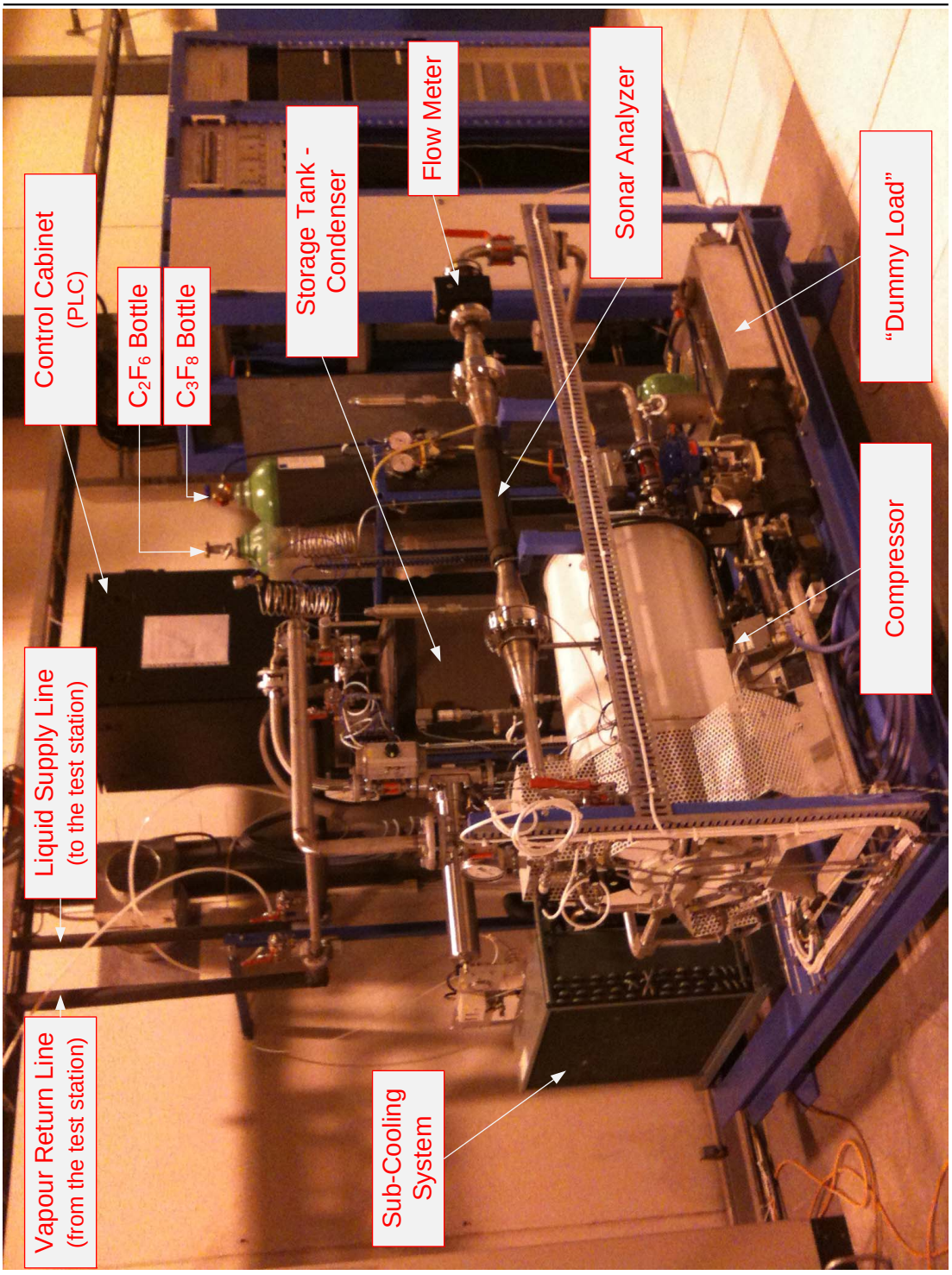

Figure 5.1: General view of the C_3F_8/C_2F_6 fluorocarbon Blending Machine.

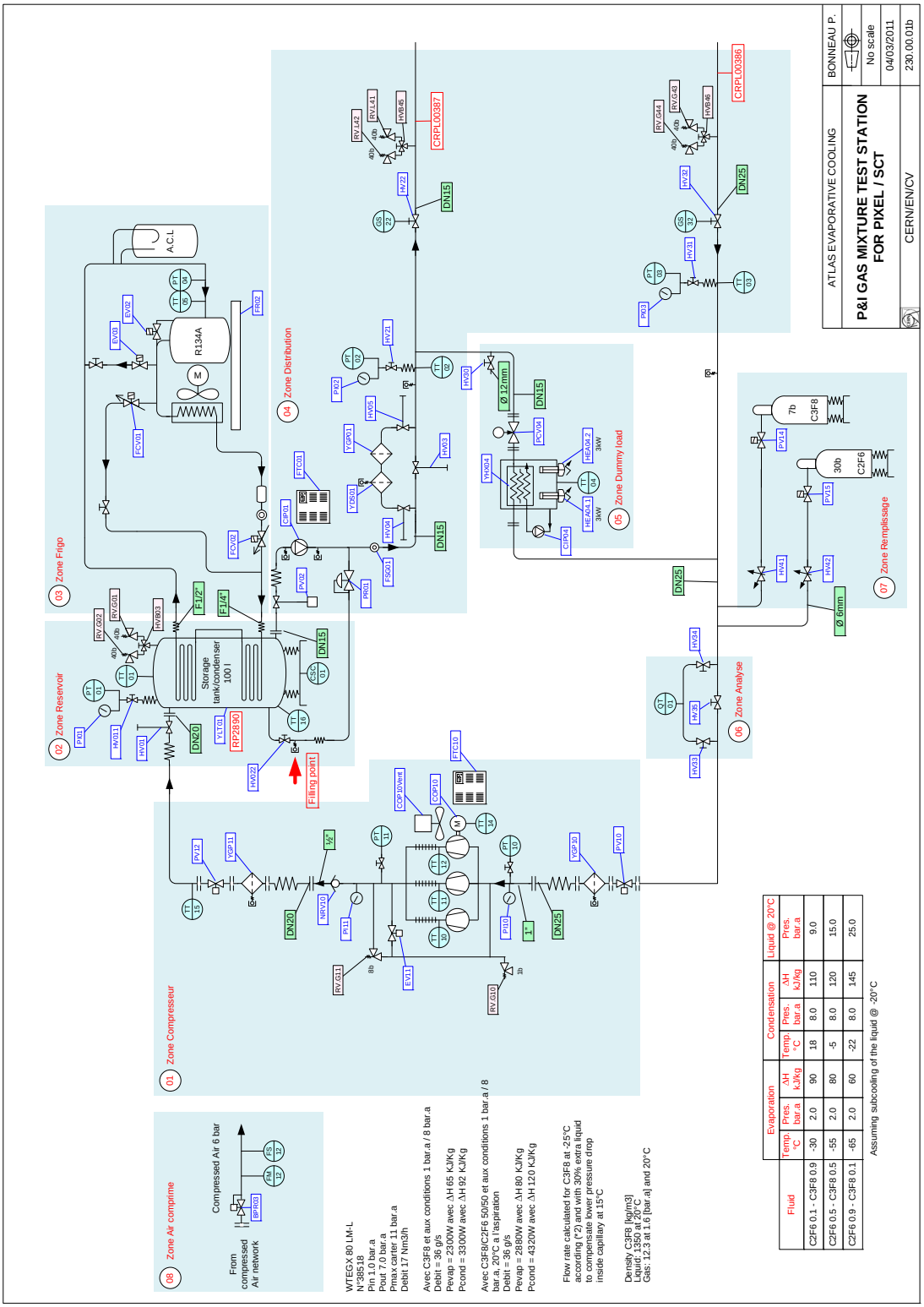

Fluid	Evaporation Temp. °C	Evaporation Pres. bar.a	Evaporation ΔH kJ/Kg	Condensation Temp. °C	Condensation Pres. bar.a	Condensation ΔH kJ/Kg	Liquid @ -20°C Pres. bar.a
C2F6 0.1 - C3F8 0.9	-30	2.0	90	18	8.0	110	9.0
C2F6 0.5 - C3F8 0.5	-55	2.0	80	-5	8.0	120	15.0
C2F6 0.9 - C3F8 0.1	-65	2.0	60	-22	8.0	145	25.0

Figure 5.2: Schematic view of the C_3F_8/C_2F_6 fluorocarbon Blending Machine.

The blending machine, (BM), consists of the several main components:

- The fluorocarbon mixture storage tank / condenser;
- The sub-cooling system for the storage tank / condenser, which represents an assembly of the small refrigeration system circulating hydrofluorocarbon (CH_2FCF_3) in a closed circuit;
- The dummy load assembly used for the refrigerants circulation inside the blending machine internal circuit;
- The sonar analyzer mounted on the vapour side of the pipe structure used for the mixture ratio determination;
- Storage bottles for the C_3F_8 and C_2F_6 freons;
- The compressor providing continuous circulation of the refrigerant inside the blending machine's internal and external circuits.
- Additional laboratory pump to increase the inlet liquid pressure and small laboratory chiller to cool the inlet lines before the pump and avoid cavitation.
- Control cabinet with the PLC, control electronics and compressed air supply for the pneumatic valves.

The pressure and temperature transducers are mounted at points of interest all over the structure to monitor pressure and temperature in the different parts of the BM system. For the component location and the piping connection see the piping and instrumentation (P&I) diagram in Figure 5.2.

During the filling-in process C_3F_8 and C_2F_6 fluorocarbon freons are injected (in the liquid phase) from the storage bottles into the storage tank / condenser of the blending machine according to the strictly defined Step-by-Step procedure [48] while the compressor and pump are off. Blending machine is restarted and condensed mixture in the liquid state under the pressure of $10\,\mathrm{bar}_{abs}$ is delivered

to the additional pump, rising refrigerant's pressure up to 15 bar_{abs}, and then is delivered to the liquid supply pipe line of the blending machine. This line is split in two; internal and external circuits. The internal circuit line is connected to the custom made "dummy load" used as an internal evaporator allowing circulation of the mixture inside the blending machine in a closed loop. The dummy load represents an assembly where the coolant liquid is evaporated by two electrical heaters. After the dummy load, the fully evaporated blend mixture is delivered to the vapour return pipe line and is circulated back to the storage tank / condenser by the compressor. On the vapour return line there is the Sonar Analyzer (Section 5.2) installed for the continuous measurement of the sound velocity in the mixed refrigerant vapour which is used for the mixture ratio determination. Next to the Sonar Analyzer there is Schlumberger Delta G16 flow meter (Section 5.2) mounted to the vapour return pipe for the measurement of the flow rate in the system. Circulation of the coolant mixture inside the blending machine structure is provided by the HAUG (model WTEGX 80 LM-L) oil free compressor. The vapour blend mixture is compressed and delivered by the compressor to the storage tank / condenser cooled (to ≈17°C) by the external refrigerant circuit (the sub-cooling system circulating hydrofluorocarbon CH_2FCF_3) and the condensed mixture is then delivered to the liquid supply lines for the continuous circulation. Control and monitoring of the blending machine parameters is provided by the PLC (located in the control cabinet) through the PVSSII [14] software platform based FSM panel. The screen-shot of the blending machine control panel is presented in Figure 5.3. From this control panel it is possible to:

- turn ON/OFF the compressor;
- change set points and monitor suction and compression pressure of the compressor;
- monitor vapour temperature, liquid temperature, pressure and liquid level inside the storage tank;

- open or close pneumatic valves for the blending machine internal circuit;
- control the dummy load assembly performance by changing the flow rate though it and heating parameters of the electrical heaters;
- monitor the temperature and the pressure in different parts of the blending machine and ensure the safe running conditions through the warning and alarm messages.

Control, data recording and data analyses for the Sonar analyzer is provided by the additional software (See Section 5.2).

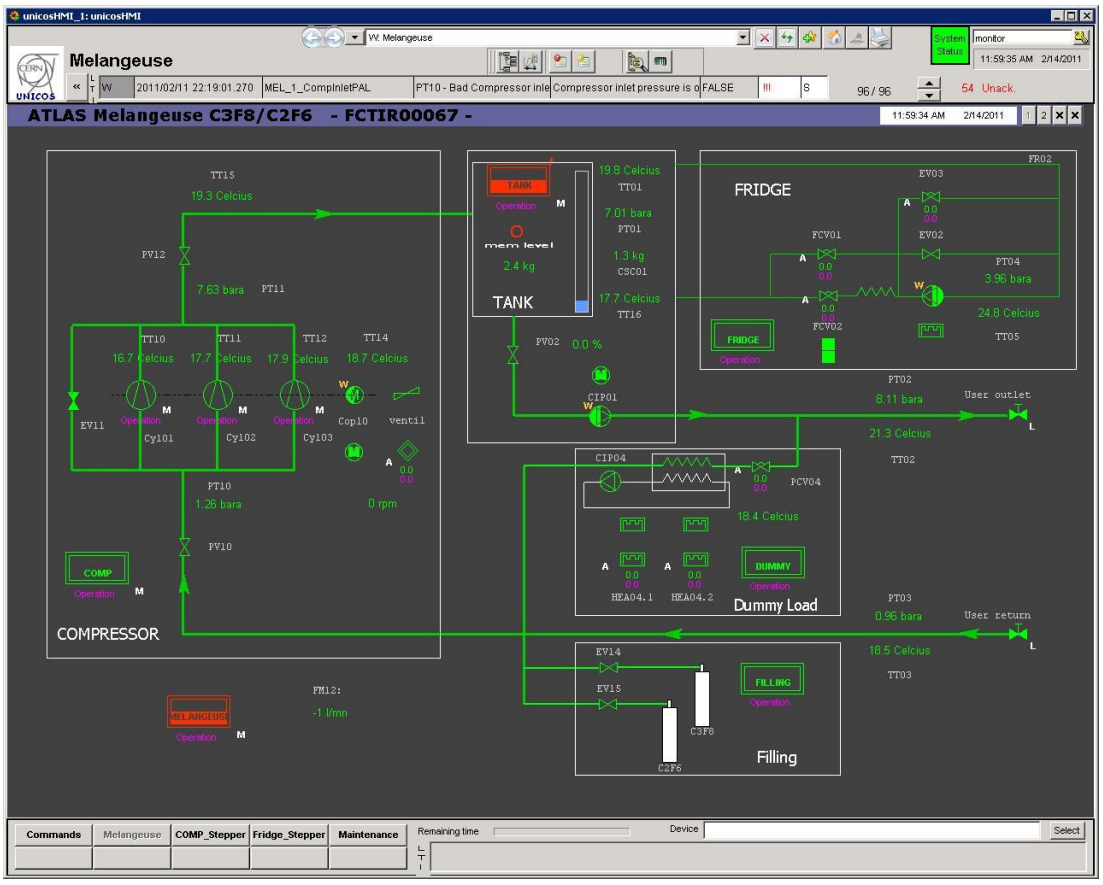

Figure 5.3: The Blending Machine control panel (Screen-shot).

A strictly defined step-by-step procedure [48] is followed for filling the system with the different fractions of the C_3F_8/C_2F_6 blends. The molar mixture of

C_3F_8/C_2F_6 blends is created by adding these blends in the liquid phase into the storage tank and after the circulation inside the blending machine is verified by sound velocity measurements made by the sonar analyzer in the superheated vapour phase. The blend machine storage tank / condenser and freon bottles are each located on the balance and their weight is measured. A precondition for making or modifying the mixture (concentration) is that all the fluid must be recovered back to the storage tank from the system (test station and 50 meter supply lines) and it's total weight must be measured. (In respect of the leaks in the system definition of the new mass baseline is important). The recovery is done using the compressor when the liquid supply line from the storage tank is closed. In practice it is impossible to recover all of the refrigerant in the system since a small amount of the vapour at the minimum aspiration pressure of the compressor (800 mbar) still stays in the pipes and must be evacuated to avoid changing the new blend concentration.

The blend mixing procedure is based on Raoult's law which states that the total vapour pressure above a liquid mixture is dependent on the vapour pressure of each component and the mole fraction of the component in the liquid mixture. Once the mixture components (i = A, B) have reached equilibrium the total vapour pressure can be expressed by the equation:

$$p = p'_A \times x_A + p'_B \times x_B$$

while the individual vapour pressure for each component is:

$$p_i = p'_i \times x_i$$

where:

p_i - the partial pressure of the component i in the mixture;

p'_i - the vapour pressure of the pure component i;

x_i - the mole fraction of the component i in the mixture;

The number of moles per kilogram weight of the C_2F_6 and C_3F_8 are given by there inverse molar masses:

$$C_2F_6 = 1/0.138 = 7.246 \text{ moleskg}^{-1}$$
$$C_3F_8 = 1/0.188 = 5.319 \text{ moleskg}^{-1}$$

Therefore the mole fraction of C_2F_6 in the mixture resulting from X kg of C_2F_6 liquid added to Y kg of C_3F_8 liquid is given by:

$$(X/0.138)/((X/0.138)+(Y/0.188))$$

To achieve the final desired molar concentration in the mixture X kg of C_2F_6 liquid is added to Y kg of C_3F_8 liquid to achieve the total liquid mass of Z kg:

$$X= (\%C_2F_6/\% \ C_3F_8)\times Y$$
$$Z_{final(X\%+Y\%=100\%)} = (\%C_2F_6/\% \ C_3F_8)\times Y + Y$$

For example, in the case of a desired ratio of $5\%C_2F_6$ / $95\%C_3F_8$ by liquid weight, X kg of C_2F_6 must be added to the Y kg of C_3F_8 so that the total weight in the storage tank $Z_{final(X\%+Y\%=100\%)}$ becomes $(0.05/0.95) \times Y + Y$

After the circulation of the desired mixture for a couple of hours inside the blending machine's internal closed loop (this is necessary to be sure that the blends are completely mixed) and mixture ratio verification by the Sonar Analyzer, the manual valves on the inlet supply and vapour return lines are opened and refrigerant is injected into the external circuit. This circuit represents the inlet and outlet pipe lines through which refrigerant is delivered to the distribution rack located in the clean room and supplying the laboratory cooling test station (Section 4.1). 50 metres of OD33.7 and OD21.3 stainless steel (SS) pipes were installed all the way through the SR1 laboratory connecting the blending machine to the distribution rack. 5×10 meter pieces of these SS pipes were orbital-welded together according to the laboratory welding procedure and all orbital welding connections were checked with X-ray imaging. These 50 meter liquid supply and vapour return lines were fixed to the special supports located on the inside wall of the laboratory clean room. The system was tested and approved to the PN40 pressure standard. All pipes are thermally isolated. A schematic view of the

distribution rack and Inlet / Outlet pipe lines is presented in Figure 5.4. From the distribution rack the refrigerant mixture is supplied to the test station for the laboratory measurements.

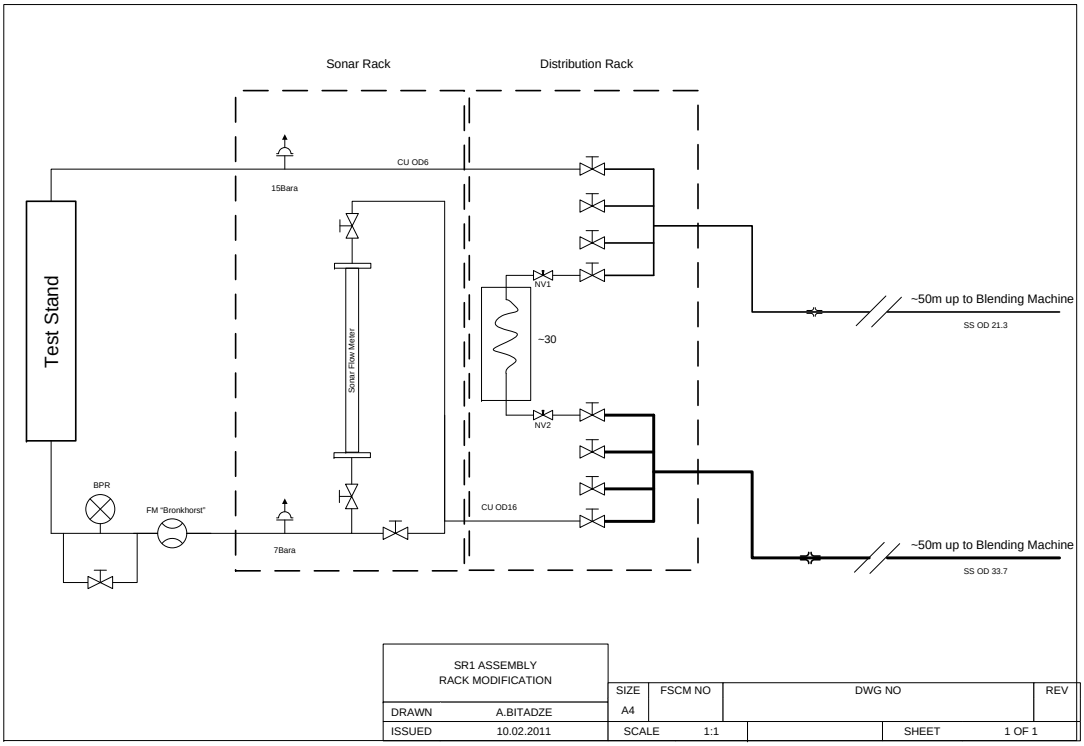

Figure 5.4: Schematic view of the Distribution Rack (in SR1 Laboratory).

5.2 Sonar Analyzer

For the precise measurement of the C_3F_8/C_2F_6 mixture ratio and for the measurement of the flow, a new device the "Sonar Analyzer" was assembled, tested and installed in the system [49] [50]. The concentration of the blends is monitored in the vapour return region where the vapour mixture is in the superheated state (single phase); One Sonar Analyzer is installed on the Blending Machine, inside the internal circuit, on the vapour return pipe (see Figure 5.2) and a second Sonar Analyzer is mounted on the vapour return line of the laboratory test station before the distribution rack (see Figure 5.4). By-pass piping is assembled around the both devices for easy exchange and maintenance.

The mixture ratio is monitored based on measured sound velocity in the mixture (at known temperature and pressure) since it exclusively depends on the molar concentration of the mixture components. Measured sound velocity is compared to the sound velocity measurement data from the look-up table to determine concentration of blends in the mixture. In this look-up table data is collected from prior measurements of sound velocity within the calibration mixtures or from the theoretical thermodynamic calculations from the NIST REFPROP[1] and PC-SAFT [51] databases. The NIST REFPROP package represents currently available one of the most accurate thermodynamic properties database of pure fluids and mixtures. Based on the three models of the thermodynamic properties: equations of state explicit in Helmholtz energy [52], the modified Benedict-Webb-Rubin (BWR) equation of state [53], and extended corresponding states (ECS) model [54]; it represents one of the best tools for the calculation of the sound velocity in the fluorocarbon mixtures, including C_3F_8/C_2F_6 blends. Since the NIST REFPROP is not well configured for the calculation of the sound velocity in the fluorocarbon mixtures with the other gases, the PC-SAFT equation of state is used for this purpose. In the ATLAS experiment the sonar analyzer is used for high leak detection inside the inner detector volume, to detect the leak of C_3F_8 evaporative coolant into the pixel detector nitrogen envelope [50].

Picture of the 3D model for the Sonar Analyzer with dimensions and disassembled parts showing ultrasonic transducer position is presented on Figure 5.5 [49].

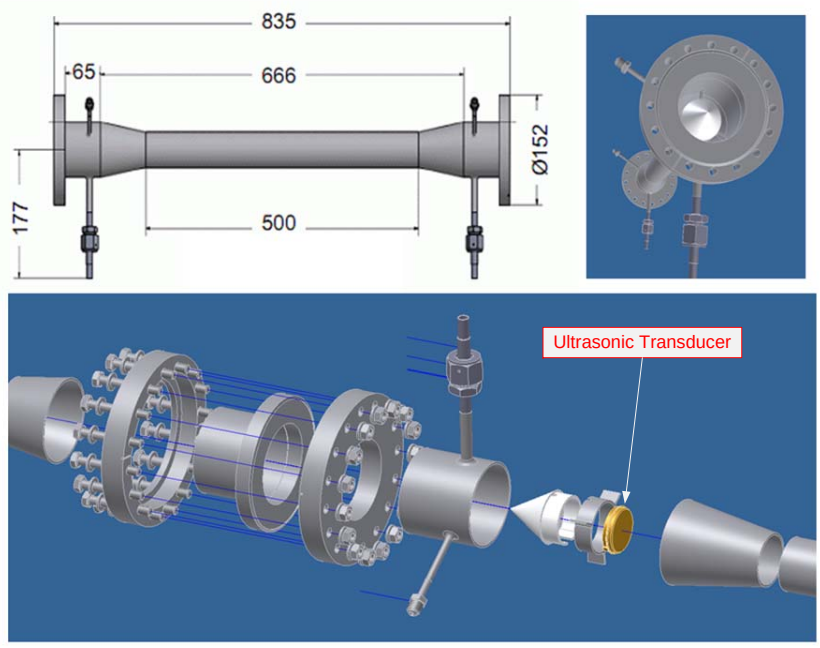

Figure 5.5: Sonar Analyzer (3D model representation).

The mechanical envelope of this device represents a flanged stainless steel tube with the overall length of 835 mm. Ultrasonic transducers are centered and mounted inside this envelope 660 mm apart on the wide bore sections of the tube. In between there is a pair of diameter reduction cones and the pinched region of 500 mm long tube; these are all welded together. Through this pinched region of a diameter of 44.3 mm (compare to the transducers diameter of 42.9 mm) all the vapour is channeled. The vapour around the transducers is diverted by the 5 cm long axial flow deflection peek cones.

Six NTC [46] thermistors are used to monitor temperature inside the device with the measurement precision of ± 0.2°C and the pressure is measured by a Huba® [55] pressure transmitter with the measurement precision of ± 15 mbar.

A SensComp® Model 600 series 50 kHz capacitative ultrasonic transducer used in the sonar analyzer is presented in Figure 5.6 [50]. Originally these trans-

ducers were developed by Polaroid® during the 1980s for the auto focus instant cameras and now are produced by SensComp®.

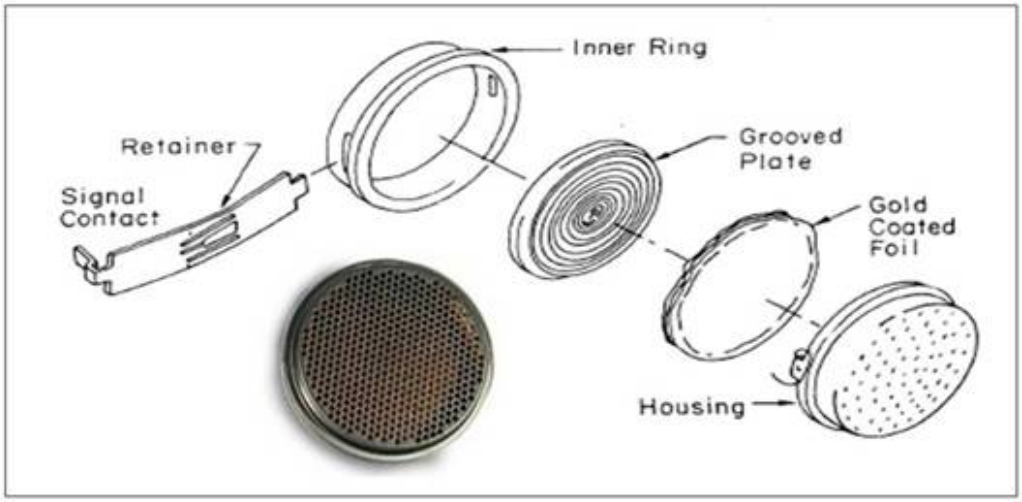

Figure 5.6: SensComp® Model 600 series 50 kHz capacitative ultrasonic transducer.

The SensComp® transducer represents the assembly, of the gold coated mylar foil stretched over the metallic backing plate etched with a spiral groove, located inside the metallic housing with a outside diameter of 42.9 mm. The housing case and foil are grounded and the back plate is biased and excited at high voltage in the range of 180-360 V. Originally transducers were designed to work in air with ambient temperature and atmospheric pressure, but since the gas can access both sides of the diaphragm through the spiral groove this gives the possibility of using this transducer with a wide range of pressure. Transducers were tested in non corrosive gases within the pressure range of 100 $mbar_{abs}$ to 5 bar_{abs} and a temperature range of -30°C to 45°C [50].

The custom made electronics, based on a Microchip® dsPIC 16 bit microcontroller, is used for the sound transit time measurements. The principle of operation of the Sonar Analyzer is presented in Figure 5.7 [50].

50 kHz square wave pulses, generated by the microcontroller, are sent from the transmitting transducer to the receiving transducer which is connected to

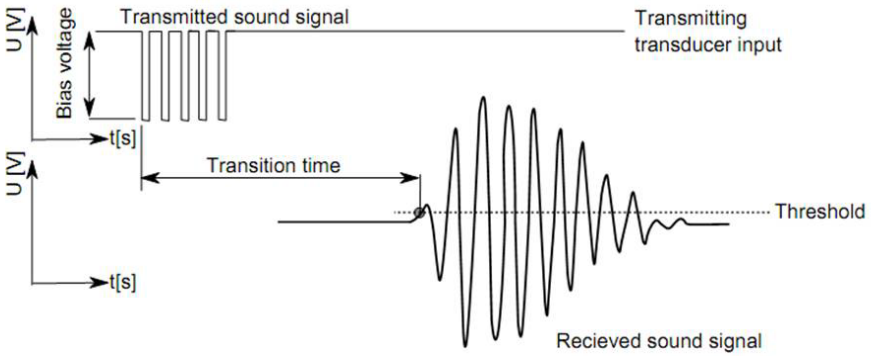

Figure 5.7: The principle of measurement of the sound signal transit time.

a DC biasing circuit followed by an amplifier and a comparator. At the same time a 40 MHz transit time clock is started simultaneously and is stopped when the first received amplified sound signal from the receiving transducer crosses the predefined comparator threshold. Both transducers serve as transmitting and receiving devices allowing sound signal to be sent in both direction, upstream and downstream of the vapour flow in the Sonar Analyzer. The time between the transmitted and the received sound pulses is measured by the microcontroller and along with temperatures and pressure values is sent to the control computer. The block diagram of the custom made electronics for the sonar analyzer and it's implementation is presented in Figure 5.8 [50].

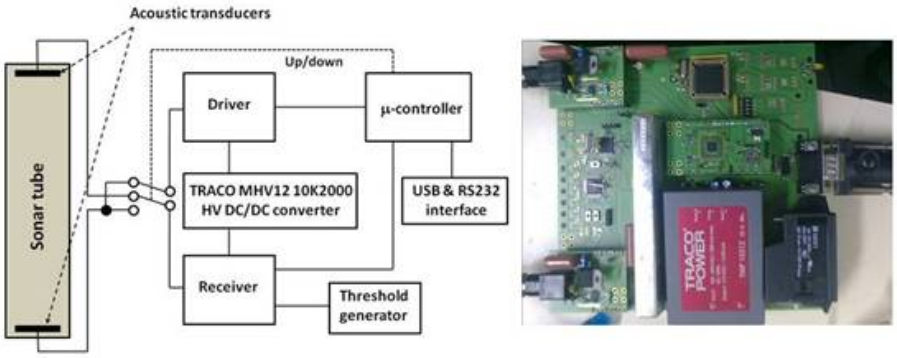

Figure 5.8: The block diagram of the sound transit time measuring electronics and it's implementation.

DC-DC converter generates HV bias for the vibrating foils of the transducers

in the range 180-360 V. During the transmitting process the transmitting transducer is excited with a chain (1-8) of the HV square wave pulses built by the microcontroller (using 50 kHz LV pulses) and the DC-DC converter output. The receiving transducer is biased with a flat HVDC bias and transmits signal to the amplifier which is followed by the comparator. Sound transit time between the transmitting and receiving transducers is computed from the counted number of the 40 MHz pulses between the rising edge of the first transmitted 50 kHz sound pulse and the time when the first received amplified pulse crosses the comparator threshold. Computed sound transit time (in both directions) is continuously entered into the internal FIFO memory and, when the measuring cycle is requested from the supervising software, the time stamped average of the most recent 300 computed transit times (in each direction) is output from the FIFO memory. At the same time average temperature and pressure inside the sonar analyzer (≈20 averaged samples per second) are recorded. Data is taken over the serial bus cable running under the USB and RS232 protocols. Custom made electronics described above is controlled by the supervisory software implemented as the PVSS II [14] project. Software is used to send start, stop and reset commands to the instrument and to retrieve the data from the FIFO memory.

In addition to the supervisory and control functions, the main purpose of this specialized software based on PVSS II SCADA (Supervisory, Control and Data Acquisition software) environment [14] [56] is to analyze data received from the sonar device. The block diagram of the measurement process and the measurement chain schematics is presented in Figure 5.9 [50].

The main tasks of the supervisory, control and analyzing software are:

- Communication with the custom electronics (control and data retrieval);
- Communication control (communication error detection and recovery);
- Pressure and Temperature monitoring and recording;
- Visualization via the Graphical User Interface (GUI);

- Determination of the vapour flow rate;
- Determination of the blend Molar concentration in the vapour mixture;
- Archiving of the sound transit time, velocity, flow, mixture composition, temperature and pressure values into a local or remote database.

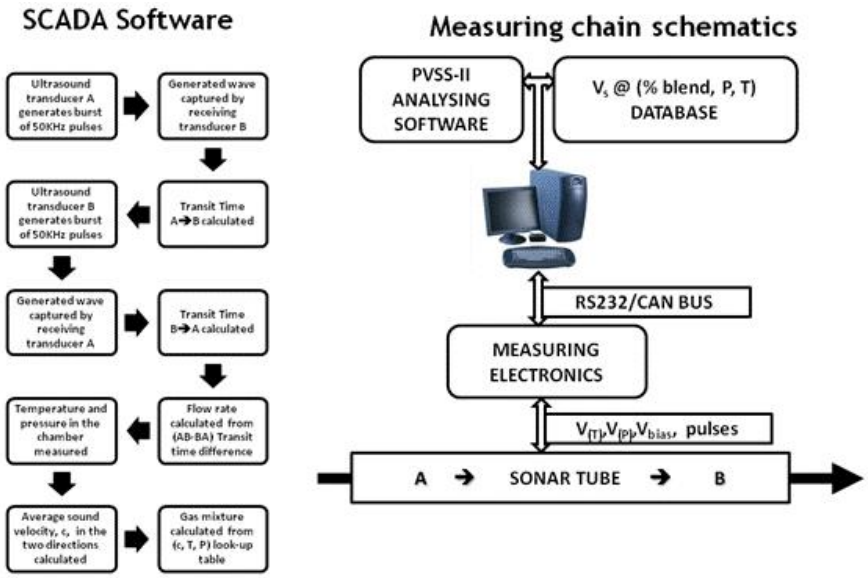

Figure 5.9: The block diagram of the measurement process by the SCADA software and the schematics of the measuring chain.

In the communication/commissioning cycle software communicates with the custom electronics through the CAN bus using the CANOpen protocol and sends and receives messages with the standardized length (1 or 8 bytes) and follows the preset rules that define message-related actions. Messages can be sent in normal, service (8-byte) and emergency (1-byte) regimes and each message is composed of three parts: read/write operator, identification number and the data bytes. All sent messages are confirmed by the electronics within a 100 ms time period by sending back a message with the proper format, otherwise a communication alarm is triggered. In this case communication emergency mode is activated and software starts to send messages that perform software or hardware reset of the electronics and after that sends verification message to check if the communication

was properly restored. An alarm is also triggered in the case where there is no reply from the electronics to three consecutively sent messages; which means the communication chain is broken on the hardware level and in this case operators action is required.

The estimation cycle, when mixture ratio and vapour flow is determined, consist of two sub-processes; the calculation, and the prediction sub-processes. In the calculation sub-process average values of the all process variables, which are: sound velocity, temperature and pressure are calculated; noise in the data is eliminated; data from the temperature and pressure sensors are filtered. In the prediction sub-process gas mixture composition and vapour flow is calculated based on the calculated average values of the sound velocity, temperature and pressure. For the prediction of the vapour mixture concentration "c, t, p look-up tables" [50] are used. The tables provide empirical information about molar ratio in the binary mixture based on the transit sound velocity (c), temperature (t) and pressure (p) in the analyzed vapour. As described above, data in these look-up tables is compiled from the measurements in the calibrated mixtures and from the predictions made using equations from the NIST REFPROP [1] and PC-SAFT [51]. In the current software a single preloaded look-up table was used, consisting of the data for the C_3F_8/C_2F_6 mixture with a 0.25% granularity and covers temperature and pressure ranges from 16°C to 26°C and from 800 mbar to 1600 mbar with the granularity of 0.3°C and 50 mbar respectivly. These conditions correspond to the superheated C_3F_8/C_2F_6 gas mixture environment in the vapour return line where the sonar analyzer is installed. A new version of the software is under development and will operate with the multiple look-up tables covering a much wider range of temperature and pressure (from -40°C to 80°C and from 800 mbar to 12 bar). For the precise determination of the blend composition in the mixture several algorithms were tested empirically and currently an algorithm using minimize quadratic norm is adopted [56]. The algorithm calculates ratio of C_3F_8 and C_2F_6 blends in the mixture by minimizing

the quadratic norm n_i for each pressure (p_i), temperature (t_i) and sound velocity (c_i) table entries via equation:

$$n_i = k_1(p_{i,table} - p_{run.\ average})^2 + k_2(t_{i,table} - t_{run.\ average})^2 + k_3(c_{i,table} - c_{run.\ average})^2$$

where $p_{i,table}$, $t_{i,table}$ and $c_{i,table}$ are look-up table entries; $p_{run.\ average}$, $t_{run.\ average}$ and $c_{run.\ average}$ are the real time outputs from the electronics FIFO memory; and k_1, k_2, k_3 are the weight coefficients that express the dependence of the mixture precision on the error coming from the difference between the measured and the look-up table c, t, p values [56].

To ensure good precision of the measurements, by minimizing uncertainty in the sound traveling distance in the sonar analyzer, the distance between transducers was calibrated using a pure gas having well-known sound velocity dependence on the temperature and the pressure. The distance was calculated by measuring the sound transit time in this calibration gas. Calibration was done with Xenon (Xe) having closest sound velocity (175.5 ms^{-1} at 20°C) and molar weight (131 gmol^{-1}) to C_3F_8 and C_2F_6 fluorocarbons used in SR1 laboratory experiment and having the thermo-physical behavior of an ideal gas. Calibration demonstrated the average uncertainty in the transducers inter distance of ±0.1 mm. Calibration with the pure Nitrogen (N_2) and Argon (Ar) showed the same precision. After this calibration measurements were done in pure C_3F_8 and C_2F_6 separately, showing average difference of 0.04% [50] between measured sound velocities and the predictions from NIST REFPROP [1] and PC-SAFT [51].

During the laboratory tests (see Section 5.3) multiple measurements were done for the different concentration of C_3F_8/C_2F_6 blends in the mixture (from 0% up to 35% of C_2F_6). The average difference between the measurement values and the predictions from NIST REFPROP [1] is 0.05% and predictions from PC-SAFT [51] is 0.25% (note: NIST is more precise in prediction of the thermo-physical properties of the mixtures of the saturated fluorocarbons). Measurement

results from the Sonar Analyzer and predicted values from NIST REFPROP and PC-SAFT are presented in Figure 5.10 [50].

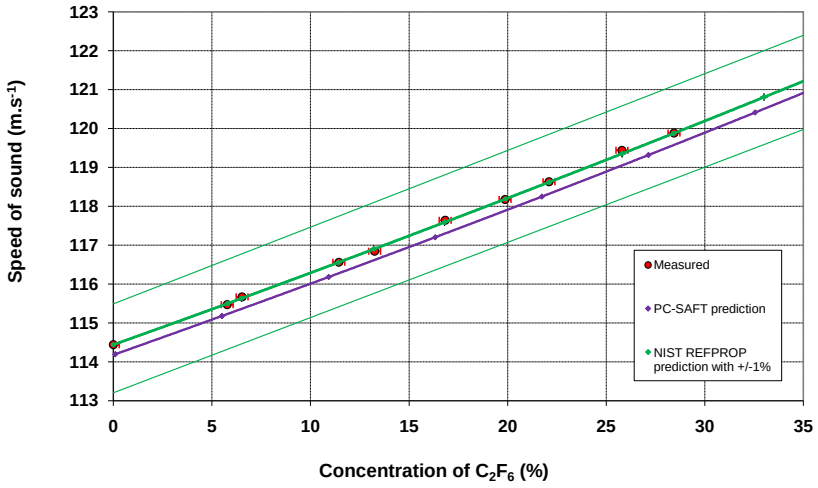

Figure 5.10: Comparison between measured sound velocity data and theoretical predictions in molar C_3F_8/C_2F_6 mixtures of thermodynamic interest, at 1.14 bar_{abs} and 19.2°C. NIST-REFPROP sound velocity predictions shown within ±1% band. The binary gas mixture uncertainty of 0.3% is illustrated in red.

The uncertainty in the mixture concentration caused by the uncertainty in the sound velocity measurement can be defined as $\delta_{mix} = \delta_c/m$, where δ_c is uncertainty in sound velocity measurement and m is the local slope of the sound velocity/concentration curve.

Calculation shows that uncertainty in the mixture concentration, based on the measurement results from the Sonar Analyzer, is around ±0.3% [50] (see Appendix D).

As mentioned above, in the SR1 Laboratory tests the Sonar Analyzer is used as a vapour mixture concentration analyzing device, but it can also be used as a gas flow meter. The flow rate is calculated from the sound transit times measured upstream and downstream to the direction of the flow inside the sonar analyzer according to the formulas presented in Table 5.1 [50].

Where:

V - The gas volume flow [m^3s^{-1}].

c - The sound velocity in the gas [ms^{-1}].

v - The linear flow velocity [ms^{-1}].

L - The distance between transducers [m].

A - The internal cross sectional area of the tube between the transducers [m^2].

Parameter	Formula
t_{down} [ns]	$t_{down} = \frac{L}{(c+v)}$
t_{up} [ns]	$t_{up} = \frac{L}{(c-v)}$
V [m^3s^{-1}]	$V = \frac{L \times A \times (t_{up} - t_{down})}{2 \times (t_{up} \times t_{down})}$
c [ms^{-1}]	$c = \frac{L \times (t_{up} + t_{down})}{2 \times (t_{up} \times t_{down})}$

Table 5.1: Flow Rate Calculation.

The measured flow values using the sonar analyzer were compared to the measurement results from the Schlumberger Delta G16 (max. flow rate $25\,m^3hr^{-1}$ ($417\,lmin^{-1}$); precision ±1% of FS;) volumetric gas flow meter installed next to the sonar device in the vapour pipe line of the blending machine (see Section 5.1). Measurements were performed in case of different flows in the system up to the maximum possible flow in the blending machine of $230\,lmin^{-1}$ ($30\,gs^{-1}$) and results are presented in Figure 5.11 [50].

The measurement error of the Schlumberger Delta G16 flow meter (1% of FS) is presented on the plot as the horizontal error bars. The vertical error bars represent the combination of the uncertainty in the tube diameter (±0.5 mm), timing precision (±100 ns) and distance between transducers (±0.1 mm) in sonar analyzer measurement results. The standard deviation (rms) of the sonar analyzer/ultrasonic flow meter relative to the fit equals to $\pm 4.9\,lmin^{-1}$ (2% of full scale) and is presented on the plot as the red band.

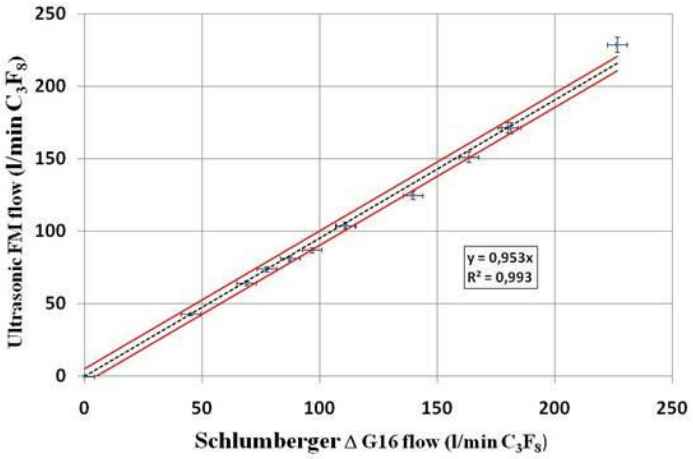

Figure 5.11: The Sonar Analyzer flow measurement linearity comparison with the Schlumberger Delta G16 flow meter. C_3F_8 vapour at $1\,\mathrm{bar}_{abs}$ and 20°C (density $\approx$7.9 kgm^{-3}). The standard deviation (rms) of the measured points from the fit represents $\pm$2% of the full flow of 230 lmin^{-1}.

5.3 Mixture measurements and Results

After assembling blending machine and making necessary pipe modification from blending machine to distribution rack, tests were repeated with pure C_3F_8 to ensure same operating conditions for the Laboratory Test Station. Results show the same pressure and thermal conditions over the system as before (Section 4.2).

A new series of measurements were done and new data from the test system was recorded and analyzed to investigate different proportions of C_3F_8/C_2F_6 blends in the mixture and try to find improved / best conditions of mixture, temperature distribution, pressure drops and flow parameters over the system, to ensure the best cooling performance of SCT Barrel cooling loop.

Measurements were done with 13 bar_{abs} inlet pressure (as this is the nominal inlet pressure for ATLAS ID cooling system), with different power (0 W, 3 W, 6 W, 9 W, 10.5 W) applied to dummy modules and with different vapour back pressure (1.2 [1], 1.6, 2.0, 2.5, 3.0 bar_{abs}) in system. All these measurements were done for different percentage concentration (0%, 1%, 3%, 5%, 10%, 20%, 25%) of C_2F_6 fluorocarbon coolant in the C_3F_8/C_2F_6 mixture.

Thermal profile of cooling stave was studied in details to define evaporation temperature over the stave with respect to new conditions dictated by C_3F_8/C_2F_6 coolant mixture. Max.Temp. over the stave as a function of dome pressure (pressure applied to BPR) for different power loads on modules, for 0% C_2F_6 (pure C_3F_8) blend in mixture is presented in Figure 5.12 and for 25% C_2F_6 blend in mixture is presented in Figure 5.13.

Max.Temp. over the Stave as a function of real back pressure (pressure measured before the BPR) for different power loads on modules, for 0% C_2F_6 blend in mixture is presented in Figure 5.14 and for 25% C_2F_6 blend in mixture is presented in Figure 5.15.

[1] With current piping system (from BM to rack) having smaller pressure drop, it is possible to replicate minimum back pressure of 1.2 bar_{abs} as it is in real ID Ev.cool system

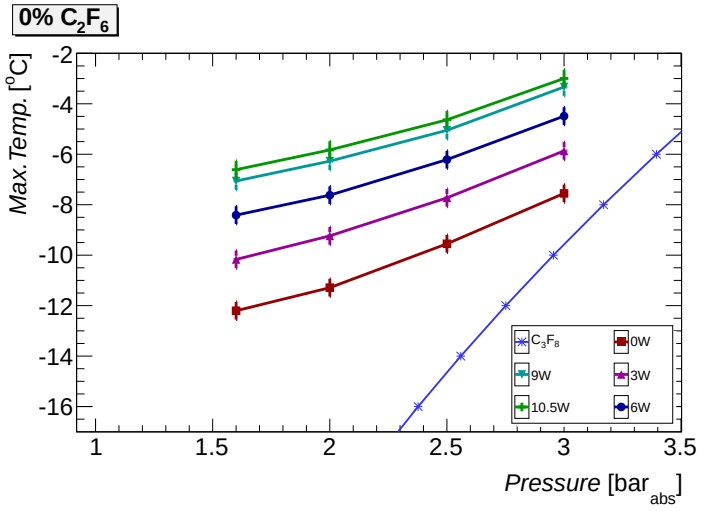

Figure 5.12: Max.Temp. as a function of *Dome pressure* for different module power loads, with C_3F_8 saturation temperature line, in case of $13\,\mathrm{bar}_{abs}$ input liquid pressure. 0% C_2F_6. ($\sigma_{P.tot.Out} = 9.86\,\mathrm{mbar}$, $\sigma_{T.tot} = 0.35°\mathrm{C}$)

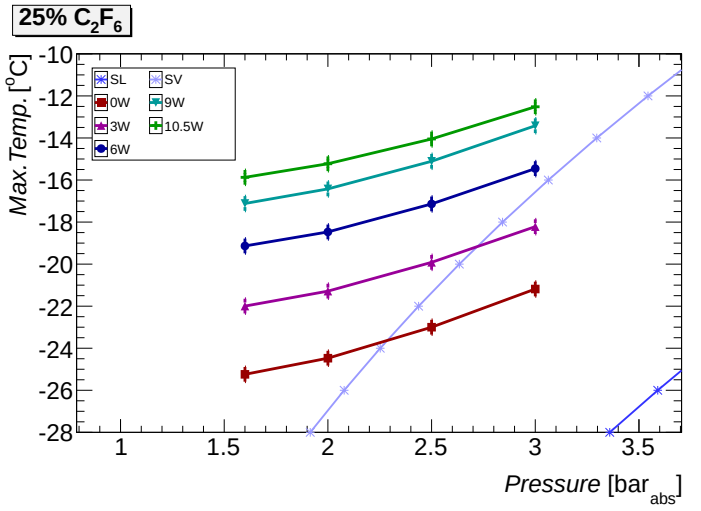

Figure 5.13: Max.Temp. as a function of *Dome pressure* for different module power loads, with C_3F_8/C_2F_6 mixture liquid saturation and vapour saturation temperature lines, in case of $13\,\mathrm{bar}_{abs}$ input liquid pressure. 25% C_2F_6. ($\sigma_{P.tot.Out} = 9.86\,\mathrm{mbar}$, $\sigma_{T.tot} = 0.35°\mathrm{C}$)

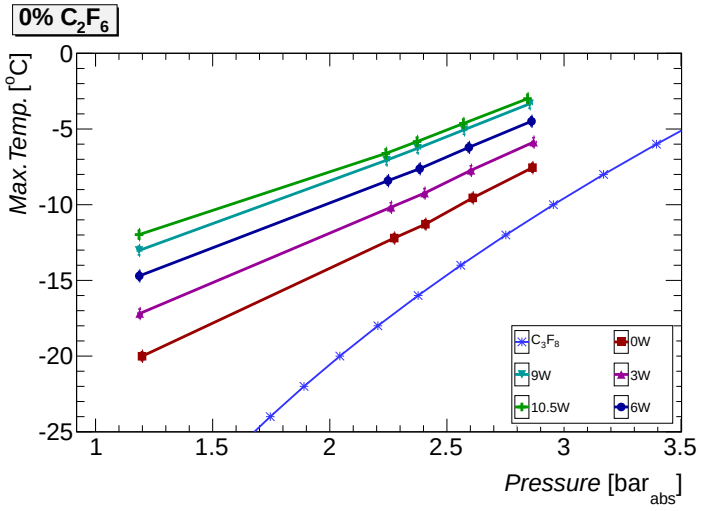

Figure 5.14: Max.Temp. as a function of *back pressure* for different module power loads, with C_3F_8 saturation temperature line, in case of 13 bar_{abs} input liquid pressure. 0% C_2F_6. ($\sigma_{P.tot.Out} = 9.86$ mbar, $\sigma_{T.tot} = 0.35$°C)

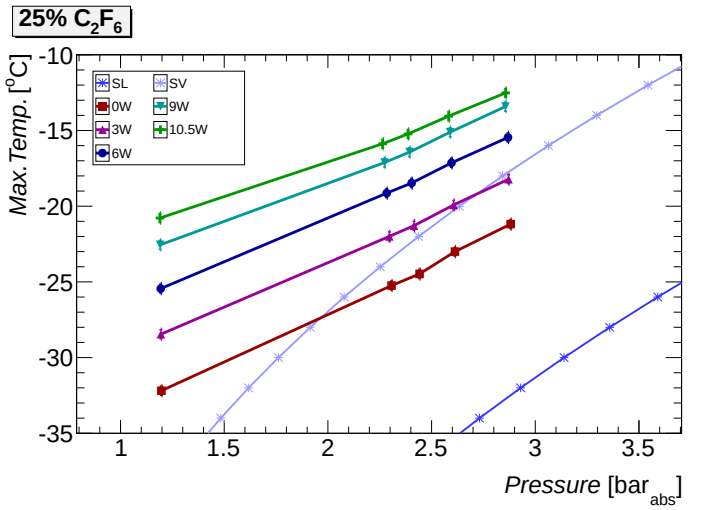

Figure 5.15: Max.Temp. as a function of *back pressure* for different module power loads, with C_3F_8/C_2F_6 mixture liquid saturation and vapour saturation temperature lines, in case of 13 bar_{abs} input liquid pressure. 25% C_2F_6. ($\sigma_{P.tot.Out} = 9.86$ mbar, $\sigma_{T.tot} = 0.35$°C)

Max.Temp. over the Stave as a function of measured pressure at the middle of the Stave (P_A2 pressure sensor, See schematic 4.2) for different power loads on modules, for 0% C_2F_6 blend in mixture is presented in Figure 5.16 and for 25% C_2F_6 blend in mixture is presented in Figure 5.17.

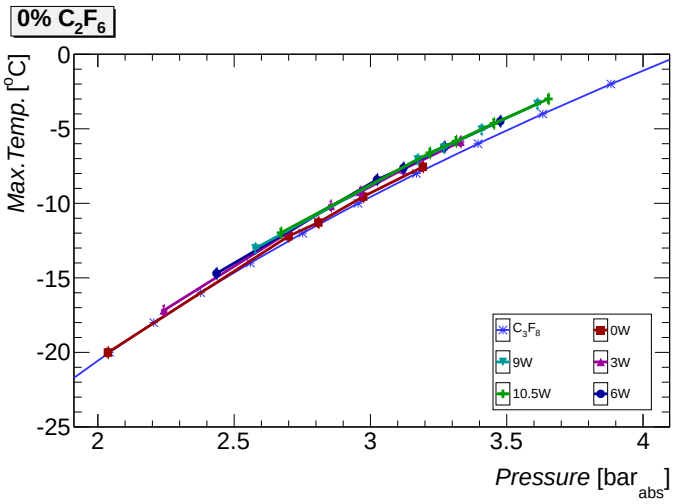

Figure 5.16: Max.Temp. as a function of measured *pressure at the middle of the Stave* for different module power loads, with C_3F_8 saturation temperature line, in case of 13 bar_{abs} input liquid pressure. 0% C_2F_6. ($\sigma_{P.tot.Out} = 9.86$ mbar, $\sigma_{T.tot} = 0.35°C$)

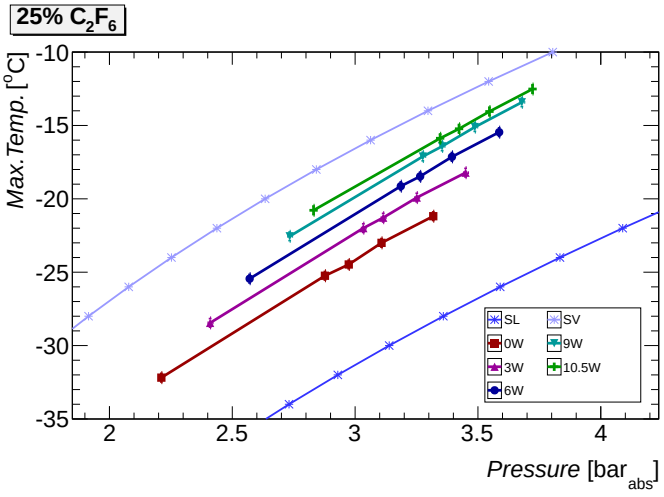

Figure 5.17: Max.Temp. as a function of measured *pressure over the Stave* for different module power loads,with C_3F_8/C_2F_6 mixture liquid saturation and vapour saturation temperature lines, in case of 13 bar_{abs} input liquid pressure. 25% C_2F_6. ($\sigma_{P.tot.Out} = 9.86$ mbar, $\sigma_{T.tot} = 0.35°C$)

By comparing these results, it becomes obvious that by adding a higher percentage of C_2F_6 to the coolant mixture, the evaporation temperature over the stave falls down. To show a clear picture for temperature propagation over the Stave in case of pure C_3F_8 (0% C_2F_6) and 25% C_2F_6 blend in mixture, measured temperature is plotted as a function of position (of NTC sensors) over the Stave. Measurement results in case of 1.2 bar_{abs} (open by-pass) back pressure in system are presented on Figure 5.18 and in case of 2.0 bar_{abs} back pressure in system are presented on Figure 5.19. (results are presented for one half stave, sensors from T_A1 to T_A25, since the second half is symmetrical and has a similar temperature profile, See schematic 4.2)

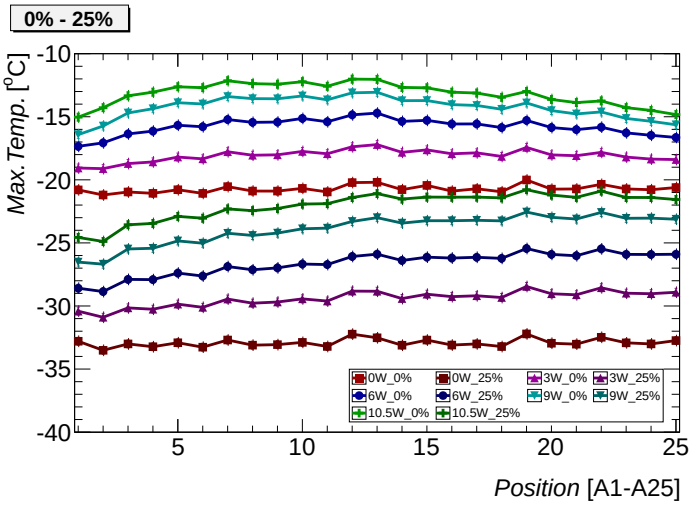

Figure 5.18: Max.Temp. for each temperature transducers for different power load on modules, in the case of a 13 bar_{abs} inlet pressure and 1.2 bar_{abs} back pressure in system. Results for pure C_3F_8 (0% C_2F_6) and 25% C_2F_6 blend in mixture. ($\sigma_{T.tot} = 0.35°C$)

The difference between maximum temperature over the stave in the case of pure C_3F_8 (0% C_2F_6) and 25% C_2F_6 blend in the mixture, for different power loads on modules, as a function of back pressure in the system, is presented in Figure 5.20. Results show that by adding 25% C_2F_6 to the blend mixture it is possible to lower the evaporation temperature over the stave by ≈9°C (with the maximum 10.5 W power per module).

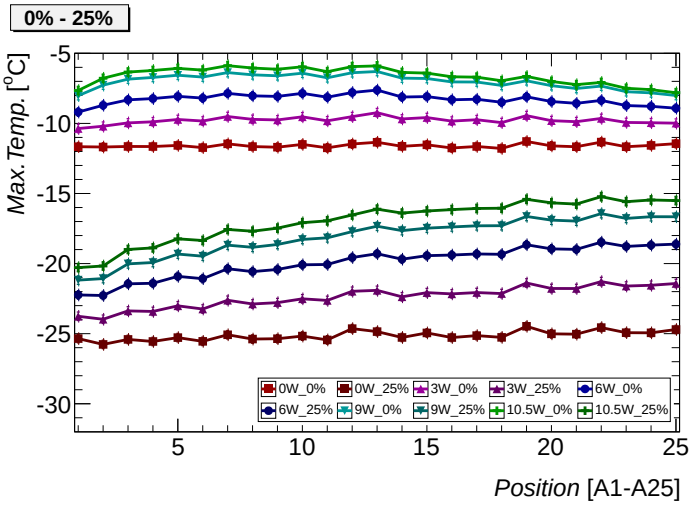

Figure 5.19: Max.Temp. for each temperature transducers for different power load on modules, in case of 13 bar_{abs} inlet pressure and 2.0 bar_{abs} back pressure in system. Results for pure C_3F_8 (0% C_2F_6) and 25% C_2F_6 blend in mixture. ($\sigma_{T.tot} = 0.35°\text{C}$)

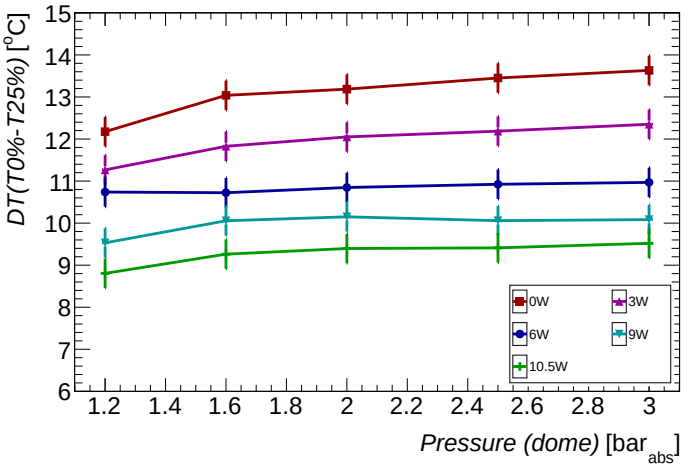

Figure 5.20: Difference in Max.Temp. over the Stave in case of pure C_3F_8 (0% C_2F_6) and 25% C_2F_6 blend in mixture, for different power load on modules, as a function of back pressure in system. ($\sigma_{P.tot.Out} = 9.86\,\text{mbar}$, $\sigma_{T.tot} = 0.35°\text{C}$)

Measurement results for Max.Temp. over the stave as a function of each percentage concentration of C_2F_6 blend in coolant mixture is presented in Figure 5.21. Results for 0%, 1%, 3%, 5%, 10%, 20%, 25% clearly show that temperature over the stave is lowered by adding more and more C_2F_6 to the blend.

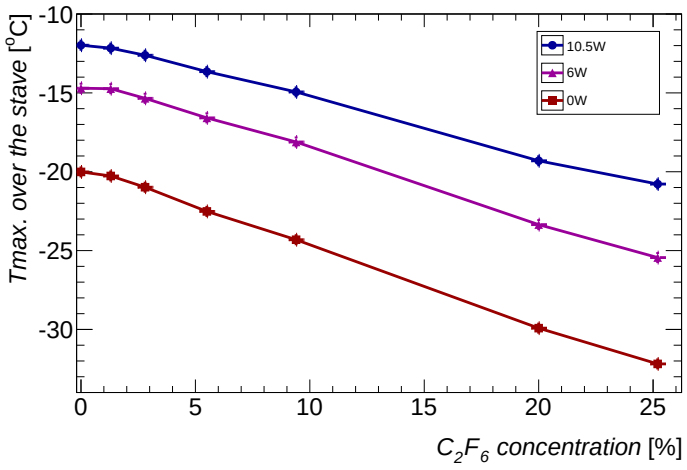

Figure 5.21: Max.Temp. over the stave changing according to the concentration of C_2F_6 blend in the coolant mixture, for different module power loads, with 13 bar_{abs} input liquid pressure and 1.2 bar_{abs} back pressure in system. ($\sigma_{Mix\%} = 0.32\%$, $\sigma_{T.tot} = 0.35°C$)

With nominal running conditions for the SCT Barrel cooling circuit, presuming 13 bar_{abs} input liquid pressure and 1.2 bar_{abs} vapour back pressure in the system, nominal 6 W power load per unirradiated module and 10.5 W power load per irradiated module, now it is possible to keep the evaporation temperature of the coolant over the stave below the necessary -15°C (Section 3.1). Therefore it becomes possible to guarantee the thermal stability of the Inner Detector, even at the end of the 10 year operational period.

Work done and measurements made in the laboratory, using the cooling Test Station and Blending Machine, prove that problems (stated above in Chapter 3) for the SCT Barrel evaporative cooling system can be overcome by finding the proper concentration of C_3F_8/C_2F_6 for the coolant mixture.

Measurements for each percentage concentration were repeated in two cycles to recheck / reassure the validity of the results. Maximum Temperature over the stave as a function of C_2F_6 concentration in the blend mixture measured in first and second cycles is presented in Figure 5.22. Results are presented incorporating a correction coefficient (See Appendix C).

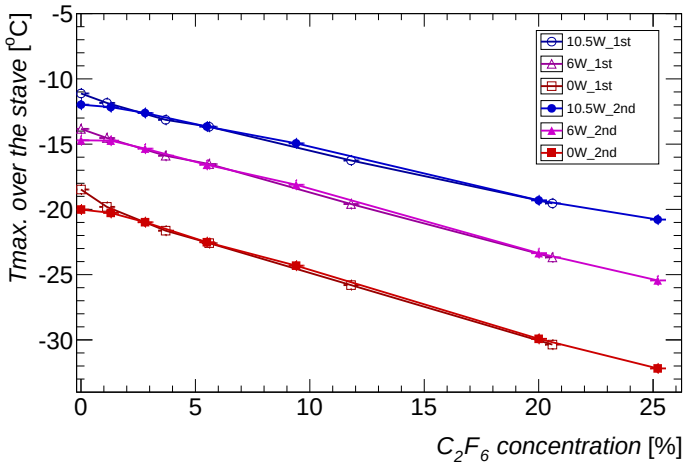

Figure 5.22: Max.Temp. over the Stave changing according to concentration of C_2F_6 blend in coolant mixture, for different module power loads, in case of 13 bar_{abs} input liquid pressure and 1.2 bar_{abs} back pressure in system. First and Second cycle of measurements. ($\sigma_{Mix\%} = 0.32\%$, $\sigma_{T.tot} = 0.35°C$)

Since the 0% measurements for the first cycle were the very first measurements done with laboratory station, the values were measured not entirely correct (temperature inside the Plexiglass box was higher than necessary, giving almost 1°C mistake in measurement), otherwise measurements made approximately six months apart, for different percentage concentration and different power per module match very well, proving the accuracy of the measurement procedure used in laboratory with cooling Test Stand.

The overall thermodynamic behavior of the system in case of pure C_3F_8 is shown on the Pressure-Enthalpy diagram in Figure 5.23 and in case of 25% C_2F_6 blend in the mixture in Figure 5.24. Each of the stages are described in Table 5.2.

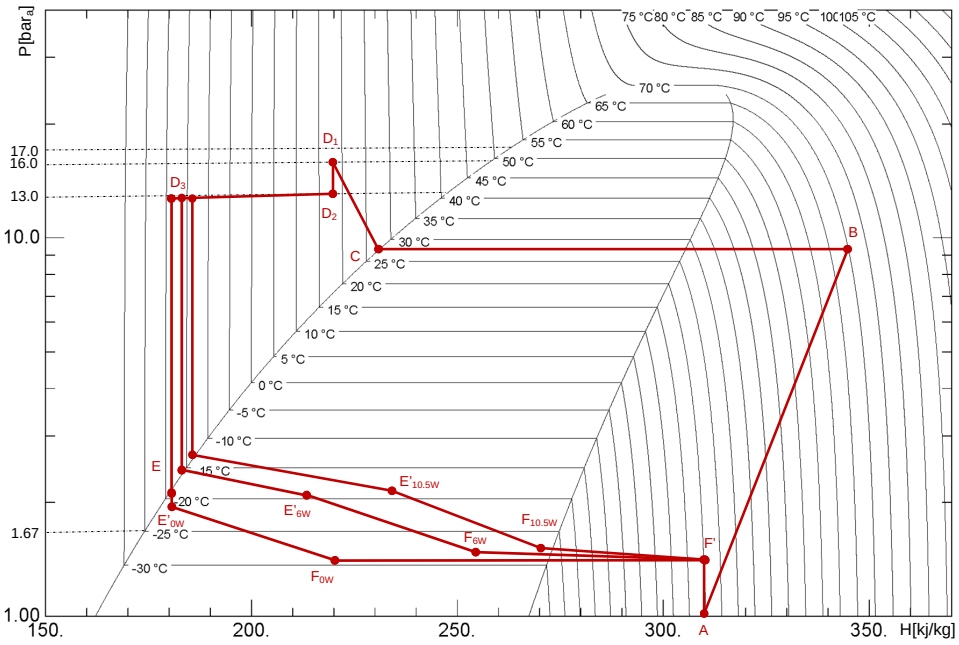

Figure 5.23: Phase Diagram of the SR1 laboratory test station. pure C_3F_8.

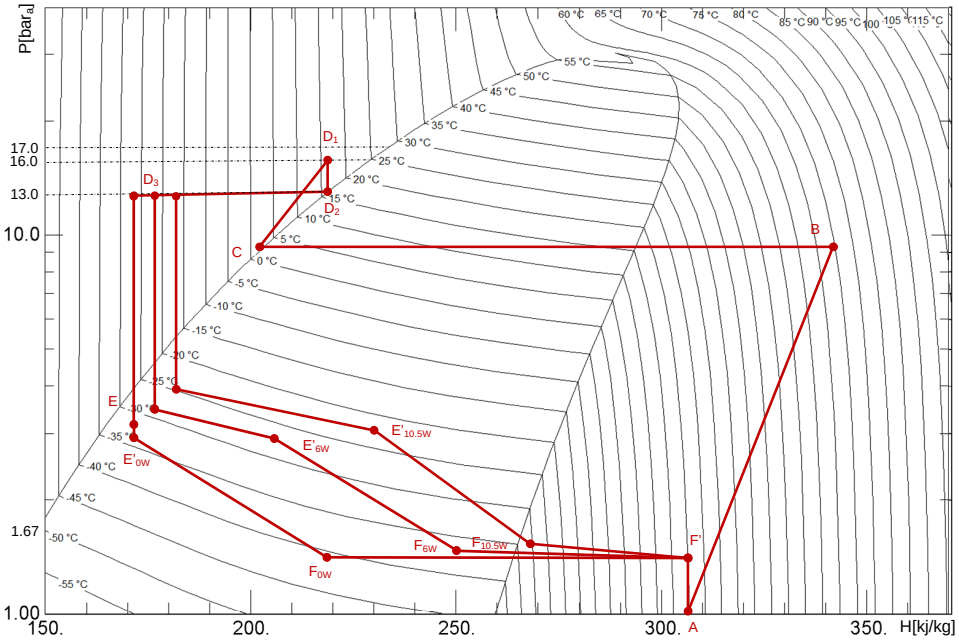

Figure 5.24: Phase Diagram of the SR1 laboratory test station. 25% C_2F_6 blend in mixture.

Between Points	Description
A to B	refrigerant vapour is compressed at 9 bar_{abs} and 70°C and is delivered to the condenser / storage tank.
B to C	refrigerant vapour condenses inside the condenser / storage tank into liquid at 27°C and is delivered to the additional pump for the continuous running cycle. in case of 25% C_2F_6 blend in mixture, refrigerant vapour condenses into the liquid at 3°C.
C to D_1	refrigerant in liquid state from the storage tank is sub-cooled before the pump to 17°C and pressure is raised by the pump to 16 bar_{abs} and refrigerant in liquid state is delivered to the distribution rack. in case of 25% C_2F_6 blend in mixture, refrigerant is warmed up to 17°C.
D_1 to D_2	the pressure drop over the pressure regulator in the distribution rack where the pressure value on the pressure regulator is set to 13 bar_{abs}.
D_2 to D_3	sub-cooling system (heat exchanger) where inlet liquid is sub-cooled to -15°C (-25°C in case of 25% C_2F_6 blend in mixture) by the counter flow vapour/liquid remaining in the exhaust line to provide as big an enthalpy budget as possible. Note: sub-cooling temperature (position of point D_3) changes depending on heat load on the modules.
D_3 to E	the pressure drop over the throttling element (Capillary). Note: position of point E changes depending on heat load on the modules.
E to E'	refrigerant evaporates inside the cooling stave removing heat from the modules. Note: on the diagram there are presented three different positions corresponding to the different power load on the modules (0 W, 6 W, 10.5 W). Note the difference in evaporation temperature between pure C_3F_8 and 25% C_2F_6 blend in mixture.
E' to F	the amount of the enthalpy used in the heat exchanger to cool down the inlet liquid (corresponding to D_2 to D_3). Note: different positions for 0 W, 6 W, 10.5 W.
F to F'	the heater evaporates the remaining liquid and the vapour is warmed up to 20°C (above the dew point). Note: different positions for 0 W, 6 W, 10.5 W.
F to A	the pressure drops over the return lines, from the exit of the heater to the front of the compressor; including pressure drop over the back pressure regulator and over the return lines from rack to the compressors.

Table 5.2: Description of the thermodynamic stages in the SR1 laboratory test station Phase Diagrams Figure 5.23 and Figure 5.24.

Laboratory measurement results were also compared to theoretical predictions made using NIST REFPROP [1]. Measured values of maximum temperature over the stave as a function of C_2F_6 blend concentration in the coolant mixture, compared to theoretical predictions are presented on Figure 5.25 for 0 W power load per module, on Figure 5.26 for 6 W power load per module and on Figure 5.27 for 10.5 W power load per module. The lower border line for the theoretical prediction band represents the saturated liquid temperature line for C_3F_8/C_2F_6 coolant mixture and the top border line represents the saturated vapour temperature line for the same mixture. Therefore the theoretical prediction band can also be assumed as mixture's "vapour quality field" (changing from liquid to vapour). It clearly can be seen that measured values perfectly match theoretically predicted values.

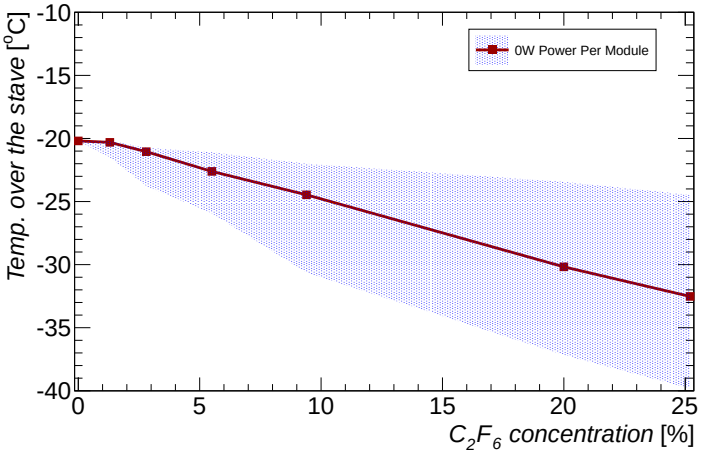

Figure 5.25: Measured Max.Temp. over the Stave changing according to concentration of C_2F_6 blend in coolant mixture, compared to theoretical predictions from NIST REFPROP [1], for 0 w power load per module, in case of 13 bar_{abs} input liquid pressure and 1.2 bar_{abs} back pressure in system. ($\sigma_{Mix\%} = 0.32\%$, $\sigma_{T.tot} = 0.35°C$)

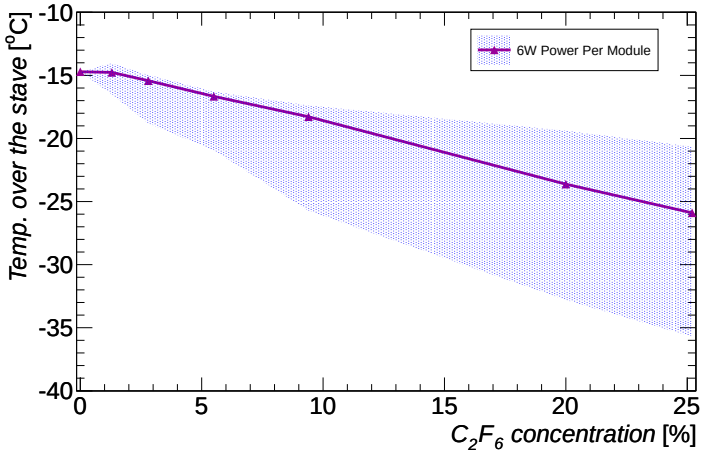

Figure 5.26: Measured Max.Temp. over the Stave changing according to concentration of C_2F_6 blend in coolant mixture, compared to theoretical predictions from NIST REFPROP [1], for 6 w power load per module, in case of 13 bar_{abs} input liquid pressure and 1.2 bar_{abs} back pressure in system. ($\sigma_{Mix\%} = 0.32\%$, $\sigma_{T.tot} = 0.35°C$)

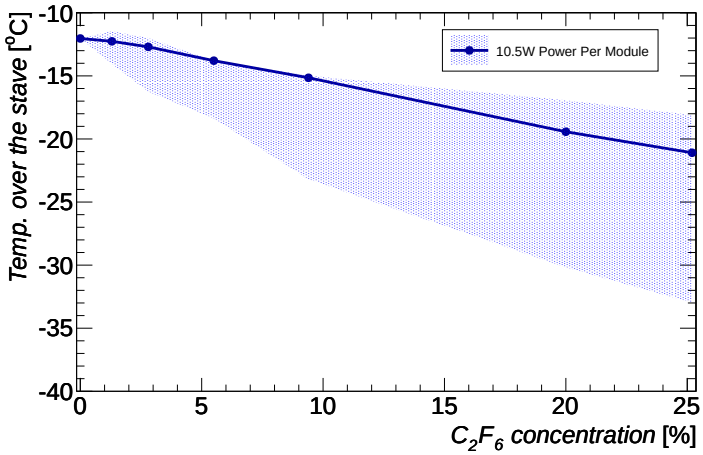

Figure 5.27: Measured Max.Temp. over the Stave changing according to concentration of C_2F_6 blend in coolant mixture, compared to theoretical predictions from NIST REFPROP [1], for 10.5 w power load per module, in case of 13 bar_{abs} input liquid pressure and 1.2 bar_{abs} back pressure in system. ($\sigma_{Mix\%} = 0.32\%$, $\sigma_{T.tot} = 0.35°C$)

Predicted temperature values from NIST REFPROP [1], for the coolant mixture in liquid phase and in vapour phase, for a measured pressure at the middle of the stave (P_A2), for different concentrations of C_2F_6 and different power applied to modules are presented in Table 5.3.

%	W	P_A2	VT	LT
0	0	2036.9	-20.075	-20.075
	6	2435.2	-15.352	-15.352
	10.5	2671.6	-12.823	-12.823
%	W	P_A2	VT	LT
1	0	2027	-20.438	-21.496
	6	2443.9	-15.498	-16.51
	10.5	2671.8	-13.064	-14.054
%	W	P_A2	VT	LT
3	0	2041.8	-20.738	-23.772
	6	2454.7	-15.885	-18.798
	10.5	2689.2	-13.397	-16.249
%	W	P_A2	VT	LT
5	0	2051.6	-21.095	-25.931
	6	2464.8	-16.28	-20.934
	10.5	2699.1	-13.81	-18.372
%	W	P_A2	VT	LT
10	0	2078.7	-21.999	-30.633
	6	2482.8	-17.376	-25.736
	10.5	2714.8	-14.976	-23.196
%	W	P_A2	VT	LT
20	0	2178.5	-23.439	-37.165
	6	2550.9	-19.381	-32.809
	10.5	2799.2	-16.929	-30.174
%	W	P_A2	VT	LT
25	0	2211.1	-24.465	-39.815
	6	2570.6	-20.637	-35.704
	10.5	2830.9	-18.105	-32.98

Table 5.3: Predicted temperature values from NIST REFPROP [1] for measured pressure at the middle of the Stave in case of different concentration of C_2F_6 blend in coolant mixture and different power applied to modules.

Laboratory measurement results for the pressure drop over the stave are also compared to the theoretical predictions done based on the two-phase pressure drop calculation theoretical model by Whalley [57] [58] which uses separated flow models: Friedel correlation [57] [59], Lockhart-Martinelli correlation [57] [60] and Chisholm correlations [57] [61] for the calculation of the frictional pressure drop.

To calculate pressure drop values based on these theoretical models, special software FLUDY [57] is used. Calculations are done for the pressure drops over the stave pipe (half of the by-stave with 24 modules mounted on it, second half is symmetrical) with the different power load on the modules : 0 W, 6 W, 10.5 W. Since the physical geometry of the custom design manifold connecting stave to the heat exchanger is very complicated, as is also the heat exchanger which is custom made and has flattened (instead of cylindrical) pipe part at the exit, it is impossible/very complicated to calculate pressure drops over the entire cooling circuit. Calculations are done for the pressure drop over the stave pipe (P_A1 to P_A3): straight stave tube part (1st_half), bend, straight stave tube part (2nd_half), see the drawing of the SCT Barrel stave on Figure 2.4.

Calculation results for the predicted pressure drop over the stave in case of different power load on the modules are presented on the P-H diagrams on Figure 5.28.

Calculation results for the predicted pressure drop as a function of the position over the stave in case of different power load on the modules are presented on Figure 5.29.

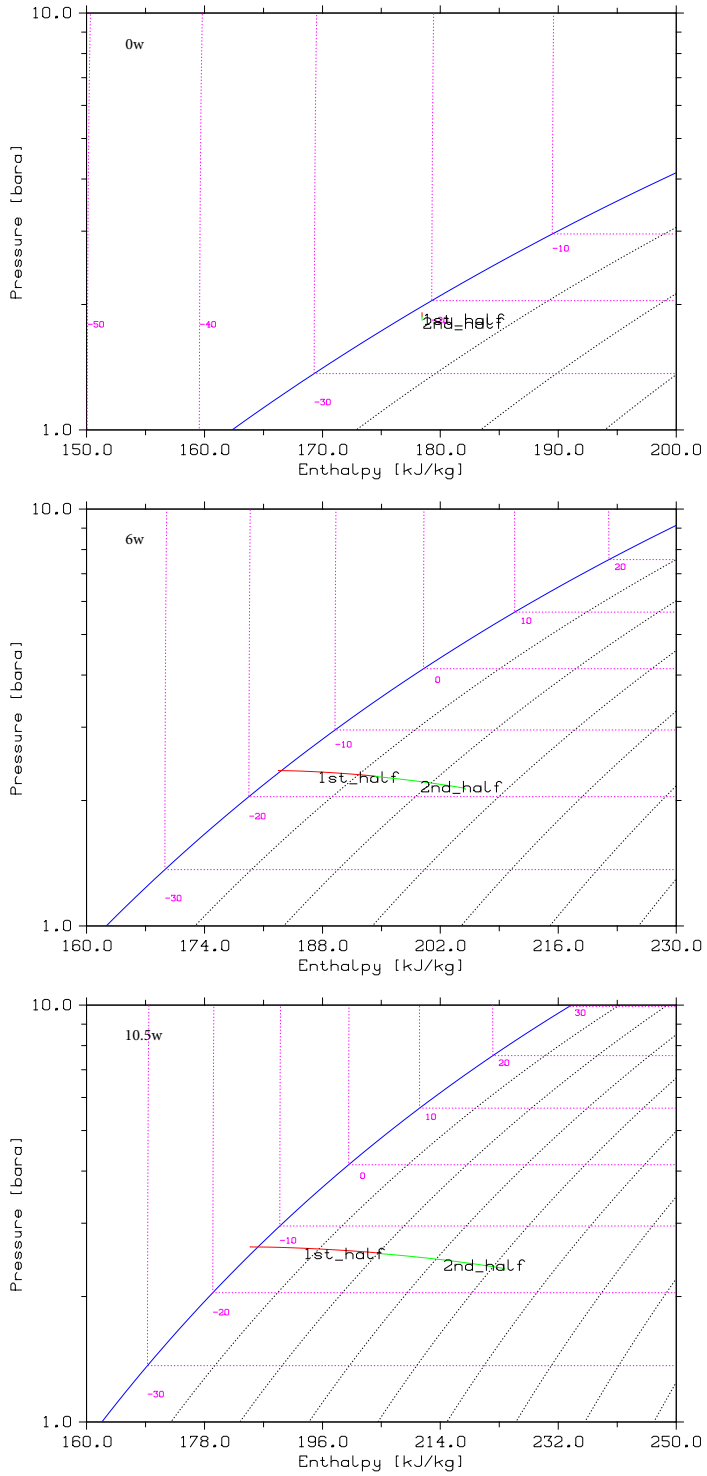

Figure 5.28: Calculation results for the predicted pressure drop over the stave in case of 0 W, 6 W, 10.5 W power load per module.

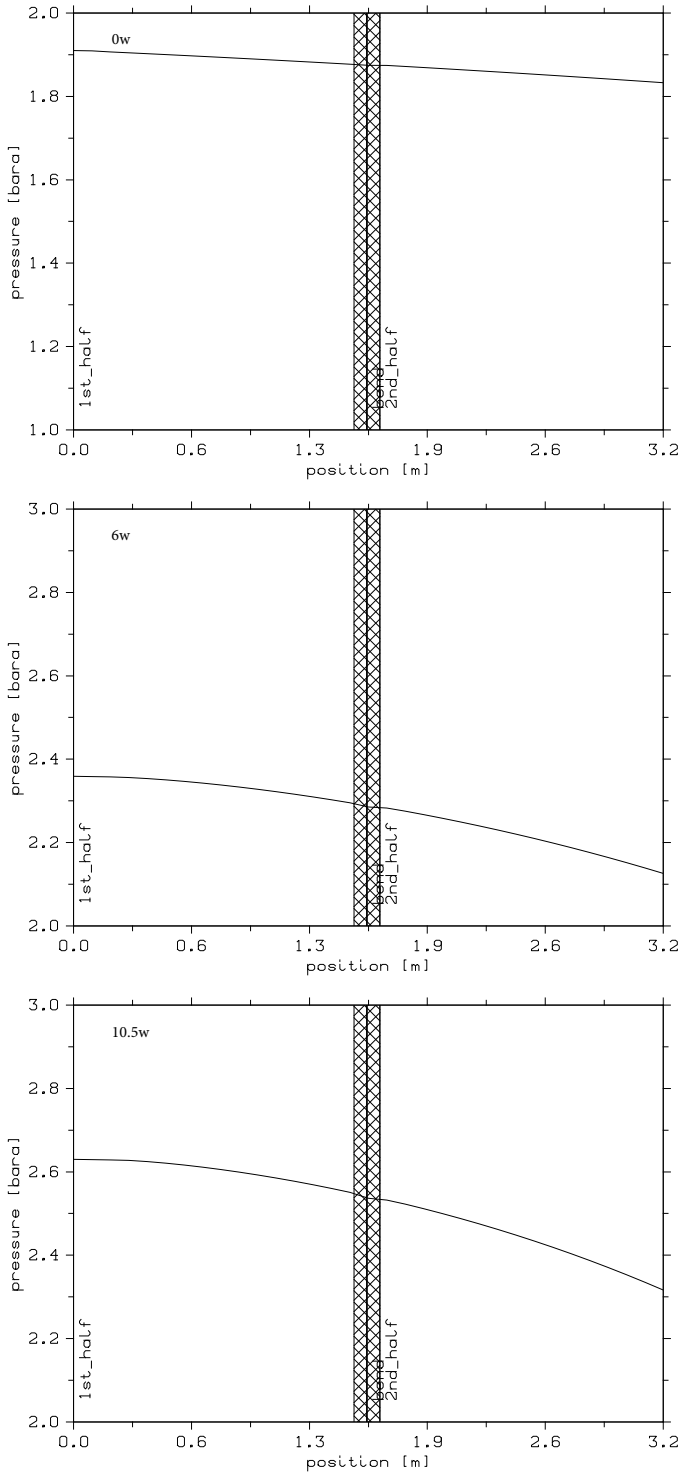

Figure 5.29: Calculation results for the predicted pressure drop as a function of the position over the stave in case of 0 W, 6 W, 10.5 W power load per module.

Calculated values for the predicted pressure drop over the stave (P_A1 to P_A3) are compared to the measured pressure drop values (see Appendix C.7) in Table 5.4.

Δ P	0w	6w	10.5w
Predicted	77.0	233.0	313.0
Measured	85.8	213.0	334.7

Table 5.4: Δ P compared predicted and measured values in case of 0w, 6w, 10.5w power load on the modules.

As it can bee seen from Table 5.4 measured and theoretical values for the pressure drop over the stave agree quite well. Therefore the pressure drops in the stave, which make up approximately 25% of the total vapour side pressure drop, can be considered well understood and in agreement with theory. As mentioned above, due to the very complex geometry, the pressure drops in the HEX and stave manifold which contribute together approximately 60% of the total vapour side pressure drops were not calculable.

Heat transfer coefficient change for the C_2F_6/C_3F_8 blends

To ensure that by adding 25% C_2F_6 blend into the coolant mixture heat transfer coefficient does not change significantly and this change does not affect temperature difference between the coolant and the module itself, additional temperature sensors are installed under the modules (between the ceramic plate and the cooling block). Temperature sensors are installed under every second module (M1, M3, M5, ..., M23), in the direct path of the heat flow. Temperature over the stave pipe (coolant temperature) and temperature under the modules is measured for 0 W, 6 W, 10.5 W power load per module, in case of pure C_3F_8, 13 bar_{abs} input liquid pressure and 1.2 bar_{abs} back pressure in system. Measurement results are presented on Figure 5.30.

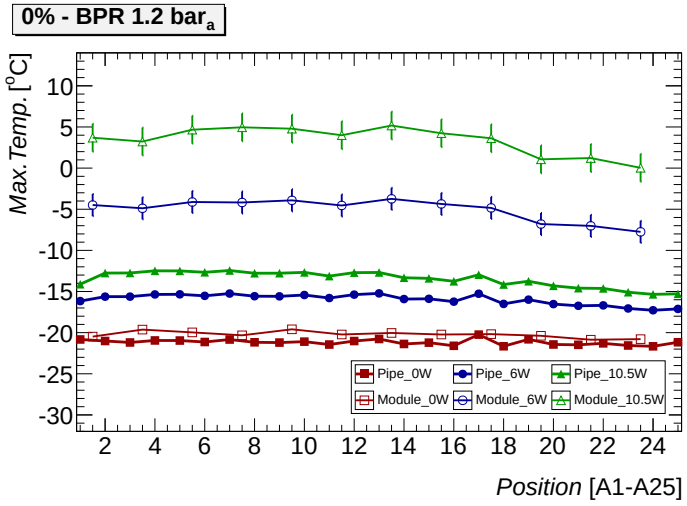

Figure 5.30: Measured temperature over the stave pipe and measured temperature under the modules, for 0 W, 6 W, 10.5 W power load per module, in case of pure C_3F_8, 13 bar_{abs} input liquid pressure and 1.2 bar_{abs} back pressure in system. ($\sigma_{T.pipe} = 0.35°C, \sigma_{T.module.0w} = 0.39°C, \sigma_{T.module.6w} = 1.35°C, \sigma_{T.module.10.5w} = 1.7°C$)

Measurement error is caused by the possible small variation in NTC sensor attachment (sensors could be not uniformly attached between the ceramic plate and the cooling block), standard deviation in measured temperature values is

presented as an error bars on the plot and in figure capture.

Measurements are repeated in case of 25% C_2F_6 blend into the coolant mixture. Measurement results are presented on Figure 5.31.

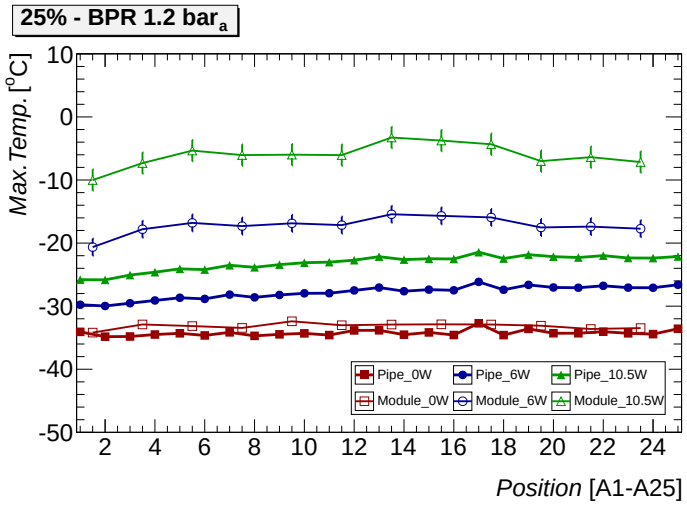

Figure 5.31: Measured temperature over the stave pipe and measured temperature under the modules, for 0 W, 6 W, 10.5 W power load per module, in case of 25% C_2F_6 blend in coolant mixture, 13 bar_{abs} input liquid pressure and 1.2 bar_{abs} back pressure in system. ($\sigma_{T.pipe} = 0.35°C, \sigma_{T.module.0w} = 0.39°C, \sigma_{T.module.6w} = 1.35°C, \sigma_{T.module.10.5w} = 1.7°C$)

Temperature of the coolant under each module is calculated as an average between the measured temperature before and after the module:

$$T_{cool.Mn} = \frac{(T\_A_n - T\_A_{n+1})}{2}$$

For each module difference between the measured temperature under the module (T_{Mn}) and the coolant temperature under the module ($T_{cool.Mn}$) is calculated as:

$$\Delta T_{Mn} = T_{Mn} - T_{cool.Mn}$$

For all modules the average in the difference between the module temperature (temperature under the module) and the coolant temperature under the module is calculated as:

$$\Delta T_{Avr} = \frac{\sum_{n=1}^{24} (\Delta T_{Mn})}{N}$$

Where:

$T_{cool.Mn}$ - Temperature of the coolant under each module [°C].

T_A_n - Temperature of the coolant before the module [°C].

T_A_{n+1} - Temperature of the coolant after the module [°C].

ΔT_{Mn} - Difference between the measured temperature under the module and the coolant temperature under the module [°C].

T_{Mn} - Measured temperature under the module [°C].

ΔT_{Avr} - Average (for all modules) in difference between the module temperature and the coolant temperature [°C].

N - Number of modules.

The average in the difference between the module temperature and the coolant temperature ΔT_{Avr} is calculated in case of different power loads on the modules (0W, 6W, 10.5W), in case of 0% and 25% C_2F_6 blend in coolant mixture. Results are presented on Figure 5.32 and in Table 5.5.

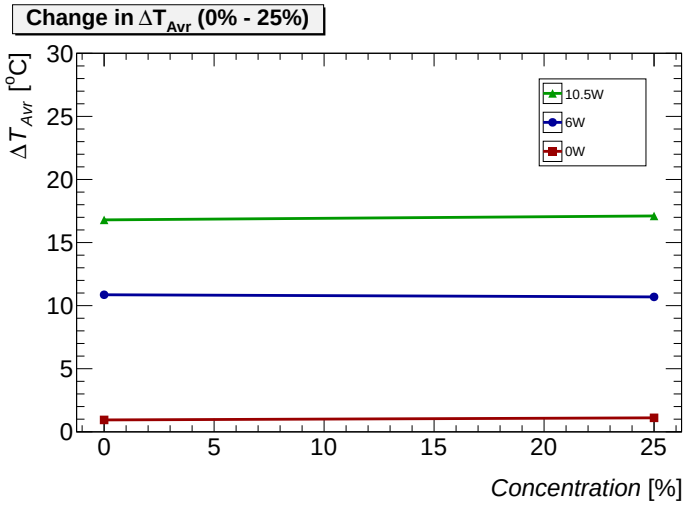

Figure 5.32: Change in difference ($\Delta\, T_{Avr}$) between the measured temperature over the stave pipe (coolant temperature) and the measured temperature under the modules, for 0 w, 6 w, 10.5 w power load per module, in case of pure C_3F_8 and 25% C_2F_6 blend in coolant mixture, 13 bar_{abs} input liquid pressure and 1.2 bar_{abs} back pressure in system. ($\sigma_{T.pipe} = 0.35°C, \sigma_{T.module.0w} = 0.39°C, \sigma_{T.module.6w} = 1.35°C, \sigma_{T.module.10.5w} = 1.7°C$)

$\Delta\, T_{Avr}$	0%	25%
0W	0.94	1.26
6W	10.86	11.32
10.5W	16.79	16.93

Table 5.5: $\Delta\, T_{Avr}$ in case of different power load on the modules (0W, 6W, 10.5W), in case of 0% and 25% C_2F_6 blend in coolant mixture .

Results clearly show that difference between the coolant temperature and the module temperature does not change significantly by adding 25% C_2F_6 blend into the coolant mixture, therefore change in heat transfer coefficient of the coolant is negligible.

Chapter 6

Summary Conclusions

Extensive tests and exhaustive measurements presented previously were performed by the author of this thesis to study in detail and to solve the problems that became appearing after the installation and initial operation of the ATLAS Inner Detector Evaporative Cooling System. After the early operational period of the cooling system concerns arose about the consistency of the system's performance and working parameters as well as with predictions made at the design stage of the project. Reassessment of LHC/ID operation scenarios, luminosity profiles and effects on silicon modules (depletion voltage, leakage current) (Section 3.1) shows that for thermal stability of the inner detector, especially at the end of 10 years operation period, the critical cooling temperature (evaporation temperature of coolant) should be around -15°C. This temperature is higher than the design temperature for ID Evaporative Cooling System (TDR) (Sections 2.2 and 2.4), but big concerns were raised about unexpected pressure drops in the cooling system, over the vapour return piping system from detector to the distribution racks, affecting temperature of coolant and therefore questioning the possibility of having the design -25°C temperature or the necessary -15°C temperature over the cooling Stave (Section 3.2).

To examine this subject in more details, a new test setup was assembled at

CERN in SR1 Laboratory (Section 4.1). This setup, assembled with spare parts from the in-pit installation, represents an exact replica of one cooling circuit of real ATLAS ID evaporative cooling system.

Measurements were performed on the laboratory setup for different operational parameters and conditions of the system. Pressure drops over the different parts of the system and the thermal profile of the cooling stave was examined for different input liquid pressure (10 bar_{abs}, 11 bar_{abs}, 12 bar_{abs}, 13 bar_{abs}), with different power load on modules (0 W, 3 W, 6 W, 9 W, 10.5 W) and different back pressure (dome pressure): "Open By-pass" (1.3 bar_{abs}), 1.6 bar_{abs}, 2 bar_{abs}, 2.5 bar_{abs}, 3 bar_{abs}, 4 bar_{abs}, 5 bar_{abs}, 6 bar_{abs} (Section 4.2). The same refrigerant, Octafluoropropane (R218) C_3F_8, was used as a coolant in the test system as it is in ATLAS ID Ev.Cooling System (Sections 2.3 and 2.4).

Measurement results for pressure drops in the system and temperature over the cooling stave (Section 4.2) showed that the ATLAS Evaporative Cooling System, running with nominal / standard operation conditions of 13 bar_{abs} inlet pressure, 1.2 bar_{abs} minimum possible back pressure and 6 W nominal power per module, cannot achieve the design evaporation temperature of -25°C nor the necessary evaporation temperature of -15°C for 10.5 W maximum power per module (after the irradiation). Therefore the thermal stability of the Inner Detector cannot be guaranteed close to the end of the operation period.

To improve the cooling performance of the system and guarantee proper operation of the ATLAS ID over the entire working period, since it is impossible to do any mechanical modifications of the system, different concentrations of Hexafluoroethane (R116) C_2F_6 and Octafluoropropane (R218) C_3F_8 mixture instead of pure C_3F_8 coolant were tested as a refrigerant utilized in the cooling system. By using this method the evaporation pressure for the same evaporation temperature can be raised, giving the possibility to overcome unexpected pressure drops in the system and to have the necessary evaporation temperature over the stave even with the minimum possible back pressure in the system.

To perform tests with a different concentration of coolant blends, a new "blending" machine was assembled in the SR1 laboratory, with a new "on-line acoustic flow meter and fluorocarbon coolant mixture analyzer" (Sonar Analyzer) attached to it (Sections 5.1 and 5.2). Tests were made for different percentages of C_2F_6 (1%, 2%, 3%, 5%, 10%, 20%, 25%) coolant in a C_3F_8/C_2F_6 mixture with different pressure and temperature parameters of the cooling test system (Section 5.3) and the best percentage concentration was found, giving the possibility to operate the existing ATLAS ID evaporative cooling system with the necessary pressure and thermal standards.

Results of extensive tests made for C_3F_8/C_2F_6 refrigerant mixture (Section 5.3) prove that with 25% of C_2F_6 in the blended mixture, with nominal operation parameters (Sections 2.2 and 2.4) and with respect to operational scenarios and predicted luminosity profiles (Section 3.1), the ATLAS Inner Detector Evaporative Cooling System can achieve the necessary evaporation temperature below the -15°C over the cooling stave and secure Inner Detector's thermal stability and proper maintenance over the entire operation period.

After three years of the LHC operation, when work on this thesis was close to finish, reassessment of the luminosity profile, depletion voltage, leakage current and the thermal runaway critical points was done again based on the current data. New values for the luminosity profile, with respect to the changes in the LHC operation plan meaning the long shut down periods in years 2012, 2013 and 2018, show that total integrated luminosity up to now equals to ≈20-25 fb^{-1} and at the end of the ten years operation period will be ≈350 fb^{-1} [62]. This value is almost twice less then it was predicted few years ago ≈629 fb^{-1} (See Section 3.1). Recent recalculation of the depletion voltage and leakage current over the silicon sensors [63] shows that total dissipated power from the irradiated modules will be less than assumed before; ≈7.5 W (silicon sensor 200 V×1.0 mA = 0.2 W + module hybrid power 6.5 W + there is no convective heat load observed for top modules + safety margin for the cooling system 0.8 W) instead of ≈10.5 W. Based on the thermal runaway critical point calculation, with respect to current luminosity profile and operation scenario, it can be assumed that ATLAS inner detector evaporative cooling system is capable to remove the heat from the irradiated modules by providing the coolant temperature in the cooling stave at -5°C (See Section 3.1, Table 3.1, Figure 3.5 and Section 4.2, Table 4.6, Figure 4.19).

This leads to the general conclusion that current evaporative cooling system for the ATLAS inner detector can safely provide proper maintenance of the inner detector over the full time of operation period.

Different concentration of C_3F_8/C_2F_6 blends in refrigerant mixture can and will be used as a back up solution for the cooling in the new project "Full Scale ThermoSiphon cooling system for the ATLAS ID" built in 2013 [64].

Bibliography

[1] M. Huber E. Lemmon and M. McLinden. NIST Reference Fluid Thermodynamic and Transport Properties Database - REFPROP. *NIST Standard Reference Database 23*, Version 9.0. [cited at p. xvii, xxi, 110, 120, 126, 127, 141, 142, 143, 178]

[2] Lyndon Evans and Philip Bryant. LHC Machine. *JINST 3 S08001 doi:10.1088/1748-0221/3/08/S08001*, 2008. [cited at p. 2]

[3] CERN Document Server. LHC/ATLAS Photo gallery. *LHC/ATLAS Photos.* [cited at p. 2, 5, 7, 19]

[4] Erk Jensen. RF Cavity Design. *CERN Accelerator School. Lectures.*, 2011. [cited at p. 3]

[5] P. Collier et al. The SPS as Injector for LHC - Conceptual Design. *CERN/SL/97-07 DI, Geneva.*, 1997. [cited at p. 3]

[6] The ATLAS Collaboration. The ATLAS Experiment at the CERN Large Hadron Collider. *JINST 3 S08003 doi:10.1088/1748-0221/3/08/S08003*, 2008. [cited at p. 3, 4, 5, 6, 7, 8, 10, 11, 12, 14, 17, 19, 21, 23, 27, 28, 30, 34, 39, 40]

[7] The CMS Collaboration et al. The CMS experiment at the CERN LHC. *JINST 3 S08004 doi:10.1088/1748-0221/3/08/S08004*, 2008. [cited at p. 4]

[8] The LHCb Collaboration et al . The LHCb Detector at the LHC . *JINST 3 S08005 doi:10.1088/1748-0221/3/08/S08005*, 2008. [cited at p. 4]

[9] The ALICE Collaboration et al. The ALICE experiment at the CERN LHC. *JINST 3 S08002 doi:10.1088/1748-0221/3/08/S08002*, 2008. [cited at p. 4]

[10] CERN Drawing Directory. Drawing Number . *LHCJUX150065*. [cited at p. 5, 44]

[11] CERN Drawing Directory. Drawing Number . *LHCJUX150001*. [cited at p. 5]

[12] The ATLAS Collaboration. Combined Performance Tests Before Installation of The ATLAS Semiconductor and Transition Radiation Tracking Detectors. *JINST 3 S08003 doi: 10.1088/1748-0221/3/08/P08003*, 2008. [cited at p. 7, 19, 21, 22, 23]

[13] S. Armstrong et al. Architecture of the ATLAS High Level Trigger Event Selection Software. *Nuclear Instruments and Methods in Physics Research A 518 (2004) 537541*, 2004. [cited at p. 15, 16, 17]

[14] ETM. PVSS2 by ETM;. *http://www.pvss.com*. [cited at p. 17, 68, 115, 124]

[15] A. Barriuso Poy et al. The Detector Control System Of The ATLAS Experiment. *JINST 3 P05006*, 2008. [cited at p. 17, 68]

[16] G. Duckeck et al. ATLAS computing: Technical Design Report. *CERN public note, CERN-LHCC-2005-022.*, 2005. [cited at p. 19]

[17] T. Sjöstrand et al. High-Energy-Physics Event Generation with Pythia 6.1. *Computer Physics Communications Volume 135, Issue 2, 1 April 2001, Pages 238259*, 2001. [cited at p. 19]

[18] S. Agostinelli et al. GEANT4 a simulation toolkit. *Nuclear Instruments and Methods in Physics Research Volume 506, Issue 3, 250303*, 2003. [cited at p. 19]

[19] The ATLAS Collaboration. ATLAS Inner detector: technical design report. 1. *CERN-LHCC-97-016*, 1997. [cited at p. 19]

[20] The ATLAS Collaboration. ATLAS Inner detector: technical design report. 2. *CERN-LHCC-97-017*, 1997. [cited at p. 19]

[21] F.Campabadal et al. Design and performance of the ABCD3TA ASIC for readout of silicon strip detectors in the atlas semiconductor tracker,. *Nucl. Instrum. Meth.A 552*, 2005. [cited at p. 22]

[22] E. Abat et al. The ATLAS Transition Radiation Tracker (TRT) Proportional Drift Tube: Design and Performance. *JINST 3 P02013*, 2008. [cited at p. 23, 27, 34]

[23] The ATLAS TRT Collaboration et al. The ATLAS TRT End-Cap Detectors. *2008 JINST 3 P10003*, 2008. [cited at p. 23, 35, 38]

[24] S.M. Sze. Physics of Semiconductor Devices. *Wiley interscience ISBN 0-471-05661-8*, 1981. [cited at p. 24, 78]

[25] G. Aad et al. ATLAS Pixel Detector Electronics and Sensors. *JINST 3 P07007*, 2008. [cited at p. 26, 29, 30, 40]

[26] A. Ahmad et al. The Silicon Microstrip Sensors of The ATLAS Semiconductor Tracker. *Nucl.Instrum. Meth. A578*, 2007. [cited at p. 26, 27, 40]

[27] A. Abdesselam et al. The Optical Links of The ATLAS SemiConductor Tracker. *2007 JINST 2 P09003.*, 2007. [cited at p. 27]

[28] A. Abdesselam et al. The Barrel Modules of The ATLAS Semiconductor Tracker. *Nucl. Instrum. Meth. A 568 (2006) 642.*, 2006. [cited at p. 30, 40]

[29] Georg Viehhauser Graham Beck. Analytic model of thermal runaway in silicon detectors. *Nucl. Instrum. Meth. A 618 (2010) 131138*, 2010. [cited at p. 32]

[30] A. Abdesselam et al. The ATLAS Semiconductor Tracker End-Cap Module. *Nucl. Instrum.Meth. A 575 (2007) 353*, 2006. [cited at p. 32, 34]

[31] F. Campabadal et al. Design and Performance of The ABCD3TA ASIC For Readout of Silicon Strip Detectors in The ATLAS Semiconductor Tracker. *Nucl. Instrum. Meth. A 552*, 2005. [cited at p. 33]

[32] V. Vacek et al. Perfluorocarbons and Their Use In Cooling Systems For Semiconductor Particle Detectors. *Fluid Phase Equilibria Volume 174*, 2000. [cited at p. 39, 41, 42]

[33] The ATLAS Collaboration. The Evaporative Cooling System For The ATLAS Inner Detector . *JINST 3 P07003 doi: 10.1088/1748-0221/3/07/P07003*, 2008. [cited at p. 39, 40, 42, 44, 48, 55, 56, 60, 85]

[34] V. Vacek, M. Galuska, M. Doubrava. Modified Cooling Circuit for Semiconductor Pixel Inner Detector, CTU Prague report. *personal communication, Prague*, 2008. [cited at p. 41, 42]

[35] V. Vacek et al. Velocity of Sound Measurements In Gaseous Per-Fluorocarbons And Their Mixtures. *Fluid Phase Equilibria Volume 185*, 2001. [cited at p. 41]

[36] M. Olcese et al. Ultra-light and stable composite structure to support and cool the ATLAS pixel detector barrel electronics modules. *Nucl. Instrum. Meth. A 518 728.*, 2004. [cited at p. 53]

[37] M. Olcese. Mechanics and cooling of pixel detectors. *Nuclear Instruments and Methods in Physics Research A 465 (2001) 5159*, 2001. [cited at p. 53]

[38] K.E. Arms et al. ATLAS pixel opto-electronics. *Nuclear Instruments and Methods in Physics Research Section A: Accelerators, Spectrometers, Detectors and Associated Equipment Volume 554, Issues 13, 1 December 2005, Pages 458468*, 2005. [cited at p. 55]

[39] R. Holt. ATLAS Inner Detector 48 volt Heater Pad Control System. *ATL-I-ER-0014 v.1*, 2006. [cited at p. 66]

[40] A. Abdesselam et al. The Data Acquisition And Calibration System For The ATLAS Semiconductor Tracker. *JINST 3 P01003*, 2008. [cited at p. 68]

[41] ATLAS Collaboration. ATLAS Inner detector: Technical Design Report. Vol. 5 . CERN/LHCC/97-1. *ISBN 92-9083-103-0*, 1997. [cited at p. 75]

[42] Taka Kondo Paul Dervan, Joost Vossebeld. Evolution of V_D and I_{LEAK} of the ATLAS barrel SCT. *ATLAS Upgrade Week. Presentation.*, 2009. [cited at p. 76, 78, 80, 83]

[43] M. Moll. Radiation Damage In Silicon Particle Detectors. *Dissertation. Hamburg 1999*, 1999. [cited at p. 78]

[44] Georg Viehhauser. Evaporative Cooling In ATLAS Present and Future. *ScienceDirect VCI2010*, 2010. [cited at p. 83]

[45] KELLER Pressure Transducers. *KELLER Corporation*. [cited at p. 89, 185]

[46] JT THERMISTOR. *SEMITEC Corporation*. [cited at p. 89, 121]

[47] Bronkhorst® model F-113AC-AAD-99-V Flow Meter. *Datasheet F-113AC*. [cited at p. 89]

[48] A.Bitadze. G. Hallewell. C_2F_6 / C_3F_8 MIXING PROCEDURE. *Technical Note. CERN EDMS DOC: 1133327*, Version 3.0. [cited at p. 114, 116]

[49] A.Bitadze. et al. A Combined On-line Acoustic Flowmeter and Fluorocarbon Coolant Mixture Analyzer for the ATLAS Silicon Tracker. *Proceedings of ICALEPCS2011, Grenoble, France. WEPMN038*, 2011. [cited at p. 120, 121]

[50] R. Bates. et al. A Combined Ultrasonic Flowmeter and Binary Vapour Mixture Analyzer For The ATLAS Silicon Tracker. . *Journal of Instrumentation*

JINST. 2013_JINST_8_P02006, 2012. [cited at p. 120, 121, 122, 123, 124, 126, 127, 128, 129]

[51] V. Vacek G. Hallewell and V. Vins. Properties of Saturated Fluorocarbons: Experimental Data and Modeling Using Perturbed-Chain-SAFT. *Fluid Phase Equilibria 292(1-2): 64-70 (2010)*, 2010. [cited at p. 120, 126, 127]

[52] E. Lemmon. Equations of State for Mixtures of R-32, R-125, R-134a, R-143a, and R-152a. *J. Phys. Chem. Ref. Data, Vol. 33, No. 2*, 2004. [cited at p. 120]

[53] M. O. McLinden S. L. Outcalt. A Modified Benedict-Webb-Rubin (BWR) equation of state for the thermodynamic Properties of R152a. *J. Phys. Chem. Ref. Data, Vol. 25, No. 2*, 1996. [cited at p. 120]

[54] M. O. McLinden; S. A. Klein; R. A. Perkins;. An Extended Corresponding State Model for the Thermal Conductivity of Refrigerants and Refrigerant Mixtures. *International Journal of Refrigeration Volume 23, Issue 1*, 2000. [cited at p. 120]

[55] Huba Control AG. *Pressure transmitter - Type 680.* [cited at p. 121, 186]

[56] R. Bates. et al. An On-Line Acoustic Fluorocarbon Coolant Mixture Analyzer for the ATLAS Silicon Tracker. *IEEE TRANSACTIONS ON NUCLEAR SCIENCE, VOL. 59, NO. 5, OCTOBER 2012,*, 2012. [cited at p. 124, 126, 127]

[57] G. Viehhauser;. FLUDY. *Manual Version 1.1*, 2000. [cited at p. 144]

[58] P. B. Whalley; G. F. Hewitt;. Multiphase flow and pressure drop. *Heat Exchanger Design Handbook, Hemisphere, Washington, DC, Vol. 2, 2.3.2-11.* [cited at p. 144]

[59] L. Friedel;. Improved friction drop correlations for horizontal and vertical two-phase pipe flow. *Proc. European Two-phase Flow Group Meeting, paper E2, JRC-Ispra, Italy.*, 1979. [cited at p. 144]

[60] R. W. Lockhart; R. C. Martinelli;. Proposed correlation of data for isothermal two-phase, two-component in pipes. *Chem. Eng. Process 45(1) (1949) 39.*, 1949. [cited at p. 144]

[61] D.Chisholm;. Pressure gradients due to friction during the flow of evaporating two-phase mixtures in smooth tubes and channels. *Int. J. Heat Mass Transf. 16 (1973) 347.*, 1973. [cited at p. 144]

[62] R.D. Heuer. CERN General Meeting 2013. *Presentation.*, 2013. [cited at p. 155]

[63] Taka Kondo. Evolution of full depletion voltage V_D. *Presentation.*, 2012. [cited at p. 155]

[64] J. A. Botelho Direito et al. GENERAL DESCRIPTION OF THE FULL SCALE THERMOSIPHON COOLING SYSTEM FOR ATLAS SCT AND PIXEL. *Technical Note. EDMS Document No.1083852*, 2010. [cited at p. 155]

Appendices

Appendix A

List of abbreviations

Abbreviation	Description	Definition
LHC	**L**arge **H**adron **C**olider	page 2
CERN	**C**onseil **E**uropen pour la **R**echerche **N**uclaire	page 2
PS	**P**roton **S**ynchrotron	page 3
SPS	**S**uper **P**roton **S**ynchrotron	page 3
ATLAS	**A** **T**oroidal **L**HC **A**pparatus	page 3
CMS	**C**ompact **M**uon **S**olenoid	page 3
LHCb	**LHC** **b**eauty experiment	page 4
ALICE	**A** **L**arge **I**on **C**ollider **E**xperiment.	page 4
LAr	**L**iquid **A**rgon	page 10
SCT	**S**emi**C**onductor **T**racer	page 19
TRT	**T**ransition **R**adiation **T**racer	page 19
ID	**I**nner **D**etector	page 19
MDT	**M**omitored **D**rift **T**tube	page 12
CSCs	**C**athode **S**trip **C**hambers	page 12
TGCs	**T**hin **G**ap **C**hambers	page 12
RPCs	**R**esistive **P**late **C**hambers	page 12
ROD	**R**ead**O**ut **D**river	page 16

Abbreviation	Description	Definition
TDR	**T**echnical **D**esign **R**eport	page 27
NTC	**N**egative **T**emperature **C**oefficient	page 30
ASIC	**A**pplication-**S**pecific **I**ntegrated **C**ircuit	page 30
TPG	**T**hermal **P**yrolitic **G**raphite	page 31
HEX	**H**eat **Ex**changer	page 45
PLC	**P**rogrammable **L**ogic **C**ontroller	page 46
DCS	**D**etector **C**ontrol **S**ystem	page 68
DAQ	**D**ata **A**cquisition **S**ystem	page 68
FSM	**F**inite **S**tate **M**achine	page 68
DPS	**D**istributed **P**ower **S**upply	page 61
ADC	**A**nalog to **D**igital **C**onverter	page 97
USB	**U**niversal **S**erial **B**us Cable	page 97
BM	**B**lending **M**achine	page 111
FS	**F**ull **S**cale	page 185
RD	**R**eading (accuracy)	page 190

Appendix B

List of publications

Below is the list of publications that arose during the time spent working on this thesis.

1. A.Bitadze. et al.
   A Combined On-line Acoustic Flowmeter and Fluorocarbon Coolant Mixture Analyzer for the ATLAS Silicon Tracker.
   Printed: Proceedings of 13th International Conference on Accelerator and Large Experimental Physics Control Systems ICALEPCS2011, Grenoble, France. WEPMN038
   http://accelconf.web.cern.ch/accelconf/icalepcs2011/papers/wepmn038.pdf

2. R. Bates. et al.
   Reassessment of cooling requirements for the ATLAS barrel SCT.
   printed: CERN Document Server. ATL-COM-INDET-2009-093
   https://cdsweb.cern.ch/record/1229424?

3. R.bates. et al.
   An On-Line Acoustic Fluorocarbon Coolant Mixture Analyzer for the ATLAS Silicon Tracker.
   Printed: IEEE TRANSACTIONS ON NUCLEAR SCIENCE, VOL. 59,

NO. 5, OCTOBER 2012

http://ieeexplore.ieee.org/stamp/stamp.jsp?tp=&arnumber=6296739

4. S.Katunin. et al.

   Development of a custom on-line ultrasonic vapour analyzer/flowmeter for the ATLAS inner detector, with application to gaseous tracking and Cherenkov detectors.

   Printed: Topical Workshop on Electronics for Particle Physics. TWEPP 2012. London. UK.

   http://arxiv.org/abs/1210.8045

5. R.bates. et al.

   A combined ultrasonic flow meter and binary vapour mixture analyzer for the ATLAS silicon tracker.

   Printed: Journal of Instrumentation JINST. 2013_JINST_8_P02006.

   http://dx.doi.org/10.1088/1748-0221/8/02/P02006

6. R.bates. et al.

   The study of C_2F_6/C_3F_8 saturated fluorocarbon refrigerant blends for the ATLAS silicon tracker.

   Printed: Submitted for publication in JINST

   http://iopscience.iop.org/1748-0221/

Appendix C

Pressure Drops and Flow Values

Below are presented tables for different Inlet / Outlet pressures in the system and different powers on the modules, showing pressure drops over the different parts of cooling structure. Values are presented in mbars and percentage (%). Refrigerant used in system is pure C_3F_8.

Flow Values are presented for different inlet pressures in the system and different powers per module, in case of minimum possible back pressure of $1.3\,\mathrm{bar}_{abs}$.

Pressure drops in the system (mBar)									
10Bar	**BPR** P_BBPR - P_BFM	**Pipe work** P_AH - P_BBPR	**Heater** P_BH - P_AH	**HEX** P_VAM - P_BH	**Manifold** P_A3 - P_VAM	**Stave** P_A1 - P_A3	**Difference** between P_dome and P_BBPR	**Total DP off-detector** P_VAM - P_BBPR	**Total DP** P_A1 - P_BBPR
Open_0W	7.8	139.4	9.6	276.9	31.4	73.1	-134.2	425.9	530.5
Open_3W	7.1	146.9	4.3	350.3	78.6	135.9	-132.1	501.6	716.1
Open_6W	7.6	133.1	11.3	405.4	128.9	202.4	-133.5	549.8	881.0
Open_9W	8.9	136.2	0.7	432.0	187.8	335.9	-136.4	569.0	1092.7
Open_10.5W	7.7	133.0	6.3	431.9	208.5	382.4	-130.6	571.1	1162.0
1.6_0W	637.6	99.2	-0.3	174.6	20.2	56.2	-371.6	273.5	350.0
1.6_3W	626.0	103.6	-2.5	241.7	56.7	107.7	-357.3	342.8	507.2
1.6_6W	612.9	108.7	-9.4	291.8	98.4	172.7	-342.9	391.1	662.1
1.6_9W	603.9	104.6	-8.9	311.3	145.9	264.9	-329.8	406.9	817.8
1.6_10.5W	599.0	103.4	-7.3	304.1	160.5	315.6	-328.0	400.3	876.4
2.0_0W	764.3	91.6	-1.6	164.2	18.6	56.5	-103.9	254.3	329.5
2.0_3W	737.3	101.7	-8.6	226.6	53.9	103.7	-84.8	319.7	477.4
2.0_6W	743.3	89.1	0.6	274.7	93.2	164.3	-77.2	364.4	621.9
2.0_9W	730.4	101.0	-12.4	293.3	131.9	234.7	-60.3	381.9	748.5
2.0_10.5W	-	-	-	-	-	-	-	-	-
2.5_0W	1002.4	95.6	-14.8	136.1	10.4	50.9	167.9	217.0	278.3
2.5_3W	998.1	87.2	-7.0	197.2	44.3	97.6	171.9	277.5	419.3
2.5_6W	992.4	79.6	-0.9	243.5	82.7	153.1	179.4	322.2	558.0
2.5_9W	984.4	85.1	-6.3	257.4	118.4	215.3	187.7	336.2	669.9
2.5_10.5W	-	-	-	-	-	-	-	-	-
3.0_0W	1496.5	80.3	-13.2	99.1	8.5	36.5	177.6	166.3	211.3
3.0_3W	1511.8	69.7	-6.3	148.8	35.1	76.4	169.0	212.2	323.7
3.0_6W	1512.4	68.4	-5.0	187.7	67.0	126.4	167.1	251.1	444.5
3.0_9W	1522.1	69.7	-8.1	195.3	94.3	181.5	160.8	257.0	532.8
3.0_10.5W	-	-	-	-	-	-	-	-	-
4.0_0W	2590.3	55.8	-8.9	65.5	-0.2	25.2	93.4	112.5	137.5
4.0_3W	2598.3	57.6	-11.4	82.7	18.7	55.8	91.7	129.0	203.6
4.0_6W	2595.3	63.0	-16.8	109.9	41.3	94.1	94.2	156.0	291.4
4.0_9W	2586.0	62.1	-18.0	111.5	59.3	129.7	104.7	155.6	344.6
4.0_10.5W	-	-	-	-	-	-	-	-	-
5.0_0W	3595.4	53.1	-15.3	60.8	-10.6	24.7	92.3	98.7	112.8
5.0_3W	3591.1	53.2	-16.0	54.8	9.4	44.0	99.8	92.0	145.4
5.0_6W	3591.3	47.7	-13.1	73.6	24.5	70.4	100.9	108.2	203.1
5.0_9W	3599.9	41.6	-7.2	62.2	37.3	99.4	91.5	96.6	233.4
5.0_10.5W	-	-	-	-	-	-	-	-	-
6.0_0W	-	-	-	-	-	-	-	-	-
6.0_3W	-	-	-	-	-	-	-	-	-
6.0_6W	-	-	-	-	-	-	-	-	-
6.0_6W	-	-	-	-	-	-	-	-	-
6.0_10.5W	-	-	-	-	-	-	-	-	-

Table C.1: Pressure drops in cooling structure (input liquid pressure $10\,\mathrm{bar}_{abs}$ / table items given in mbars).

Pressure drops in the system (% from Total DP)									
10Bar	**BPR** P_BBPR - P_BFM	**Pipe work** P_AH - P_BBPR	**Heater** P_BH - P_AH	**HEX** P_VAM - P_BH	**Manifold** P_A3 - P_VAM	**Stave** P_A1 - P_A3	**Difference** between P_dome and P_BBPR	**Total DP off-detector** P_VAM - P_BBPR	**Total DP** P_A1 - P_BBPR (mBar)
Open_0W	-	26	2	52	6	14	-	80	530.5
Open_3W	-	21	1	49	11	19	-	70	716.1
Open_6W	-	15	1	46	15	23	-	62	881.0
Open_9W	-	12	0	40	17	31	-	52	1092.7
Open_10.5W	-	11	1	37	18	33	-	49	1162.0
1.6_0W	-	28	0	50	6	16	-	78	350.0
1.6_3W	-	20	0	48	11	21	-	68	507.2
1.6_6W	-	16	-1	44	15	26	-	59	662.1
1.6_9W	-	13	-1	38	18	32	-	50	817.8
1.6_10.5W	-	12	-1	35	18	36	-	46	876.4
2.0_0W	-	28	0	50	6	17	-	77	329.5
2.0_3W	-	21	-2	47	11	22	-	67	477.4
2.0_6W	-	14	0	44	15	26	-	59	621.9
2.0_9W	-	13	-2	39	18	31	-	51	748.5
2.0_10.5W	-	-	-	-	-	-	-	-	-
2.5_0W	-	34	-5	49	4	18	-	78	278.3
2.5_3W	-	21	-2	47	11	23	-	66	419.3
2.5_6W	-	14	0	44	15	27	-	58	558.0
2.5_9W	-	13	-1	38	18	32	-	50	669.9
2.5_10.5W	-	-	-	-	-	-	-	-	-
3.0_0W	-	38	-6	47	4	17	-	79	211.3
3.0_3W	-	22	-2	46	11	24	-	66	323.7
3.0_6W	-	15	-1	42	15	28	-	56	444.5
3.0_9W	-	13	-2	37	18	34	-	48	532.8
3.0_10.5W	-	-	-	-	-	-	-	-	-
4.0_0W	-	41	-6	48	0	18	-	82	137.5
4.0_3W	-	28	-6	41	9	27	-	63	203.6
4.0_6W	-	22	-6	38	14	32	-	54	291.4
4.0_9W	-	18	-5	32	17	38	-	45	344.6
4.0_10.5W	-	-	-	-	-	-	-	-	-
5.0_0W	-	47	-14	54	-9	22		88	112.8
5.0_3W	-	37	-11	38	6	30		63	145.4
5.0_6W	-	23	-6	36	12	35		53	203.1
5.0_9W	-	18	-3	27	16	43		41	233.4
5.0_10.5W	-	-	-	-	-	-	-	-	-
6.0_0W	-	-	-	-	-	-	-	-	-
6.0_3W	-	-	-	-	-	-	-	-	-
6.0_6W	-	-	-	-	-	-	-	-	-
6.0_6W	-	-	-	-	-	-	-	-	-
6.0_10.5W	-	-	-	-	-	-	-	-	-

Table C.2: Pressure drops in cooling structure (input liquid pressure $10\,\mathrm{bar}_{abs}$ / table items given in percentage of total pressure drop in vapour return line. %).

Pressure drops in the system (mBar)									
11Bar	**BPR** P_BBPR - P_BFM	**Pipe work** P_AH - P_BBPR	**Heater** P_BH - P_AH	**HEX** P_VAM - P_BH	**Manifold** P_A3 - P_VAM	**Stave** P_A1 - P_A3	**Difference** between P_dome and P_BBPR	**Total DP off-detector** P_VAM - P_BBPR	**Total DP** P_A1 - P_BBPR
Open_0W	9.0	126.8	35.0	305.7	33.7	81.8	-165.2	467.6	583.1
Open_3W	8.3	124.0	34.6	390.2	82.6	143.8	-153.1	548.8	775.2
Open_6W	8.1	122.6	33.5	450.0	136.4	208.8	-152.0	606.1	951.3
Open_9W	8.4	121.5	31.5	499.9	184.5	294.6	-145.2	652.9	1132.0
Open_10.5W	7.7	132.7	19.5	494.7	222.9	395.8	-143.6	646.9	1265.6
1.6_0W	727.1	83.0	20.0	188.7	19.4	56.2	-464.9	291.7	367.2
1.6_3W	705.8	83.2	21.3	260.6	60.8	108.5	-445.3	365.1	534.4
1.6_6W	694.6	81.7	19.4	318.5	99.7	174.7	-432.7	419.5	694.0
1.6_9W	687.2	81.0	19.0	345.0	136.7	242.6	-423.2	445.0	824.4
1.6_10.5W	683.5	79.3	17.6	347.5	165.2	306.1	-416.8	444.3	915.6
2.0_0W	796.4	83.7	13.1	185.4	22.3	59.3	-155.7	282.3	363.8
2.0_3W	799.9	81.4	16.8	252.3	58.1	112.7	-141.5	350.4	521.2
2.0_6W	792.9	80.8	16.3	301.1	99.1	169.0	-130.8	398.3	666.3
2.0_9W	780.8	79.0	14.2	325.0	136.4	231.9	-122.0	418.3	786.5
2.0_10.5W	800.3	77.4	13.3	319.1	158.5	311.0	-143.0	409.9	879.4
2.5_0W	1020.2	72.6	14.1	154.2	17.1	50.0	130.4	240.9	308.0
2.5_3W	1016.7	71.4	14.3	221.5	48.6	99.7	135.6	307.2	455.5
2.5_6W	1003.4	71.2	15.3	272.0	90.4	157.7	149.9	358.6	606.7
2.5_9W	999.3	71.3	11.2	287.2	128.1	217.2	155.6	369.7	715.0
2.5_10.5W	1030.3	69.5	12.1	287.7	145.2	286.2	127.4	369.2	800.6
3.0_0W	1462.9	59.7	8.7	121.3	10.6	38.6	196.5	189.7	238.9
3.0_3W	1473.8	57.0	13.4	171.7	41.9	83.1	195.7	242.2	367.2
3.0_6W	1476.5	56.0	13.6	217.4	74.0	138.0	186.6	287.0	498.9
3.0_9W	1472.6	56.7	12.5	237.5	104.3	190.8	191.4	306.7	601.9
3.0_10.5W	1475.2	54.3	10.9	238.9	119.6	229.6	190.0	304.2	653.4
4.0_0W	2603.7	43.3	3.6	74.2	4.1	27.1	59.6	121.1	152.3
4.0_3W	2603.2	41.5	4.0	103.4	22.6	60.9	60.5	148.9	232.4
4.0_6W	2598.9	40.6	5.9	135.0	46.8	101.0	61.9	181.5	329.2
4.0_9W	2594.2	42.1	2.4	147.1	69.7	142.9	71.0	191.6	404.2
4.0_10.5W	2591.9	40.5	3.5	139.8	75.5	166.5	73.1	183.8	425.8
5.0_0W	3578.9	22.1	7.0	63.7	5.2	21.7	93.2	92.8	119.7
5.0_3W	3564.4	28.1	4.2	73.2	12.9	47.2	108.1	105.5	165.5
5.0_6W	3563.5	29.2	4.5	95.1	30.9	77.4	110.6	128.8	237.1
5.0_9W	3561.8	27.8	7.4	95.3	45.9	110.1	112.8	130.6	286.6
5.0_10.5W	3547.3	27.6	6.3	85.2	48.1	130.4	125.9	119.1	297.6
6.0_0W	4611.9	15.8	11.7	67.5	-2.1	21.8	51.1	95.0	114.7
6.0_3W	4618.6	15.4	11.9	57.1	6.7	39.5	53.9	84.4	130.7
6.0_6W	4612.4	11.3	10.9	65.2	18.1	65.5	51.6	87.3	171.0
6.0_9W	4600.3	14.5	10.1	60.4	29.1	83.1	74.0	85.0	197.1
6.0_10.5W	-	-	-	-	-	-	-	-	-

Table C.3: Pressure drops in cooling structure (input liquid pressure 11 bar_{abs} / table items given in mbars).

Pressure drops in the system (% from Total DP)									
11Bar	**BPR** P_BBPR - P_BFM	**Pipe work** P_AH - P_BBPR	**Heater** P_BH - P_AH	**HEX** P_VAM - P_BH	**Manifold** P_A3 - P_VAM	**Stave** P_A1 - P_A3	**Difference** between P_dome and P_BBPR	**Total DP off-detector** P_VAM - P_BBPR	**Total DP** P_A1 - P_BBPR (mBar)
Open_0W	-	22	6	52	6	14	-	80	583.1
Open_3W	-	16	4	50	11	19	-	71	775.2
Open_6W	-	13	4	47	14	22	-	64	951.3
Open_9W	-	11	3	44	16	26	-	58	1132.0
Open_10.5W	-	10	2	39	18	31	-	51	1265.6
1.6_0W	-	23	5	51	5	15	-	79	367.2
1.6_3W	-	16	4	49	11	20	-	68	534.4
1.6_6W	-	12	3	46	14	25	-	60	694.0
1.6_9W	-	10	2	42	17	29	-	54	824.4
1.6_10.5W	-	9	2	38	18	33	-	49	915.6
2.0_0W	-	23	4	51	6	16	-	78	363.8
2.0_3W	-	16	3	48	11	22	-	67	521.2
2.0_6W	-	12	2	45	15	25	-	60	666.3
2.0_9W	-	10	2	41	17	29	-	53	786.5
2.0_10.5W	-	9	2	36	18	35	-	47	879.4
2.5_0W	-	24	5	50	6	16	-	78	308.0
2.5_3W	-	16	3	49	11	22	-	67	455.5
2.5_6W	-	12	3	45	15	26	-	59	606.7
2.5_9W	-	10	2	40	18	30	-	52	715.0
2.5_10.5W	-	9	2	36	18	36	-	46	800.6
3.0_0W	-	25	4	51	4	16	-	79	238.9
3.0_3W	-	16	4	47	11	23	-	66	367.2
3.0_6W	-	11	3	44	15	28	-	58	498.9
3.0_9W	-	9	2	39	17	32	-	51	601.9
3.0_10.5W	-	8	2	37	18	35	-	47	653.4
4.0_0W	-	28	2	49	3	18	-	80	152.3
4.0_3W	-	18	2	44	10	26	-	64	232.4
4.0_6W	-	12	2	41	14	31	-	55	329.2
4.0_9W	-	10	1	36	17	35	-	47	404.2
4.0_10.5W	-	10	1	33	18	39	-	43	425.8
5.0_0W		18	6	53	4	18	-	78	119.7
5.0_3W	-	17	3	44	8	28	-	64	165.5
5.0_6W	-	12	2	40	13	33	-	54	237.1
5.0_9W	-	10	3	33	16	38	-	46	286.6
5.0_10.5W	-	9	2	29	16	44	-	40	297.6
6.0_0W	-	14	10	59	-2	19	-	83	114.7
6.0_3W	-	12	9	44	5	30	-	65	130.7
6.0_6W	-	7	6	38	11	38	-	51	171.0
6.0_9W	-	7	5	31	15	42	-	43	197.1
6.0_10.5W	-	-	-	-	-	-	-	-	-

Table C.4: Pressure drops in cooling structure (input liquid pressure 11 bar_{abs} / table items given in percentage of total pressure drop in vapour return line. %).

Pressure drops in the system (mBar)									
12Bar	**BPR** P_BBPR - P_BFM	**Pipe work** P_AH - P_BBPR	**Heater** P_BH - P_AH	**HEX** P_VAM - P_BH	**Manifold** P_A3 - P_VAM	**Stave** P_A1 - P_A3	**Difference** between P_dome and P_BBPR	**Total DP off-detector** P_VAM - P_BBPR	**Total DP** P_A1 - P_BBPR
Open_0W	9.5	152.3	29.8	333.0	38.5	84.3	-153.0	515.1	637.9
Open_3W	9.4	151.0	31.7	418.5	87.1	145.1	-152.2	601.2	833.4
Open_6W	9.4	144.4	31.7	488.0	139.4	214.9	-152.4	664.0	1018.4
Open_9W	8.9	141.8	30.1	536.3	190.3	287.2	-148.8	708.1	1185.6
Open_10.5W	9.0	139.6	29.6	549.2	220.3	358.1	-149.9	718.3	1296.7
1.6_0W	781.7	95.1	16.3	200.1	22.4	55.4	-521.5	311.5	389.3
1.6_3W	757.4	94.5	18.7	276.7	60.0	113.9	-495.1	389.9	563.9
1.6_6W	758.8	94.6	16.9	335.9	102.7	177.8	-493.6	447.4	728.0
1.6_10.5W	744.3	92.4	17.5	379.1	163.0	282.7	-483.9	489.0	934.7
2.0_0W	896.3	89.2	16.1	184.3	23.6	54.0	-246.3	289.6	367.3
2.0_3W	888.4	86.9	18.7	257.5	57.9	110.2	-234.5	363.1	531.1
2.0_6W	880.1	86.4	18.7	318.3	99.8	172.3	-221.4	423.4	695.5
2.0_9W	872.4	85.9	14.9	343.4	139.6	236.4	-213.2	444.3	820.2
2.0_10.5W	866.6	86.9	15.5	358.4	156.8	271.3	-205.1	460.8	888.9
2.5_0W	1115.4	79.4	13.5	162.8	16.1	49.9	35.7	255.7	321.7
2.5_3W	1120.1	76.9	16.5	228.5	53.8	98.7	44.9	321.8	474.3
2.5_6W	1108.8	77.5	16.9	286.2	92.1	158.7	56.9	380.5	631.3
2.5_9W	1108.2	75.8	14.8	314.5	126.7	222.1	60.0	405.0	753.8
2.5_10.5W	1101.5	75.5	13.5	324.5	145.2	254.3	66.5	413.4	812.8
3.0_0W	1440.7	75.8	12.8	125.8	11.8	50.0	211.1	214.4	276.1
3.0_3W	1448.7	74.0	12.8	187.8	46.6	90.6	207.5	274.6	411.8
3.0_6W	1451.0	72.8	14.3	238.3	81.1	146.3	208.8	325.4	552.8
3.0_9W	1445.0	70.6	15.9	262.1	114.8	202.3	211.7	348.6	665.6
3.0_10.5W	1448.6	71.0	15.2	266.9	129.1	229.2	212.5	353.1	711.4
4.0_0W	2436.0	52.0	10.6	75.7	3.2	32.1	213.8	138.2	173.6
4.0_3W	2444.0	51.4	15.8	108.2	28.1	65.8	218.0	175.3	269.2
4.0_6W	2439.3	50.6	13.8	152.3	55.5	110.7	222.8	216.7	382.9
4.0_9W	2433.6	49.6	14.1	175.2	80.2	154.3	229.5	238.9	473.4
4.0_10.5W	2440.6	49.5	12.6	170.0	89.7	176.5	223.8	232.1	498.3
5.0_0W	3577.2	37.6	13.1	57.8	-1.9	26.2	90.8	108.5	132.8
5.0_3W	3579.6	36.5	14.4	66.0	18.7	46.4	93.9	116.8	182.0
5.0_6W	3575.8	36.5	13.1	95.7	36.1	83.3	98.0	145.3	264.6
5.0_9W	3580.2	35.9	13.3	109.5	53.6	123.2	95.6	158.7	335.5
5.0_10.5W	3568.0	36.0	11.4	105.2	60.6	139.3	108.7	152.5	352.4
6.0_0W	4625.0	26.2	18.7	61.1	-7.9	25.7	49.3	105.9	123.6
6.0_3W	4616.9	24.9	16.3	47.1	10.6	44.7	44.9	88.3	143.6
6.0_6W	4611.0	24.6	19.0	61.0	23.5	69.1	54.9	104.7	197.2
6.0_9W	4603.5	33.0	16.9	62.7	40.4	91.7	59.4	112.6	244.7
6.0_10.5W	4640.5	13.4	18.4	63.8	26.7	112.7	36.6	95.6	235.0

Table C.5: Pressure drops in cooling structure (input liquid pressure $12\,\mathrm{bar}_{abs}$ / table items given in mbars).

Pressure drops in the system (% from Total DP)									
12Bar	**BPR** P_BBPR - P_BFM	**Pipe work** P_AH - P_BBPR	**Heater** P_BH - P_AH	**HEX** P_VAM - P_BH	**Manifold** P_A3 - P_VAM	**Stave** P_A1 - P_A3	**Difference** between P_dome and P_BBPR	**Total DP off-detector** P_VAM - P_BBPR	**Total DP** P_A1 - P_BBPR (mBar)
Open_0W	-	24	5	52	6	13	-	81	637.9
Open_3W	-	18	4	50	10	17	-	72	833.4
Open_6W	-	14	3	48	14	21	-	65	1018.4
Open_9W	-	12	3	45	16	24	-	60	1185.6
Open_10.5W	-	11	2	42	17	28	-	55	1296.7
1.6_0W	-	24	4	51	6	14	-	80	389.3
1.6_3W	-	17	3	49	11	20	-	69	563.9
1.6_6W	-	13	2	46	14	24	-	61	728.0
1.6_10.5W	-	10	2	41	17	30	-	52	934.7
2.0_0W	-	24	4	50	6	15	-	79	367.3
2.0_3W	-	16	4	48	11	21	-	68	531.1
2.0_6W	-	12	3	46	14	25	-	61	695.5
2.0_9W	-	10	2	42	17	29	-	54	820.2
2.0_10.5W	-	10	2	40	18	31	-	52	888.9
2.5_0W	-	25	4	51	5	16	-	79	321.7
2.5_3W	-	16	3	48	11	21	-	68	474.3
2.5_6W	-	12	3	45	15	25	-	60	631.3
2.5_9W	-	10	2	42	17	29	-	54	753.8
2.5_10.5W	-	9	2	40	18	31	-	51	812.8
3.0_0W	-	27	5	46	4	18	-	78	276.1
3.0_3W	-	18	3	46	11	22	-	67	411.8
3.0_6W	-	13	3	43	15	26	-	59	552.8
3.0_9W	-	11	2	39	17	30	-	52	665.6
3.0_10.5W	-	10	2	38	18	32	-	50	711.4
4.0_0W	-	30	6	44	2	19	-	80	173.6
4.0_3W	-	19	6	40	10	24	-	65	269.2
4.0_6W	-	13	4	40	14	29	-	57	382.9
4.0_9W	-	10	3	37	17	33	-	50	473.4
4.0_10.5W	-	10	3	34	18	35	-	47	498.3
5.0_0W		28	10	44	-1	20	-	82	132.8
5.0_3W	-	20	8	36	10	26	-	64	182.0
5.0_6W	-	14	5	36	14	31	-	55	264.6
5.0_9W	-	11	4	33	16	37	-	47	335.5
5.0_10.5W	-	10	3	30	17	40	-	43	352.4
6.0_0W	-	21	15	49	-6	21	-	86	123.6
6.0_3W	-	17	11	33	7	31	-	61	143.6
6.0_6W	-	12	10	31	12	35	-	53	197.2
6.0_9W	-	13	7	26	16	37	-	46	244.7
6.0_10.5W	-	6	8	27	11	48	-	41	235.0

Table C.6: Pressure drops in cooling structure (input liquid pressure $12\,\mathrm{bar}_{abs}$ / table items given in percentage of total pressure drop in vapour return line. %).

Pressure drops in the system (mBar)									
13Bar	**BPR** P_BBPR - P_BFM	**Pipe work** P_AH - P_BBPR	**Heater** P_BH - P_AH	**HEX** P_VAM - P_BH	**Manifold** P_A3 - P_VAM	**Stave** P_A1 - P_A3	**Difference** between P_dome and P_BBPR	**Total DP off-detector** P_VAM - P_BBPR	**Total DP** P_A1 - P_BBPR
Open_0W	10.9	179.7	16.8	347.9	37.9	85.8	-177.4	544.4	668.0
Open_3W	10.4	176.5	20.9	429.8	88.3	145.6	-171.9	627.2	861.1
Open_6W	9.7	169.6	23.1	512.3	143.7	213.0	-166.9	705.1	1061.8
Open_9W	9.6	162.8	25.5	548.8	195.5	287.5	-167.6	737.2	1220.2
Open_10.5W	9.8	162.6	25.2	592.7	221.6	334.7	-162.5	780.5	1336.8
1.6_0W	845.1	120.1	0.0	201.3	22.0	59.9	-596.7	321.4	403.4
1.6_3W	832.4	113.8	8.7	280.4	59.5	114.1	-584.2	402.9	576.5
1.6_6W	821.2	108.8	15.1	344.5	104.5	178.1	-574.1	468.4	751.0
1.6_9W	812.0	114.4	6.5	383.8	147.5	242.3	-560.9	504.7	894.4
1.6_10.5W	807.9	119.0	0.7	386.4	167.0	274.3	-557.0	506.1	947.4
2.0_0W	965.9	118.2	-3.7	184.0	18.7	57.6	-316.8	298.5	374.8
2.0_3W	957.5	115.7	-0.7	260.6	60.4	107.1	-306.4	375.6	543.1
2.0_6W	946.0	110.0	4.7	325.7	102.6	167.8	-294.6	440.4	710.8
2.0_9W	939.4	103.4	8.5	366.7	140.9	235.1	-286.4	478.6	854.6
2.0_10.5W	932.4	106.2	5.9	363.7	162.4	266.3	-281.9	475.8	904.5
2.5_0W	1179.7	102.1	-0.1	164.3	17.8	56.5	-25.7	266.3	340.6
2.5_3W	1170.2	97.6	9.2	234.2	56.6	100.9	-15.4	341.0	498.5
2.5_6W	1152.4	99.5	6.0	295.9	95.7	160.9	-4.8	401.4	658.0
2.5_9W	1143.5	107.4	-4.3	335.6	136.0	221.1	8.2	438.7	795.8
2.5_10.5W	1141.3	105.2	-3.4	335.8	148.3	254.1	10.7	437.6	840.0
3.0_0W	1491.0	99.6	-7.7	134.0	15.7	47.0	178.3	225.9	288.6
3.0_3W	1485.2	94.6	-1.0	198.8	47.5	91.4	182.9	292.4	431.2
3.0_6W	1482.9	88.2	5.1	256.6	84.4	147.3	186.7	350.0	581.7
3.0_9W	1476.4	86.6	3.7	295.3	119.9	206.6	193.2	385.6	712.2
3.0_10.5W	1476.0	89.9	-0.1	295.3	135.7	233.3	193.7	385.1	754.1
4.0_0W	2463.3	70.9	-5.0	86.0	5.3	36.2	196.8	151.9	193.4
4.0_3W	2461.2	66.3	-1.2	126.9	33.9	68.3	202.1	192.1	294.3
4.0_6W	2456.2	70.0	-3.5	170.1	60.9	114.2	208.6	236.6	411.6
4.0_9W	2446.8	75.2	-9.8	201.2	87.3	160.6	218.7	266.7	514.6
4.0_10.5W	2444.0	75.3	-12.4	207.5	97.6	182.8	223.1	270.5	551.0
5.0_0W	3583.0	52.3	-4.6	69.7	-3.4	30.7	81.1	117.4	144.7
5.0_3W	3576.4	54.0	-5.8	80.3	19.1	54.4	85.0	128.5	201.9
5.0_6W	3593.8	67.8	-14.6	105.2	38.0	87.0	78.4	158.3	283.4
5.0_9W	3597.5	62.7	-11.4	128.7	57.4	124.9	76.4	180.0	362.3
5.0_10.5W	3600.7	60.0	-9.7	132.3	66.4	140.6	75.0	182.6	389.6
6.0_0W	4617.7	54.6	-9.5	67.4	-7.5	25.9	60.7	112.4	130.8
6.0_3W	4607.6	58.7	-16.9	62.2	5.6	51.9	63.6	104.1	161.5
6.0_6W	4602.9	60.1	-17.0	73.5	27.5	74.2	74.9	116.6	218.3
6.0_9W	4600.6	55.5	-13.2	89.5	41.7	104.4	77.2	131.9	278.0
6.0_10.5W	4608.6	53.7	-11.8	86.6	47.5	114.8	64.9	128.6	290.9

Table C.7: Pressure drops in cooling structure (input liquid pressure $13\,\mathrm{bar}_{abs}$ / table items given in mbars).

Pressure drops in the system (% from Total DP)									
13Bar	**BPR** P_BBPR - P_BFM	**Pipe work** P_AH - P_BBPR	**Heater** P_BH - P_AH	**HEX** P_VAM - P_BH	**Manifold** P_A3 - P_VAM	**Stave** P_A1 - P_A3	**Difference** between P_dome and P_BBPR	**Total DP off-detector** P_VAM - P_BBPR	**Total DP** P_A1 - P_BBPR (mBar)
Open_0W	-	27	3	52	6	13	-	81	668.0
Open_3W	-	20	2	50	10	17	-	73	861.1
Open_6W	-	16	2	48	14	20	-	66	1061.8
Open_9W	-	13	2	45	16	24	-	60	1220.2
Open_10.5W	-	12	2	44	17	25	-	58	1336.8
1.6_0W	-	30	0	50	5	15	-	80	403.4
1.6_3W	-	20	2	49	10	20	-	70	576.5
1.6_6W	-	14	2	46	14	24	-	62	751.0
1.6_9W	-	13	1	43	16	27	-	56	894.4
1.6_10.5W	-	13	0	41	18	29	-	53	947.4
2.0_0W	-	32	-1	49	5	15	-	80	374.8
2.0_3W	-	21	0	48	11	20	-	69	543.1
2.0_6W	-	15	1	46	14	24	-	62	710.8
2.0_9W	-	12	1	43	16	28	-	56	854.6
2.0_10.5W	-	12	1	40	18	29	-	53	904.5
2.5_0W	-	30	0	48	5	17	-	78	340.6
2.5_3W	-	20	2	47	11	20	-	68	498.5
2.5_6W	-	15	1	45	15	24	-	61	658.0
2.5_9W	-	13	-1	42	17	28	-	55	795.8
2.5_10.5W	-	13	0	40	18	30	-	52	840.0
3.0_0W	-	35	-3	46	5	16	-	78	288.6
3.0_3W	-	22	0	46	11	21	-	68	431.2
3.0_6W	-	15	1	44	15	25	-	60	581.7
3.0_9W	-	12	1	41	17	29	-	54	712.2
3.0_10.5W	-	12	0	39	18	31	-	51	754.1
4.0_0W	-	37	-3	44	3	19	-	79	193.4
4.0_3W	-	23	0	43	12	23	-	65	294.3
4.0_6W	-	17	-1	41	15	28	-	57	411.6
4.0_9W	-	15	-2	39	17	31	-	52	514.6
4.0_10.5W	-	14	-2	38	18	33	-	49	551.0
5.0_0W		36	-3	48	-2	21	-	81	144.7
5.0_3W	-	27	-3	40	9	27	-	64	201.9
5.0_6W	-	24	-5	37	13	31	-	56	283.4
5.0_9W	-	17	-3	36	16	34	-	50	362.3
5.0_10.5W	-	15	-3	34	17	36	-	47	389.6
6.0_0W	-	42	-7	52	-6	20	-	86	130.8
6.0_3W	-	36	-10	39	3	32	-	64	161.5
6.0_6W	-	28	-8	34	13	34	-	53	218.3
6.0_9W	-	20	-5	32	15	38	-	47	278.0
6.0_10.5W	-	18	-4	30	16	39	-	44	290.9

Table C.8: Pressure drops in cooling structure (input liquid pressure $13\,\mathrm{bar}_{abs}$ / table items given in percentage of total pressure drop in vapour return line. %).

Input pressure [bar_a]	Power per module [W]	Power per circuit [W]	Heater power [%]	T_C2, HEX input temp [°C]	T_C1, HEX exit temp [°C]	Volume Flow [l_n/min]	Mass Flow [g/s]
10	0	0	52	16.64	-20.82	**51.8**	**10.9**
10	3	144	40	16.56	-19.57	**51.2**	**10.7**
10	6	288	26	16.92	-18.49	**50.7**	**10.6**
10	9	432	17	16.82	-12.38	**49.3**	**10.3**
10	10.5	504	11	16.65	-5.77	**49.5**	**10.4**
11	0	0	56	16.67	-19.74	**55.4**	**11.6**
11	3	144	43	16.68	-18.65	**54.6**	**11.5**
11	6	288	30	16.69	-17.83	**53.9**	**11.3**
11	9	432	18	16.70	-15.95	**53.3**	**11.2**
11	10.5	504	12	16.97	-7.59	**52.8**	**11.1**
12	0	0	65	16.64	-19.18	**58.4**	**12.2**
12	3	144	55	16.64	-17.95	**58.1**	**12.2**
12	6	288	35	16.64	-17.17	**57.6**	**12.1**
12	9	432	24	16.69	-15.65	**56.6**	**11.9**
12	10.5	504	18	16.65	-13.12	**56.2**	**11.8**
13	0	0	66	17.15	-18.62	**61.6**	**12.9**
13	3	144	55	16.8	-17.6	**60.9**	**12.8**
13	6	288	41	16.91	-16.61	**60.3**	**12.7**
13	9	432	27	16.98	-15.46	**59.8**	**12.5**
13	10.5	504	22	16.81	-14.29	**59.3**	**12.5**

Table C.9: Measurement results for Flow in system.

First and Second Cycle of measurements.

Measurements for each percentage concentration were repeated in two cycles. Results are presented on Figure 5.22. Results are presented with respect of correction coefficient calculated based on pressure and temperature difference caused by mechanical modifications done between these two cycles. At the end of the first cycle of measurements (before the 20% measurements) vapour return pipe structure (after the Heat Exchanger and before the Heater) and inlet liquid line were split into three different lines giving opportunity for other tests to be performed on the Test Station. New test structures were connected to the existing one for future tests with fluorocarbon blend mixtures for Pixel detector loops and for Heat Transfer Coefficient measurements. Installation of a new panel (presented in Figure C.1) caused an unexpected additional pressure drop over that region, causing a slight rise in temperature over the stave.

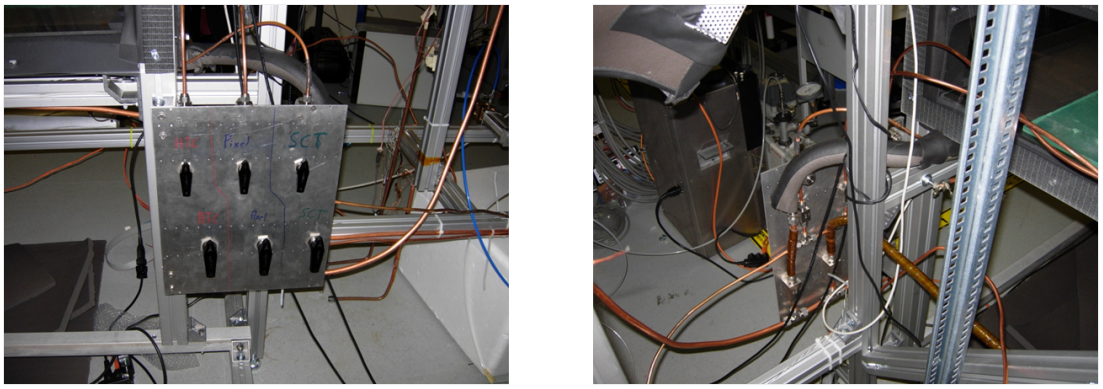

Figure C.1: Panel with manual valves. Splitted inlet and outlet pipe lines.

Pressure and temperature difference and correction coefficient is presented in Table C.10. Pressure was measured at the middle of the stave (by PS P_A2) for both cycles, for each percentage concentration and for different power load on modules. The temperature difference ΔT (correction coefficient) between the first and the second cycles, for each percentage concentration and for each power load, was calculated using predictions from NIST REFPROP [1] based on these measured pressure values. Correction coefficients were added to the

first cycle measurement values and resulted in the corrected results from the first measurement cycle matching very well the second cycle measurement results (See Figure 5.22).

%	W	P_A2_I	P_A2_II	DP	DT
0	0	1876.7	2036.9	160.2	2.113
	6	2276.4	2435.2	158.8	1.799
	10.5	2524.8	2671.6	146.8	1.543

%	W	P_A2_I	P_A2_II	DP	DT
1	0	1908.9	2027.0	118.1	1.552
	6	2283.8	2444.0	160.2	1.83
	10.5	2532.8	2671.8	139.0	1.488

%	W	P_A2_I	P_A2_II	DP	DT
3	0	1921.7	2041.8	120.1	1.589
	6	2296.3	2454.7	158.4	1.821
	10.5	2543.3	2689.2	145.9	1.563

%	W	P_A2_I	P_A2_II	DP	DT
5	0	1934.0	2051.6	117.6	1.556
	6	2313.8	2464.8	151.0	1.735
	10.5	2562.2	2699.1	136.9	1.472

%	W	P_A2_I	P_A2_II	DP	DT
10	0	1991.7	2078.7	87.0	1.149
	6	2349.1	2482.8	133.7	1.54
	10.5	2596.2	2714.8	118.6	1.27

%	W	P_A2_I	P_A2_II	DP	DT
20	0	2178.5	2178.5	0	0
	6	2550.9	2550.9	0	0
	10.5	2799.2	2799.2	0	0

%	W	P_A2_I	P_A2_II	DP	DT
25	0	---	2211.1	0	---
	6	---	2570.6	0	---
	10.5	---	2830.9	0	---

Table C.10: Calculation of Correction Coefficients for First and Second cycle of measurements.

Appendix D

Error Estimation

Temperature Measurements.

Systematic and Statistical error was calculated for measured temperature values. Standard Deviation was calculated using formula presented below:

$$\sigma = \sqrt{\frac{\sum_{i=1}^{N}(x_i - \overline{x})^2}{N-1}}$$

and Relative Standard Deviation was calculated using formula presented below:

$$\sigma_{\%} = \frac{\sigma}{\overline{x}} \times 100$$

Where:

σ - Standard deviation.

x_i - Measured value.

$\overline{x}$ - Measured mean value.

N - Number of measurements.

Systematic error values and source of this error is presented in Table D.1 and Table D.2.

Systematic Error $[\sigma_{sys1}]$

NTC Sensor $[\sigma_N]$	$\pm 1.05\%$	$\pm 1\%$ Systematic error at $10\,\mathrm{k}\Omega$ resistance value at 25°C
Readout system (ADC) $[\sigma_R]$	$\pm 0.1\%$	Systematic error of Referance resistor in ADC
Total $[\sigma_{sys\%}]$	$\mathbf{\pm 1.054\%}$	$\sigma^2_{sys\%} = \sigma^2_N + \sigma^2_R$
Total $[\sigma_{sys}]$	$\mathbf{\pm 0.213}$°C	$\sigma_{sys} = \overline{x} \times \sigma_{sys\%}/100$

Table D.1: Temperature measurement systematic error (NTC sensor and readout system).

Systematic Error $[\sigma_{sys2}]$

$[\sigma_{sys}]$	$\mathbf{\pm 0.283}$°C	Standard Deviation (attachment to the cooling pipe)
$[\sigma_{sys\%}]$	$\mathbf{\pm 1.36\%}$	Relative Standard Deviation

Table D.2: Temperature measurement systematic error caused by possible variation in NTC attachment to the cooling pipe.

For the calculation of the temperature fluctuation inside the Plexiglass box (statistical error), temperature was measured over the SCT Barrel stave by 48 NTC sensors (T_A1 - T_A25 and T_B1 - T_B25) over the 24 hours with no cooling in system. Measured temperature as a function of time is presented in Figure D.1. Fluctuation of measured temperature for each sensor is caused by temperature change of ±2°C in SR1 laboratory clean room (caused by air conditioning). As it can bee seen, this temperature change is propagated into not more than ±0.1°C change in temperature inside the Plexiglass box, due to the box being very well thermally isolated. Since the data for each test point (different pressure in system or power per module) was recorded over the 5 min time period, temperature fluctuation described above is negligible (See Figure D.2). Standard Deviation for each sensor, calculated for 24 hour and 10 min recorded data is presented in Table D.3.

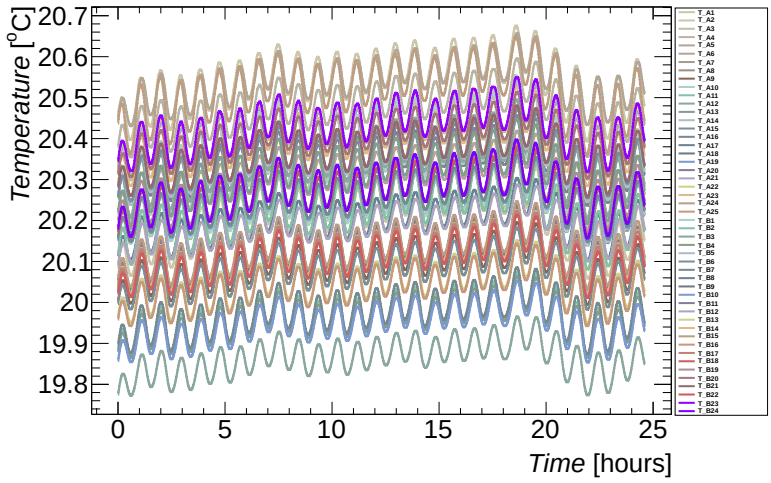

Figure D.1: Temperature measured over the SCT Barrel stave by 48 NTC sensors, over the 24 hours. Cooling is OFF.

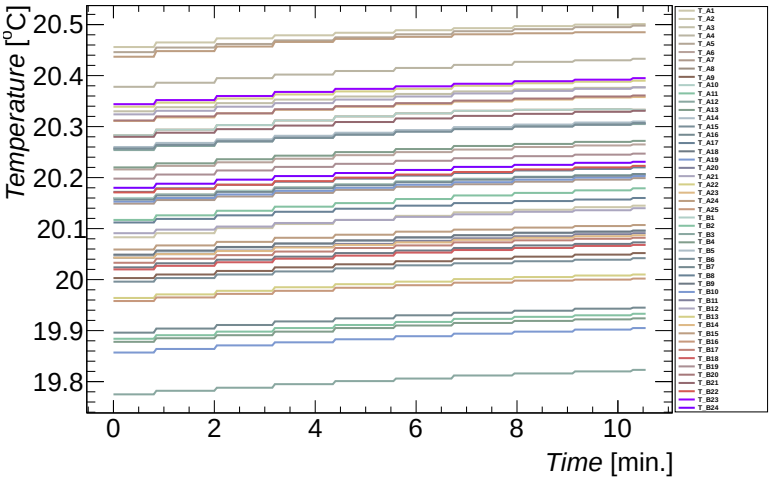

Figure D.2: Temperature measured over the SCT Barrel stave by 48 NTC sensors, over the 10 minutes. Cooling is OFF.

Sensor:	σ (24 hours)	σ (10 min.)
T_A1	0.066	0.019
T_A2	0.061	0.014
T_A3	0.055	0.015
T_A4	0.053	0.017
T_A5	0.049	0.016
T_A6	0.047	0.015
T_A7	0.045	0.015
T_A8	0.046	0.014
T_A9	0.044	0.015
T_A10	0.046	0.015
T_A11	0.045	0.015
T_A12	0.042	0.015
T_A13	0.043	0.014
T_A14	0.046	0.015
T_A15	0.044	0.014
T_A16	0.047	0.015
T_A17	0.045	0.015
T_A18	0.048	0.015
T_A19	0.046	0.015
T_A20	0.048	0.015
T_A21	0.049	0.016
T_A22	0.053	0.016
T_A23	0.054	0.015
T_A24	0.064	0.015
T_A25	0.081	0.017
T_B1	0.061	0.019
T_B2	0.062	0.016
T_B3	0.055	0.016
T_B4	0.051	0.015
T_B5	0.047	0.015
T_B6	0.046	0.015
T_B7	0.045	0.015
T_B8	0.045	0.015
T_B9	0.044	0.015
T_B10	0.045	0.015
T_B11	0.041	0.015
T_B12	0.044	0.014
T_B13	0.045	0.014
T_B14	0.046	0.015
T_B15	0.044	0.014
T_B16	0.047	0.015
T_B17	0.044	0.015
T_B18	0.048	0.015
T_B19	0.046	0.015
T_B20	0.049	0.016
T_B21	0.048	0.016
T_B22	0.052	0.015
T_B23	0.053	0.016
T_B24	0.067	0.017
T_B25	0.081	0.016

Table D.3: Standard Deviation [σ] for each temperature sensors. (24 hour and 10 min recorded data)

For the calculation of the temperature measurement error caused by the possible small variation in NTC sensor attachment (sensors could be not uniformly attached to the cooling pipe), standard deviation in measured temperature values is calculated based on the data recorded for 13 bar_{abs} inlet pressure, 1.2 bar_{abs} back pressure and 0 W power per module for 0% C_2F_6. Distribution of temperature values measured over the stave and Standard Deviation (RMS) is presented in Figure D.3.

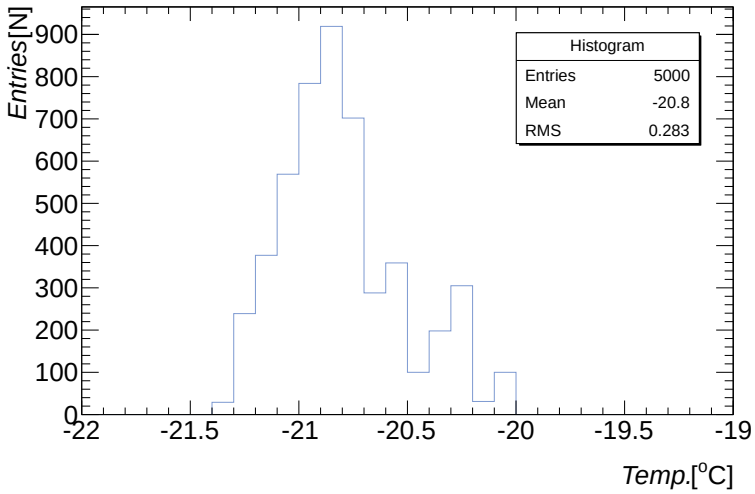

Figure D.3: Distribution of temperature values measured over the stave and Standard Deviation (RMS) .

The total error in temperature measurement is calculated using the equation:

$$\sigma_{T.tot} = \sqrt{\sigma_{sys1}^2 + \sigma_{sys2}^2} = \sqrt{0.213^2 + 0.283^2} = 0.35\,^{\circ}\text{C}$$
$$\sigma_{T.tot\%} = \sqrt{\sigma_{sys\%1}^2 + \sigma_{sys\%2}^2} = \sqrt{1.054^2 + 1.36^2} = 1.72\%$$

Error in the temperature measurement is presented as an error bars in figures in Chapter 4 and Chapter 5.

Pressure Measurements.

For pressure measurement in points of interest over the Test System there are KELLER Type PAA-33X [45] pressure transducers mounted into the system. Parameters for KELLER PT are listed in Table D.4.

Description	**PAA-33X / 30bar / 80794**
Pressure	0...30 [bar_{abs}]
Output signal	4...20 [mA, RS485]
Pressure port	G1/4”
Electrical connection	Binder 723/5-p
Supply	8...28 [V]

Table D.4: Parameters for KELLER PT.

Accuracy for KELLER Pressure transmitters equals to 0.15% FS and Precision equals to 0.01 %FS (giving measurement uncertainty of ±19.5 mbar in case of Inlet pressure measurements and ±1.8 mbar in case of Outlet pressure measurements).

For the calculation of the pressure measurement error caused by the pressure instability in the system, standard deviation in measured pressure values is calculated based on the data recorded by the pressure sensor at the exit of the stave (P_A3 sensor) in case of 13 bar_{abs} inlet pressure, 1.2 bar_{abs} back pressure and 0 W power per module for 0% C_2F_6. Distribution of the measured pressure values and Standard Deviation (RMS) is presented in Figure D.4.

The total error in pressure measurement is calculated using the equation:

$$\sigma_{P.tot.Out} = \sqrt{\sigma_{sys1}^2 + \sigma_{sys2}^2} = \sqrt{9.7^2 + 1.8^2} = 9.86\,\text{mbar}.$$
$$\sigma_{P.tot.Out\%} = \frac{\sigma}{\overline{x}} \times 100 = \frac{9.7}{1947} \times 100 = 0.49\%$$

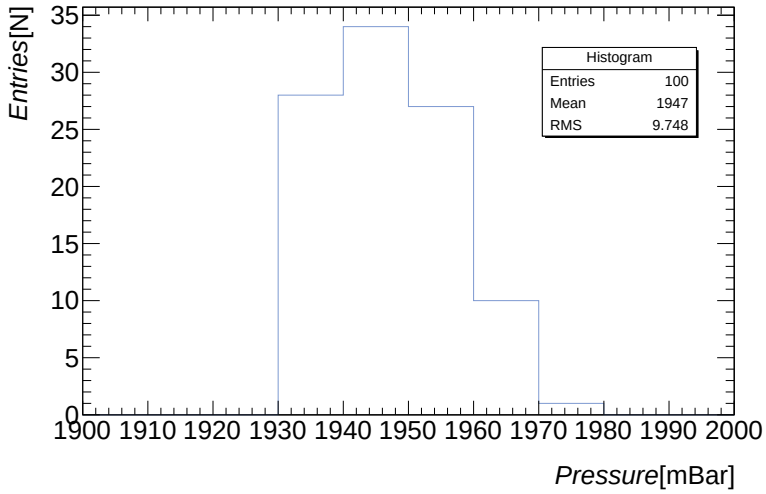

Figure D.4: Distribution of the pressure values measured at the exit of the stave (P_A3 sensor) and Standard Deviation (RMS) .

For pressure measurements in Sonar Analyzer, Huba® [55] pressure transmitter is used. Parameters for Huba PT are listed in Table D.5.

Description	**Type 680**
Pressure	0...6 [bar_{abs}]
Output signal	0...10 [V (DC)]
Pressure port	G1/4”
Electrical connection	Binder 723/5-p
Supply	15...30 [V (DC)]

Table D.5: Parameters for Huba PT.

Total Error band (including characteristic line deviation, temperature error zero point and operating range, hysteresis and repeatability at max. signal range.) for Huba Pressure transmitters equals to 1.5% FS giving measurement uncertainty of ± 15 mbar at the measured pressure of 1 bar. Standard Deviation (Statistical Error) for measured pressure values $\sigma \leq 4.2$ mbar (Data for 24 hours) and $\sigma \leq 2.05$ mbar (Data for 10 min).

Error in the pressure measurement is presented as an error bars in figures in Chapter 4 and Chapter 5.

Sound Velocity and Mixture Concentration Measurements.

Uncertainty / Standard deviation in sound velocity measurements made by Sonar Analyzer (Section 5.2) is calculated using formula presented below:

$$\sigma_{Vs(tot)} = \sqrt{(\sigma^2_{Vs(temp.)} + \sigma^2_{Vs(press.)} + \sigma^2_{Vs(dist.)} + \sigma^2_{Vs(time)})}$$

Where:

$\sigma_{Vs(tot)}$ - Total Uncertainty in sound velocity measurement.

$\sigma_{Vs(temp.)}$ - Temp. dependent uncertainty in sound velocity measurement.

$\sigma_{Vs(press.)}$ - Pressure dependent uncertainty in sound velocity measurement.

$\sigma_{Vs(dist.)}$ - Distance dependent uncertainty in sound velocity measurement.

$\sigma_{Vs(time)}$ - Timing dependent uncertainty in sound velocity measurement.

Step by step calculation, as an example for 80%C_3F_8/20%C_2F_6 mixture, is presented below:

[1.]Temp. dependent uncertainty in sound velocity measurement:

NTC statistical error = ± 0.2°C

Sound velocity $c = \sqrt{(\gamma \times R \times T)/M}$

$\gamma = 1.021$

$R = 8.3145$ Jmol^{-1}K^{-1}

Molar mass C3F8 = 188.02 [gmol^{-1}]

Molar mass C2F6 = 138.01 [gmol^{-1}]

Velocity (20°C) c = 118.237 [ms^{-1}]

$[c = \sqrt{(1.021 \times 8.3145 \times (273.15 + 20))/(0.2 \times 0.138 + 0.8 \times 0.188)}]$

Velocity (20+0.2°C) c = 118.277 [ms^{-1}]

$[c = \sqrt{(1.021 \times 8.3145 \times (273.15 + 20 + 0.2))/(0.2 \times 0.138 + 0.8 \times 0.188)}]$

$\sigma_{Vs(temp.)}$ **= 0.040326346 [ms^{-1}]**

$\sigma_{Vs\%(temp.)}$ **= 0.034** %

[2.]Pressure dependent uncertainty in sound velocity measurement:

Pressure transducer precision ±15 mbar

Sound velocity NIST prediction 1 bar, 20°C 80%C_3F_8/20%C_2F_6 c = 118.68 [ms^{-1}]

Sound velocity NIST prediction 1.015 bar, 20°C 80%C_3F_8/20%C_2F_6 c = 118.65 [ms^{-1}]

$\sigma_{Vs(press.)}$ **= 0.03 [ms^{-1}]**

$\sigma_{Vs\%(press.)}$ **= 0.025** %

[3.]Distance dependent uncertainty in sound velocity measurement:

Distance (between sound transducers) uncertainty L = ±0.0001 m

Sound velocity c = L/t

Typical sound velocity 20°C 80%C_3F_8/20%C_2F_6 c = 118.237 [ms^{-1}]

Typical transit time (0.666 m) t = 0.005632762 [s]

Transit time (0.666+0.0001 m) t = 0.005633608 [s]

Transit time difference Δt = 0.00000084576 [s]

Sound velocity with modified distance c = 118.2545974 [ms^{-1}]

$\sigma_{Vs(dist.)}$ **= 0.01775328 [ms^{-1}]**

$\sigma_{Vs\%(dist.)}$ **= 0.015** %

[4.]Timing dependent uncertainty in sound velocity measurement:

Clock frequency of 40 MHz ==> 25μs

(Likely uncertainty in finding zero time of first pulse 1μs)

Sound velocity c = L/t

Typical sound velocity 20°C 80%C_3F_8/20%C_2F_6 c = 118.237 [ms^{-1}]

Canonical distance L = 0.666 [m]

Typical transit time (0.666 m) t = 0.005632762 [s]

Typical time +1μs uncertainty t = 0.005633762 [s]

Sound velocity with modified time c = 118.2158569 [s]

$\sigma_{Vs(time)}$ **= 0.020987192 [ms^{-1}]**

$\sigma_{Vs\%(time)}$ **= 0.01775328** %

Total Uncertainty in sound velocity measurement:

$\sigma_{Vs(tot)} = \sqrt{\sigma^2_{Vs(temp.)} + \sigma^2_{Vs(press.)} + \sigma^2_{Vs(dist.)} + \sigma^2_{Vs(time)}}$

$\sigma_{Vs(tot)} = \sqrt{(0.040326346)^2 + (0.03)^2 + (0.01775328)^2 + (0.020987192)^2}$

$\sigma_{\mathbf{Vs(tot)}} = \mathbf{0.05728748}\ [\mathbf{ms^{-1}}]$

$\sigma_{\mathbf{Vs\%(tot)}} = \mathbf{0.04845139}\ \%$

Uncertainty in mixture concentration:

$\sigma_{Mix\%} = \sigma_{Vs(tot)}/m$

Local slope of the sound velocity/concentration curve $m = 0.1769$ [$\mathrm{ms^{-1}\%^{-1}}$]

$\sigma_{Mix\%} = 0.05728748/0.1769$

$\sigma_{\mathbf{Mix\%}} = \mathbf{0.323841041}\ [\%]$*****

*note that uncertainty in mixture concentration (Measurement Error) is presented in percentage of mixture concentration, not the relative % value. (For example in case of 20%C_2F_6 blend into mixture, real concentration will be between 19.68% and 20.32%)

Measurement Error, for the binary gas mixture, of $\pm$**0.3%** is presented as an error bars in Figure 5.10 and Figure 5.21.

Flow Measurements.

Standard accuracy (based on actual calibration) of Bronkhorst® flow meter (model F-113AC-AAD-99-V) is ±0.8% RD + ±0.2% FS.

Standard Deviation [σ] of measured flow values were calculated and presented in Table D.6. Biggest standard deviation $\sigma = 0.235\,\mathrm{lmin}^{-1}$ or $\sigma = 0.049\,\mathrm{gs}^{-1}$. Error bars are presented on the plots (Figure 4.22, Figure 4.23) but they are too small to be visible.

$\mathbf{P}_{in}$ / **W**	**Standard Deviation** σ**[lmin**$^{-1}$**]**	**Standard Deviation** σ**[gs**$^{-1}$**]**
10 bar_a / 0 W	0.226	0.047
10 bar_a / 3 W	0.153	0.032
10 bar_a / 6 W	0.090	0.019
10 bar_a / 9 W	0.235	0.049
10 bar_a / 10.5 W	0.063	0.013
11 bar_a / 0 W	0.232	0.049
11 bar_a / 3 W	0.153	0.032
11 bar_a / 6 W	0.117	0.025
11 bar_a / 9 W	0.108	0.023
11 bar_a / 10.5 W	0.156	0.033
12 bar_a / 0 W	0.191	0.040
12 bar_a / 3 W	0.106	0.022
12 bar_a / 6 W	0.126	0.026
12 bar_a / 9 W	0.145	0.030
12 bar_a / 10.5 W	0.092	0.019
13 bar_a / 0 W	0.180	0.038
13 bar_a / 3 W	0.144	0.030
13 bar_a / 6 W	0.091	0.019
13 bar_a / 9 W	0.093	0.020
13 bar_a / 10.5 W	0.081	0.017

Table D.6: Standard Deviation of measured flow values.

Volume flow [lmin^{-1}] is recalculation into Mass flow [gs^{-1}] using formula :

$$M = \frac{X}{60} \times \frac{R}{1000} \times \frac{P}{P_s} \times 1000$$

Where: M - Mass flow [gs^{-1}], X - Volume flow [lm^{-1}], R - Density of Vapour for 20°C(73.44)[kgm^{-3}], P - Pressure in pipe [bar_{abs}], P_s - Saturation Pressure (7.58)[bar_{abs}].